

Editorial corner – a personal view

Polymeric nanofibers for medical applications: A real disco

Eva Kuželová Košťáková*^{id}

Faculty of Science, Humanities, and Education, Department of Chemistry, Bioengineering Group, Technical University of Liberec, Studentská 2, 46117 Liberec, Czech Republic

Polymeric nanofibers produced from biocompatible and biodegradable materials are being investigated for a variety of applications in the 21st century. They have significant application potential in the field of medicine. Polymeric nanofibers as scaffolds for tissue engineering, wound dressings, or drug delivery systems offer production variability and a huge number of flexible structures with changes in morphology, topography, or internal structure. The uniqueness of polymeric nanofibrous materials for medical applications is that their structure very closely mimics the tissue's extracellular matrix.

The spinnability of a polymer liquid (solution or melt) into the form of nanofibers depends on many parameters, and the essence of spinnability as a property of a polymer liquid is still not easily defined. Obviously, it is necessary to use a certain force for polymer liquid transformation and to overcome the force from the liquid surface tension, which keeps the liquid in the form with the lowest free surface energy. But the properties of materials in general, including nanofibers, are determined by their structure and chemical composition. Thus the choice of the base material, *i.e.*, the polymer, is crucial for polymeric nanofibrous materials.

Popular biocompatible and biodegradable polymers for the formation of nanofibers for medical applications are aliphatic polyesters, especially the well-spinnable polycaprolactone (PCL) (<https://doi.org/10.1016/j.progpolymsci.2010.04.002>), which has outstanding properties (<https://doi.org/10.1016/j.compscitech.2010.01.010>). However, the crystal morphology and molecular orientation – internal structure of PCL nanofibers has rarely been investigated. The

known information on PCL indicates that under normal conditions (temperature, humidity) in the post-process time (storage), there are changes in the internal structure, the arrangement, and the surface. The internal arrangement, which can basically be described by the degree of crystallinity, changes rapidly after processing (cold recrystallization occurs). The surface of such biodegradable materials is certainly also rebuilt due to air humidity in the post-processing time. In the case of initially hydrophobic PCL nanofibers, this is manifested by a change in water wettability over time. Then moisture penetrates inside and degradation, which is led by hydrolysis, has space to express itself. Amorphous parts prefer to decompose, and secondary restructuring – rearrangement – occurs in the decomposed parts. Not only the surface but also the volume changes.

Polymeric nanofibers are extremely interesting in general, but if they are made of biodegradable aliphatic polyesters, they undergo almost constant changes in their arrangement and, therefore, their internal structure. And when they are subjected to an external stimulus such as sterilization, the effect can be even more complex. We should not think of polymer nanofibers as stable, unchanging solid materials. Inside polymeric biodegradable nanofibers, there is still going on a real disco.



Eva Kuželová Košťáková

*Corresponding author, e-mail: eva.kostakova@seznam.cz
© BME-PT

Review article

Recent insight into the biomedical applications of polybutylene succinate and polybutylene succinate-based materials

Asanda Mtibe^{1*}, Sudhakar Muniyasamy^{1,2}, Teboho Clement Mokhena⁴, Osei Ofosu^{1,3}, Vincent Ojijo¹, Maya John^{1,2}

¹Centre for Nanostructures and Advanced Materials, DSI-CSIR Nanotechnology Innovation Centre, Council for Scientific and Industrial Research, Pretoria, South Africa

²Department of Chemistry, Nelson Mandela University, Port Elizabeth, South Africa

³Department of Textile Science, Nelson Mandela University, Port Elizabeth, South Africa

⁴DSI/Mintek – Nanotechnology Innovation Centre, Advanced Materials, Mintek, 2125 Randburg, South Africa

Received 16 May 2022; accepted in revised form 13 August 2022

Abstract. The development of biodegradable and biocompatible materials to replace non-biodegradable synthetic polymers has received significant interest in biomedical applications. Amongst all biopolymers, polybutylene succinate (PBS) possesses excellent properties, such as biocompatibility, easy processability, biodegradability, non-toxic, good mechanical and thermal properties, which makes it a suitable candidate to replace non-biodegradable synthetic polymers in biomedical applications. This review provides recent advancements, trends, and challenges for the utilization of polybutylene succinate (PBS) and PBS-based materials for biomedical applications, *viz.* drug delivery, tissue engineering, and biomedical devices. In addition, the design of medical devices from PBS using 3D and 4D printing is also presented. The market analysis, comparison of virgin PBS and synthetic polymer properties, as well as the end of service life, are summarized briefly. The current status, challenges, and future directions are also discussed.

Keywords: *biopolymers, polymer composites, polymer blends, properties, biomedical applications*

1. Introduction

In recent years, advances in material science have led to the discovery and development of novel biodegradable and biocompatible materials for biomedical applications as a substitute for non-biodegradable synthetic polymers [1]. Synthetic polymers contribute to waste disposal problems because they are resistant to microbial degradation [2]. The properties of biopolymers being biodegradable and biocompatible have garnered considerable attention in biomedical applications, such as tissue engineering, drug delivery system, and wound dressing, because, after the end of service life, they hydrolyze within

the body system and do not leave any toxic byproducts thus, showing a potential for these applications. Aliphatic polyesters, such as polylactic acid (PLA), polycaprolactone (PCL), and polybutylene succinate (PBS) have demonstrated great potential in biomedical applications due to their attractive features, such as environmental friendliness, biocompatibility, non-immunogenicity, and good thermal and mechanical properties [3–7]. For example, PLA is the most studied biopolymer, however, it has shortcomings, *i.e.*, brittleness, and low impact resistance, which have been major concerns, especially for biomedical applications. PBS has recently become a research hotspot

*Corresponding author, e-mail: AMtibe@csir.co.za

© BME-PT

due to its impressive features, such as good processability, chemical and heat resistance, biodegradability, good mechanical and thermal properties, biocompatibility, and non-toxicity [8]. In addition, its properties can be tuned by copolymerization and other modifications to achieve desired application. Unfortunately, PBS has shown some drawbacks, which include insufficient osteoblast compatibility and bioactivity, poor wettability with a contact angle of $\sim 130^\circ$, and high production cost [8–11]. These drawbacks have greatly hindered the wide-scale applications of PBS in biomedical applications, and hence, the modification of PBS is critical to expanding its applications.

Several approaches that are reported to mitigate PBS limitations include reinforcing, blending, and copolymerization. For instance, a copolymer poly(butylene-co-dilinoic succinate) (PBS-co-DLS) was developed for heart tissue engineering in order to overcome some limitations associated with virgin PBS. The copolymer demonstrated good mechanical properties matching properties of cardiac tissues, improved cell proliferation, and excellent biocompatibility. In addition, PBS copolymer degraded into non-cytotoxic byproducts [12]. Generally, the science of modification of PBS is relatively new when compared to their synthetic polymer counterparts. Therefore, further research is necessary to achieve the full potential of PBS.

A number of reviews related to PBS properties, biodegradation, and expanded applications, such as food packaging, biomedical, tableware, and mulch films, as well as modification of PBS have been published [8, 13, 14]. However, reviews on PBS and PBS-based blends and composites focusing specifically on biomedical applications are very few. For instance, Gigli *et al.* [13] published a comprehensive review on PBS-based materials for biomedical applications. However, in their study, they only focused on the drug delivery system. This contribution is aimed at providing recent advances in PBS-based materials in biomedical applications, specifically for drug delivery systems, tissue engineering, and biomedical devices. The application of PBS and PBS materials in 3D and 4D are also highlighted for future healthcare purposes. Moreover, the end-of-service life options of PBS-based materials, current status, and future outlook will also be discussed.

2. PBS market size

PBS comprises repeated $C_8H_{12}O_4$ units as shown in Figure 2, and is synthesized via the polycondensation method from 1,4 butanediol and succinic acid, which can be obtained from both petroleum and biobased sources. However, PBS obtained from petroleum-based monomers is usually referred to as conventional PBS, whereas the one obtained from biobased monomers is often referred to as Biobased PBS or BioPBS. Although the sources differ, their characteristics remain the same.

PBS offers a great opportunity to replace non-biodegradable synthetic polymers, such as polypropylene (PP) and polyethylene (PE). Since the first synthesis of PBS in the 1930s, over the years, it has been synthesized by well-established companies as well as in some research laboratories. The major producers and suppliers are in China, the United States of America, Thailand, and Germany. The key producers and suppliers of commercially available PBS are Kingfa, BioAmber (DNP/ARD), Myriant, PTT MCC Biochem, Reverdia, and BASF, with a production capacity of 30 000 metric tonnes per annum. The global market of PBS is growing immensely, and it is projected to grow fast in the next few years. Recently, Data Bridge Market Research analyses have reported that the market PBS is expected to grow at a Compound Annual Growth Rate (CAGR) of 7.3% from 2021 to 2028 and is anticipated to reach a market of USD 242,803.69 thousand [15]. To achieve the predicted 7.3% increase, there is a need to start up new companies for PBS production as well as to expand the production capacity of the existing well-established companies. In addition, PBS is an emerging biopolymer and therefore, diversification of PBS applications is a necessity to ensure its market growth [15].

The growth in market size and the demand for PBS is attributed to the increasing demand for biodegradable and biocompatible based products in various sectors, such as food packaging, agricultural, automotive, biomedical, and others. Several program – circular economy. The main aim is to address plastic waste pollution and global warming in the long run. In addition, according to the Web of science, over the past 10 years, there has been a growth in the number of publications on PBS topic, as depicted in Figure 1. Another boost towards the growing market of PBS is its excellent properties which include biodegradability,

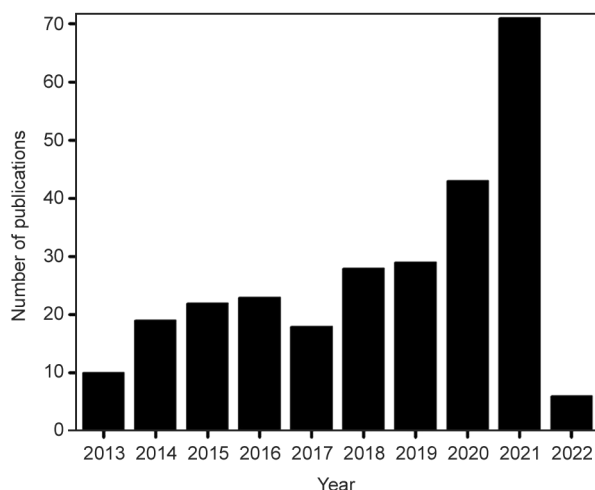


Figure 1. Publications of polybutylene succinate.

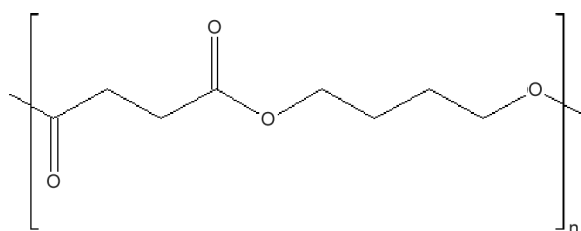


Figure 2. Polybutylene succinate (PBS).

eco-friendliness, good mechanical and thermal properties, as well as heat and chemical resistance. PBS properties are similar to those of non-biodegradable synthetic polymers, and they are summarized in

Table 1. Moreover, the properties of PBS make it a suitable candidate for biomedical applications. However, further research is still needed to exploit PBS to achieve its full potential since it is an emerging biopolymer. Even though the projections demonstrated the rapid growth of the PBS market, PBS faces significant challenges that may negatively impact its market. The first challenge includes inadequate properties of PBS to be used as virgin biopolymer, and thus, it requires blending and reinforcing technology to improve their properties. The blending technique has shown several drawbacks, such as the immiscibility of polymers and the cost of the final product becoming high in most cases. On the other hand, the reinforcing challenge is agglomeration which affects the properties of the final product. The second challenge is the high cost and fluctuation cost of raw materials, which makes PBS expensive biopolymer and negatively impacts their market size.

3. Biomedical applications of PBS and PBS-based materials

Various processing technologies such as electrospinning, compression moulding, and 3D printing have been employed to develop PBS-based materials for biomedical applications, specifically, drug delivery, tissue engineering, wound dressing as well

Table 1. Mechanical and thermal properties (glass transition temperature (T_g), melting temperature (T_m)) of PBS and synthetic polymers counterparts.

PBS	Tensile strength [MPa]	Tensile modulus [MPa]	Elongation at break [%]	T_g [°C]	T_m [°C]	Molecular weight [g/mol]	Crystallinity [%]	References
Lab scale	31.08±0.3	513±60	8.9±0.2	n.r.	114.0	47 500	35.0	[16]
Lab scale	6.2±0.7	20±3	151±7	-32	114	50 000	n.r.	[17]
Lab scale	30±2	330±13	23±4	-32	115	48 300	56	[18]
Medical-grade PBS	33	–	700	-32	114	n.r.	n.r.	[9]
PBS (Bionolle 3001, Showa Denko)	37.29±2.01	287±16.7	605±62.19	n.r.	112.5	n.r.	3.2	[19]
PBS (Natureplast)	39.37±0.28	790±0.02	17.85±.02	n.r.	n.r.	n.r.	n.r.	[20]
PBS (Xinjiang Blue Ridge Tunhe Polyester Co. Ltd.)	41.5±2.8	554±45	324±36	n.r.	114.8	83 000	47.82	[21]
PBS (Bionolle 3002, Showa Denko)	18.3±1.6	159±61	432.7±57.4	-45	95.2±1.4	n.r.	n.r.	[22]
BioPBS (FZ71PM, PTT MCC Biochem Co., Ltd., Bangkok)	40.7	740	119	-17.0	115.4	n.r.	34.5	[23]
PP (Shazand Petrochemical Company)	29	850	28	n.r.	164.6	n.r.	51.5	[24]
High-density polyethylene (HDPE) (SABIC)	24.2±0.9	1220±29	50.0±14.9	n.r.	132.7	n.r.	71.0	[25]

n.r. = not reported

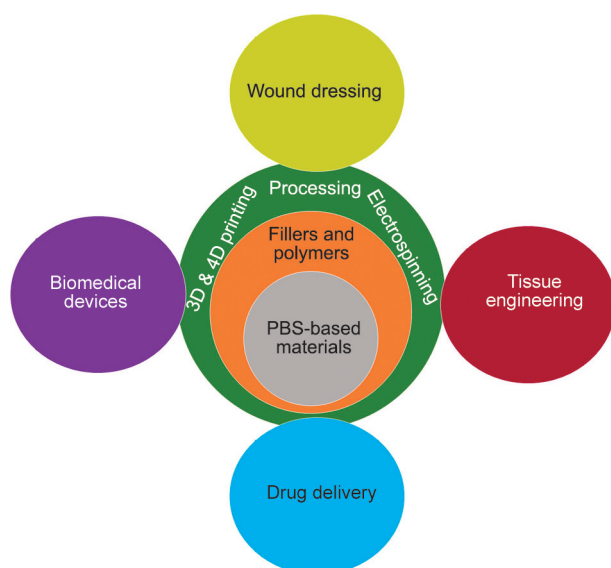


Figure 3. Biomedical applications of PBS-based materials.

as biomedical devices. Much research and development have been focusing on tissue engineering and drug delivery system. However, research on PBS-based wound dressing and biomedical devices is still in the developmental phase. Figure 3 summarizes the process of developing PBS-based material for medical applications. Due to the growing market size of PBS, it is anticipated that new applications such as 3D and 4D printing will be introduced yearly. In this section, the applications of PBS in drug delivery, tissue engineering, and biomedical devices will be discussed, citing recent literature on the new developments.

3.1. Polybutylene succinate (PBS) based materials for drug delivery system

In drug delivery systems, polymers are used to control the release of drugs into the body by either oral administration and/or implant [26]. A drug delivery system is used to sustain the release of drugs and avoid or minimize the daily taking of drugs as well as reduce the side effects [1].

Drug release depends on many factors to obtain the desired results. These factors include preparation method, distribution of drugs into the matrix, concentration of drug, and the interaction between drugs and polymer matrix [1, 26]. For instance, the direct compression process has been used to develop a drug delivery system to control the release of drugs. This is due to the low cost and industrial scalability of the process [1]. It was reported in the study of Llorens *et al.* [26] that poor interaction between drug and polymer matrix resulted in drug migration.

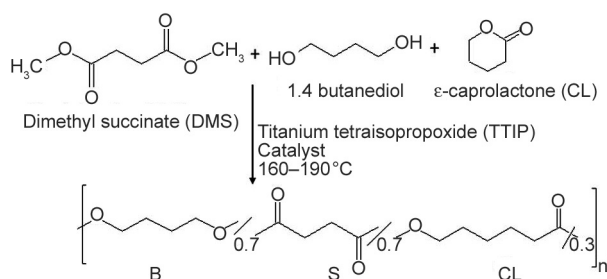


Figure 4. Synthesis of poly(butylene succinate-*co*- ϵ -caprolactone). Redraw from [1].

There are several methods reported in the literature used to fabricate drug delivery systems with prolonged release of drugs for oral administration and/or implant. These methods include compression moulding and melt extrusion. For instance, Fabbri *et al.* [18], Khalil *et al.* [27], and Galdón *et al.* [1] fabricated PBS-based materials for drug delivery using hot melt processing. In the case of Galdón *et al.* [1], a copolymer poly(butylene succinate-*co*- ϵ -caprolactone) (Figure 4) was developed to control the release of theophylline, a drug used for lung disease using direct compression, ultrasound-assisted compression, and hot melt extrusion.

A blend of 70/30 (PBS/ ϵ -caprolactone) was prepared, and various loadings (12 to 47%) of theophylline were added to the blends. It was reported that 100% release in 240 min was achieved when 12% was loaded. However, higher loading of more than 12% has resulted in the prolonged release of 100% theophylline to 300 min [1]. Furthermore, the use of PBS-based blend controlled the release dosage of theophylline.

Even though the aforementioned methods (compression moulding and melt extrusion) are widely used in drug delivery systems, there are some inherent drawbacks. For instance, compression moulding and melt extrusion use high temperatures, which can destroy the integrity of the drug. In some cases, plasticizers are added during the melt extrusion processing to improve the processabilities of polymeric material, which is used for drug delivery systems. Some of the widely used plasticizers (*e.g.*, phthalate esters) have been found to be carcinogenic [28].

Most recently, the use of electrospinning techniques to fabricate drug delivery systems has become a research hotspot for developing PBS-based drug delivery systems [12, 17, 26]. Llorens *et al.* [26], a novel scaffold comprising PBS and poly(ethylene glycol) (PEG) for drug delivery system using coaxial electrospinning was developed to control the release

of triclosan and curcumin. This novel technology allows the fabrication of micro and/or nanofibers with a core-shell structure consisting of different compositions. The ensued PBS/PEG electrospun fibres were loaded with triclosan and curcumin. The results suggested that the release of triclosan in phosphate buffer saline was low. This was due to the adsorption of hydrophobic triclosan in hydrophobic PBS. However, it was reported that the lower release of triclosan was adequate to inhibit bacterial colonization. It was also highlighted that the addition of ethanol in phosphate buffer saline led to the higher release rate of triclosan. In the case of curcumin, the medium release was observed due to its hydrophobic nature and good interaction with PBS. PBS can be functionalized to enhance the interaction with the cellular environment [29]. It is worth noting that the release of curcumin was independent of fibre structure and fibre composition, as well as the presence of ethanol in the medium. In addition, the adhesion and cell proliferation results revealed that both drugs were released during culture.

There are several methods reported to fabricate a drug delivery system. These methods include compression moulding, extrusion, and electrospinning. Recently, there has been a welcomed paradigm shift towards PBS-based nanospheres and microspheres as alternative drug delivery systems [30–33]. This is attributed to the fact that they can be tailored to attain desired particle size morphology and size distribution for good control of drug release.

Mohanraj *et al.* [30] developed PBS microspheres for the delivery of L-dopa. The cationic surfactant cetyl trimethylammonium bromide (CTAB), which produced smooth surface microspheres, as well as non-ionic poly(vinyl alcohol) (PVA), which produced porous microspheres were selected. Phosphate buffer saline and cerebrospinal fluid were used as release media. It was reported that the encapsulation efficiency for smooth and porous microspheres was 62.28 ± 1.08 and $53.93 \pm 1.58\%$, respectively. In addition, the release of L-dopa using phosphate buffer saline from smooth and porous were 25.52 and 30.95%, respectively, within 1 hour. In the case of cerebrospinal fluid, the release of L-dopa within 1 hour from smooth and porous were 28.56 and 58.02%, respectively. Furthermore, the drug release rate was reported to increase over a period due to the slow degradation of microspheres. Based on their findings, the authors suggested that microspheres

loaded with drugs can be administered by intravenous injection so that it reaches the target organ very quickly. Brunner *et al.* [32] reported similar observations. In their study, they investigated the effect of concentration of PVA, encapsulation efficiency of all-trans retinoic acid (atRA), and drug loading. The results revealed that atRA was successfully encapsulated with the encapsulation efficiency of 75% and drug loading of 14% when 4% of PVA concentration was used. The release rate was 9% in 4 weeks. In another study reported by Murase *et al.* [31] PBS microsphere was developed to control the delivery of indoles (indole, 1-methylindole, 2-methylindole, 3-methylindole, 2-phenylindole). The authors indicated that the encapsulation efficiency of the drugs studied was not the same. For instance, 1-methylindole had the lowest encapsulation efficiency, whereas 2-phenylindole had the highest when compared to all other drugs studied. It is worth mentioning that the lower the encapsulation efficiency, the weaker the interaction between the drug and the polymeric matrix. The major drawback of indoles is their slight solubility in water. The authors reported that about 80% of indoles were released from microspheres after 4 hours. However, due to the slight solubility in water, the release was halted after 4 hours of exposure. The solubility of drugs was improved by the addition of ethanol into a release medium (phosphate buffer saline). The authors reported that ethanol enhances the hydrophobicity and the swelling of microspheres which results in the improvement of drug diffusion to the medium. Moreover, the results demonstrated that indoles could be used as antiproliferative drugs for cancer cells.

Some of the drawbacks restricting the widespread use of PBS in the biomedical sector include hydrophobicity, slow degradation rate, inadequate biocompatibility, and lack of reactive centers for binding with drugs [29]. In recent years, three main strategies have been used to mitigate these challenges and expand its applications; these include copolymerization and developing blends of PBS with different polymers to improve their properties. The blending technique is an interesting solution to enhance the properties, but it is limited by compatibility considerations. The third strategy involves reinforcements with fillers or fibres to enhance their performance while the PBS matrix provides structural properties.

Different research groups synthesized various novel PBS copolymers possessing unique properties, such

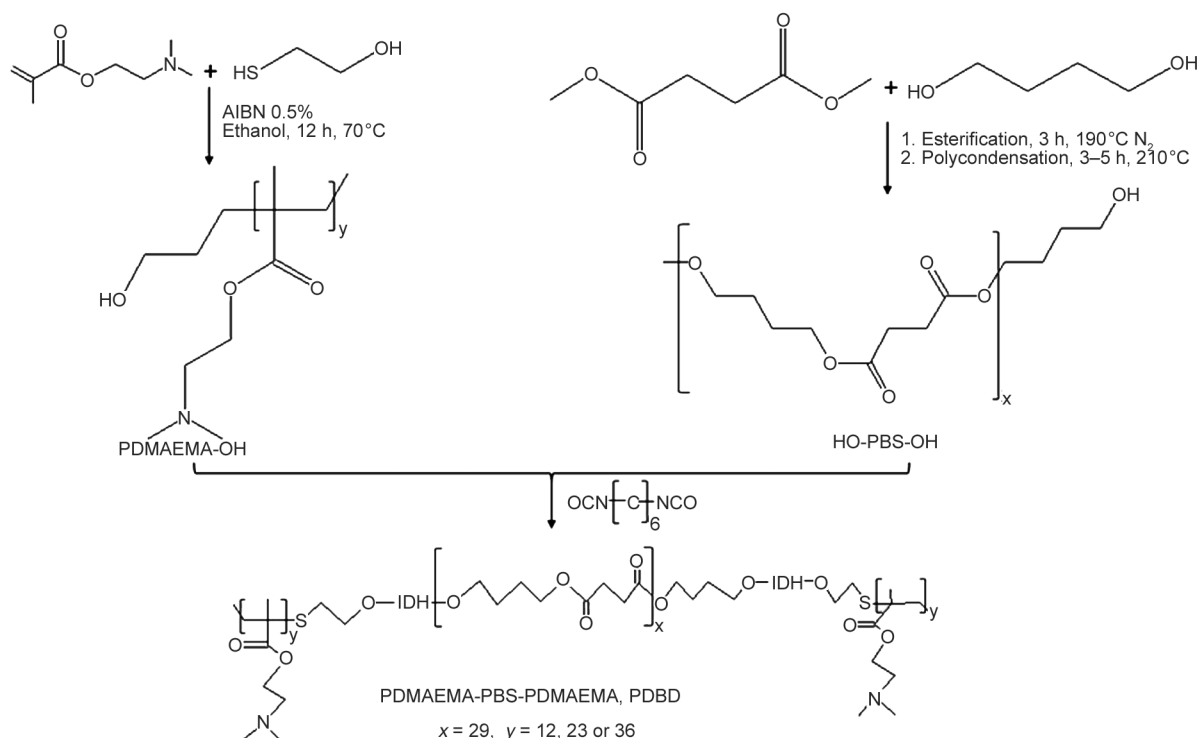


Figure 5. Synthesis of poly[2-(dimethylamino)ethylmethacrylate]–poly(butylene succinate)–poly[2-(dimethylamino)ethylmethacrylate] (PDMAEMA–PBS–PDMAEMA, PDBD). Redraw from [29].

as biodegradation, hydrophilicity, and biocompatibility for drug delivery [18, 29, 34–36]. In addition, the introduction of functional groups in ether linkages of PBS chains triggers the hydrolysis degradation process and their flexibility [18]. These researchers successfully synthesized PBS copolymers by modifying PBS chains to control the delivery of drugs. In the case of Zhao *et al.* [29], a novel copolymer poly[2-(dimethylamino)ethylmethacrylate]–poly(butylene succinate)–poly[2-(dimethylamino)ethylmethacrylate] (PDMAEMA–PBS–PDMAEMA, PDBD) (Figure 5) was successfully prepared through a chain-extension reaction.

The results revealed that these copolymers formed spherical micelles with small particle sizes of about 90 nm. The micelles developed had a hydrophobic core structure of PBS and hydrophilic poly[2-(dimethylamino)ethyl methacrylate] outer shell. The introduction of doxorubicin drug into the micelles resulted in the micelles with small particle sizes with narrow size distribution, which suggest good performance of micelles. The authors reported that 34% of doxorubicin was released after 6 hours from micelles prepared at neutral pH. However, it was noticed that at lower pH (pH = 4) about 56% of doxorubicin was released. The increase in the release of doxorubicin at lower pH was due to higher solubility

of the drug in acidic medium and swelling of micelles attributed to protonation of amino groups in the copolymer in an acidic medium. Furthermore, the resulting micelles demonstrated very low toxicity, making them a suitable candidate for drug delivery. In contrast, da Costa *et al.* [35] reported that the introduction of the drug (Meloxicam) did not significantly affect the size of particles. The results showed that the encapsulation efficiency of the drug was 79%. Unlike in Zhao *et al.* [29] study, in this study, the release of drug was faster at a higher pH medium than in a lower pH medium. This behavior was due to the good interaction between drug and polymer in alkali media. The developed materials showed the potential to be used as transdermal patches.

In another study [18], PBS copolymers containing ether-oxygen atoms were fabricated to deliver the drug dexamethasone. The results showed that the modification of PBS with triethylene glycol (TEG) resulted in improved hydrolytic degradation. In addition, copolymers sustained good cell adhesion and proliferation. The particle size of copolymers was larger than those of neat PBS. Also, the results revealed that copolymers had lower encapsulation efficiency than that neat PBS due to the high hydrophobicity nature of PBS. It was also observed that the drug release was faster in the copolymer in

comparison to neat PBS due to the higher hydrophilicity of copolymers and improved degradation rate. Most recently, Ferreira *et al.* [36] modified PBS using biobased rutin, also known as vitamin P and castor oil, in order to investigate their potential as a delivery system of silybin. The results revealed that the modification of PBS with rutin and castor oil led to the lower release of silybin.

In recent years, blending PBS with various polymers such as starch, keratin, and polyethylene glycol (PEG) as well as reinforcing PBS with fillers has received considerable interest in biomedical applications, especially in drug delivery [27, 37–39]. In general, the drug release depends on the blend composition and blend morphology [27]. For instance, Guidotti and co-workers [17, 38] prepared a blend of PBS and keratin at the ratio of 50:50 through electrospinning for drug delivery. The developed blend exhibited excellent drug release properties and improved the biodegradability of PBS. The release rate further improved when the loading of keratin was increased. Soares *et al.* [37] developed a blend of PBS/PEG, and PBS/PEG reinforced with montmorillonite (MMT) organoclay for the release of praziquantel. The addition of organoclay in a blend enables a controlled release of praziquantel dissolution process by allowing praziquantel to be in a dissolution medium for 72 hours. In the case of the neat blend, the dissolution of praziquantel in the medium occurred within 24 hours.

3.2. PBS-based materials for tissue engineering

Over the past decades, thermoplastic polymers have been widely used in biomedical applications because they can easily be designed into customized shapes depending on the intended applications. The selection of suitable polymeric materials for biomedical applications, such as scaffolds for tissue engineering, is the most crucial step toward the fabrication of the resultant materials [39]. Research on tissue engineering has gained considerable attention in the last decades for restoring, maintaining, and/or improving tissue functions that are damaged [40, 41]. Recently, tissue engineering has been used for the regeneration of different types of tissues such as bones, skin, *etc.* [39, 42]. For instance, Deepthi *et al.* [42] fabricated a ternary hydrogel scaffold comprising PBS/chitin/chondroitin sulfate nanoparticles for skin tissue engineering. The resultant scaffold demonstrated a large surface area suitable for more human dermal

fibroblasts adhesion, better cell proliferation, and low cytotoxicity, thereby, promoting skin regeneration. Scaffolds for tissue engineering can be made from synthetic polymers or natural polymers, blend polymers, and/or polymer-based composites.

In recent years, there has been a paradigm shift toward the development of biopolymer-based scaffolds for tissue engineering. Poly(lactic acid) (PLA), polycaprolactone (PCL), poly(glycolic acid) (PGA), poly(3-hydroxybutyrate-*co*-3-hydroxyvalerate) (PHBV), and poly-(butylene succinate) (PBS) are amongst the widely used biopolymers to fabricate scaffolds for tissue engineering. This is due to their unique properties, *i.e.*, biodegradability, biocompatibility, good mechanical, and non-toxicity [7]. PBS has been one of the most widely used biopolymers for developing scaffolds for tissue engineering due to its flexibility, biodegradability, high degree of crystallinity, and non-toxic [43].

Studies have demonstrated that PBS is biocompatible as it supports attachment, proliferation, and differentiation of human fibroblast cells [43]. PBS also possesses good degradation behavior in phosphate-buffered saline. The biocompatibility and degradation behavior together with other properties, such as good mechanical and thermal properties as well as good processability indicate that PBS is one of the most suitable biopolymers for tissue engineering applications [44, 45]. One of the most crucial advantages of PBS is that it can be easily tailored through copolymerization using various monomers (*e.g.*, dilinoleic acid, lactic acid, terephthalic acid, *etc.*) to improve its properties to afford their application in tissue engineering [46]. Poly(butylene succinate-*co*-dilinoleic succinate) (Figure 6) has been explored as the material

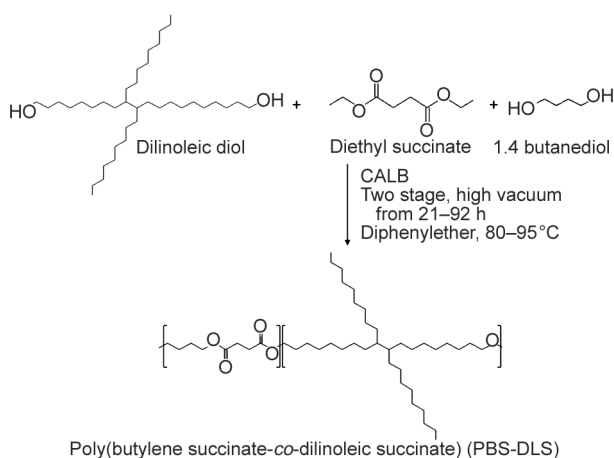


Figure 6. Synthesis of poly(butylene succinate-*co*-dilinoleic succinate). Redrawn from [47].

of choice to fabricate helically coiled scaffolds that can be used for heart-related tissue engineering. The resulting three-dimensional (3D) materials were analogous in terms of architecture and behavior of human tissues, especially heart muscle perimysium which is composed of microscale coiled fibers [12]. On the other hand, copolymerization of PBS with carboxylic acid induces enzymatic degradation, making it a suitable candidate for different biomedical applications [46].

The ideal scaffolds should allow cells to adhere and proliferate, leading to the formation of an extracellular matrix (ECM), displaying high porosity, interconnected structure, good mechanical properties, and uniform distribution throughout the scaffolds [41], as depicted in Figure 7.

In this context, numerous researchers have developed highly porous electrospun fibres made from PBS for soft tissue engineering and wound dressing [12, 43, 46, 48]. The high-quality fibres with less bead

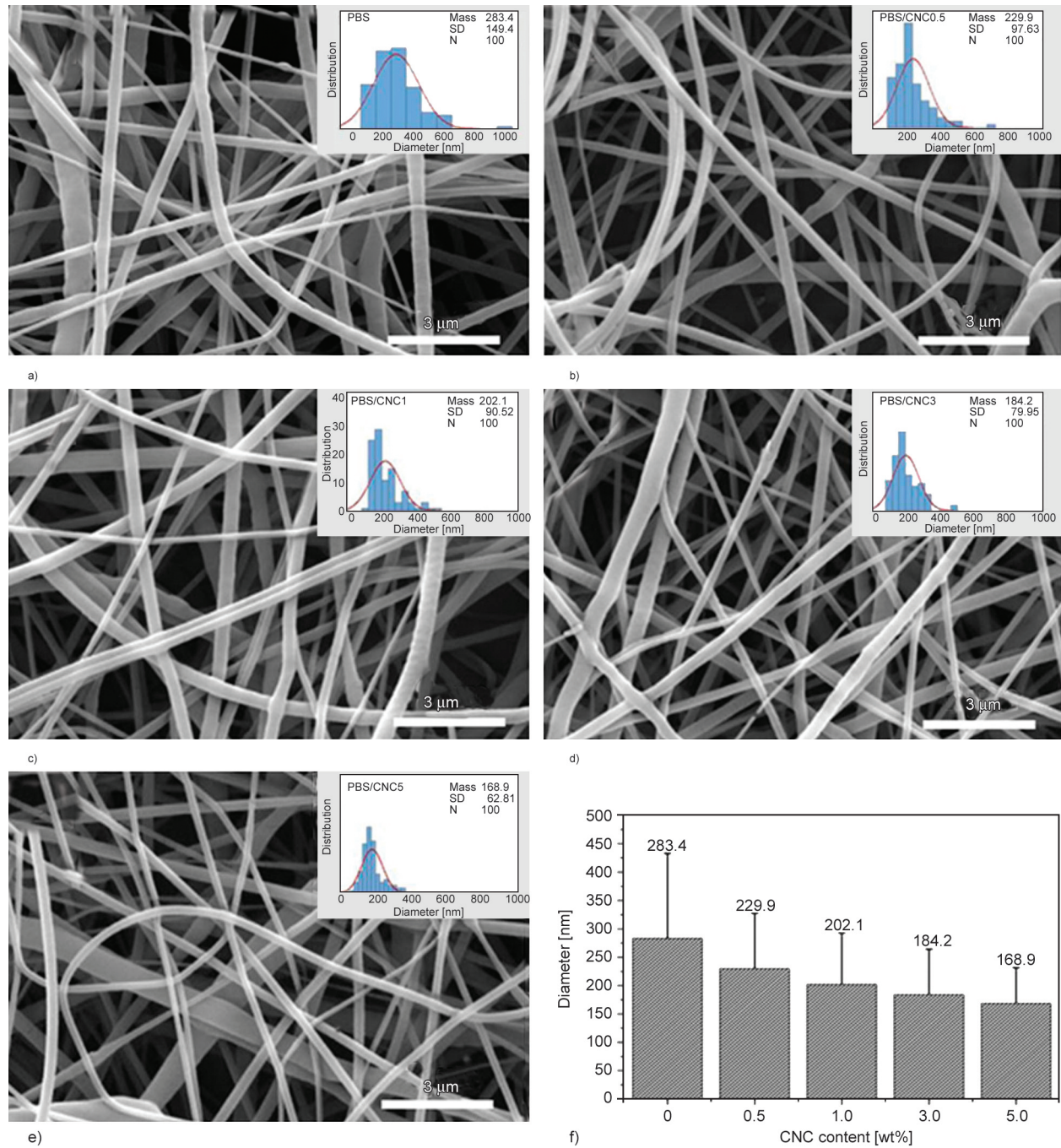


Figure 7. SEM micrographs of electrospun fibres. a) neat PBS, b) PBS reinforced with 0.5 wt% CNC c) PBS reinforced with 1 wt% CNC, d) PBS reinforced with 3 wt% CNC, e) PBS reinforced with 0.5 wt% CNC and f) electrospun fibre diameters reproduced from [41].

or bead-free are achieved by optimizing parameters such as the solvent system used, grade of PBS, the concentration of PBS, applied voltage, and distance between the electrodes [48]. For instance, 15% (w/v) of bio PBS was prepared by dissolving it in a mixture of chloroform and dimethyl sulfoxide (DMSO) at 50 °C under vigorous stirring for 2 hours. The electrospinning process was conducted at 15 kV applied voltage, 1.5 ml/h flow rate, 20 cm tip-top-collector distance, and 18-gauge blunt-tipped needle, under ambient conditions (19–21 °C, 55–65% relative humidity). The resultant electrospun fibres exhibited good tensile strength and modulus as well as high porosity at micro and nano levels which makes them preferable for soft tissue engineering [48].

The main challenge associated with conventional electrospinning is the production of two-dimensional (2D) non-woven mats, which limits their applications. In order to mitigate those challenges, a number of researchers fabricated 3D electrospun fibres [12, 41]. Sonseca *et al.* [12] developed 3D PBS-based scaffolds for smooth muscle tissue engineering. The scaffolds consist of large surface area, high porosity, and good elasticity which afforded the scaffolds with facilitated cell proliferation. The development of artificial scaffolds for peripheral nerve regeneration using electrospinning was demonstrated by Cicero and colleagues [49]. The resultant 3D PBS-based scaffolds were flexible thin sheets with diameters ranging

between 1–5 microns. The scaffolds were implanted in rats to stimulate, and repair severed peripheral nerves, as shown in Figure 8. The findings revealed that after 120 days, there was a complete re-adsorption which indicates the biocompatibility of scaffolds and hence demonstrates that 3D PBS-based scaffolds have a great potential for nerve regeneration.

3D scaffolds made from PBS alone are, however, limited in terms of mechanical properties, performance, and surface structure. Huang *et al.* [41] and Ju *et al.* [50] incorporated cellulose nanocrystals (CNC) in PBS to address the aforementioned challenges of PBS. The findings revealed that the introduction of 3 wt% CNC into PBS led to the improvement in crystallinity, mechanical properties, and hydrophilicity. It is noteworthy mentioning that the incorporation of CNC into PBS also improved the overall porosity, biodegradation, and biocompatibility when compared to neat PBS. The cell proliferation was better in the case of PBS reinforced with CNC in comparison to neat PBS. This is because the NIH-3T3 cell spread very well in the PBS-based composite in comparison to neat PBS. In addition, PBS-based composite comprises an open pore and bimodal structure which favors cell attachment and proliferation.

A literature study indicates that the overall properties of PBS-based materials for tissue engineering were enhanced by blending with other polymers [43]. In this interesting study, the optimum properties and bioactivity were reported for PBS/PLA in ratios of 50/50 wt%. Additionally, blending PBS with PLA (50/50 wt%) resulted in uniform and smooth fibres without beads. The properties of PBS/PLA (50/50 wt%) blend were improved by reinforcing with cellulose nanofibres (CNF). The results revealed that the incorporation of CNF into the blend enhanced the mechanical performance of the blends due to the strong interaction between CNF and the polymer matrix. Also, the incorporation of CNF led to the reduction in fibre size and improved the human dermal fibroblast attachment of the resultant scaffold, cell proliferation as well as protein attachment on the scaffold due to the reduced size of the fibres. Therefore, the resultant scaffolds demonstrated a potential for vascular tissue engineering applications [43].

Another major drawback of PBS is inadequate osteoblast biocompatibility and bioactivity which limit their applications for bone tissue regeneration [9]. To overcome these challenges and to improve biocompatibility and bioactivity, surface modification

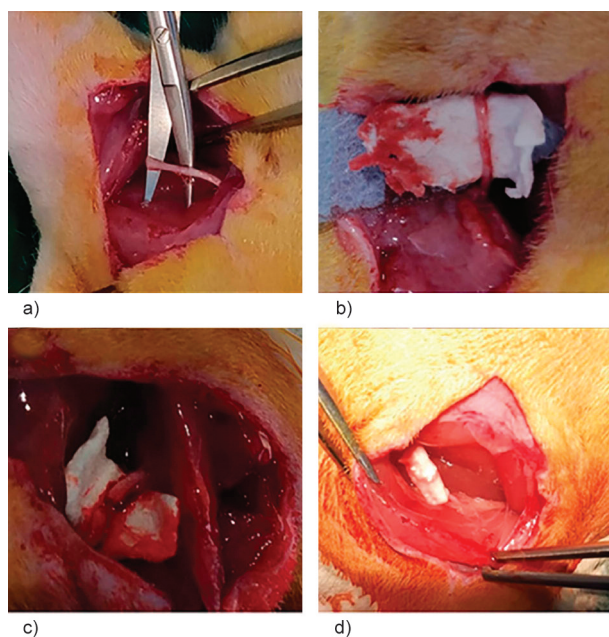


Figure 8. a) Nerve isolation, b) implantation of PBS scaffolds, c) nerve section, d) nerve wrapping. Reproduced from [49].

and reinforcing PBS should be considered [9, 51–53]. Wang, *et al.* [9] modified PBS with H₂O or NH₃ plasma immersion ion implantation (PIII) to enhance biocompatibility and bioactivity. The results revealed that plasma treatment improved the hydrophilicity and roughness of the polymer. As a result, osteoblast biocompatibility was enhanced after the treatment which suggests that the resultant material is suitable for bone replacement implant. Another strategy for improving biological performance such as biocompatibility and bioactivity is to introduce material which can readily degrade and maintain high bioactivity. Ceramics, such as hydroxyapatite, and nano-fluorapatite have been widely used as bioactive materials for bone regeneration because they can easily bond with living cells through the apatite layer formed on the ceramic surface [54]. However, natural bone tissue is made up of inorganic compounds (apatite) as well as organic material (collagen). Therefore, in order to promote bone regeneration and design bone tissue engineering the material must contain both inorganic and organic materials such as a polymer. The ensued material must have good properties in comparison to neat inorganic and organic material. In addition, the developed material must mimic the natural bone structure in terms of properties. Recent studies on PBS reinforced with bioactive materials such as hydroxyapatite [54], nano-fluorapatite [52], nanolaponite [11], silica-nanotubes, and strontium hydroxyapatite [55, 56], magnesium phosphate [57] have shown a significant improvement in bone functions. In the study investigated by Prowans and

co-workers [54], poly(butylene succinate-butylene dilinoleate) (PBS-DLA) copolymer reinforced with 30 wt% hydroxyapatite was fabricated for bone healing. The incorporation of hydroxyapatite into PBS copolymer resulted in the increased tensile modulus while maintaining good elongation at break. The healing process of bone after fracture, as depicted in Figure 9, stabilized with implanted PBS copolymer reinforced with 30 wt% hydroxyapatite. The histology results revealed that the healing process was taking place after implanting PBS copolymer-based composites due to the presence of hydroxyapatite. In addition, the presence of calcium and phosphate ions in the hydroxyapatite triggered bone regeneration. Another study investigated the incorporation of nano-fluorapatite into PBS. The results demonstrated that the presence of nano-fluorapatite promoted biocompatibility and bioactivity in the resulting composite material [52]. Similar observations were reported by other researchers [11, 57]. In addition, the fabricated PBS composites reinforced with nano-fluorapatite exhibited a highly reactive surface which enables it to combine with living cells of bone tissue without fibrous capsule tissue. Thus, displaying good osteoconductive [52]. Moreover, the presence of inorganic fillers in PBS inhibited the growth of *Escherichia coli* (*E. coli*) and *Staphylococcus aureus* (*S. aureus*) indicating that the resultant materials have antimicrobial activity [11]. The incorporation of inorganic fillers into PBS-based materials can also trigger the hydrolytic degradation process [55–57]. Other researchers have blended PBS with natural polymers such as chitosan to fabricate scaffolds for tissue engineering to overcome the aforementioned drawbacks of PBS [39, 58, 59]. Chitosan has been investigated in biomedical applications due to its advantages such as non-cytotoxicity, biodegradability, non-antigenicity, and biocompatibility. The results showed that the introduction of chitosan into PBS blends promoted the adsorption of human serum albumin (HSA) and human plasma fibronectin (HFN). However, the highest adsorption was noticed in the case of HSA. The *in vitro* studies revealed that the human osteosarcoma cell proliferated in the blend. In contrast, high proliferation was noticed in neat PBS [58]. Further studies were performed using human bone marrow mesenchymal stem cells (hBMSCs) on the PBS blended with chitosan scaffolds. The scanning electron microscopy (SEM) results showed excellent cell adhesion on the surface of the

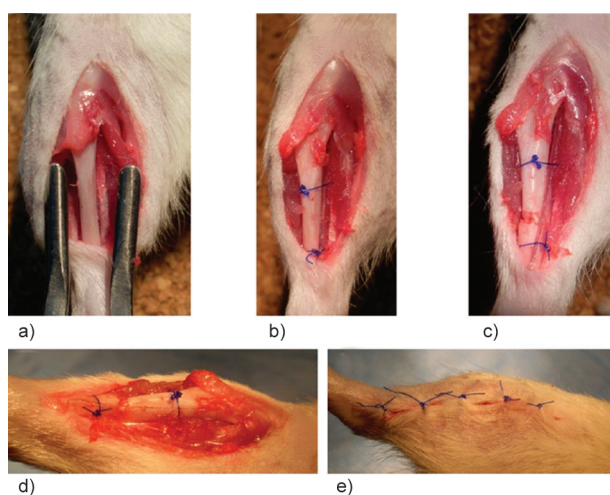


Figure 9. Images of a) limb prepared for a procedure, b) limb exposed in tibia, c) implanted composites stabilized with two nonabsorbable Prolen 5.0 stitches, d) bone cut and stabilized with the composites, e) stitched after surgery. Reproduced from [54].

scaffold and cell proliferation. The *in vivo* studies were performed on critical cranial bone defects in nude mice using PBS blend scaffold and hBMSCs. The micro-computed tomography (μ CT) findings demonstrated that the cell construct enabled bone regeneration after 8 weeks of implantation [39].

3.3. PBS-based shape memory for biomedical devices

Shape memory polymers (SMP) are often fabricated based on the structure and the properties of the intended applications as depicted in Figure 10. PBS-based SMP has received great attention due to its biodegradability, biocompatibility, and non-toxicity. PBS based SMP are designed using various strategies; namely: (i) crosslinked homopolymer, (ii) segmented block copolymers, (iii) blending polymers, (iv) supramolecular polymer network, (v) polymer composites [60, 61]. Blending is the most popular strategy to design multi-shape materials with multiple properties. For instance, Zheng *et al.* [62] fabricated multiple shape memory consisting of PBS, PCL, and polyurethane (TPU). The resultant multi-shape memory is comprised of temporary and permanent shapes. The shape memory test results revealed that the system had a larger fixing ratio and recovery ratio. These results suggest that the resultant material has potential in the field of biomedical devices.

However, to the best of our knowledge, there is little information reported in the literature about designing biomedical devices from PBS-based SMP. Much

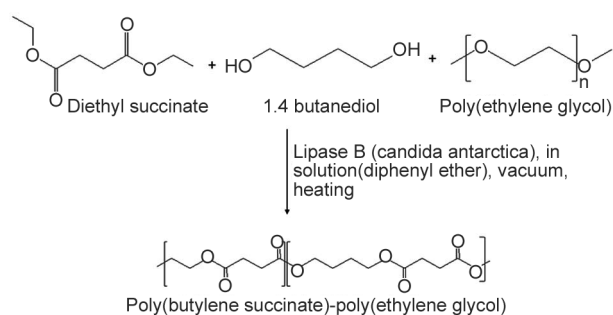


Figure 11. Synthesis of poly(butylene succinate)-poly(ethylene glycol). Redraw from [71].

research is only focusing on the synthesis and characterization of PBS-based SMPs [62, 64–70]. The newly developed PBS-based SMPs demonstrated good ductility which allows remarkable reversible deformation, good thermal properties, good crystallinity for biomedical devices, and are more hydrophilic [62, 64–70]. Huang *et al.* [66] synthesized and characterized poly(butylene succinate)-poly(ethylene glycol) (Figure 11) multiblock copolymer for biomedical devices.

The results showed that the synthesized multiblock possess two different crystalline regions. These crystalline regions showed both temporary and permanent shapes. In addition, multiblock demonstrated good elongation at break as well as high hydrophilicity, indicating that the material can be used to fabricate biomedical devices.

In another study, Lin *et al.* [72] designed a shape memory blend of PBS and PLA for biomedical

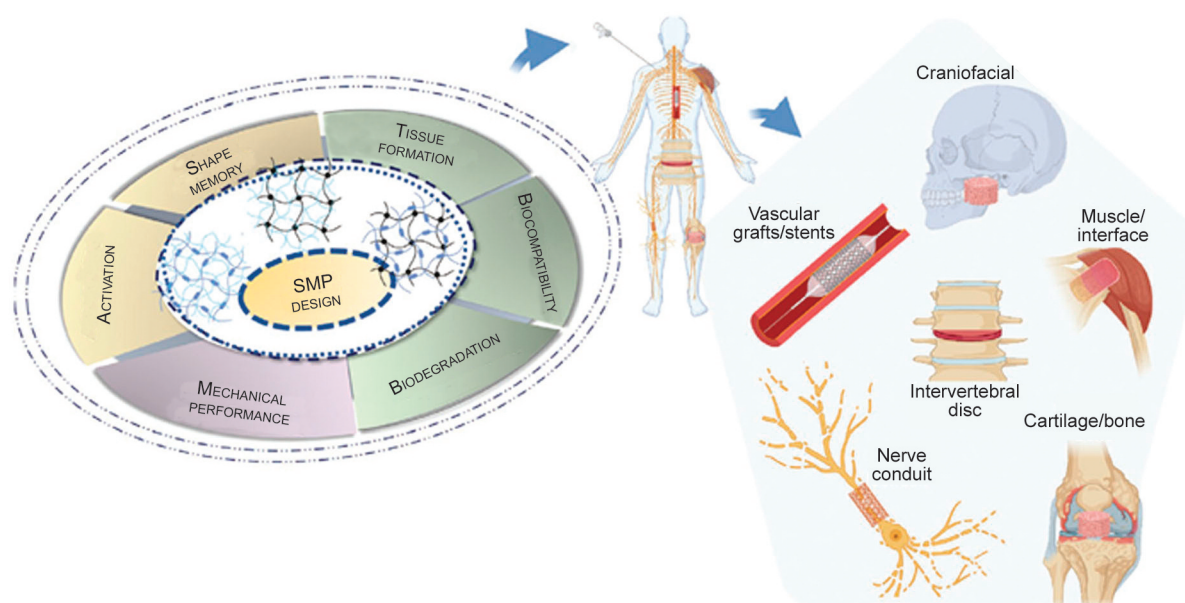


Figure 10. Shape memory polymers used in various biomedical applications. Reproduced from [63].

applications using 4D printing. 4D printing was used to develop the patient customized biomedical device, such as an aneurysm model because the structure and dimensions of the final product can be regulated. The resultant PBS SMP consisted of hard and soft phases. The soft phase is responsible for shape fixation performance whereas the hard phase is for shape recovery performance. In addition, the ensued SMP displayed improvement in flexibility which has potential in tissue engineering and photothermal therapy. Since the market for PBS is growing and the

fact that it possesses good properties, it is projected that variety of applications such as biomedical devices, sensors and others will be explored.

4. Other applications of PBS-based polymers

PBS has garnered tremendous interest in other applications such as food packaging, the agricultural sector, *etc.*, as shown in Table 2 [13, 73]. As previously mentioned, PBS offers unique properties which match those of non-biodegradable synthetic polymers

Table 2. Other applications of PBS-based materials.

Material	Processing methods	Intended applications	Summary of results	References
Aerogel PBS	Compression moulding	RF and Microwave	A composition of 97 wt% PBS and 3wt% silica aerogel PBS covered a bandwidth of 9.4 GHz with stopbands from 5.5 to 5.8 GHz and 7 to 8.3 GHz.	[78]
PBS reinforced with inorganic fillers (ZnO, silver zeolite)	Twin screw extruder and blown film	Food packaging	<ul style="list-style-type: none"> – The incorporation of 0.5 to 6 wt% of ZnO and silver zeolite into PBS resulted in decrease in mechanical properties of PBS films – Also, cold crystallization temperature (T_{cc}) and T_g of composites decreased whereas crystallinity increased – PBS-based composites reinforced with ZnO and silver zeolite displayed antimicrobial properties. Release test in the case of PBS reinforced with ZnO demonstrated that Zn^{2+} migrated over 15 days 	[79, 80]
Poly(butylene succinate-co-hexamethylene succinate) (Figure 12a)	Melt polycondensation	Greener coatings for paper packaging	<ul style="list-style-type: none"> – PBS copolymer composed of 1:1.1 ratio of succinic acid and diol(s) resulted in decreased crystallinity while flexibility increases – The solubility of the resultant copolymer increased with the loading of hexamethylene succinate (HS) was increasing 	[81]
Poly(butylene succinate-co-propylene succinate) (Figure 12b)	Esterification and polycondensation	Medical support, coating, and phase-change material	<ul style="list-style-type: none"> – T_m, T_{cc}, crystallinity, T_g, and degradation temperature decreased with an increase propylene succinate (PS) loading up to 40% – In addition, tensile strength and modulus decreased with increasing PS loading 	[82]
PBS/curaua fibres	Compression moulding	Rigid packaging or interior car parts	<ul style="list-style-type: none"> – Incorporation of 20 wt% of fibres into PBS improves impact and flexural strength and water absorption of composites 	[83]
PBS/PCL membranes	Immersion precipitation.	Wastewater treatment	<ul style="list-style-type: none"> – Blending 30 wt% PBS and 70 wt%PCL improved water uptake due to increased porosity – The blend had high water flux, flux recovery, and permeate flux of 106, 26, and 37%, respectively – In addition, the blend demonstrated higher rejection of pollution indices when compared to neat PCL 	[84]
Poly(butylene succinate-co-terephthalate) (PBST) (Figure 12c)	Electrospinning	Wastewater treatment	<ul style="list-style-type: none"> – Functionalized PBST with cyclodextrin demonstrated higher efficiency in removing methylene blue (MB) dye – Also, functionalized PBST membrane exhibited a maximum adsorption capacity of 90.9 mg/g 	[85]

Table 2. Continuously 1.

Material	Processing methods	Intended applications	Summary of results	References
PBS/acrylonitrile butadiene styrene (ABS)	Solvent casting	Wastewater treatment	<ul style="list-style-type: none"> – Tensile strength and modulus of the blends improved with increasing ABS loading from 10–30wt% – Blends had less irreversible fouling and the water filtration suggested that chemical oxygen demand rejection dropped whereas permeable flux increased with the increasing ABS loading from 10–30 wt%. In addition, all membranes rejected 100% of turbidity 	[86]
PBS/cyclic olefin copolymer (COC)	Solvent casting	Packaging	<ul style="list-style-type: none"> – Blending 30 wt% PBS and 70 wt% COC enhanced mechanical properties and demonstrated good resistance to the bacterial growth 	[87]
PBS/starch, chitin, and cellulose nanocrystals	Chill-roll cast film extrusion, twin screw extruder	Packaging	<ul style="list-style-type: none"> – Incorporation of 1 wt% nanocrystals into PBS enhanced tensile and barrier properties. In addition, the increase in nanocrystals loading to 3 wt% results in to increase in both mechanical and barrier properties – The composites were biodegraded in approximately 3 months using wastewater treatment sludge 	[88, 89]
PBS/geraniol	Twin screw extruder	Bread shelf-life extension	<ul style="list-style-type: none"> – PBS-based material containing 10 wt% geraniol showed good antimicrobial properties – Release test revealed that the migration concentration of geraniol increased with increasing humidity – Shelf-life extension results indicated that the spoilage of bread stored using the resultant material was delayed by three weeks 	[90]
PBS/Curcumin and Carvacrol	Solvent casting	Active packaging	<ul style="list-style-type: none"> – The PBS films containing 1 wt% of curcumin and carvacrol demonstrated antimicrobial properties and improved antioxidant activities 	[91]
Poly(butylene-succinate-co-adipate) (PBSA) based materials (Figure 12d)	Melt mixer and blown film	Active packaging of bread	<ul style="list-style-type: none"> – The films possess lower tensile strength and modulus while elongation at break was higher when compared to neat PLA – Mould was observed after 7 days on the bread package in comparison to 6 days observed when neat PLA was used 	[92–95]
PBS/quercetin	Solvent casting	Food packaging	<ul style="list-style-type: none"> – Introduction of quercetin 0.05 to 0.25 phr resulted in changing of color, opacity, and UV-blocking effect – There were no significant changes observed in mechanical properties of the resultant PBS-based films – The resultant films displayed some bactericidal activity 	[96]
PBS/modified tapioca starch/natural fibres	Twin screw extruder and compression moulding	Agricultural Mulch Films	<ul style="list-style-type: none"> – PBS composites reinforced with natural fibres (5 to 30 wt%) exhibited decreased tensile modulus, elongation at break, and flexural properties – Biodegradation was enhanced in the soil burial test 	[97, 98]
PBS/maghemite	Hot melting	Oil spill clean-up	<ul style="list-style-type: none"> – Results showed that 1g of the PBS-based composites containing 5 wt% maghemite was able to remove 11 g of the petroleum from the water. 	[99]
PBS/CNC	Melt mixing and supercritical CO ₂	Thermal insulation	<ul style="list-style-type: none"> – Composite containing 1 wt% CNC demonstrated a high volume expansion ratio of 37.1 times and outstanding thermal conductivity of 0.021 W(m·K)⁻¹ 	[100]

Table 2. Continuously 2.

Material	Processing methods	Intended applications	Summary of results	References
PBS containing thioether-linkages	Melt polycondensation	Food packaging	<ul style="list-style-type: none"> – Co-polymers exhibited lower tensile strength and modulus and higher elongation at break when compared to neat PBS – Co-polymers displayed improved barrier properties to both CO₂ and O₂ gases when compared to neat PBS 	[101–103]
PBS and PBSA	Blown film	Poultry meat packaging	<ul style="list-style-type: none"> – Both films had higher water vapor transmission rate (WVTR) and oxygen permeability than commercially used polyamide (PA)/PE film – Both PBS films produced complied with European legislation (Regulations 1935/2004 and 10/2011) 	[95, 104]
PBS/PLA reinforced with cellulose fibres	Melt mixer, compression moulding, injection moulding	Hot cups and food packaging	<ul style="list-style-type: none"> – Blend composition of 20 wt%PBS and 80 wt% PLA containing various loading (0.5 to 15 wt%) of cellulosic fibres were investigated – Results revealed that low loadings (0.5 to 1.5 wt%) reduced the mechanical properties of the blend whereas high loadings (5 to 15 wt%) improves mechanical properties – Addition of low loadings improved the thermal stabilities of the composites whereas the incorporation of high loadings resulted in intermediate thermal stabilities 	[105, 106]

with the added biodegradable and sustainable features. As a result, these materials are anticipated to replace non-biodegradable synthetic polymers and alleviate environmental pollution caused by plastics. Although PBS-based products have demonstrated potential in various applications, however, the shelf life and disposal should be taken into consideration to alleviate environmental pollution. Unlike a biomedical application, PBS-based products after the end of service life undergo biodegradability in soil and compost conditions. Numerous studies have investigated the biodegradation of PBS-based materials in soil and compost [74–77]. The findings revealed that the rate of biodegradation of PBS was

slower than that of PBS composites reinforced with natural fibres. In addition, composting environmental conditions provide a high rate of biodegradability for both PBS and its biocomposites in comparison to soil environmental conditions.

5. End-life options of PBS biobased materials

Figure 13 shows a variety of mechanisms responsible for biodegradable poly(butylene succinate) PBS-based polyesters degradation. Polymer chemical bond degradation mainly takes place through polymer chain scission either through the main chain or side chains of polymer molecules, induced by their thermal

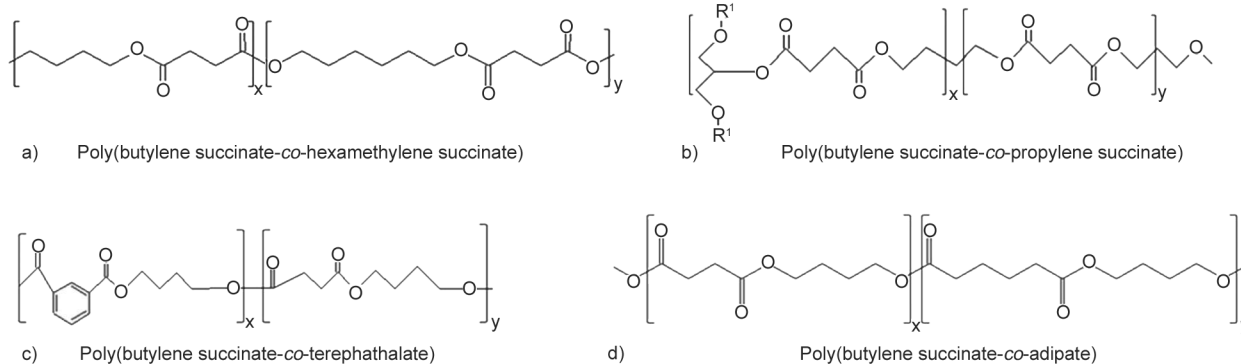


Figure 12. Structure of copolymers presented in Table 2. a) Poly(butylene succinate-co-hexamethylene succinate), b) poly(butylene succinate-co-propylene succinate), c) poly(butylene succinate-co-terephthalate), and d) poly(butylene succinate-co-adipate).

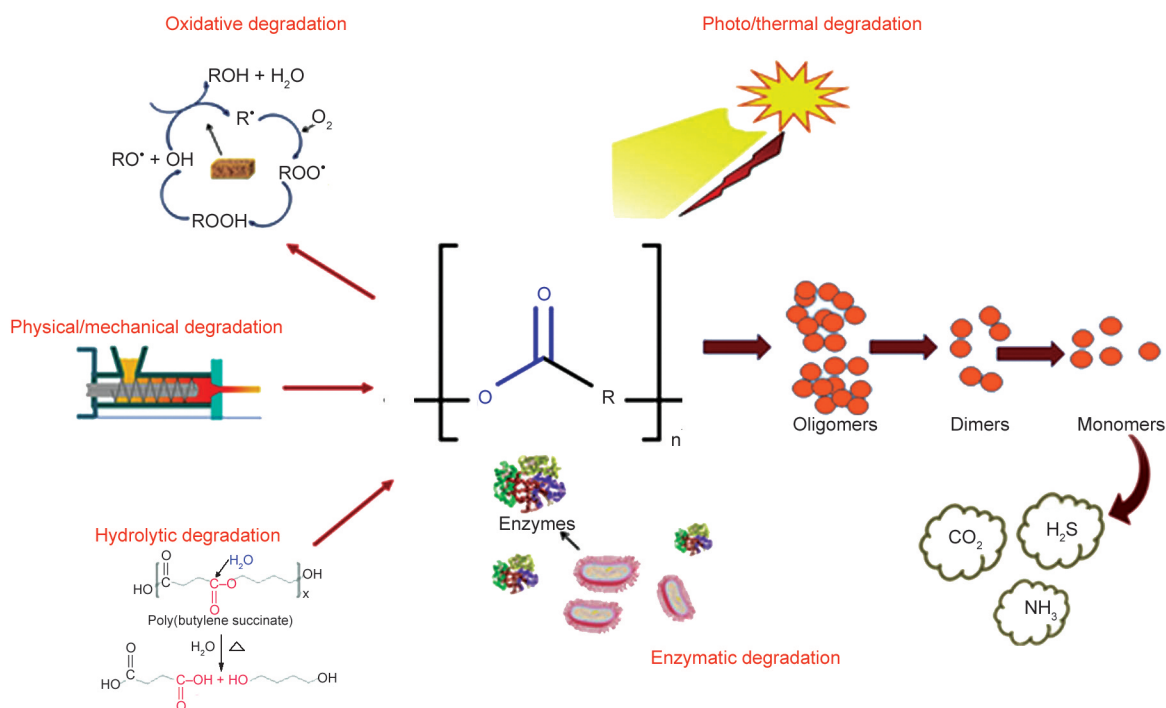


Figure 13. Modes of polymer degradation. Redrawn from [13, 73, 107].

activation, oxidation, photolysis, and hydrolysis (Figure 13). Photodegradation refers to polymers degraded by photolysis to give lower molecular weight molecules, whereas mechanical degradation refers to polymers that can be degraded into smaller pieces by an external load, such as polymer processing, shearing forces, and others. Oxidative degradation refers to polymer degradation induced by atmospheric oxygen, especially in the autocatalytic process of attack on the hydrogen atoms, to form hydroperoxides. Hydrolytic degradation refers to polymers having hetero backbone chains degradation induced by hydrolysis reaction either biotic (living cell or microorganisms) or abiotic (mainly pH) or both. Biodegradation of polymers refers to polymers undergoing degradation in biological environments when living cells or microorganisms are present around the polymers. Such biological conditions include soil and water as well as the body of human beings and animals [73].

Since this review is dedicated to describing the application of PBS in biomedical applications, our discussion on the degradation of biodegradable polymers will only focus on the degradation processes that occur under biological environments either through enzymatic or non-enzymatic hydrolysis and/or oxidation. In this context, the degradation of PBS and PBS-based materials will be described in comparison with other bio-polyesters. Biodegradable polyesters (*e.g.*, polybutylene succinate PBS, polylactides PLAs, and

other biodegradable aliphatic-aromatic co-polyesters) are hydrolyzed in our body to their respective monomers and oligomers that are soluble in aqueous media [13].

The rate of degradation of PBS-based biodegradable polymers and blends is mainly dependent on polymeric characteristics, such as chemical structure, distribution of repeating units, molecular weight, polydispersity, presence of low molecular compounds (monomers, oligomers, solvents, plasticizers, presence of ionic groups, presence of chain defects, morphology (crystallinity, microstructure, orientation), processing methods and conditions and mechanism of hydrolysis (enzymes *vs* water) [13].

Generally, the weight loss of biopolymers that occur over time in the living body is referred to as absorbable or resorbable polymers under enzymatic or non-enzymatic hydrolysis or/and both conditions. The term ‘biodegradable’ is often used only for such industrial and ecological applications which have been developed aiming to address post-consumer pollution issues in natural environments (terrestrial and aquatic). Polymers used for medical purposes by implanting or contact with the human body should not be called biodegradable but can be called resorbable or adsorbable polymer or even sometimes polymeric biomaterials [13, 73].

In this review article, however, the term biodegradable is used since the term has been widely utilized

in the polymeric biomaterials world the biomedical polymers that are absorbed in the body even through non-enzymatic hydrolysis. In other words, the term biodegradable is used here with the broad meaning that polymer will eventually disappear after introduction into the body.

Hydrolytic and enzymatic degradation

In biomedical applications, the degradation of biodegradable polymers in hydrolytic and enzymatic conditions is widely studied under physiological conditions (mostly at 37 °C, pH 7.4, phosphate-buffered saline). In in-vitro conditions, the hydrolytic degradation of aliphatic polyesters is influenced by different factors, e.g., chemical structure, hydrophilic–hydrophobic nature of materials, molecular weight and molecular weight distribution, surface morphology and degree of crystallinity, and the physiological conditions exposed [13]. The hydrolytic degradation of polyesters, including PBS and its biodegradable blends and composites, undergo two-step processes. In the first step, a random chain scission occurs on

the polymeric molecules where a decrease in the molecular weight, weight loss, and increasing water-soluble low molecular compounds during incubation time occurs [13, 108]. In the second step, when the polymeric material undergoes molecular weight reduction of less than 13 000 Da, the low molecular compounds of oligomers, dimers, and monomers become water soluble with less incubation time. Understanding each polymeric system and its composition degradation behavior requires an extensive study of the degradation profile, molecular weight changes, and weight losses as a function of incubation time by various analytical techniques. Table 3 provides the hydrolytic and enzymatic degradation studies conducted on PBS and PBS-based polymeric materials under different degradation conditions. Many authors observed that neat PBS undergoes slow hydrolytic degradation under physiological conditions and the molecular weight remains the same for several weeks due to its molecular weight distribution, high crystallinity, and hydrophobicity [44, 110, 118–120]. On the other hand, copolymerization

Table 3. Hydrolytic and enzymatic degradation studies of PBS-based systems. The copolymers' molecular structures are presented in Figure 14.

Polymeric material	Degradation conditions	Time [d]	Weight loss [%]	References
Poly(butylene succinate) (PBS)	Hydrolytic: physiological conditions (37 °C, pH = 7.4).	105	65	[44]
Poly(butylene succinate-co-cyclic carbonate)s (PBS-co-CC)	Hydrolytic: physiological conditions (37 °C, pH = 7.4).	40	0	[109]
	Enzymatic: lipase Novozyme 435	25	40–70	
	Enzymatic: lipase porcine pancreas	20	40–90	
Poly(butylene succinate-co-dimethyl 5-sulfoisophthalate sodium salt)s (PBS-co-BSi)	Hydrolytic: physiological conditions (37 °C, pH = 7.4).	80	3–5	[110]
Poly(butylene succinate)-block-poly(triethylene succinate) (PBS-b-PTES)	Hydrolytic: physiological conditions (37 °C, pH = 7.4).	225	0–35	[111]
Poly(butylene succinate)–silica nanocomposites (PBS/Si); poly(butylene succinate)–strontium hydroxyapatite nanocomposites (PBS/SrHA)	Enzymatic: <i>R. delemar</i> and <i>P. cepacia</i> lipases	30	2–16	[55]
Poly(butylene succinate) urethane ionenes (PBSUI)	Hydrolytic: physiological conditions (37 °C, pH = 7.4).	4	5–35	[112]
Poly(butylene terephthalate)-co-poly(butylene succinate)-block-poly(ethylene glycol) (P(BSBT)-b-PEG)	Hydrolytic: physiological conditions (37 °C, pH = 7.4).	63	3–33	[113]
Poly(butylene succinate)-blend-chitosan (PBS/Chitosan)	Hydrolytic: physiological conditions (37 °C, pH = 7.4).	30	1–7	[114]
Poly(butylene-co-2,4,3,5-di-O-methylene-D-mannitol succinate) (PBxManxyS)	Hydrolytic: phys. cond.; pH 2.0, 37 °C	56	10–15	[115]
	Enzymatic: porcine pancreas lipase	56	24–29	
Poly(butylene-co-2,4,3,5-di-O-methylene-D-glucitol succinate) (PBxGluxyS)	Hydrolytic: phys. cond.; pH 2.0, 37 °C	40	10–24	[116]
	Enzymatic: porcine pancreas lipase	40	15–25	
Poly(butylene succinate-co-butylene sulphonated succinate) (PBS _x SS _y)	Hydrolytic: physiological conditions (37 °C, pH = 7.4).	56	1–25	[117]
	Hydrolytic: pH 4.0, 37 °C	56	5–35	
	Hydrolytic: pH 10, 37 °C	56	15–60	

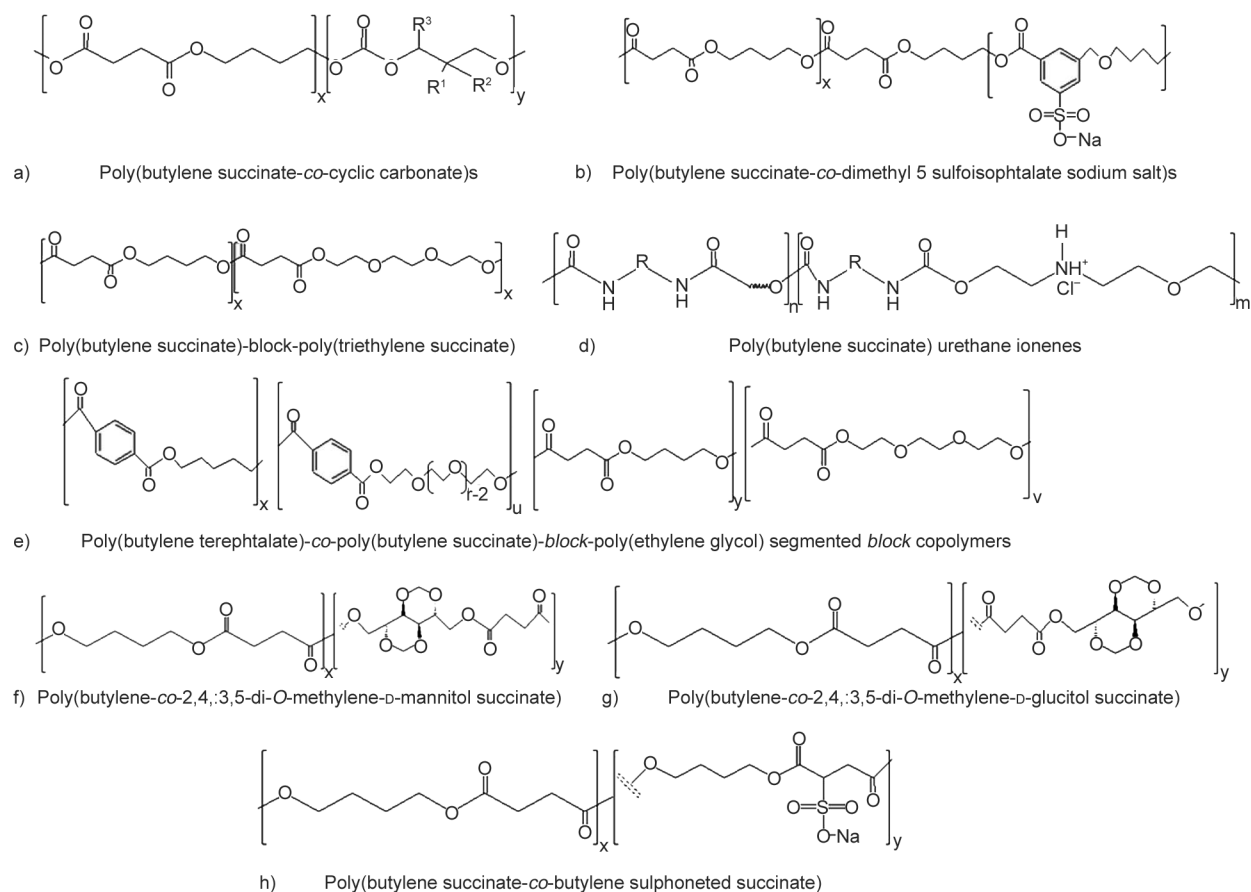


Figure 14. Structure of copolymers presented in Table 3. a) Poly(butylene succinate-co-cyclic carbonate)s, b) poly(butylene succinate-co-dimethyl 5 sulfoisophthalate sodium salt)s, c) poly(butylene succinate)-block-poly(triethylene succinate), d) poly(butylene succinate) urethane ionenes, e) poly(butylene terephthalate)-co-poly(butylene succinate)-block-poly(ethylene glycol) segmented block copolymers, f) poly(butylene-co-2,4,3,5-di-O-methylene-D-mannitol succinate), g) poly(butylene-co-2,4,3,5-di-O-methylene-D-glucitol succinate), and h) poly(butylene succinate-co-butylene sulphonated succinate).

of PBS with hydrophilic molecules showed a noticeable effect on the hydrolysis rate [118, 119, 121]. The increased degradation was mainly due to the cleavage of the ester bonds of chain segments. Also, it was reported that the introduction of ionic groups into PBS increased the hydrolytic degradation with the increased amount of urethane ionenes groups [110, 112, 113, 118]. On the other hand, the introduction of carboxylic groups into the PBS matrix is the key to increasing and controlling the rate of degradation by catalyzing the hydrolysis of the macromolecular chains [119, 122]. These demonstrate that PBS copolymerization with the water-soluble molecule, viz. PEG and other hydrophilic molecules, help in increasing the rate of degradation in both enzymatic and non-enzymatic conditions.

Jager *et al.* [123] reported that nanoparticles made of poly(butylene succinate-co-dilinoleate) showed a substantial decrease in molecular weight after 3 weeks of incubation. The rate of hydrolysis was mainly

influenced by nanoparticle structure that contains a high amount of water molecules. Grigoriadou *et al.* [55] studied the effect of silica-nanotubes and strontium hydroxyapatite incorporated PBS composites on the degradation behavior. The increased hydrolytic degradation was mainly influenced by the presence of hydroxyl groups on the surface of both nanoparticles and porous structure formation which helps to facilitate the lipase diffusion in the polymer matrix and accelerate the degradation. Costa-Pinto *et al.* [124] reported that the presence of chitosan in the PBS/chitosan composite increased hydrolytic degradation with surface erosion and water uptake due to swelling and higher hydrophilicity.

Enzymatic degradation of PBS-based polymeric materials have conducted in the presence of various enzymes, *i.e.*, *Pseudomonas cepacia lipase*, *Candida antarctica lipase* (Novozyme 435), *Aspergillus oryzae lipase*, *lysozyme*, *Rizopus delemar* [52, 109, 124]. Lipases are well-known enzymes for catalyzing

hydrolytic degradation of aliphatic polyesters, however, the degradation kinetics depends on various factors *i.e.* chemical structure, hydrophilic–hydrophobic balance, molecular weight, morphology, degree of crystallinity, and others. Therefore, the approach of copolymerization or blending favored the enzymatic degradation of PBS-based biodegradable polyester materials.

6. Current status and future directions

It is worth mentioning that PBS is facing some challenges such as high production costs and inadequate properties which make it difficult for PBS to be used as a virgin polymer for product development without blending, reinforcing, and copolymerization. Despite these challenges, the production of PBS has been showing an exponential increase in various countries, such as North America, Europe, and Asian countries such as China.

The increase in the market and the demand for PBS has opened opportunities for exploring PBS in both research and industry. The growth in the market size of PBS has encouraged research and innovation to diversify the applications of PBS leading to the development of PBS and PBS-based products for a variety of applications such as food packaging, agricultural and biomedical. The biocompatibility, non-toxicity, and biodegradability have widened the use of PBS in biomedical applications. Extensive research has focused on biomedical applications, such as tissue engineering, drug delivery, wound dressing as well as biomedical devices as they provide a platform for the development of biodegradable products. The increase in medical needs has further the interest in the development of PBS-based products for biomedical applications due to the aforementioned features. The research for biomedical applications has led to the design and fabrication of scaffolds for tissue engineering as well as drug delivery system. The current progress on designing 3D scaffolds for smooth tissue engineering has become a research hotspot. The ideal scaffolds for tissue engineering require high porosity which enables proper integration of cells as well as blood vessels and allows the movement of nutrients and waste [48]. 3D PBS-based scaffolds have proved to be biocompatible as the osteoblast proliferates and degrades in the system without leaving toxic byproducts. Additionally, PBS-based scaffolds have demonstrated potential in nerve regeneration, vascular tissue engineering, bone tissue

regeneration as well as skin tissue regeneration. Moreover, since the body system is very complex, it is necessary to perform modeling studies to predict the challenges of PBS-based products prior to conducting clinical trials [125].

Although investigations have been conducted for the fabrication of PBS-based products for wound dressing, there are few reports documented on PBS and PBS-based products for wound dressings. The ongoing research on wound dressing is focusing on designing smart and bioactive products. This can be achieved by introducing antimicrobial agents and therapeutic elements into bandages for various types of wounds to accelerate the healing process of the wound [126]. This opens doors for further investigation to explore PBS for wound dressings. For instance, the design and fabrication of biodegradable wound dressings which have controlled porosity contained antimicrobial agents, and had similar features to natural extracellular matrix (ECM) could benefit from the progress in the fabrication of PBS fibrous wound dressings. The PBS wound dressing possesses good mechanical properties, a large surface area-to-volume ratio, and increased levels of porosity. In addition, they allow cell proliferation, removing exudates, moisture retention, and haemostasis [126]. Furthermore, PBS-based wound dressing shows potential and they open opportunities for designing bioactive and cost-effective biobased wound dressing.

In the case of medical devices, 3D printing has been used to design patient-customized biomedical devices. 3D printing can also enhance the uniformity of mechanical properties as well as allow the spatial localization of bioactive agents within the devices [127]. Currently, best to our knowledge there are only two studies reported about 3D printing of virgin PBS and few PBS-based materials [21, 128]. These researchers investigated the printability of PBS using fused deposition modeling (FDM) or fused filament fabrication (FFF) 3D printability. They reported that PBS was successfully printed via FDM or FFF. In addition, PBS demonstrated good thermal and mechanical properties. PBS has low melt strength which makes it difficult to form filament thus, limit their printability. Therefore, due to the limitations of printing PBS Candal *et al.* [128] investigated the effect of talc on the printability of PBS. In this study, the PBS reinforced with talc filament was obtained from the twin-screw extruder and the filaments were fed

into FDM 3D printer. The incorporation of talc resulted in the improvement in processability, increased crystallization temperatures, enhanced mechanical properties, and improved rheological properties. Other researchers [129] blended PBS with PLA to improve the printability of PBS. The results indicated that the blending of PBS with PLA improved the printability of the blend. However, it was noticed that the increase in PLA loading led to the improvement in melt viscosity and increased tensile properties which is the requirement for FDM 3D printing. Although various researchers have demonstrated that PBS and PBS-based materials can be printed via FDM or FFF, there is still little information about the fabrication of medical devices using 3D printing. This has opened opportunities for designing various biomedical devices from PBS-based materials using FDM 3D printing due to its simplicity and low-cost production. Moreover, much research is required to explore PBS and to develop biomedical devices from PBS since it has demonstrated excellent properties, and its market is growing at a rapid rate. Even though 3D printing of PBS and PBS-based materials were successful, some drawbacks of 3D printing were identified. The major drawback of 3D printing is that the printed objects are static and cannot undergo any dynamic reshaping when subjected to external stimuli. Many scholars have proposed the use of 4D technology to address the limitations associated with 3D technology [72, 130, 131]. The concept of 4D technology is regarded as an emerging area to design customized patient designs which can provide researchers with a wide range of therapeutic control personalized to each patient [63]. Up to date, there are very few studies on the fabrication of 4D printed PBS-based biomedical devices. A recent study [72], investigated the 4D printing aspects of PBS/PLA blends. PBS/PLA blends were prepared by melt compounding and 3D printed into two types of prototypes: Starfish and Endoluminal stents). The shape memory behaviors of the printed stents were investigated by placing them in a hot water bath and observing smooth and complete shape recovery processes. Additionally, graphene oxide functionalized PBS/PLA blends were also prepared and displayed photothermal properties and 4D transformation of a porous scaffold under near-infrared (NIR). The 4D printed PBS/PLA filament showed promising application prospects in tissue engineering and photothermal therapy.

4D printing of biopolymers is at a nascent stage but has enormous potential for developing customized materials that react to various stimuli. These smart materials have the potential to be used in advanced industrial sectors, such as aerospace, medical and defense industries. No study, to the best of our knowledge, has reported on the printing of virgin PBS using 4D printing technology. In the near future, there will be a shift towards 4D printing because of the low production cost, simple processing, and the realization of fabricating complex structures and composites [132].

Despite the fact that 3D PBS-based scaffolds have shown potential in tissue engineering and drug delivery systems, significant challenges still remain when considering the use of PBS in the long run for biomedical applications. For instance, one of the major challenges of PBS is the high production cost which limits its full potential. The issue of inadequate properties such as required melt strength in the case of developing medical devices will be addressed by either reinforcing, blending, and/or copolymerization. In addition, the material that will be used for reinforcing, blending, and/or copolymerization PBS should be eco-friendly and sustainable to avoid compromising the biodegradation feature of PBS. It is worth noting that the temperature of a body system differs from those of room temperature.

The clinical studies of PBS-based scaffolds have been conducted using rats in various labs such as Istituto Zooprofilattico Sperimentale della Sicilia in Italy which was authorized by the Ministry of Health. The findings indicated that PBS scaffold has the potential as an implantable material for improving the regeneration of injured tissue in rats as well as shortening the time for nerve regeneration [49]. However, to the best of our knowledge, there is no study performed clinical trials on humans. Further investigation is required for the exploration of PBS-based products in human trials. In addition, although various grades of PBS are available on the market, according to our understanding, there is little information reported about medical grades which limits PBS for clinical applications. This opens opportunities for suppliers to carefully consider producing medical-grade PBS.

7. Summary

The growing concerns over non-biodegradable conventional plastics derived from petroleum-based

resources have encouraged the use of biodegradable polymers. Amongst biopolymers, polybutylene succinate is a suitable alternative to conventional plastic materials. The market and the research outputs of PBS and PBS-based materials over the last 10 years have been growing immensely. The properties of PBS are similar to those of synthetic polymers such as polypropylene (PP) and polyethylene (PE) with the added biodegradable and biocompatible features. These properties make PBS a favorable material for biomedical applications while demonstrating some shortcomings. The limitations of PBS include inferior properties and high production costs, which can be addressed by blending or reinforcing with cheap materials to reduce the cost as well as enhance the properties.

This study presents the current status and the future directions of PBS-based materials in biomedical applications. Extensive investigations have been conducted on the fabrication of PBS and PBS-based products for tissue engineering and drug delivery with a focus on the biological response to these materials. The areas that remain not sufficiently explored are wound dressing and biomedical devices 3D and 4D printing of PBS-based materials present an opportunity for the development of customized biomedical devices and need to be explored further. *In vivo* studies were performed in a rat model for the implantation of PBS-based scaffolds. The results revealed that the scaffolds integrated well with surrounding tissue and showed degradation after one month, although their degradation is slow. Even though PBS-based products displayed potential in various biomedical applications, there are no studies on clinical trials in humans. Therefore, much research focusing on *in vitro* and *in vivo* testing and optimization is required before the material will be applied in clinical trials. Additionally, the production of PBS with medical grade is needed to ensure the material is suitable for medical procedures and clinical trials. Furthermore, to the best of our knowledge PBS based products have not yet been approved by Food and Drug Administration for biomedical applications, especially clinical trials.

Acknowledgements

This work was supported by the Technology Innovation Agency (TIA) and National Research Foundation (NRF) Thuthuka funding, South Africa.

References

- [1] Galdón E., Millán-Jiménez M., Mora-Castaño G., de Ilarduya A. M., Caraballo I.: A biodegradable copolyester, poly(butylene succinate-*co*- ϵ -caprolactone), as a high efficiency matrix former for controlled release of drugs. *Pharmaceutics*, **13**, 1057 (2021).
<https://doi.org/10.3390/pharmaceutics13071057>
- [2] Muthuraj R., Misra M., Mohanty A. K.: Biocomposite consisting of miscanthus fiber and biodegradable binary blend matrix: Compatibilization and performance evaluation. *RSC Advances*, **7**, 27538–27548 (2017).
<https://doi.org/10.1039/C6RA27987B>
- [3] Mokhena T. C., Sefadi J. S., Sadiku E. R., John M. J., Mochane M. J., Mtibe A.: Thermoplastic processing of PLA/cellulose nanomaterials composites. *Polymers*, **10**, 1363 (2018).
<https://doi.org/10.3390/polym10121363>
- [4] Mokhena T. C., Mochane M. J., Mokhothu T. H., Mtibe A., Tshifularo C. A., Motsoeneng T. S.: Preparation and characterization of antibacterial sustainable nanocomposites. in ‘Sustainable polymer composites and nanocomposites’ (eds.: Inamuddin, Thomas S., Mishra R. K., Asiri A. M.) Springer, Cham, 215–244 (2019).
https://doi.org/10.1007/978-3-030-05399-4_7
- [5] Mokhothu T. H., Mtibe A., Mokhena T. C., Mochane M. J., Ofosu O., Muniyasamy S., Tshifularo C. A., Motsoeneng T. S.: Mechanical, thermal and viscoelastic properties of polymer composites reinforced with various nanomaterials. in ‘Sustainable polymer composites and nanocomposites’ (eds.: Inamuddin, Thomas S., Mishra R. K., Asiri A. M.) Springer, Cham, 185–213 (2019).
https://doi.org/10.1007/978-3-030-05399-4_6
- [6] Muniyasamy S., Mohanrasu K., Gada A., Mokhena T. C., Mtibe A., Boobalan T., Paul V., Arun A.: Biobased biodegradable polymers for ecological applications: A move towards manufacturing sustainable biodegradable plastic products. in ‘Integrating green chemistry and sustainable engineering’ (ed.: ul-Islam S.) Scrivener Publishing, Beverly, 215–253 (2019).
<https://doi.org/10.1002/9781119509868.ch8>
- [7] Mtibe A., Motloung M. P., Bandyopadhyay J., Ray S. S.: Synthetic biopolymers and their composites: Advantages and limitations – An Overview. *Macromolecular Rapid Communications*, **42**, 2100130 (2021).
<https://doi.org/10.1002/marc.202100130>
- [8] Rafiqah S. A., Khalina A., Harmaen A. S., Tawakkal I. A., Zaman K., Asim M., Nurrazi M. N., Lee C. H.: A review on properties and application of bio-based poly(butylene succinate). *Polymers*, **13**, 1436 (2021).
<https://doi.org/10.3390/polym13091436>
- [9] Wang H., Ji J., Zhang W., Zhang Y., Jiang J., Wu Z., Pu S., Chu P. K.: Biocompatibility and bioactivity of plasma-treated biodegradable poly(butylene succinate). *Acta Biomaterialia*, **5**, 279–287 (2009).
<https://doi.org/10.1016/j.actbio.2008.07.017>

- [10] Wei Z., Gu J., Ye Y., Fang M., Lang J., Yang D., Pan Z.: Biodegradable poly(butylene succinate) nanofibrous membrane treated with oxygen plasma for superhydrophilicity. *Surface and Coatings Technology*, **381**, 125147 (2020).
<https://doi.org/10.1016/j.surfcoat.2019.125147>
- [11] Tang X., Dai J., Sun H., Nabanita S., Petr S., Tang L., Cheng Q., Wang D., Wei J.: Copper-doped nano laponite coating on poly(butylene succinate) scaffold with antibacterial properties and cytocompatibility for biomedical application. *Journal of Nanomaterials*, **2018**, 5470814 (2018).
<https://doi.org/10.1155/2018/5470814>
- [12] Sonseca A., Sahay R., Stepien K., Bukala J., Wcislek A., McClain A., Sobolewski P., Sui X. M., Puskas J. E., Kohn J., Wagner H. D., el Fray M.: Architected helically coiled scaffolds from elastomeric poly(butylene succinate) (PBS) copolyester via wet electrospinning. *Materials Science and Engineering C*, **108**, 110505 (2020).
<https://doi.org/10.1016/j.msec.2019.110505>
- [13] Gigli M., Fabbri M., Lotti N., Gamberini R., Rimini B., Munari A.: Poly(butylene succinate)-based polyesters for biomedical applications: A review. *European Polymer Journal*, **75**, 431–460 (2016).
<https://doi.org/10.1016/j.eurpolymj.2016.01.016>
- [14] Zhao X., Zhang D., Yu S., Zhou H., Peng S.: Recent advances in compatibility and toughness of poly(lactic acid)/poly(butylene succinate) blends. *e-Polymers*, **21**, 793–810 (2021).
<https://doi.org/10.1515/epoly-2021-0072>
- [15] Data Bridge Market Research: Polybutylene succinate (PBS) market – Industry trends and forecast to 2028 (2022).
- [16] Nerantzaki M., Koliakou I., Kaloyianni M. G., Koumentakou I., Siska E., Diamanti E., Karakassides M. A., Boccaccini A. R., Bikiaris D. N.: A biomimetic approach for enhancing adhesion and osteogenic differentiation of adipose-derived stem cells on poly(butylene succinate) composites with bioactive ceramics and glasses. *European Polymer Journal*, **87**, 159–173 (2017).
<https://doi.org/10.1016/j.eurpolymj.2016.12.014>
- [17] Guidotti G., Soccio M., Bondi E., Posati T., Sotgiu G., Zamboni R., Torreggiani A., Corticelli F., Lotti N., Aluigi A.: Effects of the blending ratio on the design of keratin/poly(butylene succinate) nanofibers for drug delivery applications. *Biomolecules*, **11**, 1194 (2021).
<https://doi.org/10.3390/biom11081194>
- [18] Fabbri M., Guidotti G., Soccio M., Lotti N., Govoni M., Giordano E., Gazzano M., Gamberini R., Rimini B., Munari A.: Novel biocompatible PBS-based random copolymers containing PEG-like sequences for biomedical applications: From drug delivery to tissue engineering. *Polymer Degradation and Stability*, **153**, 53–62 (2018).
<https://doi.org/10.1016/j.polymdegradstab.2018.04.011>
- [19] John M. J., Dyanti N., Mokhena T., Agbakoba V., Sithole B.: Design and development of cellulosic bio-nanocomposites from forestry waste residues for 3D printing applications. *Materials*, **14**, 3462 (2021).
<https://doi.org/10.3390/ma14133462>
- [20] Domínguez-Robles J., Larrañeta E., Fong M. L., Martín N. K., Irwin N. J., Mutjé P., Tarrés Q., Delgado-Aguilar M.: Lignin/poly(butylene succinate) composites with antioxidant and antibacterial properties for potential biomedical applications. *International Journal of Biological Macromolecules*, **145**, 92–99 (2020).
<https://doi.org/10.1016/j.ijbiomac.2019.12.146>
- [21] Ou-Yang Q., Guo B., Xu J.: Preparation and characterization of poly(butylene succinate)/polylactide blends for fused deposition modeling 3D printing. *ACS Omega*, **3**, 14309–14317 (2018).
<https://doi.org/10.1021/acsomega.8b02549>
- [22] Lascano D., Quiles-Carrillo L., Balart R., Boronat T., Montanes N.: Toughened poly(lactic acid)-PLA formulations by binary blends with poly(butylene succinate-co-adipate)-PBSA and their shape memory behaviour. *Materials*, **12**, 622 (2019).
<https://doi.org/10.3390/ma12040622>
- [23] Gowman A., Wang T., Rodriguez-Urbe A., Mohanty A. K., Misra M.: Bio-poly(butylene succinate) and its composites with grape pomace: Mechanical performance and thermal properties. *ACS Omega*, **3**, 15205–15216 (2018).
<https://doi.org/10.1021/acsomega.8b01675>
- [24] Karimi M. H., Mortazavi S. M. M., Ahmadjo S., Azizi H., Rostami-Daroukola M. R.: Improvement in the thermal and mechanical properties of PP/clay nanocomposite using novel ethoxylated oxidized PE wax as a compatibilizer. *Polymer Composites*, **43**, 389–398 (2022).
<https://doi.org/10.1002/pc.26383>
- [25] Mysiukiewicz O., Kosmela P., Barczewski M., Hejna A.: Mechanical, thermal and rheological properties of polyethylene-based composites filled with micrometric aluminum powder. *Materials*, **13**, 1242 (2020).
<https://doi.org/10.3390/ma13051242>
- [26] Llorens E., Ibañez H., del Valle L. J., Puiggalí J.: Biocompatibility and drug release behavior of scaffolds prepared by coaxial electrospinning of poly(butylene succinate) and polyethylene glycol. *Materials Science and Engineering C*, **49**, 472–484 (2015).
<https://doi.org/10.1016/j.msec.2015.01.039>
- [27] Khalil F., Galland S., Cottaz A., Joly C., Degraeve P.: Polybutylene succinate adipate/starch blends: A morphological study for the design of controlled release films. *Carbohydrate Polymers*, **108**, 272–280 (2014).
<https://doi.org/10.1016/j.carbpol.2014.02.062>
- [28] Mtibe A., Msagati T. A. M., Mishra A. K., Mamba B. B.: Determination of phthalate ester plasticizers in the aquatic environment using hollow fibre supported liquid membranes. *Physics and Chemistry of the Earth*, **50–52**, 239–242 (2012).
<https://doi.org/10.1016/j.pce.2012.08.019>

- [29] Zhao Y., Guo W., Lu Q., Zhang S.: Preparation of poly(butylene succinate)-poly[2-(dimethylamino)ethyl methacrylate] copolymers and their applications as carriers for drug delivery. *Polymer International*, **67**, 708–716 (2018).
<https://doi.org/10.1002/pi.5559>
- [30] Mohanraj K., Sethuraman S., Krishnan U. M.: Development of poly(butylene succinate) microspheres for delivery of levodopa in the treatment of Parkinson's disease. *Journal of Biomedical Materials Research Part B: Applied Biomaterials*, **101B**, 840–847 (2013).
<https://doi.org/10.1002/jbm.b.32888>
- [31] Murase S. K., Aymat M., Calvet A., del Valle L. J., Puiggali J.: Electrosprayed poly(butylene succinate) microspheres loaded with indole derivatives: A system with anticancer activity. *European Polymer Journal*, **71**, 196–209 (2015).
<https://doi.org/10.1016/j.eurpolymj.2015.07.047>
- [32] Brunner C. T., Baran E. T., Pinho E. D., Reis R. L., Neves N. M.: Performance of biodegradable microcapsules of poly(butylene succinate), poly(butylene succinate-co-adipate) and poly(butylene terephthalate-co-adipate) as drug encapsulation systems. *Colloids and Surfaces B: Biointerfaces*, **84**, 498–507 (2011).
<https://doi.org/10.1016/j.colsurfb.2011.02.005>
- [33] Subramanian K., Poorani T. R., Venupriya V., Madhumitha S.: Synthesis and *in-vitro* evaluation of poly(butylene succinate) nano particle as a drug carrier for the controlled delivery of curcumin. *World Journal of Pharmaceutical Research*, **5**, 1237–1261 (2016).
<https://doi.org/10.20959/wjpr20165-6194>
- [34] de Lima N. R. B., Junior F. G. S., Roullin V. G., Pal K.: Amphipathic Au-sulfur-poly(ethylene glycol)-*b*-poly(butylene succinate) system prepared by interfacial reaction as *in-silico* photosensitizer and antineoplastic carrier. *Journal of Drug Delivery Science and Technology*, **64**, 102584 (2021).
<https://doi.org/10.1016/j.jddst.2021.102584>
- [35] da Costa V. C., de Souza Pinto G. L., Nascimento M. V. F., de Campos V. E. B., de Souza Junior F. G.: Poly(butylene succinate)-*g*-poly(hydroxypropyl methacrylate) as a new meloxicam delivery system. *Macromolecular Symposia*, **380**, 1800109 (2018).
<https://doi.org/10.1002/masy.201800109>
- [36] Ferreira L. P., da Cunha B. P., Kuster R. M., Pinto J. C., Souza M. N., de Souza F. G.: Synthesis and chemical modification of poly(butylene succinate) with rutin useful to the release of silybin. *Industrial Crops and Products*, **97**, 599–611 (2017).
<https://doi.org/10.1016/j.indcrop.2016.12.064>
- [37] Soares D. Q. P., Souza Jr F. G., Freitas R. B. V., Soares V. P., Ferreira L. P., Ramon J. A., Oliveira G. E.: Praziquantel release systems based on poly(butylene succinate)/polyethylene glycol nanocomposites. *Current Applied Polymer Science*, **1**, 45–51 (2017).
<https://doi.org/10.2174/2452271601666160922163508>
- [38] Guidotti G., Soccio M., Posati T., Sotgiu G., Tiboni M., Barbalinardo M., Valle F., Casettari L., Zamboni R., Lotti N., Aluigi A.: Regenerated wool keratin-polybutylene succinate nanofibrous mats for drug delivery and cells culture. *Polymer Degradation and Stability*, **179**, 109272 (2020).
<https://doi.org/10.1016/j.polymdegradstab.2020.109272>
- [39] Costa-Pinto A. R., Correlo V. M., Sol P. C., Bhattacharya M., Srouji S., Livne E., Reis R. L., Neves N. M.: Chitosan-poly(butylene succinate) scaffolds and human bone marrow stromal cells induce bone repair in a mouse calvaria model. *Journal of Tissue Engineering and Regenerative Medicine*, **6**, 21–28 (2012).
<https://doi.org/10.1002/term.391>
- [40] Mtibe A., Mokhena T. C., Mokhothu T. H., Mochane M. J.: Recent developments of cellulose-based biomaterials. in 'Soil microenvironment for bioremediation and polymer production' (eds.: Jamil N., Kumar P., Batool R.) Scrivener Publishing, Beverly, 319–338 (2019).
<https://doi.org/10.1002/9781119592129.ch18>
- [41] Huang A., Peng X., Geng L., Zhang L., Huang K., Chen B., Gu Z., Kuang T.: Electrospun poly(butylene succinate)/cellulose nanocrystals bio-nanocomposite scaffolds for tissue engineering: Preparation, characterization and *in vitro* evaluation. *Polymer Testing*, **71**, 101–109 (2018).
<https://doi.org/10.1016/j.polymertesting.2018.08.027>
- [42] Deepthi S., Viha C. V. S., Thitirat C., Furuike T., Tamura H., Jayakumar R.: Fabrication of chitin/poly(butylene succinate)/chondroitin sulfate nanoparticles ternary composite hydrogel scaffold for skin tissue engineering. *Polymers*, **6**, 2974–2984 (2014).
<https://doi.org/10.3390/polym6122974>
- [43] Abudullah T., Saeed U., Memci A., Gauthaman K., Hussain M. A., Al-Turaif H.: Electrospun cellulose nano fibril reinforced PLA/PBS composite scaffold for vascular tissue engineering. *Journal of Polymer Research*, **26**, 110 (2019).
<https://doi.org/10.1007/s10965-019-1772-y>
- [44] Li H., Chang J., Cao A., Wang J.: *In vitro* evaluation of biodegradable poly(butylene succinate) as a novel biomaterial. *Macromolecular Bioscience*, **5**, 433–440 (2005).
<https://doi.org/10.1002/mabi.200400183>
- [45] Ojansivu M., Johansson L., Vanhatupa S., Tamminen I., Hannula M., Hyttinen J., Kellomäki M., Miettinen S.: Knitted 3D scaffolds of polybutylene succinate support human mesenchymal stem cell growth and osteogenesis. *Stem Cells International*, **2018**, 5928935 (2018).
<https://doi.org/10.1155/2018/5928935>

- [46] Liverani L., Piegat A., Niemczyk A., el Fray M., Boccaccini A. R.: Electrospun fibers of poly(butylene succinate-co-dilinoleic succinate) and its blend with poly(glycerol sebacate) for soft tissue engineering applications. *European Polymer Journal*, **81**, 295–306 (2016).
<https://doi.org/10.1016/j.eurpolymj.2016.06.009>
- [47] Hevilla V., Sonseca A., Echeverría C., Muñoz-Bonilla A., Fernández-García M.: Enzymatic synthesis of polyesters and their bioapplications: Recent advances and perspectives. *Macromolecular Bioscience*, **21**, 2100156 (2021).
<https://doi.org/10.1002/mabi.202100156>
- [48] Cooper C. J., Mohanty A. K., Misra M.: Electrospinning process and structure relationship of biobased poly(butylene succinate) for nanoporous fibers. *ACS Omega*, **3**, 5547–5557 (2018).
<https://doi.org/10.1021/acsomega.8b00332>
- [49] Cicero L., Licciardi M., Cirincione R., Puleio R., Giammona G., Giglia G., Sardo P., Vigni G. E., Cioffi A., Sanfilippo A., Cassata G.: Polybutylene succinate artificial scaffold for peripheral nerve regeneration. *Journal of Biomedical Materials Research Part B Applied Biomaterials*, **110**, 125–134 (2022).
<https://doi.org/10.1002/jbmb.b.34896>
- [50] Ju J., Gu Z., Liu X., Zhang S., Peng X., Kuang T.: Fabrication of bimodal open-porous poly(butylene succinate)/cellulose nanocrystals composite scaffolds for tissue engineering application. *International Journal of Biological Macromolecules*, **147**, 1164–1173 (2020).
<https://doi.org/10.1016/j.ijbiomac.2019.10.085>
- [51] Ribeiro V. P., Almeida L. R., Martins A. R., Pashkuleva I., Marques A. P., Ribeiro A. S., Silva C. J., Bonifácio G., Sousa R. A., Oliveira A. L., Reis R. L.: Modulating cell adhesion to polybutylene succinate biotextile constructs for tissue engineering applications. *Journal of Tissue Engineering and Regenerative Medicine*, **11**, 2853–2863 (2017).
<https://doi.org/10.1002/term.2189>
- [52] Niu Y., Cao L., Wei J., Ma Y., Song S., Weng W., Li H., Liu C., Su J.: Development of a bioactive composite of nano fluorapatite and poly(butylene succinate) for bone tissue regeneration. *Journal of Materials Chemistry B*, **2**, 1174–1181 (2014).
<https://doi.org/10.1039/c3tb21371d>
- [53] Wang H., Ji J., Zhang W., Wang W., Zhang Y., Wu Z., Zhang Y., Chu P. K.: Rat calvaria osteoblast behavior and antibacterial properties of O₂ and N₂ plasma-implanted biodegradable poly(butylene succinate). *Acta Biomaterialia*, **6**, 154–159 (2010).
<https://doi.org/10.1016/j.actbio.2009.07.026>
- [54] Prowans P., Kowalczyk R., Wiszniewska B., Czaplak N., Bargiel P., el Fray M.: Bone healing in the presence of a biodegradable PBS-DLA copolyester and its composite containing hydroxyapatite. *ACS Omega*, **4**, 19765–19771 (2019).
<https://doi.org/10.1021/acsomega.9b02539>
- [55] Grigoriadou I., Nianias N., Hoppe A., Terzopoulou Z., Bikiaris D., Will J., Hum J., Roether J. A., Detsch R., Boccaccini A. R.: Evaluation of silica-nanotubes and strontium hydroxyapatite nanorods as appropriate nano-additives for poly(butylene succinate) biodegradable polyester for biomedical applications. *Composites Part B: Engineering*, **60**, 49–59 (2014).
<https://doi.org/10.1016/j.compositesb.2013.12.015>
- [56] Nerantzaki M., Filippousi M., van Tendeloo G., Terzopoulou Z., Bikiaris D., Goudouri O. M., Detsch R., Grüenewald A., Boccaccini A. R.: Novel poly(butylene succinate) nanocomposites containing strontium hydroxyapatite nanorods with enhanced osteoconductivity for tissue engineering applications. *Express Polymer Letters*, **9**, 773–789 (2015).
<https://doi.org/10.3144/expresspolymlett.2015.73>
- [57] Zhao Q., Tang H., Ren L., Wei J.: *In vitro* apatite mineralization, degradability, cytocompatibility and *in vivo* new bone formation and vascularization of bioactive scaffold of polybutylene succinate/magnesium phosphate/wheat protein ternary composite. *International Journal of Nanomedicine*, **15**, 7279–7295 (2020).
<https://doi.org/10.2147/IJN.S255477>
- [58] Coutinho D. F., Pashkuleva I. H., Alves C. M., Marques A. P., Neves N. M., Reis R. L.: The effect of chitosan on the *in vitro* biological performance of chitosan-poly(butylene succinate) blends. *Biomacromolecules*, **9**, 1139–1145 (2008).
<https://doi.org/10.1021/bm701268s>
- [59] Oliveira J. T., Crawford A., Mundy J. L., Sol P. C., Corrello V. M., Bhattacharya M., Neves N. M., Hatton P. V., Reis R. L.: Novel melt-processable chitosan-polybutylene succinate fibre scaffolds for cartilage tissue engineering. *Journal of Biomaterials Science, Polymer Edition*, **22**, 773–788 (2011).
<https://doi.org/10.1163/092050610X494604>
- [60] Alauzen T., Ross S., Madbouly S.: Biodegradable shape-memory polymers and composites. *Physical Sciences Reviews*, in press (2022).
<https://doi.org/10.1515/psr-2020-0077>
- [61] Karasu F., Weder C.: Blends of poly(ester urethane)s and polyesters as a general design approach for triple-shape memory polymers. *Journal of Applied Polymer Science*, **138**, 49935 (2021).
<https://doi.org/10.1002/app.49935>
- [62] Zheng Y., Ji X., Yin M., Shen J., Guo S.: Strategy for fabricating multiple-shape-memory polymeric materials *via* the multilayer assembly of *co*-continuous blends. *ACS Applied Materials and Interfaces*, **9**, 32270–32279 (2017).
<https://doi.org/10.1021/acsaami.7b10345>
- [63] Ramaraju H., Akman R. E., Safranski D. L., Hollister S. J.: Designing biodegradable shape memory polymers for tissue repair. *Advanced Functional Materials*, **30**, 2002014 (2020).
<https://doi.org/10.1002/adfm.202002014>

- [64] Huang M., Zheng L., Wang L., Dong X., Gao X., Li C., Wang D.: Double crystalline multiblock copolymers with controlling microstructure for high shape memory fixity and recovery. *ACS Applied Materials and Interfaces*, **9**, 30046–30055 (2017).
<https://doi.org/10.1021/acsami.7b08403>
- [65] Suchao-in K., Chirachanchai S.: ‘Grafting to’ as a novel and simple approach for triple-shape memory polymers. *ACS Applied Materials and Interfaces*, **5**, 6850–6853 (2013).
<https://doi.org/10.1021/am402214j>
- [66] Huang C-L., Jiao L., Zhang J-J., Zeng J-B., Yang K-K., Wang Y-Z.: Poly(butylene succinate)-poly(ethylene glycol) multiblock copolymer: Synthesis, structure, properties and shape memory performance. *Polymer Chemistry*, **3**, 800–808 (2012).
<https://doi.org/10.1039/c2py00603k>
- [67] Paderni K., Fabbri P., Toselli M., Messori M.: Shape memory properties of PBS-silica hybrids. *Materials*, **7**, 751–768 (2014).
<https://doi.org/10.3390/ma7020751>
- [68] Tcharkhtchi A., Abdallah-Elhirsiti S., Ebrahimi K., Fitoussi J., Shirinbayan M., Farzaneh S.: Some new concepts of shape memory effect of polymers. *Polymers*, **6**, 1144–1163 (2014).
<https://doi.org/10.3390/polym6041144>
- [69] Zeng X., Wu B., Wu L., Hu J., Bu Z., Li B-G.: Poly(L-lactic acid)-*block*-poly(butylene succinate-*co*-butylene adipate) multiblock copolymers: From synthesis to thermo-mechanical properties. *Industrial and Engineering Chemistry Research*, **53**, 3550–3558 (2014).
<https://doi.org/10.1021/ie403623f>
- [70] Huang C-L., He M-J., Huo M., Du L., Zhan C., Fan C-J., Yang K-K., Chin I-J., Wang Y-Z.: A facile method to produce PBS-PEG/CNTs nanocomposites with controllable electro-induced shape memory effect. *Polymer Chemistry*, **4**, 3987–3997 (2013).
<https://doi.org/10.1039/c3py00461a>
- [71] Gradzik B., Stenzel A., Boccaccini A. R., el Fray M.: Influence of functionalized halloysite clays (HNT) on selected properties of multiblock (e)PBS-EG copolymer obtained by enzymatic catalysis. *Designed Monomers and Polymers*, **18**, 501–511 (2015).
<https://doi.org/10.1080/15685551.2015.1041080>
- [72] Lin C., Liu L., Liu Y., Leng J.: 4D printing of shape memory polybutylene succinate/polylactic acid (PBS/PLA) and its potential applications. *Composite Structures*, **279**, 114729 (2022).
<https://doi.org/10.1016/j.compstruct.2021.114729>
- [73] Ikada Y., Tsuji H.: Biodegradable polyesters for medical and ecological applications. *Macromolecular Rapid Communications*, **21**, 117–132 (2000).
[https://doi.org/10.1002/\(SICI\)1521-3927\(20000201\)21:3<117::AID-MARC117>3.0.CO;2-X](https://doi.org/10.1002/(SICI)1521-3927(20000201)21:3<117::AID-MARC117>3.0.CO;2-X)
- [74] Platnieks O., Gaidukovs S., Barkane A., Sereda A., Gaidukova G., Grase L., Thakur V. K., Filipova I., Fridrihsone V., Skute M., Laka M.: Bio-based poly(butylene succinate)/microcrystalline cellulose/nanofibrillated cellulose-based sustainable polymer composites: Thermo-mechanical and biodegradation studies. *Polymers*, **12**, 1472 (2020).
<https://doi.org/10.3390/polym12071472>
- [75] Anstey A., Muniyasamy S., Reddy M. M., Misra M., Mohanty A.: Processability and biodegradability evaluation of composites from poly(butylene succinate) (PBS) bioplastic and biofuel *co*-products from Ontario. *Journal of Polymers and the Environment*, **22**, 209–218 (2014).
<https://doi.org/10.1007/s10924-013-0633-8>
- [76] Adhikari D., Mukai M., Kubota K., Kai T., Kaneko N., Araki K. S., Kubo M.: Degradation of bioplastics in soil and their degradation effects on environmental microorganisms. *Journal of Agricultural Chemistry and Environment*, **5**, 23–34 (2016).
<https://doi.org/10.4236/jacen.2016.51003>
- [77] Jayasekara R., Sheridan S., Loubakos E., Beh H., Christie G. B. Y., Jenkins M., Halley P. B., Mcglashan S., Lonergan G. T.: Biodegradation and ecotoxicity evaluation of a bionolle and starch blend and its degradation products in compost. *International Biodeterioration and Biodegradation*, **51**, 77–81 (2003).
[https://doi.org/10.1016/S0964-8305\(02\)00090-2](https://doi.org/10.1016/S0964-8305(02)00090-2)
- [78] Habib Ullah M., Mahadi W. N. L., Latef T. A.: Aerogel poly(butylene succinate) biomaterial substrate for RF and microwave applications. *Scientific Reports*, **5**, 12868 (2015).
<https://doi.org/10.1038/srep12868>
- [79] Petchwattana N., Covavisaruch S., Wibooranawong S., Naknaen P.: Antimicrobial food packaging prepared from poly(butylene succinate) and zinc oxide. *Measurement: Journal of the International Measurement Confederation*, **93**, 442–448 (2016).
<https://doi.org/10.1016/j.measurement.2016.07.048>
- [80] Wattanawong N., Chatchaipaboon K., Sreekirin N., Aht-Ong D.: Migration, physical and antibacterial properties of silver zeolite/poly(butylene succinate) composite films for food packaging applications. *Journal of Reinforced Plastics and Composites*, **39**, 95–110 (2020).
<https://doi.org/10.1177/0731684419893440>
- [81] Tan B., Bi S., Emery K., Sobkowicz M. J.: Bio-based poly(butylene succinate-*co*-hexamethylene succinate) copolyesters with tunable thermal and mechanical properties. *European Polymer Journal*, **86**, 162–172 (2017).
<https://doi.org/10.1016/j.eurpolymj.2016.11.017>

- [82] Hsu K-H., Chen C-W., Wang L-Y., Chan H-W., He C-L., Cho C-J., Rwei S-P., Kuo C-C.: Bio-based thermoplastic poly(butylene succinate-co-propylene succinate) copolyesters: Effect of glycerol on thermal and mechanical properties. *Soft Matter*, **15**, 9710–9720 (2019).
<https://doi.org/10.1039/c9sm01958h>
- [83] Frollini E., Bartolucci N., Sisti L., Celli A.: Biocomposites based on poly(butylene succinate) and curaua: Mechanical and morphological properties. *Polymer Testing*, **45**, 168–173 (2015).
<https://doi.org/10.1016/j.polymertesting.2015.06.009>
- [84] Sadeghi A., Mousavi S. M., Saljoughi E., Kiani S.: Biodegradable membrane based on polycaprolactone/polybutylene succinate: Characterization and performance evaluation in wastewater treatment. *Journal of Applied Polymer Science*, **138**, 50332 (2021).
<https://doi.org/10.1002/app.50332>
- [85] Wei Z., Liu Y., Hu H., Yu J., Li F.: Biodegradable poly(butylene succinate-co-terephthalate) nanofibrous membranes functionalized with cyclodextrin polymer for effective methylene blue adsorption. *RSC Advances*, **6**, 108240–108246 (2016).
<https://doi.org/10.1039/c6ra22941g>
- [86] Sadeghi A., Mottie A., Kiani S., Mahand S. N., Khonakdar H. A.: Polybutylene succinate (PBS)/acrylonitrile butadiene styrene (ABS) membrane with improved mechanical properties for wastewater treatment. *Polymer Bulletin*, in press (2021).
<https://doi.org/10.1007/s00289-021-03881-w>
- [87] Janjua S., Hussain Z., Khan Z., Liaqat M. A., Umer M. A.: Biopolymer blended films of poly(butylene succinate)/cyclic olefin copolymer with enhanced mechanical strength for packaging applications. *Journal of Applied Polymer Science*, **138**, 50081 (2021).
<https://doi.org/10.1002/app.50081>
- [88] Saeng-on J., Aht-Ong D.: Compatibility of banana starch nanocrystals/poly(butylene succinate) bio-nanocomposite packaging films. *Journal of Applied Polymer Science*, **135**, 46836 (2018).
<https://doi.org/10.1002/app.46836>
- [89] Xu J., Manepalli P. H., Zhu L., Narayan-Sarathy S., Alavi S.: Morphological, barrier and mechanical properties of films from poly(butylene succinate) reinforced with nanocrystalline cellulose and chitin whiskers using melt extrusion. *Journal of Polymer Research*, **26**, 188 (2019).
<https://doi.org/10.1007/s10965-019-1783-8>
- [90] Petchwattana N., Naknaen P., Cha-aim K., Suksri C., Sanetuntikul J.: Controlled release antimicrobial sachet prepared from poly(butylene succinate)/geraniol and ethylene vinyl alcohol coated paper for bread shelf-life extension application. *International Journal of Biological Macromolecules*, **189**, 251–261 (2021).
<https://doi.org/10.1016/j.ijbiomac.2021.08.119>
- [91] Łopusiewicz Ł., Macieja S., Bartkowiak A., el Fray M.: Antimicrobial, antibiofilm, and antioxidant activity of functional poly(butylene succinate) films modified with curcumin and carvacrol. *Materials*, **14**, 7882 (2021).
<https://doi.org/10.3390/ma14247882>
- [92] Suwanamornlert P., Kerddonfag N., Sane A., Chinsirikul W., Zhou W., Chonhenchob V.: Poly(lactic acid)/poly(butylene-succinate-co-adipate) (PLA/PBSA) blend films containing thymol as alternative to synthetic preservatives for active packaging of bread. *Food Packaging and Shelf Life*, **25**, 100515 (2020).
<https://doi.org/10.1016/j.foodpack.2020.100515>
- [93] Palai B., Mohanty S., Nayak S. K.: Synergistic effect of polylactic acid(PLA) and poly(butylene succinate-co-adipate) (PBSA) based sustainable, reactive, super toughened eco-composite blown films for flexible packaging applications. *Polymer Testing*, **83**, 106130 (2020).
<https://doi.org/10.1016/j.polymertesting.2019.106130>
- [94] Delorme A. E., Radusin T., Myllytie P., Verney V., Askanian H.: Enhancement of gas barrier properties and durability of poly(butylene succinate-co-butylene adipate)-based nanocomposites for food packaging applications. *Nanomaterials*, **12**, 978 (2022).
<https://doi.org/10.3390/nano12060978>
- [95] Siracusa V., Lotti N., Munari A., Dalla Rosa M.: Poly(butylene succinate) and poly(butylene succinate-co-adipate) for food packaging applications: Gas barrier properties after stressed treatments. *Polymer Degradation and Stability*, **119**, 35–45 (2015).
<https://doi.org/10.1016/j.polymdegradstab.2015.04.026>
- [96] Łopusiewicz Ł., Zdanowicz M., Macieja S., Kowalczyk K., Bartkowiak A.: Development and characterization of bioactive poly(butylene-succinate) films modified with quercetin for food packaging applications. *Polymers*, **13**, 1798 (2021).
<https://doi.org/10.3390/polym13111798>
- [97] Ayu R. S., Khalina A., Harmaen A. S., Zaman K., Nurrazi N. M., Isma T., Lee C. H.: Effect of empty fruit bunch reinforcement in polybutylene-succinate/modified tapioca starch blend for agricultural mulch films. *Scientific Reports*, **10**, 1166 (2020).
<https://doi.org/10.1038/s41598-020-58278-y>
- [98] Hongsriphan N., Pinpueng A.: Properties of agricultural films prepared from biodegradable poly(butylene succinate) adding natural sorbent and fertilizer. *Journal of Polymers and the Environment*, **27**, 434–443 (2019).
<https://doi.org/10.1007/s10924-018-1358-5>
- [99] Figueiredo A. S., Icart L. P., Marques F. D., Fernandes E. R., Ferreira L. P., Oliveira G. E., Souza F. G.: Extrinsically magnetic poly(butylene succinate): An up-and-coming petroleum cleanup tool. *Science of the Total Environment*, **647**, 88–98 (2019).
<https://doi.org/10.1016/j.scitotenv.2018.07.421>
- [100] Yin D., Mi J., Zhou H., Wang X., Tian H.: Fabrication of branching poly(butylene succinate)/cellulose nanocrystal foams with exceptional thermal insulation. *Carbohydrate Polymers*, **247**, 116708 (2020).
<https://doi.org/10.1016/j.carbpol.2020.116708>

- [101] Siracusa V., Genovese L., Munari A., Lotti N.: How stress treatments influence the performance of biodegradable poly(butylene succinate)-based copolymers with thioether linkages for food packaging applications. *Materials*, **10**, 1009 (2017).
<https://doi.org/10.3390/ma10091009>
- [102] Genovese L., Lotti N., Gazzano M., Siracusa V., Rosa M. D., Munari A.: Novel biodegradable aliphatic copolyesters based on poly(butylene succinate) containing thioether-linkages for sustainable food packaging applications. *Polymer Degradation and Stability*, **132**, 191–201 (2016).
<https://doi.org/10.1016/j.polymdegradstab.2016.02.022>
- [103] Negrin M., Macerata E., Consolati G., Quasso F., Genovese L., Soccio M., Giola M., Lotti N., Munari A., Mariani M.: Gamma radiation effects on random copolymers based on poly(butylene succinate) for packaging applications. *Radiation Physics and Chemistry*, **142**, 34–43 (2018).
<https://doi.org/10.1016/j.radphyschem.2017.05.011>
- [104] Vytejková S., Vápenka L., Hradecký J., Dobiáš J., Hajšlová J., Lorient C., Vannini L., Poustka J.: Testing of polybutylene succinate based films for poultry meat packaging. *Polymer Testing*, **60**, 357–364 (2017).
<https://doi.org/10.1016/j.polymertesting.2017.04.018>
- [105] Rasheed M., Jawaid M., Parveez B., Bhat A. H., Alamery S.: Morphology, structural, thermal, and tensile properties of bamboo microcrystalline cellulose/poly(Lactic acid)/poly(butylene succinate) composites. *Polymers*, **13**, 465 (2021).
<https://doi.org/10.3390/polym13030465>
- [106] Vorawongsagul S., Pratumpong P., Pechyen C.: Preparation and foaming behavior of poly (lactic acid)/poly (butylene succinate)/cellulose fiber composite for hot cups packaging application. *Food Packaging and Shelf Life*, **27**, 100608 (2021).
<https://doi.org/10.1016/j.foodpack.2020.100608>
- [107] Su S., Kopitzky R., Tolga S., Kabasci S.: Polylactide (PLA) and its blends with poly(butylene succinate) (PBS): A brief review. *Polymers*, **11**, 1193 (2019).
<https://doi.org/10.3390/polym11071193>
- [108] Gigli M., Lotti N., Gazzano M., Finelli L., Munari A.: Novel eco-friendly random copolyesters of poly(butylene succinate) containing ether-linkages. *Reactive and Functional Polymers*, **72**, 303–310 (2012).
<https://doi.org/10.1016/j.reactfunctpolym.2012.02.013>
- [109] Yang J., Tian W., Li Q., Li Y., Cao A.: Novel biodegradable aliphatic poly(butylene succinate-co-cyclic carbonate)s bearing functionalizable carbonate building blocks: II. Enzymatic biodegradation and *in vitro* biocompatibility assay. *Biomacromolecules*, **5**, 2258–2268 (2004).
<https://doi.org/10.1021/bm049705>
- [110] Han S-I., Kang S-W., Kim B-S., Im S. S.: A novel polymeric ionomer as a potential biomaterial: Crystallization behavior, degradation, and *in-vitro* cellular interactions. *Advanced Functional Materials*, **15**, 367–374 (2005).
<https://doi.org/10.1002/adfm.200400079>
- [111] Gualandi C., Soccio M., Saino E., Focarete M. L., Lotti N., Munari A., Moroni L., Visai L.: Easily synthesized novel biodegradable copolyesters with adjustable properties for biomedical applications. *Soft Matter*, **8**, 5466–5476 (2012).
<https://doi.org/10.1039/c2sm25308a>
- [112] Wu F., Huang C-L., Zeng J-B., Li S-L., Wang Y-Z.: Synthesis and characterization of segmented poly(butylene succinate) urethane ionenes containing secondary amine cation. *Polymer*, **55**, 4358–4368 (2014).
<https://doi.org/10.1016/j.polymer.2014.05.059>
- [113] Wang L-C., Chen J-W., Liu H-L., Chen Z-Q., Zhang Y., Wang C-Y., Feng Z-G.: Synthesis and evaluation of biodegradable segmented multiblock poly(ether ester) copolymers for biomaterial applications. *Polymer International*, **53**, 2145–2154 (2004).
<https://doi.org/10.1002/pi.1645>
- [114] Pinho E. D., Martins A., Araújo J. V., Reis R. L., Neves N. M.: Degradable particulate composite reinforced with nanofibres for biomedical applications. *Acta Biomaterialia*, **5**, 1104–1114 (2009).
<https://doi.org/10.1016/j.actbio.2008.11.018>
- [115] Lavilla C., Alla A., de Ilarduya A. M., Muñoz-Guerra S.: High T_g bio-based aliphatic polyesters from bicyclic d-mannitol. *Biomacromolecules*, **14**, 781–793 (2013).
<https://doi.org/10.1021/bm301854c>
- [116] Zakharova E., Alla A., de Ilarduya A. M., Muñoz-Guerra S.: Bio-based PBS copolyesters derived from a bicyclic d-glucitol. *RSC Advances*, **5**, 46395–46404 (2015).
<https://doi.org/10.1039/c5ra03844h>
- [117] Bautista M., de Ilarduya A. M., Alla A., Muñoz-Guerra S.: Poly(butylene succinate) ionomers with enhanced hydrodegradability. *Polymers*, **7**, 1232–1247 (2015).
<https://doi.org/10.3390/polym7071232>
- [118] Soccio M., Lotti N., Gazzano M., Govoni M., Giordano E., Munari A.: Molecular architecture and solid-state properties of novel biocompatible PBS-based copolyesters containing sulphur atoms. *Reactive and Functional Polymers*, **72**, 856–867 (2012).
<https://doi.org/10.1016/j.reactfunctpolym.2012.08.002>
- [119] Gualandi C., Soccio M., Govoni M., Valente S., Lotti N., Munari A., Giordano E., Pasquini G., Focarete M. L.: Poly(butylene/diethylene glycol succinate) multiblock copolyester as a candidate biomaterial for soft tissue engineering: Solid-state properties, degradability, and biocompatibility. *Journal of Bioactive and Compatible Polymers*, **27**, 244–264 (2012).
<https://doi.org/10.1177/0883911512440536>

- [120] Almeida L. R., Martins A. R., Fernandes E. M., Oliveira M. B., Correlo V. M., Pashkuleva I., Marques A. P., Ribeiro A. S., Durães N. F., Silva C. J., Bonifácio G., Sousa R. A., Oliveira A. L., Reis R. L.: New biotextiles for tissue engineering: Development, characterization and *in vitro* cellular viability. *Acta Biomaterialia*, **9**, 8167–8181 (2013).
<https://doi.org/10.1016/j.actbio.2013.05.019>
- [121] Correlo V. M., Boesel L. F., Pinho E., Costa-Pinto A. R., da Silva M. L. A., Bhattacharya M., Mano J. F., Neves N. M., Reis R. L.: Melt-based compression-molded scaffolds from chitosan-polyester blends and composites: Morphology and mechanical properties. *Journal of Biomedical Materials Research: Part A*, **91**, 489–504 (2009).
<https://doi.org/10.1002/jbm.a.32221>
- [122] Göpferich A.: Mechanisms of polymer degradation and erosion. *Biomaterials*, **17**, 103–114 (1996).
[https://doi.org/10.1016/0142-9612\(96\)85755-3](https://doi.org/10.1016/0142-9612(96)85755-3)
- [123] Jäger E., Jäger A., Chytil P., Etrych T., Říhová B., Giacomelli F. C., Štěpánek P., Ulbrich K.: Combination chemotherapy using core-shell nanoparticles through the self-assembly of HPMA-based copolymers and degradable polyester. *Journal of Controlled Release*, **165**, 153–161 (2013).
<https://doi.org/10.1016/j.jconrel.2012.11.009>
- [124] Costa-Pinto A. R., Martins A. M., Castelhana-Carlos M. J., Correlo V. M., Sol P. C., Longatto-Filho A., Bhattacharya M., Reis R. L., Neves N. M.: *In vitro* degradation and *in vivo* biocompatibility of chitosan-poly (butylene succinate) fiber mesh scaffolds. *Journal of Bioactive and Compatible Polymers*, **29**, 137–151 (2014).
<https://doi.org/10.1177/0883911514521919>
- [125] Serrano M. C., Ameer G. A.: Recent insights into the biomedical applications of shape-memory polymers. *Macromolecular Bioscience*, **12**, 1156–1171 (2012).
<https://doi.org/10.1002/mabi.201200097>
- [126] Aliko K., Aldakhlalla M. B., Leslie L. J., Worthington T., Topham P. D., Theodosiou E.: Poly(butylene succinate) fibrous dressings containing natural antimicrobial agents. *Journal of Industrial Textiles*, **51**, 6948S–6967S (2021).
<https://doi.org/10.1177/1528083720987209>
- [127] Mokhena T. C., John M. J., Mochane M. J., Sadiku R. E., Motsoeng T. S., Mtibe, Tsipa P. C.: Antibiotic 3D printed materials for healthcare applications. in ‘Antibiotic materials in healthcare’ (eds.: Kokkarachedu V., Kanikireddy V., Sadiku R. E.) Elsevier, London 141–158 (2020).
<https://doi.org/10.1016/B978-0-12-820054-4.00009-4>
- [128] Candal M. V., Calafel I., Aranburu N., Fernández M., Gericca-Echevarria G., Santamaría A., Müller A. J.: Thermo-rheological effects on successful 3D printing of biodegradable polyesters. *Additive Manufacturing*, **36**, 101408 (2020).
<https://doi.org/10.1016/j.addma.2020.101408>
- [129] Prasong W., Ishigami A., Thumsorn S., Kurose T., Ito H.: Improvement of interlayer adhesion and heat resistance of biodegradable ternary blend composite 3D printing. *Polymers*, **13**, 740 (2021).
<https://doi.org/10.3390/polym13050740>
- [130] Momeni F., Hassani S. M. M. N., Liu X., Ni J.: A review of 4D printing. *Materials and Design*, **122**, 42–79 (2017).
<https://doi.org/10.1016/j.matdes.2017.02.068>
- [131] Falahati M., Ahmadvand P., Safae S., Chang Y-C., Lyu Z., Chen R., Li L., Lin Y.: Smart polymers and nanocomposites for 3D and 4D printing. *Materials Today*, **40**, 215–245 (2020).
<https://doi.org/10.1016/j.mattod.2020.06.001>
- [132] Ma S., Jiang Z., Wang M., Zhang L., Liang Y., Zhang Z., Ren L., Ren L.: 4D printing of PLA/PCL shape memory composites with controllable sequential deformation. *Bio-Design and Manufacturing*, **4**, 867–878 (2021).
<https://doi.org/10.1007/s42242-021-00151-6>

Research article

Interphase percolation phenomena in chitosan-graphene oxide nanocomposites, the role of water content

Yevgen Prokhorov*^{ID}, Gabriel Luna-Barcenas^{ID}, Yuriy Kovalenko^{ID}

Cinvestav, Unidad Querétaro, 76230 Querétaro, QRO, Mexico

Received 14 April 2022; accepted in revised form 17 August 2022

Abstract. Herein, we report interphase percolation phenomena in chitosan-graphene oxide (CS-GO) nanocomposites as a function of water content. The dependencies of the DC conductivity and the static dielectric constant have been investigated in a wide range of GO concentrations (0–12 wt%) and water contents (0, 4, 9, and 24%). Fourier-transform infrared spectroscopy (FTIR), Raman spectroscopy and X-ray diffraction (XRD) measurements reveal the presence of strong interaction between the CS matrix and GO fillers. For annealed CS-GO films in a vacuum (no water content), the DC conductivity and dielectric constant do not depend upon the GO concentration. When the water content increases, a percolation phenomenon is now detected; by increasing water content, the percolation threshold shifts to a lower GO concentration. A three-phase model which includes the conductivities of CS and GO, and an interphase layer fits well DC conductivity data; this model-based analysis suggests that upon increasing the water content, the conductivity of the interphase layer is higher than the one of both neat CS and GO. Water molecules at the interface drive a high-conductivity interfacial shell supporting a proton transfer mechanism; this mechanism is a plausible scenario for percolation in wet CS-GO nanocomposites. Our results may be of great importance in the applications of such nanocomposites in flexible electronics, biomedicine, proton exchange membranes, and sensors.

Keywords: nanocomposites, biocomposites, material testing, percolation, interphase layer

1. Introduction

In the last decade, chitosan-graphene oxide (CS-GO) nanocomposites have been extensively studied in different research fields for applications in biomedicine [1], adsorption of various water pollutants [2], food packaging [3], biosensing [4], proton exchange membranes [5], pharmacology [6], organic electronics [7], *etc.* Such wide applications are related to good film-forming capability, biocompatibility, excellent mechanical properties, and proton conductivity. Additionally, graphene oxide contains carboxyl and epoxy groups that help GO disperse readily in aqueous media; its surface is negatively charged due to an apparent ionization of carboxylic acid and phenolic hydroxyl groups on the GO sheets [8]. When CS dissolves in acids NH_3^+ groups form and adhere

to negatively charged GO surfaces. Therefore, the surface groups of GO can interact with the CS matrix via hydrogen bonding and electrostatic interactions to achieve good dispersion [9]. Both CS and GO are hydrophilic materials with high proton conductivity due to proton hopping among hydrogen-bonding networks along the adsorbed water via Grotthuss and/or vehicle mechanisms [9]. Moreover, the proton conductivity of GO can reach up to 10^{-2} S/cm [10]. Consequently, the addition of graphene oxide in a CS matrix tends to increase proton conductivity, and a percolation effect may be observed as in the case of other GO-polymer based membranes [10–12]. The conductivity percolation effect is related to an abrupt increase in conductivity upon increasing fillers concentration and an eventual saturation. On the other

*Corresponding author, e-mail: prokhorov@cinvestav.mx
© BME-PT

hand, the dielectric constant ϵ of a percolating system increases before the percolation threshold according to power-law dependence [13, 14]. However, in the literature percolation effect has only been reported for CS-poly(vinyl pyrrolidone)-polycarboxylate functionalized graphene nanoplates with a percolation threshold at 25 wt% of graphene nanoplates [15], CS-polymetitaniline-functionalized graphene with a percolation threshold at 3.5 vol% [16], and CS-GO functionalized with sulphonic acid with a percolation threshold at 0.49 wt% [17]. Conversely, in CS-bio-functionalized graphene [18] and CS-sulfonated GO [19] the percolation effect has not been observed.

Additionally, the values of dielectric constant (ϵ) of CS-GO nanocomposites reported in the literature exhibit large dispersion. For example, at the frequency of 1 kHz, in ref. [20] for CS-GO (with 4 wt% of GO) $\epsilon \approx 1$; in ref. [21] for 2 wt% of GO $\epsilon \approx 0.45$ and in CS-GO functionalized with sulphonic acid [16] for 0.08 volume fraction of GO ϵ can reach 3500.

It is well known that the conductivity and the dielectric constant of CS-GO nanocomposites strongly depend upon water content [19]. However, to the best of our knowledge, in the literature, there are no reports on how water content will affect the percolation properties of CS-GO nanocomposites. The knowledge about the influence of water on the percolation properties of such nanocomposites plays an essential role in a variety of applications, including the development of proton exchange membranes, sensors, organic electronics, and in biomedicine; the conductivity and dielectric constant of nanocomposites affect their biocompatibility [22].

Based on the above discussion, the aim of this work is to investigate the percolation phenomena associated with CS-GO nanocomposites in a wide range of GO concentrations and under different water content. Additionally, Fourier-transform infrared spectroscopy (FTIR), Raman spectroscopy and X-ray diffraction (XRD), weight, and dielectric spectroscopy measurements were carried out to shed light on the properties of wet CS-GO nanocomposites for many different modern applications.

2. Experimental

Chitosan (CS, medium molecular weight, deacetylation 75–85%), acetic acid (99.7%), and graphene oxide sheets dispersed in water were purchased from Merck (Mexico). All the reagents were of analytical grade.

1 g of chitosan was dissolved in 99 ml of a 0.1 M acetic acid solution with subsequent stirring to promote dissolution. Different amounts of colloidal GO suspensions were sonicated (0–12 wt% GO, CS dry base) and dispersed in the CS solution by ultrasound for 60 min. Nanocomposite films (with a thickness of about 30–60 μm) were prepared by the solvent cast method by pouring the solution into a plastic Petri dish and allowing the solvent to evaporate at 60 °C for 24 hours. A thin layer of gold was sputtering onto both sides of the film previously to electrical measurements to serve as electrodes.

FTIR measurements were carried out on a Perkin Elmer Spectrum spectrophotometer (USA) using an attenuated total reflection (ATR) accessory in the range 4000–650 cm^{-1} and with a resolution of 4 cm^{-1} . Raman spectroscopic measurements were carried out using a Dilor Labram II (USA) with an excitation laser of 632.8 nm.

XRD measurements were performed using a Rigaku diffractometer ULTIMA IV (Japan), equipped with Cu K_{α} radiation ($\lambda = 1.5406 \text{ \AA}$).

Impedance measurements were carried out on films with different water content in air and vacuum at room temperature using Agilent 4249 A (USA) in the frequency range 40 Hz–70 MHz with an amplitude of AC voltage 100 mV. DC resistance R and capacitance C at the limit of zero frequency were calculated from fitting impedance spectra using ZView[®] program (USA). Conductivity (σ) and static dielectric constant (ϵ_s) (at the limit of zero frequency) were calculated from the following relationship: $\sigma = d/(R \cdot S)$, $\epsilon_s = (C \cdot d)/(\epsilon_0 \cdot S)$, where d and S are the thickness and area of samples, respectively. Film thickness was measured in each sample using a micrometer Mitutoyo (Japan) with a resolution of 1 μm .

The water content of CS–GO films was determined by measuring the change in weight between the dry and wet films using Sartorius AZ214 analytical balance (USA) with readability of 0.0001 gm. Weight of dry films (W_d) was obtained on films annealing to the temperature of 120 °C in a vacuum cell for 1 hour, followed by cooling to room temperature for further measurements. Due to water absorption, the weight of CS–GO films changes when compared with those annealed. Moisture content (W [%]) was calculated using the Equation (1):

$$W [\%] = \frac{W_0 - W_d}{W_0} \quad (1)$$

where W_0 is the sample weight measured after the different treatments.

As the prepared films have a water content *ca.* 9%. The nanocomposite films soaked in a vacuum at 25 °C for 30 min. have a water content *ca.* 4%. For higher water content, samples were placed in a home-made water chamber bath with deionized water at 80 °C for 40 min – exposure time. This conditioning time allows one to obtain *ca.* 24% of water.

3. Results and discussion

FTIR spectrum of GO [23, 24] and neat CS [25] are consistent with previous reports in the literature. Figure 1 shows the FTIR spectra of GO, neat CS films, and CS-GO films with 7 and 12 wt% of GO. For GO, observed broadband in the 3700–2300 cm^{-1} corresponds to the stretching vibrations of structural OH groups and water molecules. The peak at 1729 cm^{-1} is attributed to the presents of C=O stretching vibration, and the peak at 163 cm^{-1} can be assigned to the C–C stretching and absorbed hydroxyl groups in the GO. In the case of chitosan, the characteristic broadband peak centered at 3328 cm^{-1} corresponded to the overlap of stretching vibration of NH and OH groups. Additionally, it was observed the characteristic peaks at 1647 (amide I group) and 1557 cm^{-1} (bending vibrations of NH_3). The change positions of peaks in CS-GO films from 3328 to 3225 cm^{-1} ; 1647 to 1625 cm^{-1} , and 1557 to 1544 cm^{-1} , and the appearance of the weak peak of GO (at 1729 cm^{-1}) can be related to the synergetic effect of electrostatic interaction between polycationic CS and the negative charge on the surface of GO and hydrogen bond between CS and oxygen-containing functional groups in GO [20, 26].

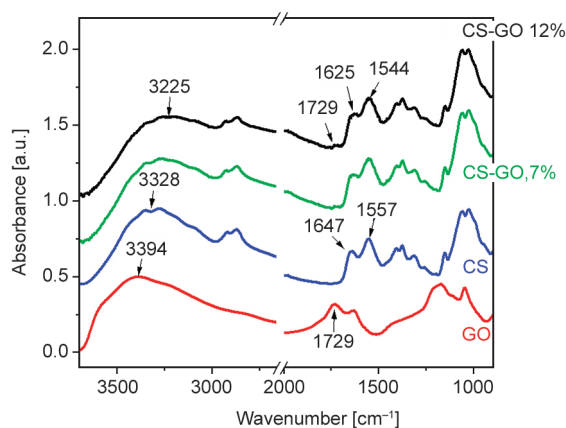


Figure 1. FTIR spectra of GO, CS, and CS-GO with 7 and 12 wt% of GO.

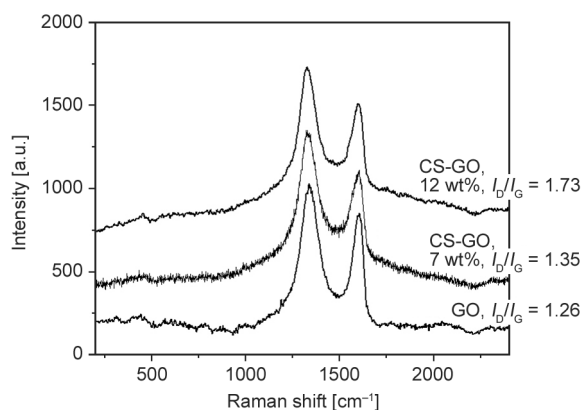


Figure 2. Raman spectra of the GO and as-prepared CS-GO films with 7 and 12 wt% of GO.

Raman measurements may be used to provide further support for the relationship between CS and GO. Figure 2 shows the Raman spectra of the GO and the prepared CS-GO films with 7 and 12 wt% of GO. The D-band (1330 cm^{-1}), which may be attributed to a defect or a disordered lattice, and the G-band (1600 cm^{-1}), which is the first order scattering of the E2g mode of sp^2 domains, are present in all spectra [27]. Typically, the I_D/I_G intensities ratio may be used to gauge the severity of structural abnormality [28]. The I_D/I_G intensity ratio for tidy GO is 1.26. In CS-GO films, this ratio rises to 1.35 for films with 7 weight percent of GO and 1.73 for films with 12 weight percent. Such a change in the D/G intensity can be attributed to the destruction of the GO layer structure and/or to the appearance of structural defects due to the interaction of GO with CS side groups [20, 27].

Moreover, the interaction between CS and GO has been observed in XRD measurements. Figure 3 shows XRD patterns of GO, neat CS, and CS-GO films

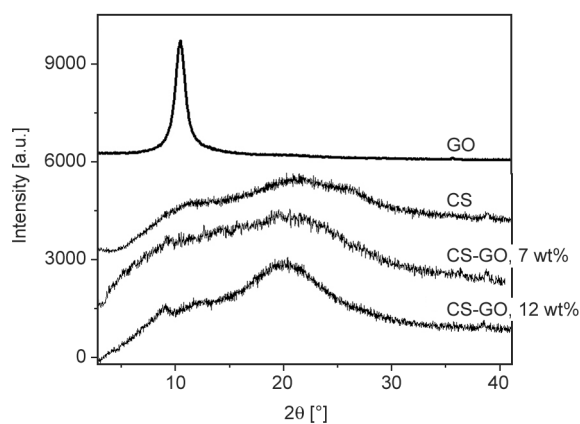


Figure 3. XRD patterns of GO, CS, and CS-GO (with 7 and 12 wt% of GO) films.

with 7 and 12 wt% of graphene oxide. The XRD pattern of GO displays a single diffraction peak at $2\theta = 10.1^\circ$ that corresponds to an interlayer spacing $d = 8.747 \text{ \AA}$, characteristic of neat GO [29]. The CS typically has a wide diffraction peak at $2\theta = 11.5^\circ$ and $2\theta = 21.5^\circ$ due to a combination of amorphous and crystalline phases [25, 30]. The incorporation of GO affected the crystalline structure of CS and increased the intensity of broad characteristic peaks of CS at *ca.* 21.5° . Additionally, in CS-GO films with 7 wt% of GO, a weak GO peak at $2\theta = 9.1950$ is observed, which is attributed to increasing GO interlayer spacing to $d = 9.61 \text{ \AA}$ and in CS-GO with 12 wt% this peak shift to $2\theta = 8.77^\circ$ which corresponds to interlayer spacing 10.079 \AA . The increasing GO layer spacing is related to the attachment of CS chains to the surface of stacked graphene nanosheets, which disrupts the van der Waals interactions and enlarges the d-spacing of the nanosheets [31]. During of film drying process, GO also affected the formation of the CS hydrogen bond, which led to a change in the crystalline structure of chitosan [30].

The results obtained from FTIR, Raman, and XRD measurements suggest that there exist strong interactions between the CS matrix and GO fillers which allow for obtaining good dispersion of GO in CS matrix.

Figure 4 illustrates the relationship between the imaginary part of impedance (Z'') and the real part of impedance (Z') (or impedance spectra) obtained on films (containing 5 wt% GO) after annealing in a vacuum cell for an hour, cooling to room temperature for measurements at 25°C (0% water, indicated

on the graph), and treatment in a water bath (*ca.* 24 percent of water). Insert displays the impedance spectra of CS-GO film that contains 12 wt% GO and 24 weight percent water.

In dry CS-GO films (annealed before measurements at 120°C), enough bonded water exists to support proton conductivity because complete removal of water from CS is only possible by heating it to temperatures *ca.* 200°C , where CS irreversibly transforms into an annealed polymorph [32].

As one can see, impedance spectra consist of a depressed semicircle and growth part at the low-frequency range which is related to contact and Maxwell-Wagner-Sillars (MWS) effects. MWS mechanism appears due to charge accumulation at the interface of CS and GO, as the current could not flow freely across it. As it is clear from Figure 4 that the frequency at which begin observed MWS effect dependent on GO wt% and water content [7, 33]. Consequently, measurements of dielectric constant ϵ at a fixed frequency, often used in the literature, did not allow to obtain real dependence of ϵ on GO concentration. Therefore, for separation of MWS and contact effects, we take into consideration only bulk properties of nanocomposite which are related to a depressed semicircle and fit the semicircle using the ZView program to zero frequency to calculate DC resistance and static dielectric constant at the limit of zero frequency as was shown on Figure 4.

According to percolation theory [13, 14], the power-law behavior of DC conductivity (σ_{DC}) above (Equation (2)) and below the percolation threshold (Equation (3)) and static dielectric constant (ϵ_s) (in the

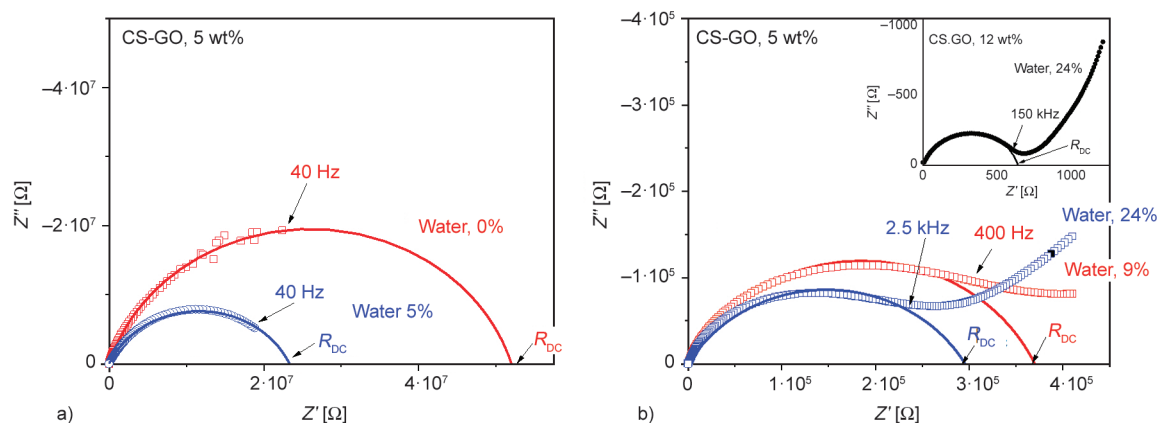


Figure 4. Impedance spectra of CS-GO films with 5 wt% of GO obtained on films with different content of water: a) with 0 and 5% of water, b) with 9 and 24% of water. Insert shows impedance spectra of CS-GO film with 12 wt% of GO and 24% of water. Note: Spectra for water 24% has been increased 100 times for better visualization. Symbols correspond to experimental points, and continuous lines represent the results of fitting using ZView program.

limit of zero frequency) below the percolation threshold (Equation (4)) can be obtained by a simple power-law:

$$\sigma_{DC} \propto (p - p_c)^t \quad \text{for } p > p_c \quad (2)$$

$$\sigma_{DC} \propto (p_c - p)^{-q} \quad \text{for } p < p_c \quad (3)$$

$$\epsilon_s \propto (p_c - p)^{-s} \quad \text{for } p < p_c \quad (4)$$

where t , q , and s are critical exponents which only depend upon the dimension of the percolation system and not on the details of cluster geometry, and p_c is the volume fraction of fillers at the percolation threshold. Therefore, to convert the weight fraction (W_t) of GO to volume fraction (V), the Equation (5) was used [34]:

$$V = \frac{W_t}{W_t + \frac{\rho_{GO}}{\rho_{CS}}(1 - W_t)} \quad (5)$$

where $\rho_{GO} = 1.7 \text{ g/cm}^3$ [35] and $\rho_{CS} = 1.4 \text{ g/cm}^3$ [36] are density of GO and CS respectively.

Figure 5 shows the DC conductivity (Figure 5a) and dielectric constant in the zero-frequency limit (Figure 5b) versus GO volume fraction and GO wt%. In the case of CS-GO films, annealing before measurements in vacuum DC conductivity (σ_{DC}) and dielectric constant (ϵ_s) does not depend on the GO concentration. In samples with 4% of water with an increasing GO content ϵ_s reaches a maximum at GO vol. frac. ca. 9% (or ca. 11wt%), and σ_{DC} increases by a power law, which is typical for the percolation effect. Figure 6a shows the log-log dependence of

the dielectric constant of the CS-GO nanocomposite films on $\log(p_c - p)$ calculated from experimental data (Figure 5), which according to Equation (4), must exhibit linearity. The least-square fitting analysis allows obtaining a percolation threshold of 9.2% vol. frac. of GO (ca. 11 wt%) and slope $q = 0.71 \pm 0.08$. In films with 9 and 24% of water, the percolation effect was observed to be more apparent in conductivity (appear saturation) and dielectric constant (the maximum is more pronounced).

The least-square fitting analysis of conductivity according to Equation (2) for above the percolation threshold gave $p_c = 4.5 \text{ vol}\%$ (or ca. 5.5 wt%) for films with 9% of water and $p_c = 3.6 \text{ vol}\%$ (or ca. 4 wt%) for films with 24% of water and critical exponent $t = 2.02 \pm 0.13$ and $t = 1.98 \pm 0.16$, respectively (Figure 6b). The best fits of the dielectric constant data below the percolation threshold (Equation (4)) gave the same values of p_c as for conductivity (4.5 and 3.6% of GO volume fraction) and critical exponent $s = 0.62 \pm 0.021$ and $s = 0.64 \pm 0.058$ for films with 9 and 24% of water respectively (Figure 6a).

According to the percolation theory in three-dimensional system values $t = 1.6-2.0$ and $s = 0.7-1.0$ [13, 14]. The values of critical exponent s obtained in CS-GO films with high water content are a little lower but are near that universal one. Therefore, it is likely that wet CS-GO films exhibit a three-dimensional percolation phenomenon.

The percolation phenomena can be observed in a mixture of two materials with different conductivity, such as dielectric polymers, with the incorporation of different types of conducting fillers such as

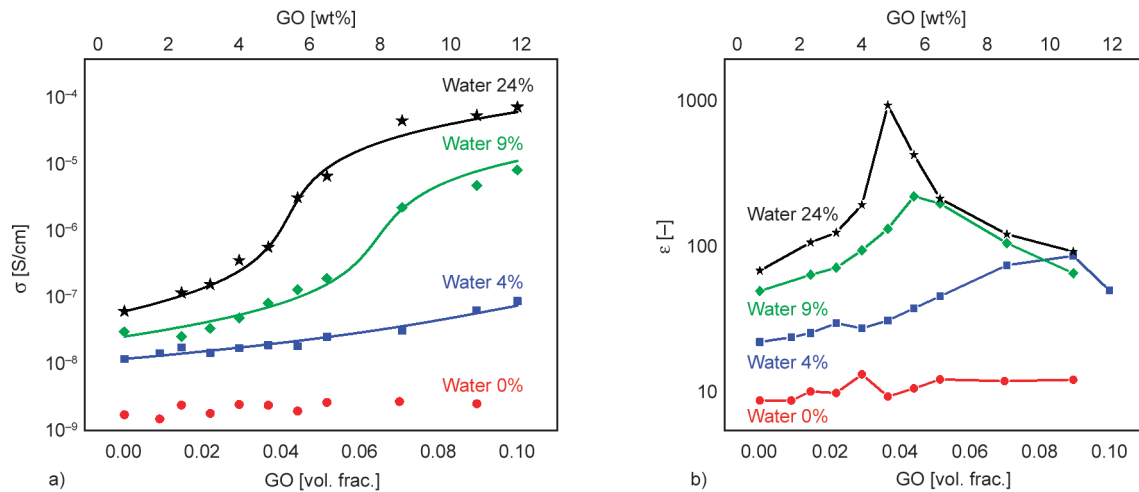


Figure 5. (a) Dependencies of conductivity (points-experimental data, continuous lines-fitting) and (b) dielectric constant as a function of GO volume fraction and GO [wt%] for films with different water content indicate on graphs.

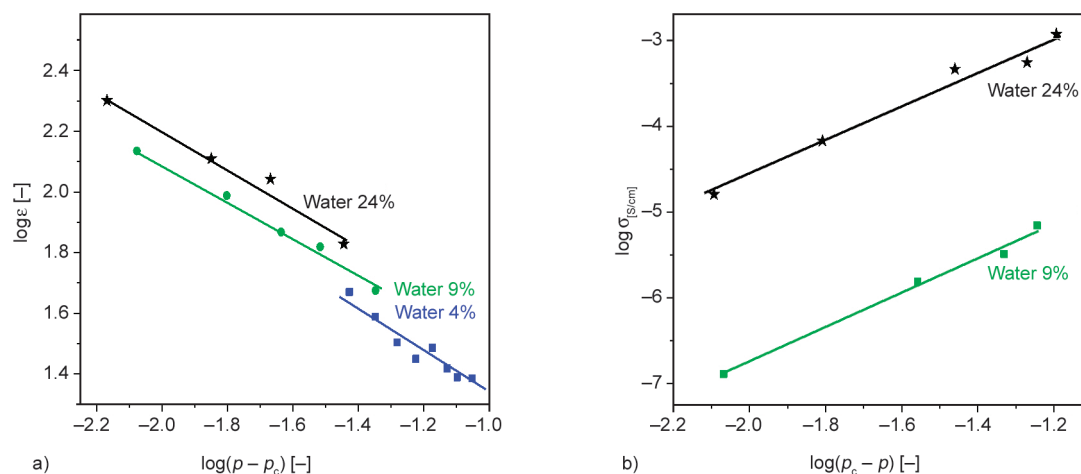


Figure 6. log-log plot of a) the dielectric constant versus $(p_c - p)$ and b) DC conductivity versus $(p - p_c)$. Points are experimental data, and lines are the results of the fitting.

metals, carbon fillers, conducting polymers, *etc.* In graphene-polymers composites, the percolation effect has been observed, as a rule, in nanocomposites with high conductivity graphene and its modification: graphene nanoplatelets, reduced graphene oxide, and doped GO [13]. However, to the best of our knowledge, there are no reports on how water content affects the percolation properties of CS-GO nanocomposites.

Some studies proposed that water shell models can explain the effect of water on the formation of percolative paths through the overlapping of the water layers (see, for example [37–40]), which promotes the conduction of charge carriers. However, these models predict only the percolation probability but not the dependencies of conductivity (especially in the saturation region) and the dielectric constant. Moreover, model calculations showed that for percolation networks, the thickness of the water shell must be as high as *ca.* 60 nm [38, 40].

From another viewpoint, it is well known that polymer matrices-nanofillers interphase interactions constitute a significant parameter that highly affects the nanocomposite behavior [37, 41–43], especially when the nanocomposite moves from an insulative material to a conductive because of the creation of a continual conductive network [37, 41]. The interphase consists of layers with different electrical and chemical structures distinct from the polymer matrix due to changes in the local chain conformation [37].

According to FTIR, Raman, and XRD measurements, there exist strong hydrogen-bonding interactions between the CS matrix and GO fillers in CS-GO films. Additionally, the water interaction in

CS-GO nanocomposites is higher than that of pure chitosan [44] due to stabilized polymer chains [45], formation of hydrogen bonds between water molecules with side groups of GO, and hydroxyl groups of CS [44, 46].

According to molecular dynamic simulation, the conductivity of CS exhibits proton conductivity through the Grotthius mechanism, which depends upon the number of protons, hydronium ions, and water content. When the amount of water in the system increased, the proton and hydronium ions were not mainly located near the functional group of chitosan, but they were diffused throughout the water clusters [47]. The addition of GO in CS improves the proton conductivity of nanocomposites due to the increasing

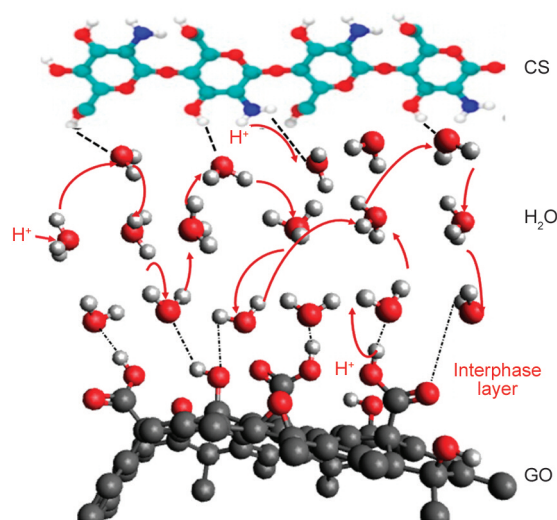


Figure 7. Schematic representation of the conductivity of wet CS-GO nanocomposite. Here, red arrows show the diffusion path of protons, and dash lines show hydrogen bonds between CS, GO and H₂O.

number of protons from carboxyl groups of GO [8] and the creation of some spatial channels; these channels facilitate the diffusion of proton and hydronium ions at the high-water content [48].

Based on the above, we can propose that the interaction of GO with CS and water molecules promotes the appearance of a high-conductivity interphase layer, as shown in Figure 7.

The protons appear from the NH₃ group of CS [47] and from carboxyl groups of GO [8] at the low water concentration located near the functional group of CS and GO. In the presence of water, the protons can diffuse through water clusters, create spatial channels, and form an interfacial layer with high conductivity (as shown in Figure 7). With increasing water content, the thickness and conductivity of the interphase layer increase due to the diffusion of proton and hydronium ions at the high-water content [48]. Therefore, the interphase provides a continuous channel for proton hopping in hydrogen-bonding networks along the adsorbed water, and it is responsible for the percolation properties of wet nanocomposites.

Direct confirmation of the proposed model can be the estimation of the conductivity and thickness of the interphase layer surrounding the GO fillers with different water content. For such an estimation, we use the model proposed in ref. [49] based on average field theory for calculating the effective conductivity of polymer-carbon nanotube composites. This model proposed that the electrical conductivity of composites depends on the concentration of fillers and the conductivity of the interphase layer. The model predicts that the percolation threshold decreases with interphase thickness and the conductivity in the saturation region increase with the interphase layer's conductivity. With increasing fillers content, the electrical conductivity of the interphase layer demonstrates a higher contribution to the effective electrical conductivity of the material.

The model has proposed that fillers can be regarded as the same rotationally prolate ellipsoids with longitude L , diameter d , and thickness of interphase layer t , which are related by the Equation (6):

$$\alpha = \frac{d^3 L}{(d + 2t)^2 (L + 2t)} \quad (6)$$

and effective conductivity of nanocomposite can be found from the Equation (7)) when $d \ll L$:

$$3\left(1 - \frac{f}{\alpha}\right) \frac{\sigma_e - \sigma_m}{2\sigma_e + \sigma_m} + \frac{f}{3\alpha} \left(\frac{\sigma_e - \sigma_{com}^{33}}{\sigma_e + 0.14 \frac{d}{L} (\sigma_{com}^{33} - \sigma_e)} \right) + 4 \frac{\sigma_e - \sigma_{com}^{11}}{\sigma_e + \sigma_{com}^{11}} = 0 \quad (7)$$

where α is given by the Equation (6), σ_c , σ_m , σ_s , and σ_e are the electrical conductivities of the fillers, the matrix, the interphase layer, and the effective conductivity of the composite, respectively; σ_{com}^{33} and σ_{com}^{11} are the longitude and the transverse conductivity, which in the case of GO are the same.

According to the scanning electron microscopic (SEM) measurements, we estimated GO sheet dimension as $L = 3 \mu\text{m}$ and $d = 20 \text{ nm}$ [50].

This model allowed us to fit not only the effective conductivity of nanocomposite but also estimated the thickness of the interphase layer, its conductivity, and the percolation threshold.

The least-squares fitting of experimental data was performed using standard genetic algorithm optimization functions in the Scilab[®] [51] numerical computational package. The conductivity of CS-matrix (σ_{CS}) has been obtained from measurements on neat CS films with different water content, and the conductivity of GO was taken as 10^{-4} S/cm [50]. The adjustable parameters are only the values of interfacial conductivity (σ_{inter}) and interfacial thickness (d_{inter}). Data fitting optimization parameters are presented in Table 1.

Results of the referred fittings are shown in Figure 5a as a continuous line. One can see that this three-phase model fits well the experimental results. It is noteworthy that the thickness of the interphase layer obtained from fitting correlates well with the thickness of the interfacial layer observed in other polymer nanocomposites, which is in the range of 2–6 nm [42, 43].

Table 1 shows that when the water content in CS-GO films rises, so do the conductivity and thickness of the interphase layer.

Table 1. Results of fitting experimental conductivity of CS-GO films with different water content.

Water content [%]	σ_{CS} (experimental) [S/cm]	σ_{inter} (estimated) [S/cm]	d_{inter} (estimated) [nm]
4	$1.18 \cdot 10^{-8}$	$9.72 \cdot 10^{-8}$	0.82
9	$3.06 \cdot 10^{-8}$	$9.58 \cdot 10^{-4}$	2.97
24	$6.19 \cdot 10^{-7}$	$4.80 \cdot 10^{-2}$	4.72

Additionally, due to the rise in water content, the interphase layer's conductivity in films with 9 and 24 percent water is higher than that of CS and neat GO (10^{-4} S/cm), increasing the thickness and conductivity of the interphase and facilitating proton transport at the high-water content. These findings support the suggested model's validity, showing that the strong molecular interactions of GO with CS and water molecules during the interphase between CS and GO cause the interphase to be more conductivity-rich (compared to pristine CS and GO). The percolation properties of wet nanocomposites are attributed to proton transport via hydrogen-bonding networks, which this study supports.

This result supports proton transport across hydrogen-bonding networks, which gives wet nanocomposites their percolation capabilities. In addition, as the model predicts, an increase in water content raises the conductivity and thickness of the interphase layer, which lowers the percolation threshold.

4. Conclusions

Chitosan-graphene oxide nanocomposite films were synthesized with varying GO concentrations (0–12 wt%). FTIR, Raman, and XRD measurements have shown strong interaction between the CS matrix and GO fillers which allows for obtaining good dispersion of GO in the CS matrix.

DC conductivity and dielectric constant dependencies in the zero-frequency limit have been investigated versus GO concentration and water content. In the case of CS-GO films annealing before measurements in a vacuum, DC conductivity and dielectric constant do not depend upon the GO concentration. The percolation effect has been observed, for the first time, at higher water content (4, 9, and 24%). The values of critical exponents obtained in CS-GO films with high water content allow us to conclude that nanocomposites exhibit a three-dimensional percolation system. Results of fitting DC conductivity using a three-phase model, which includes conductivity of CS, GO, and interphase layer, showed that by increasing water content in CS-GO films, the conductivity and thickness of the interfacial layer increase. Surprisingly, the conductivity of the interfacial layer in films with 9 and 24% of water is higher than the conductivity of both pristine CS and GO. The thickness of the interfacial layer increases with water content. A new percolation model for CS-GO nanocomposites with high water content has been

proposed to shed light on these new findings. In this regard, we propose that due to the strong molecular interactions of GO with CS and water molecules at the interface between CS and GO, a high-conductivity interphase layer appears, which supports a proton transfer mechanism among hydrogen-bonding networks. It is responsible for the percolation properties of wet nanocomposites. Additionally, increasing water content increases the conductivity and thickness of the interphase layer, which leads to shifting the percolation threshold to lower GO concentration.

Our results here may be of great importance in the applications of such nanocomposites in different areas, not only for developing proton exchange membranes, sensors, organic electronics, and biomedicine.

Acknowledgements

This work was partially supported by CONACYT Mexico (Grant A1-S-9557). The authors acknowledge to J. A. Muñoz Salas for technical assistance in electrical measurements, F. Rodriguez Melgarejo for assistance in Raman measurements, M. Adelaido Hernandez for assistance in XRD measurements, and R.A. Mauricio Sanchez for assistance in FTIR measurements.

References

- [1] Pieklarz K., Tylman M., Modrzejewska Z.: Applications of chitosan-graphene oxide nanocomposites in medical science: A review. *Progress on Chemistry and Application of Chitin and its Derivatives*, **XXIII**, 5–24 (2018).
<https://doi.org/10.15259/PCACD.23.01>
- [2] Ahmed M. J., Hameed B. H., Hummadi E. H.: Review on recent progress in chitosan/chitin-carbonaceous material composites for the adsorption of water pollutants. *Carbohydrate Polymers*, **247**, 116690 (2020).
<https://doi.org/10.1016/j.carbpol.2020.116690>
- [3] Barra A., Santos J. D. C., Silva M. R. F., Nunes C., Ruiz-Hitzky E., Gonçalves I., Yildirim S., Ferreira P., Marques P. A. A. P.: Graphene derivatives in biopolymer-based composites for food packaging applications. *Nanomaterials*, **10**, 2077 (2020).
<https://doi.org/10.3390/nano10102077>
- [4] Priftis D.: Polyelectrolyte-graphene nanocomposites for biosensing applications. *Current Organic Chemistry*, **19**, 1819–1827 (2015).
<https://doi.org/10.2174/1385272819666150526005557>
- [5] Pandey R. P., Shukla G., Manohar M., Shahi V. K.: Graphene oxide based nanohybrid proton exchange membranes for fuel cell applications: An overview. *Advances in Colloid and Interface Science*, **240**, 15–30 (2017).
<https://doi.org/10.1016/j.cis.2016.12.003>

- [6] Farion I. A., Burdukovskii V. F., Kholkhoev B. C., Timashev P. S., Chailakhyan R. K.: Functionalization of chitosan with carboxylic acids and derivatives of them: Synthesis issues and prospects of practical use: A review. *Express Polymer Letters*, **12**, 1081–1105 (2018).
<https://doi.org/10.3144/expresspolymlett.2018.95>
- [7] Feng P., Du P., Wan C., Shi Y., Wan Q.: Proton conducting graphene oxide/chitosan composite electrolytes as gate dielectrics for new-concept devices. *Scientific Reports*, **6**, 34065 (2016).
<https://doi.org/10.1038/srep34065>
- [8] Yang X., Tu Y., Li L., Shang S., Tao X.-M.: Well-dispersed chitosan/graphene oxide nanocomposites. *ACS Applied Materials and Interfaces*, **2**, 1707 (2010).
<https://doi.org/10.1021/am100222m>
- [9] Yuan H., Meng L.-Y., Park S.-J.: A review: Synthesis and applications of graphene/chitosan nanocomposites. *Carbon Letters*, **17**, 11–17 (2016).
<https://doi.org/10.5714/CL.2016.17.1.011>
- [10] Cao L., Wu H., Yang P., He X., Li J., Li Y., Xu M., Qiu M., Jiang Z.: Graphene oxide-based solid electrolytes with 3D prepercolating pathways for efficient proton transport. *Advanced Functional Materials*, **28**, 1804944 (2018).
<https://doi.org/10.1002/adfm.201804944>
- [11] Farooqui U. R., Ahmad A. L., Hamid N. A.: Graphene oxide: A promising membrane material for fuel cells. *Renewable and Sustainable Energy Reviews*, **82**, 714–733 (2018).
<https://doi.org/10.1016/j.rser.2017.09.081>
- [12] Marsden A. J., Papageorgiou D. G., Vallés C., Liscio A., Palermo V., Bissett M. A., Young R. J., Kinloch I. A.: Electrical percolation in graphene–polymer composites. *2D Materials*, **5**, 032003 (2018).
<https://doi.org/10.1088/2053-1583/aac055>
- [13] Stauffer D., Aharony A.: *Introduction to percolation theory*. Taylor and Francis, London (1992).
- [14] Nan Y.-C., Shen W., Ma J.: Physical properties of composites near percolation. *Annual Review of Materials Research*, **40**, 131–151 (2010).
<https://doi.org/10.1146/annurev-matsci-070909-104529>
- [15] Mergen O. B., Arda E., Evingür G. A.: Electrical, optical and mechanical properties of chitosan biocomposites. *Journal of Composite Materials*, **54**, 1497–1510 (2020).
<https://doi.org/10.1177/0021998319883916>
- [16] Pati M. K., Patojoshi P., Roy G. S.: Synthesis of graphene-based nanocomposite and investigations of its thermal and electrical properties. *Journal of Nanotechnology*, **2016**, 5135420 (2016).
<https://doi.org/10.1155/2016/5135420>
- [17] Layek R. K., Samanta S., Nandi A. K.: Graphene sulphonic acid/chitosan nano biocomposites with tunable mechanical and conductivity properties. *Polymer*, **53**, 2265–2273 (2012).
<https://doi.org/10.1016/j.polymer.2012.03.048>
- [18] Yadav S. K., Jung Y. C., Kim J. H., Ko Y.-I., Ryu H. J., Yadav M. K., Kim Y. A., Cho J. W.: Mechanically robust, electrically conductive biocomposite films using antimicrobial chitosan-functionalized graphene. *Particle and Particle Systems Characterization*, **30**, 721–727 (2013).
<https://doi.org/10.1002/ppsc.201300044>
- [19] Liu Y., Wang J., Zhang H., Ma C., Liu J., Cao S., Zhang X.: Enhancement of proton conductivity of chitosan membrane enabled by sulfonated graphene oxide under both hydrated and anhydrous conditions. *Journal of Power Sources*, **269**, 898–911 (2014).
<https://doi.org/10.1016/j.jpowsour.2014.07.075>
- [20] Dhayal A. V., Hashmi S. Z., Kumar U., Choudhary B. L., Kuznetsov A. E., Dalela S., Kumar S., Kaya S., Dolia S. N., Alvi P. A.: Spectroscopic studies, molecular structure optimization and investigation of structural and electrical properties of novel and biodegradable chitosan-GO polymer nanocomposites. *Journal of Materials Science*, **55**, 14829–14847 (2020).
<https://doi.org/10.1007/s10853-020-05093-5>
- [21] Dhayal V., Hashmi S. Z., Kumar U., Choudhary B. L., Dalela S., Dolia S. N., Alvi P. A.: Optical and electrical properties of biocompatible and novel (CS–GO) polymer nanocomposites. *Optical and Quantum Electronics*, **53**, 53 (2021).
<https://doi.org/10.1007/s11082-020-02723-9>
- [22] Chaudhuri B., Bhadra D., Moroni L., Pramanik K.: Myoblast differentiation of human mesenchymal stem cells on graphene oxide and electrospun graphene oxide–polymer composite fibrous meshes: Importance of graphene oxide conductivity and dielectric constant on their biocompatibility. *Biofabrication*, **7**, 015009 (2015).
<https://doi.org/10.1088/1758-5090/7/1/015009>
- [23] Krishnamoorthy K., Veerapandian M., Yun K., Kim S.-J.: The chemical and structural analysis of graphene oxide with different degrees of oxidation. *Carbon*, **53**, 38–49 (2013).
<https://doi.org/10.1016/j.carbon.2012.10.013>
- [24] Ji W. F., Chen K. Y., Ke C. J., Liao Y. J., Liu W. J., Tsai M. H., Yeh J. M.: Comparative corrosion protection studies of electroactive/non-electroactive epoxy thermoset composites containing conductive rGO/non-conductive GO platelets. *Express Polymer Letters*, **13**, 604–617 (2019).
<https://doi.org/10.3144/expresspolymlett.2019.51>
- [25] Kumar-Krishnan A. S., Prokhorov E., Ramírez M., Hernandez-Landaverde M. A., Zarate-Triviño D. G., Kovalenko Y., Sanchez I. C., Méndez-Nonell J., Luna-Bárcenas G.: Novel gigahertz frequency dielectric relaxations in chitosan films. *Soft Matter*, **10**, 8673–8684 (2014).
<https://doi.org/10.1039/C4SM01804D>
- [26] Zuo P.-P., Feng H.-F., Xu Z.-Z., Zhang L.-F., Zhang Y.-L., Xia W., Zhang W.-Q.: Fabrication of biocompatible and mechanically reinforced graphene oxide-chitosan nanocomposite films. *Chemistry Central Journal*, **7**, 39 (2013).
<https://doi.org/10.1186/1752-153X-7-39>

- [27] Qi Y., Yang M., Xu W., He S., Men Y.: Natural polysaccharides-modified graphene oxide for adsorption of organic dyes from aqueous solutions. *Journal of Colloid and Interface Science*, **486**, 84–96 (2017).
<https://doi.org/10.1016/j.jcis.2016.09.058>
- [28] Sanes J., Ojados G., Pamies R., Bermúdez M. D.: PMMA nanocomposites with graphene oxide hybrid nanofillers. *Express Polymer Letters*, **13**, 910–922 (2019).
<https://doi.org/10.3144/expresspolymlett.2019.79>
- [29] Zhang S-B., Yan Y-T., Huo Y-Q., Yang Y., Feng J-L., Chen Y-F.: Electrochemically reduced graphene oxide and its capacitance performance. *Materials Chemistry and Physics*, **148**, 903–908 (2014).
<https://doi.org/10.1016/j.matchemphys.2014.08.068>
- [30] Kosowska K., Domalik-Pyzik P., Nocuń M., Chłopek J.: Chitosan and graphene oxide/reduced graphene oxide hybrid nanocomposites – Evaluation of physicochemical properties. *Materials Chemistry and Physics*, **216**, 28–36 (2018).
<https://doi.org/10.1016/j.matchemphys.2018.05.076>
- [31] Nath A. J., Chowdhury A., Dolui S. K.: Chitosan/graphene oxide-based multifunctional pH-responsive hydrogel with significant mechanical strength, self-healing property, and shape memory effect. *Advances in Polymer Technology*, **37**, 3665–3679 (2018).
<https://doi.org/10.1002/adv.22151>
- [32] Ogawa K., Yui T., Okuyama K.: Three D structures of chitosan. *International Journal of Biological Macromolecules*, **34**, 115–120 (2004).
<https://doi.org/10.1016/j.ijbiomac.2003.11.002>
- [33] Xia X., Zhong Z., Weng G. J.: Maxwell–Wagner–Sillars mechanism in the frequency dependence of electrical conductivity and dielectric permittivity of graphene-polymer nanocomposites. *Mechanics of Materials*, **109**, 42–50 (2017).
<https://doi.org/10.1016/j.mechmat.2017.03.014>
- [34] Zakaria A. Z., Shelesh-Nezhad K.: The effects of interphase and interface characteristics on the tensile behaviour of POM/CaCO₃ nanocomposites. *International Journal of Nanomaterials, Nanotechnology and Nanomedicine*, **4**, 17 (2014).
<https://doi.org/10.5772/58696>
- [35] Gong T., Lam D. V., Liu R., Won S., Hwangbo Y., Kwon S., Kim J., Sun K., Kim J-H., Lee S-M., Lee C.: Thickness dependence of the mechanical properties of free-standing graphene oxide papers. *Advanced Functional Materials*, **25**, 3756–3763 (2015).
<https://doi.org/10.1002/adfm.201500998>
- [36] Nunthanid J., Laungtana-anan M., Sriamornsak P., Limmatvapirat S., Puttipipatkachorn S., Lim L. Y., Khor E.: Characterization of chitosan acetate as a binder for sustained release tablets. *Journal of Controlled Release*, **99**, 15–26 (2004).
<https://doi.org/10.1016/j.jconrel.2004.06.008>
- [37] Pitsa D., Danikas M.: Interfaces features in polymer nanocomposites: A review of proposed models. *NANO*, **6**, 497–508 (2011).
<https://doi.org/10.1142/S1793292011002949>
- [38] Hosier I. L., Praeger M., Vaughan A. S., Swingler S. G.: The effects of water on the dielectric properties of silicon-based nanocomposites. *IEEE Transactions on Dielectrics and Electrical Insulation*, **16**, 169–179 (2017).
<https://doi.org/10.1109/TNANO.2016.2642819>
- [39] Qiang D., Wang Y., Wang X., Chen G., Andritsch T.: The effect of filler loading ratios and moisture on DC conductivity and space charge behaviour of SiO₂ and hBN filled epoxy nanocomposites. *Journal of Physics D: Applied Physics*, **52**, 395502 (2019).
<https://doi.org/10.1088/1361-6463/ab2d5b>
- [40] Hui L., Schadler L. S., Nelson J. K.: The influence of moisture on the electrical properties of crosslinked polyethylene/silica nanocomposites. *IEEE Transactions on Dielectrics and Electrical Insulation*, **20**, 641–653 (2013).
<https://doi.org/10.1109/TDEI.2013.6508768>
- [41] Idumah C. I., Obele C. M.: Understanding interfacial influence on properties of polymer nanocomposites. *Surfaces and Interfaces*, **22**, 100879 (2021).
<https://doi.org/10.1016/j.surfin.2020.100879>
- [42] Raetzke S., Kindersberger J.: The effect of interphase structure in nanodielectrics. *IEEE Transactions on Fundamentals and Materials*, **126**, 1044–1049 (2006).
<https://doi.org/10.1541/ieejfms.126.1044>
- [43] Popov I., Carroll B., Bocharova V., Genix A-C., Cheng S., Khamzin A., Kisliuk A., Sokolov A. P.: Strong reduction in amplitude of the interfacial segmental dynamics in polymer nanocomposites. *Macromolecules*, **53**, 4126–4135 (2020).
<https://doi.org/10.1021/acs.macromol.0c00496>
- [44] Grande C. D., Mangadlao J., Fan J., de Leon A., Delgado-Ospina J., Rojas J. G., Rodrigues D. F., Advincula R.: Chitosan cross-linked graphene oxide nanocomposite films with antimicrobial activity for application in food industry. *Macromolecular Symposia*, **374**, 1600114 (2017).
<https://doi.org/10.1002/masy.201600114>
- [45] Chen T-H., Chen Y-R., Chen L-H., Chang K-S., Lin Y-F., Tung K-L.: Exploration of the nanostructures and separation properties of cross-linked mixed matrix membranes using multiscale modeling. *Journal of Membrane Science*, **543**, 328–334 (2017).
<https://doi.org/10.1016/j.memsci.2017.08.061>
- [46] Lyn F. H., Peng T. C., Ruzniza M. Z., Hanani Z. A. N.: Effect of oxidation degrees of graphene oxide (GO) on the structure and physical properties of chitosan/GO composite films. *Food Packaging and Shelf Life*, **21**, 100373 (2019).
<https://doi.org/10.1016/j.fpsl.2019.100373>
- [47] Srinophakun T., Martkumchan S.: Ionic conductivity in a chitosan membrane for a PEM fuel cell using molecular dynamics simulation. *Carbohydrate Polymers*, **88**, 194–200 (2012).
<https://doi.org/10.1016/j.carbpol.2011.11.094>

- [48] Zhang H-P., Gandhi N. S., Gu Y., Zhang Y., Tang Y.: Chitosan/graphene complex membrane for polymer electrolyte membrane fuel cell: A molecular dynamics simulation study. *International Journal of Hydrogen Energy*, **45**, 25960–25969 (2020).
<https://doi.org/10.1016/j.ijhydene.2020.03.124>
- [49] Yan K. Y., Xue Q. Z., Zheng Q. B., Hao L. Z.: The interface effect of the effective electrical conductivity of carbon nanotube composites. *Nanotechnology*, **18**, 255705 (2007).
<https://doi.org/10.1088/0957-4484/18/25/255705>
- [50] Prokhorov E., Barquera-Bibiano Z., Manzano-Ramírez A., Luna-Barcenas G., Kovalenko Y., Hernández-Landaverde M. A., Castillo Reyes B. E., Hernández Vargas J.: New insights in graphene oxide dielectric constant. *Materials Research Express*, **6**, 085622 (2019).
<https://doi.org/10.1088/2053-1591/ab22f0>
- [51] Campbell S. L., Chancelier J. P., Nikoukhah R.: *Modeling and simulation in Scilab/Scicos*. Springer, New York (2006).

Research article

Synthesis and properties of a novel waterborne photosensitive resin for 3D printing

Qinghong Luo¹, Ting Zhang², Ruijie Xu¹, Hongping Xiang¹, Yanyan Cui¹, Zhiquan Li¹, Xiaoxuan Liu^{1*}

¹School of Materials and Energy, Guangdong University of Technology, Guangzhou, 510006 Guangdong, PR China

²Chemistry & Environment Engineering, Shaoguan University, Shaoguan, 512005 Guangdong, PR China

Received 29 April 2022; accepted in revised form 22 August 2022

Abstract. A series of novel waterborne photosensitive resins were prepared successfully with poly(propylene oxide) bis(2-aminopropyl ether), tricyclodecane dimethanol diacrylate, 2-isocyanatoethyl acrylate, and hydrochloric acid by Michael addition reaction. The results show that with the increasing double bonds content, the double bonds conversion increases from 78.7, 85.6 to 92.8% in the photopolymerization, respectively, and the gel content of the UV-cured film increases from 48.05, 69.10 to 83.28%. In addition, the glass transition temperature and tensile strength of the UV-cured film follow the same increasing trend. Moreover, the content of hydrochloride has a great influence on the hydrophilicity of the waterborne photosensitive resins. The studies indicated that as the hydrochloride content decreases, the surface water contact angle of the UV-cured film increases from 10.8, 22.9 to 51.5°, and water absorption decreases from 26.55, 16.20 to 11.06%, respectively. Moreover, the waterborne photosensitive resins exhibited a high printing accuracy together with a good effect of washing and are promising for 3D printing.

Keywords: mechanical properties, waterborne photosensitive resin, Michael addition reaction, photopolymerization, 3D printing application

1. Introduction

3D printing (also known as ‘additive manufacturing’) is a manufacturing technology that transforms computer-aided and designed virtual models into 3D tangible objects through layer-by-layer deposition [1, 2]. It has the characteristics of creating unique structures, reducing material wastes, and increasing efficiency [3] and is widely used in the fields of biomedicine [4, 5], aerospace [6], education [7], and dentistry [8]. The 3D printing technology can be divided into several categories such as jetting, binder jetting, vat photopolymerization, energy deposition, powder bed fusion, material extrusion, and sheet lamination [9], where the more popular printing technology is vat photopolymerization [10] due to its incredibly high resolution and excellent surface finish for creating

concept models, rapid prototyping and building complex geometries.

Vat photopolymerization 3D Printing, utilizing radiation to selectively polymerize liquid photosensitive resin in a vat to form a solid 3D structure [11], includes several printing processes [12]. Stereolithography (SLA) was developed as the first vat photopolymerization method in the early 1980s [13]. Since then, various new vat photopolymerization methods have been developed, including digital projection lithography (DLP) [14], continuous liquid interface production (CLIP) [15], and computed axial lithography (CAL) [16], to meet the speed and resolution demands of printing.

In vat photopolymerization 3D printing, the model is first designed by CAD software and converted into

*Corresponding author, e-mail: p-xxliu@gdut.edu.cn

© BME-PT

a standard (STL) format file. Then the STL format model is sliced and printed according to the different requirements of the printing equipment. After printed, the model is removed from the platform, rinsed with organic solvents such as isopropyl alcohol (IPA) to remove the liquid resin layer from the surface of 3D printed parts, and post-cured under UV light to improve the mechanical properties [10]. The removal of support structures, rinsing, and post-curing steps are required processes for almost all 3D printing systems [17]. Without these steps, harmful monomers may remain on or inside the item, and there is an increased risk of conformational distortion [18].

In the post-processing of vat photopolymerization 3D printing, almost all printed parts need to be rinsed with organic solvents. Invernizzi [19], He *et al.* [20], and Silbert *et al.* [21] used ethanol to remove residual resin from the surface of printed parts; Peterson *et al.* [22], Mubarak *et al.* [23], and Garcia *et al.* [24] reported isopropanol as a cleaning agent for the post-processing of 3D printing; Schmidt *et al.* [25] also used phenoxyethanol for the post-processing. However, the use of organic solvents increases the risk of fire and can pollute the environment. Using waterborne photosensitive resin can eliminate safety risks associated with organic solvents for the surface cleaning of printed parts. Therefore, developing a waterborne photosensitive resin suitable for 3D printing is of great interest.

In this paper, a series of waterborne photosensitive resins were designed and synthesized via the Michael addition reaction between amino and acrylate double bond. After evaluating the mechanical properties, the waterborne photosensitive resin was applied to 3D printing, and the printing accuracy and washability of the printed objects were evaluated.

2. Experimental

2.1. Materials

Poly(propylene oxide) bis(2-aminopropyl ether) (D400): $M_n = 400$ g/mol, Huntsman Polyurethane (China) Co., Ltd., Shanghai, China. 2-isocyanatoethyl acrylate (AOI) was purchased from Shanghai Cabchem New Materials Technology Co., Ltd., Shanghai, China. Tricyclodecane dimethanol diacrylate (TCDDA) was supplied by Eternal Materials Co., Ltd., Zhuhai, China. 2-hydroxyethyl methacrylate (HEMA), tetrahydrofuran (THF), and anhydrous magnesium sulfate were purchased from Macklin,

Shanghai, China. Hydrochloric acid was purchased from Guangdong Guangshi Reagent Technology Co., Ltd., Guangzhou, China. Photoinitiator: ethyl(2,4,6-trimethylbenzoyl) phenylphosphinate (L-TPO) was provided by Tianjin Jiuri New Material Co., Ltd., Tianjin, China. Acryloyl-morpholine (ACMO) was supplied by Beijing RBL Chemicals Co., Ltd., Beijing, China. All of the reagents were used as received without further purification.

2.2. Synthesis of the asymmetrical monomer

A four-necked flask, equipped with a mechanical stirrer, condenser, thermometer, and constant funnel, was charged with HEMA (14.75 g, 0.11 mol) and cooled using a water bath while stirring, then AOI (14.11 g, 0.1 mol) was slowly added to the flask with a constant pressure funnel at 30~35 °C. The mixture was reacted at 40~42 °C for 4 h under stirring to obtain the asymmetrical monomer. The reaction continued until the absorption peak of the –NCO group in the infrared spectrum disappeared. Finally, after being washed 3 times with deionized water and dried over anhydrous MgSO₄, a transparent, colorless liquid has been obtained, namely the asymmetrical monomer (H-AOI) [26, 27]. The specific reaction route is shown in Figure 1a.

2.3. Synthesis of the waterborne photosensitive resin

The waterborne photosensitive resin (WPR) was prepared with TCDDA, D400, H-AOI, AOI, and hydrochloric acid by polyaddition reactions. The specific reaction route is shown in Figure 1b. The details of preparation were as follows [28, 29]. TCDDA and D400 were added into a flask and heated to 40 °C under stirring. After the absorption peak of the –C=C group (1640 cm⁻¹) in the infrared spectrum disappeared, H-AOI was added to the flask. The mixtures were maintained at 42 °C until the absorption peak of the –NH₂ group (1590 cm⁻¹) in the infrared spectrum disappeared completely to afford an oligomer capped with an acrylate double bond. Then, AOI was added via a dropping funnel with the temperature at 40~42 °C, keeping the temperature until the absorption peak of the –NCO group (2267 cm⁻¹) vanished. Finally, WPR was obtained after hydrochloric acid was slowly added to neutralize the secondary amino group under stirring. The waterborne photosensitive resins were named WPR-1, WPR-2, and WPR-3, respectively, according to the different amounts of the

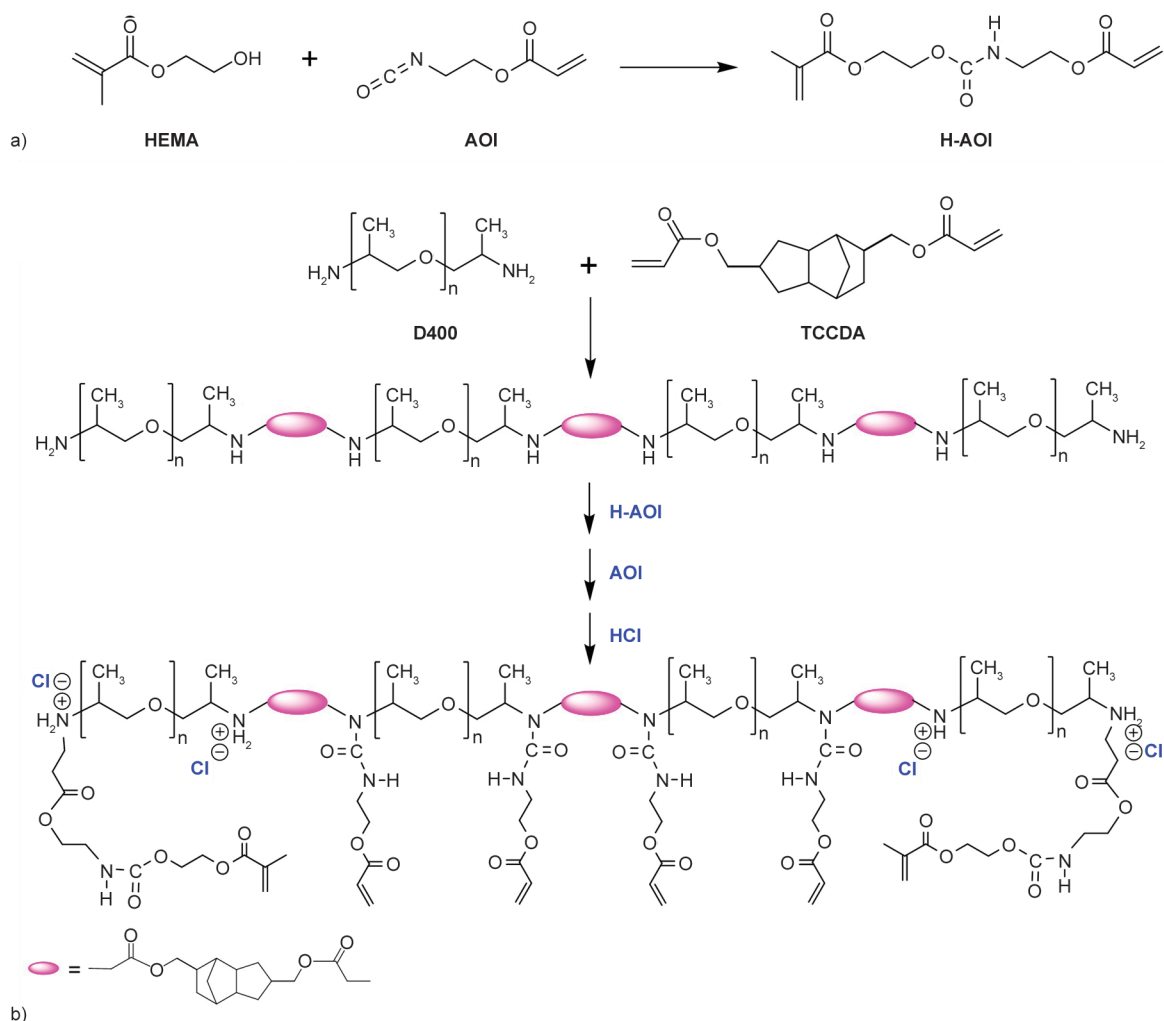


Figure 1. Synthetic routes of a) H-AOI and b) waterborne photosensitive resin.

–C=C group. The ratio of each component is illustrated in [Table 1](#).

2.4. Fabrication of the UV-cured film

First, WPR was mixed with L-TPO at a ratio of 97.0 to 3.0 to produce the acrylic composition. Second, the WPR UV-cured films were prepared by pouring the acrylic composition on a cleaned polytetrafluoroethylene mold (50 mm × 15 mm × 2 mm) and dried at room temperature under dark conditions for 12 h to form a liquid layer. Subsequently, the liquid layer was irradiated under a UV curing machine

(model: RX300-1; power lamp: 2000 W; the distance of the lamp: 10 cm, Dongguan Ergu Optoelectronics Technology Co. Ltd., Dongguan, China) for 10 s to afford the UV-cured film after dried at 50 °C under a vacuum for 12 h, the films were peeling off from the Teflon mold for a follow-up test.

3. Methods

3.1. Characterization

Fourier transform infrared (FTIR) spectra were obtained on Nicolet 560 infrared spectrometer (Thermo Fisher Scientific, Germany) using a disc of KBr in

Table 1. Synthetic composition of waterborne photosensitive resins.

Materials Samples	D400 [g]	DCPDA [g]	H-AOI [g]	AOI [g]	HCl ¹ [g]	DBC ² [mmol/g]	SC ³ [%]
WPR-1	40.00	22.83	13.56	7.06	14.72	1.02	90.58
WPR-2	40.00	22.83	13.56	14.12	9.81	1.50	93.86
WPR-3	40.00	22.83	13.56	21.18	4.91	1.95	96.99

¹The concentration of hydrochloric acid is 37.2%.

²DBC is an abbreviation for double bond content, calculated according to the formula [30]

³SC is an abbreviation for solid content.

the range of 4000~600 cm^{-1} with 4 cm^{-1} resolution over 32 scans at room temperature.

The proton nuclear magnetic resonance (^1H NMR) spectra of the samples were recorded at 25 $^\circ\text{C}$ by Bruker AVANCE III HD 400 spectrometer (Bruker, Switzerland) with deuterated chloroform as the solvent.

The loss factor curves, storage modulus, and loss modulus at different temperatures was measured with a TA Instruments DMA 50 (Metravib co., Ltd., France) in tensile mode at 1 Hz and 10 μm amplitude with a heating rate of 3 $^\circ\text{C}/\text{min}$ and temperature scan from -20 to 80 $^\circ\text{C}$. The samples were cut into squareness with approximate dimensions of 10 mm \times 5 mm \times 2 mm.

The tensile properties of the UV-cured film of WPR were evaluated using a SANS CMT 6000 Universal Tester (MTS Systems Co., Ltd., America) in accordance with GB/T 528-2009 at room temperature. Dumbbell-shaped specimens (length: 50 mm, thickness: 2 mm, the width of parallel part: 4 mm, according to GB/T 1040.2-2010) were made for the tensile tests, and a deformation speed of 50 mm/min was employed in the test process. Each measurement was repeated at least three times, and the results were averaged.

Thermal degradation behavior of the UV-cured film of WPR was assessed by thermogravimetric analysis with Mettler TGA/SDTA 851 thermogravimetric analyzer (TGA) (Mettler, Switzerland) in 20 ml/min N_2 atmosphere from 30 to 600 $^\circ\text{C}$ with a heating rate of 10 $^\circ\text{C}/\text{min}$, sample weight about 5.0~10.0 mg.

Contact angle measurements were conducted on a static drop contact angle measuring instrument (JC2000C1, Shanghai Zhongchen Digital Technic Apparatus Co., Ltd., China). The samples were fixed on a movable stage horizontally with a size of 3.0 cm \times 3.0 cm, and the water droplets were deposited on the surface of the samples by a micro-syringe. A CCD video camera was used to record the shape of the droplet and an image analyzing software to determine the contact angle evolution. The experimental results were the average values of five measurements performed for each sample.

The conversion of acrylate double bonds

The conversion of acrylate double bond during UV irradiation was determined by real-time infrared spectra on a Nicolet iS50 FTIR at room temperature. The liquid waterborne photosensitive resins were

coated on KBr disc with a thickness of approximately 100 μm and then irradiated *in situ* by an M-Ultra violet light source (MUA-165, Mejiro Genossen, Japan) with a dominant wavelength of 365 nm. Each spectrum obtained from the IR spectrometer was an average of 4 scans with a resolution of 8 cm^{-1} . The peak area variation of $-\text{C}=\text{C}-$ stretching vibration of acrylate double bond at 1640 cm^{-1} was used to determine their conversion (γ) according to Equation (1) [31]:

$$\gamma = \frac{A_0 - A_t}{A_0} \cdot 100\% \quad (1)$$

where A_0 and A_t were the normalized peak area of acrylate double bonds before and after UV radiation at time t , respectively.

The gel content, which reflected the crosslinking degree of the UV-cured film of WPR, was measured with the Soxhlet extraction method. After drying for 12 h at 40 $^\circ\text{C}$ under vacuum, the WPR films and THF were added into the Soxhlet extractor and heated to reflux for 24 h. Afterward, the remaining WPR films were dried at 40 $^\circ\text{C}$ for 12 h. We compared the residual mass with the initial mass to obtain the gel content value by Equation (2) [32]:

$$G = \frac{w_t}{w_0} \cdot 100\% \quad (2)$$

where G means gel content, w_0 represents initial mass, and w_t represents final mass.

The weighing method assessed the water absorption behaviors of the UV-cured film of WPR. The WPR cured films were cut into specimens with dimensions 10 mm \times 10 mm \times 1 mm and dried at 50 $^\circ\text{C}$ for 12 h to obtain the weight of samples (m_0). Then the samples were immersed in deionized water for 24 h. Hereafter, the samples were taken out to remove the surface moisture, and the weight of samples (m_t) was obtained. The water absorption rate (W) of the samples was calculated according to Equation (3), [33]:

$$W = \frac{m_t - m_0}{m_0} \cdot 100\% \quad (3)$$

3.2. 3D printing

The diluted monomer ACMO and L-TPO were added to WPR after evenly mixed and left to stand in the dark for defoaming before use. The 3D printing was performed on an Iron Box/CH-10 3D Printer

(Shenzhen Shengma Youchuang Technology Co., Ltd., Shenzhen, China) with $\lambda_{\max} \sim 405$ nm and layer height of 0.05 mm, bottom layer exposure time of 60 s, bottom layer count of 6 and layer exposure time of 15 s (irradiation intensity: 1.0 mW/cm², lifting speed 65 mm/min, return speed 150 mm/min).

Curing depth measurement

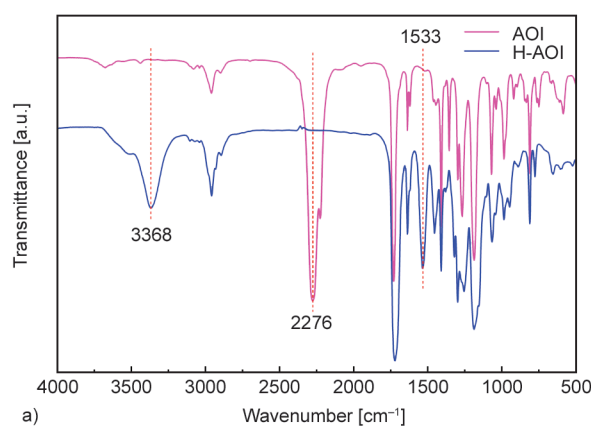
A 405 nm LED light was employed as the light source (Model: UVEC-4 II, Tianjin Lamplink Lighting Electric Co. Ltd., Tianjin, China). A spot area with a 10 mm diameter was exposed in the center of the transparent plastic container filled with waterborne photosensitive resin. The cured disks were taken out and cleaned with paper towels. The thickness of the disks was measured with an IP54 micrometer gauge (Dongguan Orient Precision Measurement Technology Co., Ltd., Dongguan, China). The light intensity was kept at 10.3 mW/cm² for all experiments and the exposure time was 2–10 s. Each exposure was done in triplicate, and the mean values were calculated.

Determination of photosensitive parameters

The light absorption of photosensitive resin follows the Beer-Lambert law [34]. The penetration depth (D_p), cure depth (C_d), exposure (E [mJ/cm²]), and the critical exposure (E_C) Equation (4):

Table 2. The waterborne photosensitive resin composition of 3D printing.

Samples	S1 [g]	S2 [g]	S3 [g]	S4 [g]
WPR-2	85.0	75.0	60.0	55.0
ACMO	15.0	25.0	40.0	45.0
L-TPO	0.3	0.3	0.3	0.3



$$Cd = Dp \ln \left[\frac{E}{E_C} \right] \quad (4)$$

where D_p is the penetration depth of the waterborne photosensitive resin, denoting the UV absorption intensity of the waterborne photosensitive resin; E is the actual exposure intensity of the waterborne photosensitive resin. E_C is the critical exposure.

By transforming Equation (4), a general linear equation is formed, as Equation (5):

$$Cd = Dp \ln E - Dp \ln E_C \quad (5)$$

where D_p and $D_p \ln E_C$ are the constants, *i.e.* the slope and intercept of the corresponding linear fitting curve, respectively. By comparing Equation (5), the value of D_p and E_C can be deduced.

4. Results and discussion

4.1. Structure analysis of H-AOI

The FTIR spectra of AOI and H-AOI are shown in Figure 2a. The absorption peak of N–H stretching vibration appears at 3368 cm⁻¹, the absorption peak of N–H bending vibration is 1533 cm⁻¹ [35], and the absorption peak at 1730 cm⁻¹ belongs to the stretching vibration of the carbonyl group (C=O). This is the characteristic peak of the carbamate group, resulting from the reaction of isocyanate groups (–NCO) with hydroxyl groups (–OH). In addition, the characteristic peak at 2267 cm⁻¹ attributed to the isocyanate group (–NCO) disappeared completely. The results of FTIR spectra clearly confirm the successful reaction between HEMA and AOI.

The ¹H NMR spectrum of H-AOI is shown in Figure 2b. The peaks at 6.10~6.45 ppm are contributed by the proton of methacrylate double bond

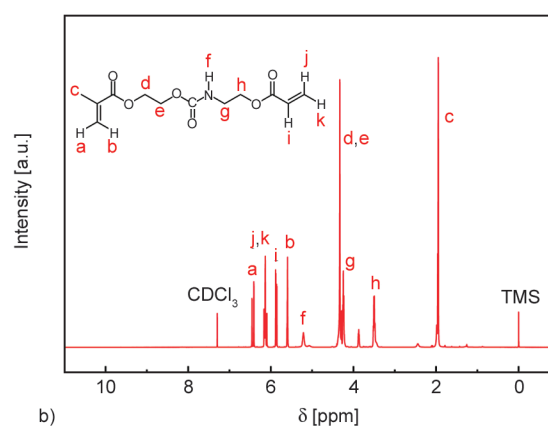


Figure 2. a) FTIR spectra of AOI and H-AOI, b) ¹H NMR spectrum of asymmetric monomer (H-AOI).

($\text{CH}_2\text{-C}(\text{CH}_3)\text{-}$). The peaks at 6.09~6.16, 5.50~5.60 ppm are ascribed to the proton of acrylate double bond (-CH=CH_2). The peaks at 4.21~4.33 and 3.47~3.5 ppm are attributed to the proton of methylene ($\text{-CH}_2\text{-}$) [36]. The peaks at 1.95 ppm correspond to the protons of methyl (-CH_3). The peaks at 5.21 ppm are attributed to the protons of the carbamate (-NHCOO-). The results of ^1H NMR indicate that H-AOI was successfully prepared.

4.2. Structure analysis of WPR

D400, TCDDA, and H-AOI are used to prepare prepolymers containing methacrylic double bonds by Michael addition reaction, and then the secondary amine groups react with isocyanate groups of AOI to insert different proportions of acrylate double bonds in the side chain of the prepolymer. Finally, hydrochloric acid is used to form a salt with the residual secondary amine groups to impart hydrophilicity to the prepolymer. The FTIR spectra of the reactants, intermediate prepolymers, and products are shown in Figure 3. Figure 3a curve (1) is the FTIR spectrum of TCDDA. The characteristic absorption peaks of the carbon-carbon double bond at 1640 and 810 cm^{-1} could be clearly observed. After the reaction, the peaks disappear completely, as shown in Figure 3a curve (2), indicating the double bonds of TCDDA are consumed when reacting with D400 by Michael addition and forming an amino-terminated prepolymer (denoted as PR-1). Figure 3a curve (3) is the FTIR spectrum of the product of PR-1 reacting with H-AOI. The characteristic absorption peaks of carbon-carbon double bonds at 1640, 810 cm^{-1} and the carbamate at 3320, 1533 cm^{-1} are observed, demonstrating that H-AOI is reintroduced successfully and

forming the prepolymer with acrylate moieties (denoted as PR-2). Figure 3a curve (4) is the FTIR spectrum of PR-2 reacting with AOI. The characteristic absorption peaks of the isocyanate group at 2267 cm^{-1} disappear, indicating AOI reacts with the secondary amine groups of PR-2, producing the prepolymer (denoted as PR-3). The FTIR spectrum of WPR is shown in Figure 3a curve (5). The characteristic absorption peak of hydrochloride at 2459 cm^{-1} appears, indicating hydrochloride formed from hydrogen chloride reacting with the secondary amino group of prepolymer PR-3.

Figure 3b is the ^1H NMR spectrum of WPR. The peaks 5.60~6.45, and 4.51~4.66 ppm are contributed by the proton of carbon-carbon double bond and carbamate, respectively. The results of ^1H NMR combined with FTIR confirmed WPR was successfully synthesized.

4.3. Photopolymerization kinetics of waterborne photosensitive resin

Real-time FTIR is robust means of monitoring polymerization *in situ*. The characteristic absorption peaks of the acrylate double bond at 1640 and 810 cm^{-1} are shown in Figure 4a as a function of irradiation time. As can be seen, the absorption intensity of characteristic peaks gradually decreased with increasing irradiation time, indicating that the double bonds were consumed during the polymerization.

Figure 4b shows the double bond conversion curves of WPR-1, WPR-2, and WPR-3. As shown in Figure 4b, the double bond conversions of WPR-1, WPR-2, and WPR-3 gradually increase up to 78.7, 85.6, and 92.8%, respectively. Under UV irradiation, the photoinitiator is cracked into free radicals. With

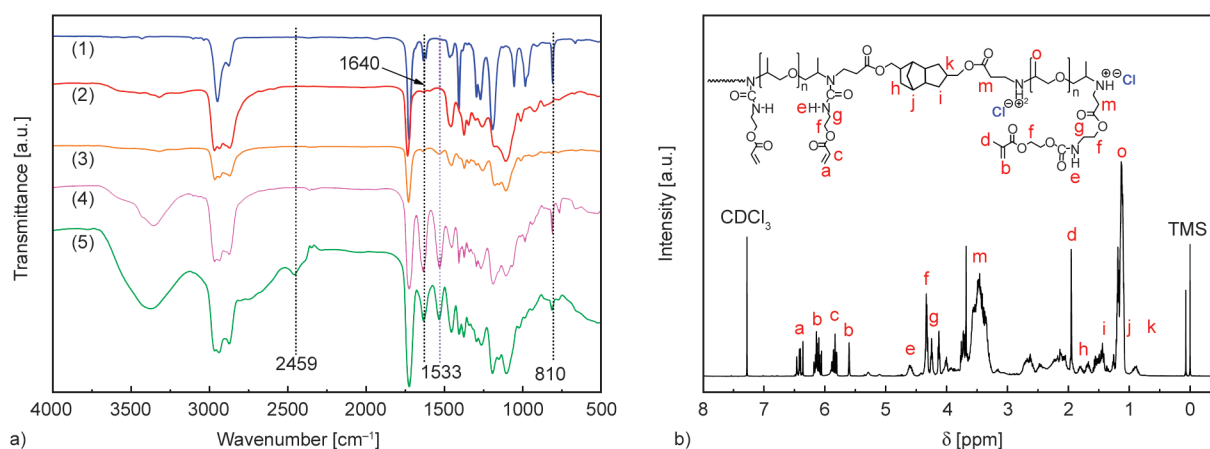


Figure 3. a) (1)–(5) are the FTIR spectra of TCDDA, PR-1, PR-2, PR-3, and WPR, respectively, b) is the ^1H NMR spectrum of WPR.

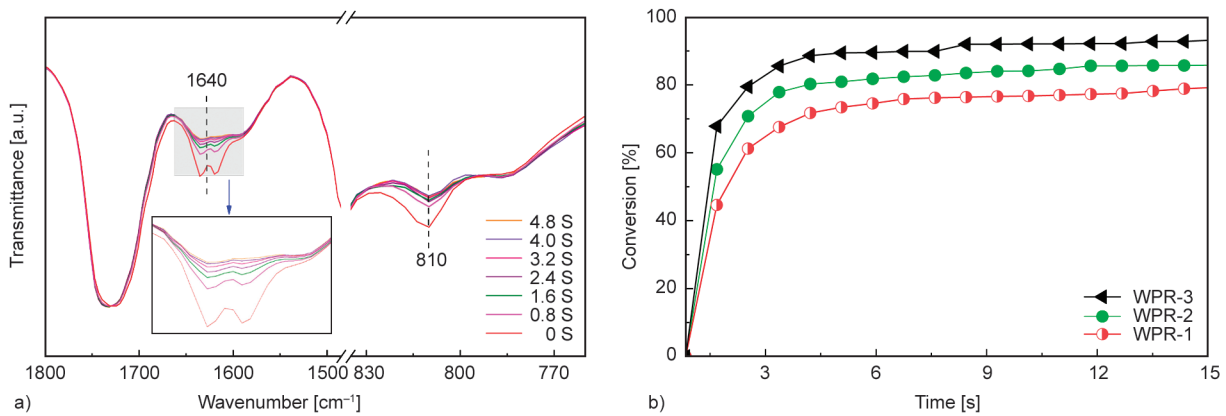


Figure 4. a) The absorption intensity vs. irradiation time for the double bonds. b) The double bonds conversion of WPR under UV irradiation with the intensity of 50 mJ/cm² and the L-TPO concentrations of 1.0 wt%.

the increasing double bond content, the probability of free radicals attacking the double bonds increases. Therefore, the number of active radicals produced by chain reaction increases, and the polymerization rate and double bond conversion of WPR increase with the increase of the double bond content.

4.4. Tensile strength

The stress-strain curves, change trend of tensile strength, and gel content of the UV-cured films of WPR is shown in Figure 5. As shown in Figure 5a, the tensile strength gradually increases from 0.35, 1.40 to 2.58 MPa, while the elongation at break decreases from 44.0, 40.9 to 40.3% for WPR-1, WPR-2, and WPR-3, respectively. This is mainly because the crosslinking density of WPR cured films increases with the increasing acrylate double bond content, leading to the formation of fixable macromolecular chains and a rigid crosslinking network. Figure 5b shows that the gel contents of WPR-1, WPR-2, and WPR-3 gradually increase from 48.05

and 69.10 to 83.28%, respectively. The tensile strength of the UV-cured films increases with increasing gel contents, demonstrating that the gel contents have a great effect on the tensile strength of the UV-cured films of WPR.

4.5. Dynamic mechanical analysis

Dynamic mechanical analysis (DMA) was conducted to measure the glass transition temperature, which is an important performance parameter of polymeric materials. Figure 6 shows the storage modulus (E') and loss factor ($\tan\delta$) of the UV-cured films of WPR as a function of temperature, respectively. As Figure 6a shows, the storage modulus E' of the UV-cured films of WPR increase for WPR-1, WPR-2, and WPR-3. In addition, the double bond content of WPR-1, WPR-2, and WPR-3 are correspondingly 1.02, 1.50, and 1.95 (Table 1). Obviously, the storage modulus E' of the UV-cured films of WPR increase with the increasing double bond content of WPR resins. This is mainly because the increasing double

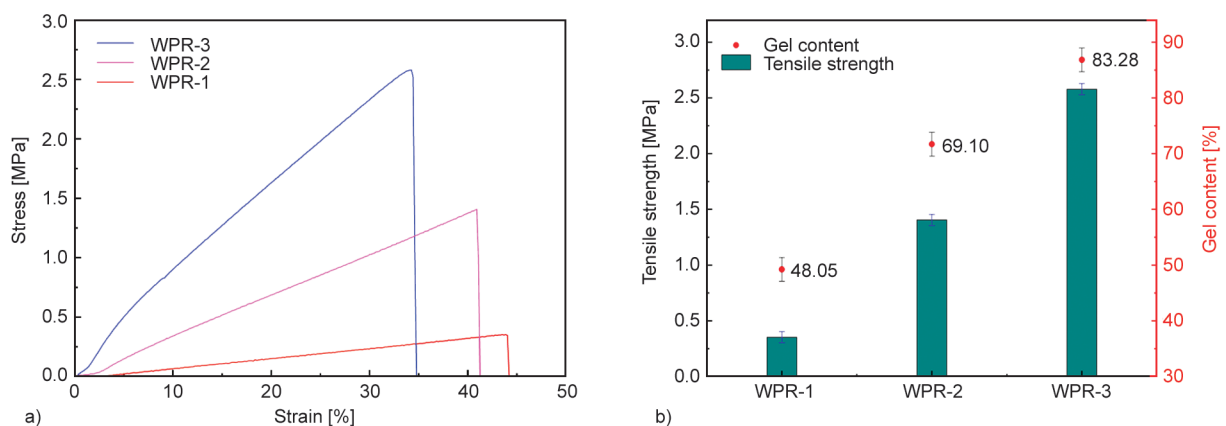


Figure 5. a) The stress-strain curves of the UV-cured films. b) The changing trend of tensile strength and gel contents of the UV-cured films.

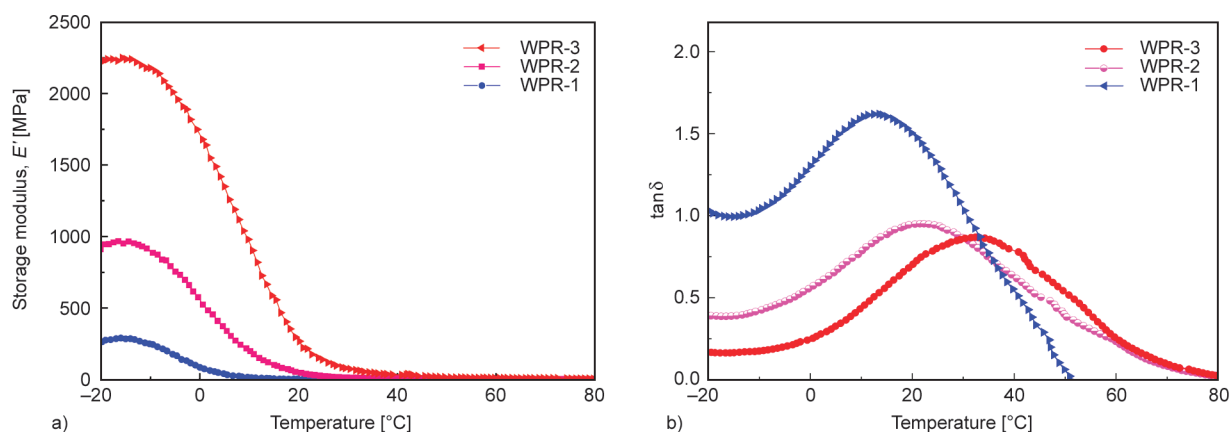


Figure 6. a) The storage modulus of the UV-cured films of WPR as a function of temperature. b) $\tan \delta$ of the UV-cured films of WPR as a function of temperature.

bond content of WPR leads to the increased crosslinking degree of the UV-cured films of WPR, which results in the storage modulus E' increasing.

The glass transition temperature of the UV-cured films of WPR was evaluated by the maximum of $\tan \delta$ curve [37]. As shown in Figure 6b and Table 1, with the increasing acrylate double bond content of WPR, the glass transition of the UV-cured films of WPR increases from 13.5 and 21.5 to 32.4 °C, respectively. The enhancement can be explained by the increase of double bond content, improving the crosslinking degree of the UV-cured film, causing restriction of the molecular chain movement.

4.6. Water absorption of WPR cured film

Figure 7a shows the water contact angle, and water absorption of WPR cured films. The surface water contact angle of the UV-cured films of WPR-1, WPR-2, and WPR-3 gradually increases with the values of 10.8, 22.9 and 51.5°, respectively. It is caused by the decreasing content of the hydrophilic groups in the corresponding WPR-1, WPR-2, and WPR-3 resin, which reduces the surface energy of the UV-cured film and leads to an increase in the surface

water contact angle. Furthermore, the crosslinking density is an important factor affecting the water contact angle of the UV-cured film. The crosslinking density of the UV-cured films increases with the increasing double bond content of the WPR resin, which leads to the surface water contact angle arising.

In addition, with the increase in water contact angle, the water absorption of the UV-cured films of WPR-1, WPR-2, and WPR-3 gradually decreased, which were 26.6, 16.2, and 11.1%, respectively. This is mainly due to the decrease of hydrophilicity of the UV-cured films with the decrease of hydrophilic group content, *i.e.*, the increase of hydrophobicity, which leads to the increase of difficulty for water molecules to enter the cured films. Furthermore, the increase in the content of acrylate double bonds in WPR-1, WPR-2, and WPR-3 also leads to an increase in the crosslinking density after UV irradiation, which reduces the water absorption of the UV-cured films. Therefore, the content of the hydrophilic group and the crosslinking density are important factors affecting the water absorption and contact angle of cured films.

In WPR resins, the hydrophilic group is hydrochloride, which has good water solubility. The increasing

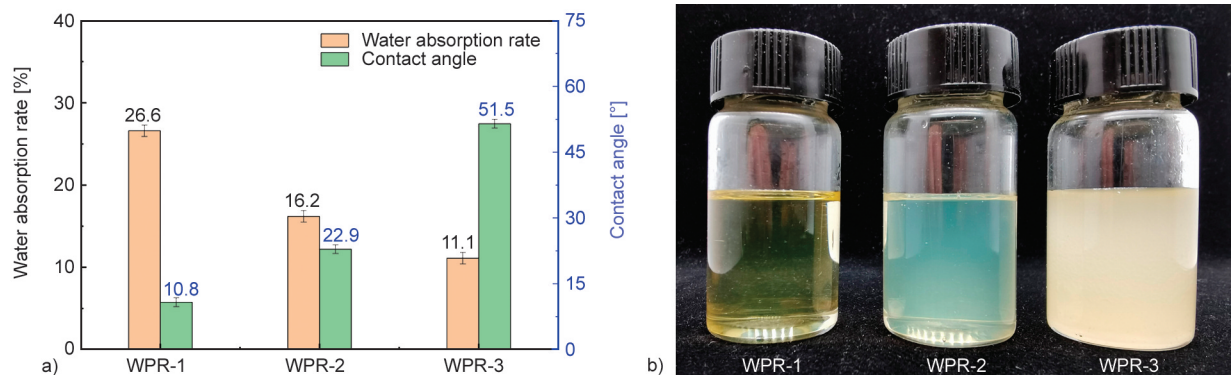


Figure 7. a) Surface water contact angle and water absorption of the UV-cured film. b) The water solubility of WPR.

content of hydrochloride could improve the hydrophilicity of WPR. Figure 7b shows the appearance of the WPR resins after the addition of 40% water. By comparing the appearance of the solutions of WPR-1, WPR-2, and WPR-3, it can be seen that WPR-1 is pale yellow and transparent, WPR-2 is light blue and transparent, and WPR-3 is cloudy. This is mainly because a decrease in the content of hydrochloride resulted in the decrease in hydrophilicity of WPR-1, WPR-2, and WPR-3. Overall, WPR resins have good water solubility and good water-washing properties.

4.7. Thermal stability of the WPR cured film

The thermal stability of WPR cured film was measured by the TG-DTG. Figure 8a shows the thermogravimetric (TG) curves of the UV-cured films of WPR-1, WPR-2, and WPR-3. It can be seen from the curves that the mass gradually decreases as the temperature increases. The temperatures are listed in Table 3. A weight loss of 5%, denoted as $T_{5\%}$, is usually considered to be the initial decomposition temperature of the materials. As shown in Table 3, the initial decomposition temperatures of the UV-cured films of WPR-1, WPR-2, and WPR-3 were 111.5, 128.3, and 218.3 °C, respectively. That is mainly due to the residual moisture in the UV-cured films of WPR-1 and WPR-2, resulting in the initial

decomposition temperature occurring at a low-temperature stage. The decomposition temperature $T_{10\%}$ of the UV-cured films of WPR-1, WPR-2, and WPR-3 increased from 212.0 and 235.0 to 260.5 °C. This is mainly because an increase in crosslinking density of the UV-cured films resulted from the acrylate double bond content of WPR arising.

Figure 8b shows the differential thermogravimetric (DTG) curves of the UV-cured films of WPR-1, WPR-2, and WPR-3. The thermal decomposition process of WPR cured films is divided into four main stages. The maximum decomposition rates for each stage are listed in Table 3. The first stage occurs before 180 °C, which is mainly due to the residual water in the cured film. The second stage occurs between 230 and 255 °C, with a mass loss of approximately 10%. The main reason for the second stage is the decomposition of hydrochloride due to the dissociation of ionic bonds. The third stage occurs between 310 and 350 °C with a mass loss of 40–48%, mainly due to the decomposition of ether bonds and carbamates. The fourth stage occurs between 380 and 450 °C and is mainly caused by the decomposition of carbon-carbon bonds. Further comparison of the three curves shows that the mass loss rate decreases with increasing temperature in the order of WPR-1, WPR-2, and WPR-3, which is mainly due to the increase in crosslinking density of the cured films.

Table 3. Thermal stability of the UV-cured film of WPR.

Samples	$T_{5\%}$ [°C]	$T_{10\%}$ [°C]	First step		Second step		Third step		Fourth step	
			T_{max} [°C]	Weight loss [%]	T_{max} [°C]	Weight loss [%]	T_{max} [°C]	Weight loss [%]	T_{max} [°C]	Weight loss [%]
WPR-1	111.5	212.0	98.2	3.9	230.8	12.2	316.3	48.2	385.2	84.9
WPR-2	128.3	235.0	98.7	2.7	244.5	11.3	327.7	41.1	392.5	77.0
WPR-3	218.3	260.5	107.3	1.7	253.3	8.9	346.5	40.1	390.3	68.2

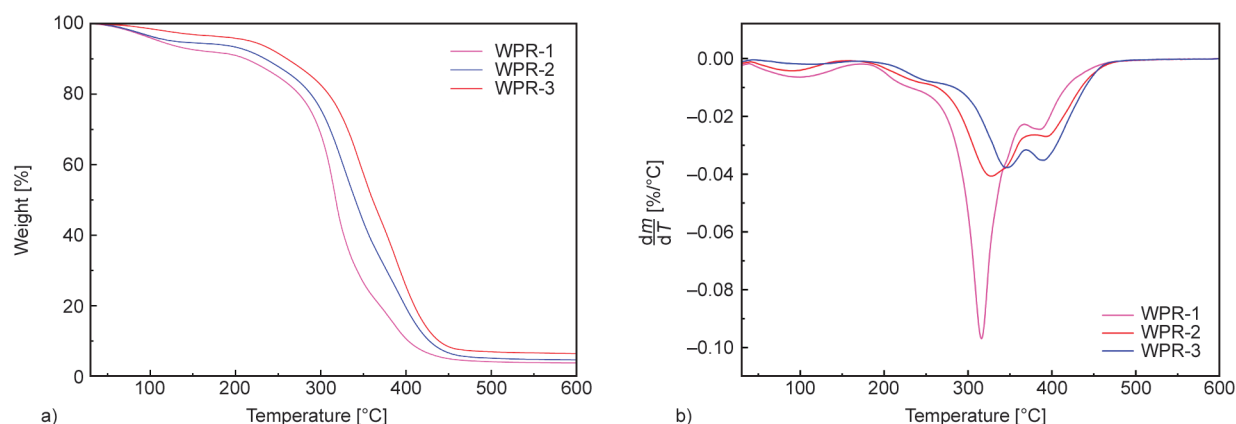


Figure 8. Thermal stability of the UV-cured film of WPR, a) TGA, and b) DTG curves.

4.8. 3D printing

UV-curing 3D printing, with the characteristics of high printing accuracy and fast printing speed, is a kind of additive manufacturing technology. In traditional UV-curing 3D printing, the photosensitive resins are oil-soluble, and a large amount of organic solvent is required to clean the surface of the printed parts. The use of organic solvents increases the risk of fire and could cause environmental pollution problems. The issues could be addressed effectively by the use of waterborne photosensitive resins for 3D printing because the residual resin of printed parts surface could be cleaned by water. The prepared WPR-2 resin was evenly mixed with diluted monomer ACOMO and the photoinitiator L-TPO in certain proportions for 3D printing tests. The specific proportions are shown in Table 2.

The viscosity of waterborne photosensitive resins has a significant impact on 3D printing. The viscosity of the resin is adjusted by adding ACOMO for the convenience of 3D printing. The added ACOMO has a great effect on the mechanical properties of 3D printed parts. The favorable ratio for 3D printing was determined by comparing the tensile strength of 3D printed parts and the viscosity of the resin. As shown in Figure 9, the tensile strength of 3D printed parts increases with the amount of added ACOMO rising. Formulation S1 and S2 are unsuitable for 3D printing due to their high viscosity. Formulation S4 and S3 with lower viscosities can be used for 3D printing. In addition, the tensile strength and the amount of ACOMO added are relatively higher.

Determination of waterborne photosensitive parameters

The penetration depth (D_p) and critical exposure (E_C) are important parameters to adjust the exposure time in a 3D printer to cure the chosen layer thickness. All

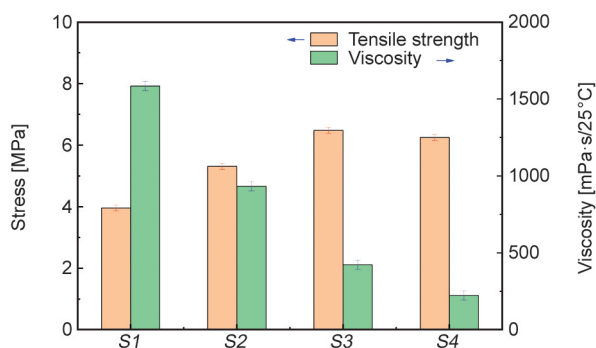


Figure 9. The viscosity of 3D printing composition and the tensile strength of the printed parts.

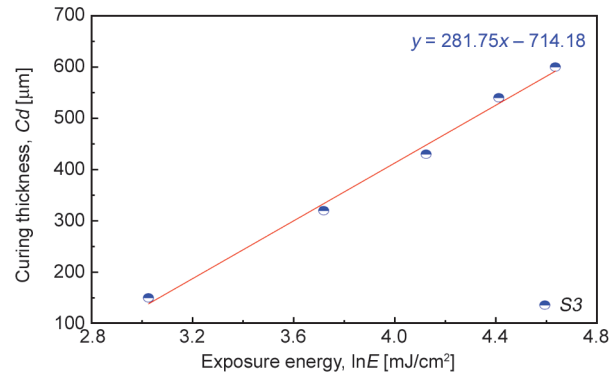


Figure 10. Curves fitted and extrapolated to determine the photosensitive parameters of S3 with 40.0 wt% ACOMO and 3.0 wt% photoinitiator (L-TPO).

3D printing photosensitive resins can be described with the parameters of D_p and E_C [38]. The exposure intensity E is a function of the exposure time multiplied with the incident light intensity of the LED light source. The penetration depth (D_p) and critical exposure (E_C) can be plotted in a linear form (10.3 mW/cm^2 for the LED light source used in this study). Thus, E is a function of exposure time (the range of 2~10 s), and Cd can be directly measured for each experiment. Hence, the critical exposure energy (E_C) and the penetration depth (D_p) can be plotted in a linear form, based on the known values of E and Cd . As shown in Figure 10, it is a linear fitting curve of critical exposure energy (E_C) and penetration depth (D_p) for formulation S3. It shows a very good fit to the data of the measured value E and Cd . The bottom-up 3D printing vat polymerization technology is a layer-by-layer additive manufacturing process. Therefore, it is necessary the value of actual cure depth is larger than the sliced layer thickness of the printed sample to ensure sufficient adhesion between the layers [34]. In addition, the exposure energy E must be larger than the critical exposure intensity E_C to initiate polymerization reaction. It can be achieved by adjusting the exposure time. From Figure 10, the value of penetration depth ($D_p = 281.75 \text{ μm}$) and critical exposure ($E_C = 12.61 \text{ mJ/cm}^2$) of the formulation S3 can be obtained by calculation. In 3D printing, the printing accuracy of photosensitive resin is an important parameter. In this paper, a hollow cube model is designed to test the printing accuracy. The printed hollow cube is shown in Figure 11a. The hollow cube model was designed by CAD, and the ridge length of a single hollow cube is 10 times the ridge width. The entire hollow cube was fabricated via 3D printing with dimensions of

15 mm × 15 mm × 15 mm (Figure 11d). The ridge width of the printed hollow cube can be calculated

(205.5 μm). The 3D printed part of the hollow cube model has a high printing accuracy (the strip width

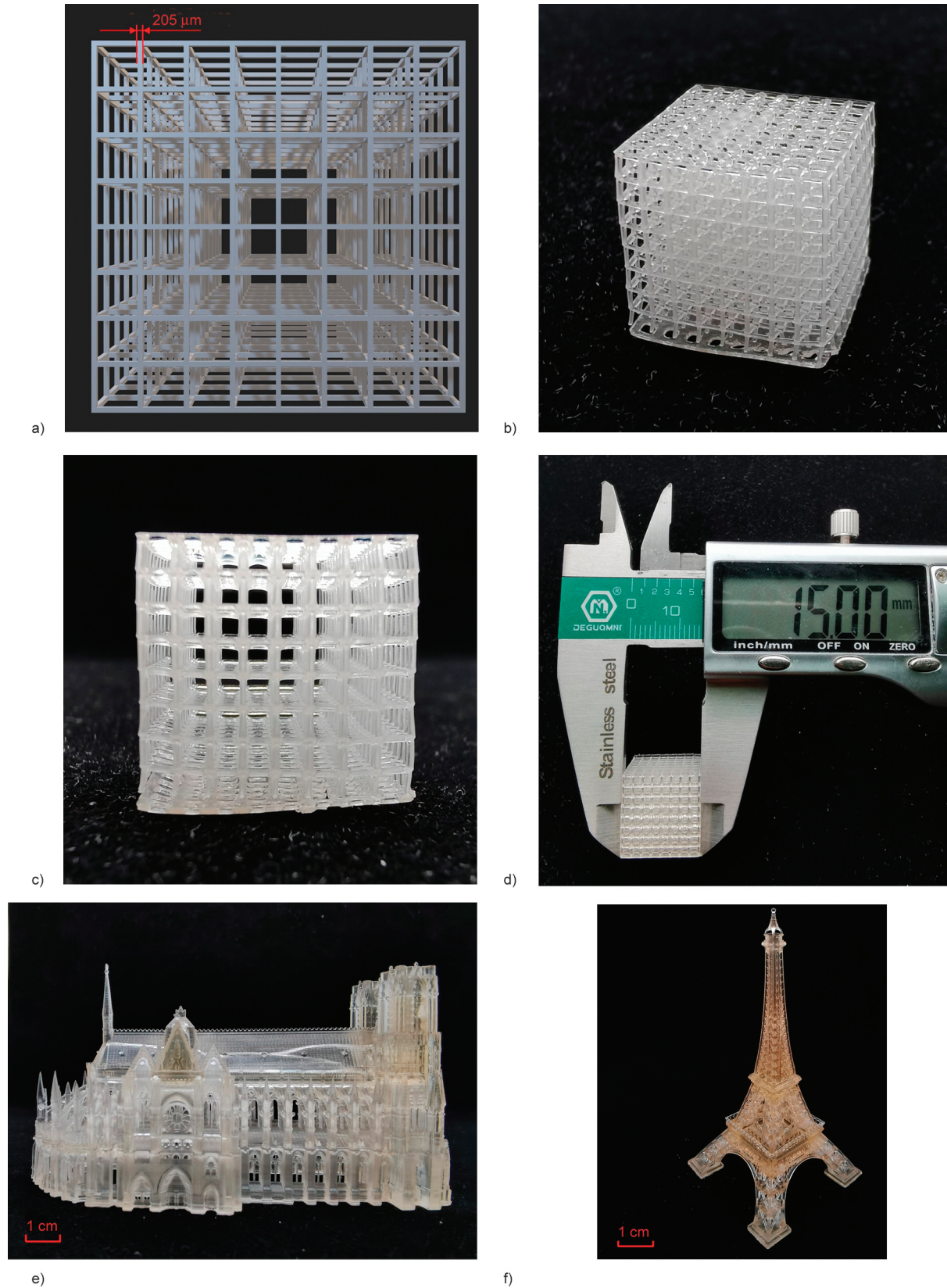


Figure 11. a) The 3D model of hollow cube design by CAD. b) Hollow cube printed using formulation S3; c) Front view of printed hollow cube. d) The size of a hollow cube. e), f) The printed model of Reims Cathedral and Eiffel tower was printed using formulation S3.

is about 205 μm). The printed hollow cube with different view aspects is shown in Figures 11b and 11c, which has a good printing effect.

As shown in Figure 11e and Figure 11f, two building models with a highly complex structure was successfully fabricated, indicating that the prepared waterborne photosensitive resin could be promising for dentistry and jewelry manufacturing.

5. Conclusions

An asymmetrical monomer and a series of novel waterborne photosensitive resins were successfully synthesized and confirmed by FTIR and ^1H NMR spectroscopy. The effects of different double bonds content were investigated and found that with increasing double bonds content, the double bonds conversion increases from 78.7, 85.6 to 92.8% in photopolymerization of WPR, and the gel content of the cured film increases from 48.05, 69.10 to 83.28%, the glass transition temperature and tensile strength of WPR cured film follow the same increasing trend. Moreover, the content of hydrochloride has a great influence on the hydrophilicity of the waterborne photosensitive resin. The studies indicated that as the hydrochloride content decreases, the surface water contact angle of the UV-cured film of WPR increases from 10.8, 22.9 to 51.5°, and water absorption decreases from 26.55, 16.20, to 11.06%. Finally, waterborne photosensitive resins were applied to 3D printing, and the photosensitive parameters, including the penetration depth ($D_p = 281.64 \mu\text{m}$) and critical exposure ($E_C = 12.78 \text{ mJ/cm}^2$) were measured. Above all, the waterborne photosensitive resins exhibited a high printing accuracy and good effect of washing and are promising for waterborne 3D printing.

Acknowledgements

The authors thank the support from the Key R&D Program of Guangdong Province (Grant No. 2020B090924001), the National Natural Science Foundation of China (Grants: 51873043) and the JieYang Sailing Program (Grants: CXTD2021001).

References





- [1] Li J., Pumera M.: 3D printing of functional microrobots. *Chemical Society Reviews*, **50**, 2794–2838 (2021). <https://doi.org/10.1039/d0cs01062f>
- [2] Frazier W. E.: Metal additive manufacturing: A review. *Journal of Materials Engineering and Performance*, **23**, 1917–1928 (2014). <https://doi.org/10.1007/s11665-014-0958-z>
- [3] Ngo T. D., Kashani A., Imbalzano G., Nguyen K. T. Q., Hui D.: Additive manufacturing (3D printing): A review of materials, methods, applications and challenges. *Composites Part B: Engineering*, **143**, 172–196 (2018). <https://doi.org/10.1016/j.compositesb.2018.02.012>
- [4] Chia H. N., Wu B. M.: Recent advances in 3D printing of biomaterials. *Journal of Biological Engineering*, **9**, 4 (2015). <https://doi.org/10.1186/s13036-015-0001-4>
- [5] Seoane-Viaño I., Januskaite P., Alvarez-Lorenzo C., Basit A. W., Goyanes A.: Semi-solid extrusion 3D printing in drug delivery and biomedicine: Personalised solutions for healthcare challenges. *Journal of Controlled Release*, **332**, 367–389 (2021). <https://doi.org/10.1016/j.jconrel.2021.02.027>
- [6] Joshi S. C., Sheikh A. A.: 3D printing in aerospace and its long-term sustainability. *Virtual and Physical Prototyping*, **10**, 175–185 (2015). <https://doi.org/10.1080/17452759.2015.1111519>
- [7] McMenamin P. G., Quayle M. R., McHenry C. R., Adams J. W.: The production of anatomical teaching resources using three-dimensional (3D) printing technology. *Anatomical Sciences Education*, **7**, 479–486 (2014). <https://doi.org/10.1002/ase.1475>
- [8] Dawood A., Marti B. M., Sauret-Jackson V., Darwood A.: 3D printing in dentistry. *British Dental Journal*, **219**, 521–529 (2015). <https://doi.org/10.1038/sj.bdj.2015.914>
- [9] Alghamdi S. S., John S., Choudhury N. R., Dutta N. K.: Additive manufacturing of polymer materials: Progress, promise and challenges. *Polymers*, **13**, 753 (2021). <https://doi.org/10.3390/polym13050753>
- [10] Pagac M., Hajnys J., Ma Q-P., Jancar L., Jansa J., Stefek P., Mesicek J.: A review of vat photopolymerization technology: Materials, applications, challenges, and future trends of 3D printing. *Polymers*, **13**, 598 (2021). <https://doi.org/10.3390/polym13040598>
- [11] Tan L. J., Zhu W., Zhou K.: Recent progress on polymer materials for additive manufacturing. *Advanced Functional Materials*, **30**, 2003062 (2020). <https://doi.org/10.1002/adfm.202003062>
- [12] Bagheri A., Jin J.: Photopolymerization in 3D printing. *ACS Applied Polymer Materials*, **1**, 593–611 (2019). <https://doi.org/10.1021/acsapm.8b00165>
- [13] Kodama H.: Automatic method for fabricating a three-dimensional plastic model with photo-hardening polymer. *Review of Scientific Instruments*, **52**, 1770–1773 (1981). <https://doi.org/10.1063/1.1136492>
- [14] Lu Y., Mapili G., Suhali G., Chen S., Roy K.: A digital micro-mirror device-based system for the microfabrication of complex, spatially patterned tissue engineering scaffolds. *Journal of Biomedical Materials Research: Part A*, **77**, 396–405 (2006). <https://doi.org/10.1002/jbm.a.30601>

- [15] Tumbleston J. R., Shirvanyants D., Ermoshkin N., Januszewicz R., Johnson A. R., Kelly D., Chen K., Pinschmidt R., Rolland J. P., Ermoshkin A., Samulski E. T., DeSimone J. M.: Continuous liquid interface production of 3D objects. *Science*, **347**, 1349–1352 (2015). <https://doi.org/10.1126/science.aaa2397>
- [16] Kelly B. E., Bhattacharya I., Heidari H., Shusteff M., Spadaccini C. M., Taylor H. K.: Volumetric additive manufacturing via tomographic reconstruction. *Science*, **363**, 1075–1079 (2019). <https://doi.org/10.1126/science.aau7114>
- [17] Karakurt I., Lin L.: 3D printing technologies: Techniques, materials, and post-processing. *Current Opinion in Chemical Engineering*, **28**, 134–143 (2020). <https://doi.org/10.1016/j.coche.2020.04.001>
- [18] Elbadawi M., McCoubrey L. E., Gavins F. K. H., Ong J. J., Goyanes A., Gaisford S., Basit A. W.: Harnessing artificial intelligence for the next generation of 3D printed medicines. *Advanced Drug Delivery Reviews*, **175**, 113805 (2021). <https://doi.org/10.1016/j.addr.2021.05.015>
- [19] Invernizzi M., Suriano R., Muscatello A., Turri S., Levi M.: Near-visible stereolithography of a low shrinkage cationic/free-radical photopolymer blend and its nanocomposite. *Journal of Applied Polymer Science*, **137**, 48333 (2020). <https://doi.org/10.1002/app.48333>
- [20] He C., Ma C., Li X., Yan L., Hou F., Liu J., Guo A.: Polymer-derived SiOC ceramic lattice with thick struts prepared by digital light processing. *Additive Manufacturing*, **35**, 101366 (2020). <https://doi.org/10.1016/j.addma.2020.101366>
- [21] Silbert S. D., Simpson P., Setien R., Holthaus M., La Scala J., Ulven C. A., Webster D. C.: Exploration of bio-based functionalized sucrose ester resins for additive manufacturing via stereolithography. *ACS Applied Polymer Materials*, **2**, 2910–2918 (2020). <https://doi.org/10.1021/acsapm.0c00417>
- [22] Peterson G. I., Schwartz J. J., Zhang D., Weiss B. M., Ganter M. A., Storti D. W., Boydston A. J.: Production of materials with spatially-controlled cross-link density via vat photopolymerization. *ACS Applied Materials and Interfaces*, **8**, 29037–29043 (2016). <https://doi.org/10.1021/acsami.6b09768>
- [23] Mubarak S., Dharmodharan D., Divakaran N., Kale M. B., Senthil T., Wu L., Wang J.: Enhanced mechanical and thermal properties of stereolithography 3D printed structures by the effects of incorporated controllably annealed anatase TiO₂ nanoparticles. *Nanomaterials*, **79**, 79 (2020). <https://doi.org/10.3390/nano10010079>
- [24] Garcia E. A., Ayranci C., Qureshi A. J.: Material property-manufacturing process optimization for form 2 VAT-photo polymerization 3D printers. *Journal of Manufacturing and Materials Processing*, **4**, 12 (2020). <https://doi.org/10.3390/jmmp4010012>
- [25] Schmidt J., Altun A. A., Schwentenwein M., Colombo P.: Complex mullite structures fabricated via digital light processing of a preceramic polysiloxane with active alumina fillers. *Journal of the European Ceramic Society*, **39**, 1336–1343 (2019). <https://doi.org/10.1016/j.jeurceramsoc.2018.11.038>
- [26] Sugimoto H., Tonouchi S., Toda K., Nakanishi E.: Preparation and mechanical properties of acryl/glass cloth composite materials with low light dispersion. *Journal of Polymer Research*, **27**, 39 (2020). <https://doi.org/10.1007/s10965-019-1998-8>
- [27] Yang Z., Peng H., Wang W., Liu T.: Crystallization behavior of poly(ϵ -caprolactone)/layered double hydroxide nanocomposites. *Journal of Applied Polymer Science*, **116**, 2658–2667 (2010). <https://doi.org/10.1002/app.31787>
- [28] Hong C-Y., You Y-Z., Wu D-C., Liu Y., Pan C-Y.: Thermal control over the topology of cleavable polymers: From linear to hyperbranched structures. *Journal of the American Chemical Society*, **129**, 5354–5355 (2007). <https://doi.org/10.1021/ja070871+>
- [29] Moszner N., Völkel T., Rheinberger V.: Synthesis, characterization and polymerization of dendrimers with methacrylic end groups. *Macromolecular Chemistry and Physics*, **197**, 621–631 (1996). <https://doi.org/10.1002/macp.1996.021970217>
- [30] Bai C. Y., Zhang X. Y., Dai J. B., Li W. H.: A new UV curable waterborne polyurethane: Effect of C=C content on the film properties. *Progress in Organic Coatings*, **55**, 291–295 (2006). <https://doi.org/10.1016/j.porgcoat.2005.12.002>
- [31] Xiang H., Wang X., Ou Z., Lin G., Yin J., Liu Z., Zhang L., Liu X.: UV-curable, 3D printable and biocompatible silicone elastomers. *Progress in Organic Coatings*, **137**, 105372 (2019). <https://doi.org/10.1016/j.porgcoat.2019.105372>
- [32] Dong X., Ren J., Duan Y., Wu D., Lin L., Shi J., Jia R., Xu X., He X.: Preparation and properties of green UV-curable itaconic acid cross-linked modified waterborne polyurethane coating. *Journal of Applied Polymer Science*, **139**, 52042 (2022). <https://doi.org/10.1002/app.52042>
- [33] Wang J., Zhang H., Miao Y., Qiao L., Wang X., Wang F.: UV-curable waterborne polyurethane from CO₂-polyol with high hydrolysis resistance. *Polymer*, **100**, 219–226 (2016). <https://doi.org/10.1016/j.polymer.2016.08.039>
- [34] Hofstetter C., Orman S., Baudis S., Stampfl J.: Combining cure depth and cure degree, a new way to fully characterize novel photopolymers. *Additive Manufacturing*, **24**, 166–172 (2018). <https://doi.org/10.1016/j.addma.2018.09.025>

- [35] Lin Z., Deng H., Hou Y., Liu X., Xu R., Xiang H., Peng Z., Rong M., Zhang M.: Dual-crosslinking side chains with an asymmetric chain structure: A facile pathway to a robust, self-healable, and re-dissolvable polysiloxane elastomer for recyclable flexible devices. *Journal of Materials Chemistry A*, **10**, 11019–11029 (2022).
<https://doi.org/10.1039/d2ta01535h>
- [36] Mori H., Miyamura Y., Endo T.: Synthesis and characterization of water-soluble silsesquioxane-based nanoparticles by hydrolytic condensation of triethoxysilane derived from 2-hydroxyethyl acrylate. *Langmuir*, **23**, 9014–9023 (2007).
<https://doi.org/10.1021/la700706a>
- [37] Pang Y., Shiraishi A., Keil D., Popov S., Strehmel V., Jiao H., Gutmann J. S., Zou Y., Strehmel B.: NIR-sensitized cationic and hybrid radical/cationic polymerization and crosslinking. *Angewandte Chemie-International Edition*, **60**, 1465–1473 (2021).
<https://doi.org/10.1002/anie.202010746>
- [38] Steyrer B., Busetti B., Harakály G., Liska R., Stampfl J.: Hot lithography vs. room temperature DLP 3D-printing of a dimethacrylate. *Additive Manufacturing*, **21**, 209–214 (2018).
<https://doi.org/10.1016/j.addma.2018.03.013>

Research article

Photocuring and digital light processing 3D printing of vitrimer composed of 2-hydroxy-2-phenoxypropyl acrylate and acrylated epoxidized soybean oil

Sigita Grauzeliene¹, Brigita Kazlauskaitė¹, Edvinas Skliutas², Mangirdas Malinauskas², Jolita Ostrauskaite^{1*}

¹Department of Polymer Chemistry and Technology, Kaunas University of Technology, Radvilenu Rd. 19, LT-50254 Kaunas, Lithuania

²Laser Research Center, Faculty of Physics, Vilnius University, Sauletekio Ave. 10, LT-10223 Vilnius, Lithuania

Received 26 May 2022; accepted in revised form 22 August 2022

Abstract. Vitrimers have gained attention as materials with recyclability, self-healing, and shape memory properties. The use of bio-based monomers for the synthesis of vitrimers is relevant because of the use of an environmentally friendly strategy. In this work, resins based on 2-hydroxy-2-phenoxypropyl acrylate and acrylated epoxidized soybean oil were designed and tested by real-time photorheometry, Fourier transform infrared spectroscopy (FT-IR), and mechanical testing to determine suitability for digital light processing 3D printing. The synthesis of vitrimer that could have good thermal properties and vitrimeric abilities, such as shape memory, self-healing, and recyclability properties, was investigated. Because of this, the vitrimer could repair cracks and defects and could have a complex design of several parts, which also contributes to recyclability and decreases costs. The rigidity and viscosity of the resins were reduced with an increasing amount of 2-hydroxy-2-phenoxypropyl acrylate-based monomer. The resin that has the highest amounts of hydroxyl and ester groups that are beneficial for transesterification reactions was chosen for vitrimer synthesis in order to show vitrimeric abilities such as self-healing, shape memory properties, reprocessability, and recyclability. The synthesized vitrimer was applied to digital light processing 3D printing and showed shape memory with a recovery ratio of 100%, self-healing and reprocessability with an efficiency of 47 and 31% and recyclability properties.

Keywords: smart polymers, biobased, rheology, vitrimers, glycerol, DLP 3D printing

1. Introduction

The attention of polymeric materials researchers is turned towards non-recyclable and non-reshapable thermosets such as Bakelite as a challenge to develop cross-linked polymers that have controllable reprocessing due to dynamic covalent bonds that bridge the gap between thermoplastics and thermosets [1]. Dynamic covalent bonds are bonds with advantages over common covalent bonds as they split into reversible groups, which can be sufficiently reconstructed [2]. These dynamic bonds also provide unique

features such as self-healing, weldability, malleability, recyclability, and shape memory properties for polymeric materials [3]. The most recently studied vitrimers based on dynamic covalent bonds are epoxy-based, relying on reversible transesterification reactions [4]. A self-healing property allows repair of cracks and defects, as well as due to weldability, polymeric materials can have complex design from several parts, which also contributes to recyclability by promoting sustainable resource management and decreasing costs [5]. Many reversible reactions, such

*Corresponding author, e-mail: jolita.ostrauskaite@ktu.lt
© BME-PT

as transamination, boronic esters-based exchanges, urethane reversion, vinylogous urethane exchange, *etc.*, have been used to design dynamic covalent bonds [6], but the most widely studied is the thermoactivated transesterification reaction of hydroxyl and ester groups [7]. The first covalently cross-linked networks based on reversible transesterification exchange reactions were introduced by Leibler and coworkers and were termed ‘vitrimers’ as they behave like vitreous silica and rearranged their topology without depolymerization, as well as being insoluble and reprocessable [8]. Vitrimers demonstrate two glass transition temperatures T_g and T_v [9]. Below T_v (topology freezing temperature), vitrimers behave as permanently cross-linked thermosets, and above T_v , exchange reactions within their network accelerate, making viscoelastic flow possible, following the Arrhenius law [10, 11]. T_g can be controlled by changing the composition of the resin [12], while T_v occurs due to reversible reactions and can be controlled by changing the transesterification catalyst and its concentration [9]. The catalysts most commonly used for vitrimer synthesis are organometallic complexes and organic bases, such as triazabicyclodecene and zinc acetylacetonate hydrate ($Zn(acac)_2$) [13, 14]. However, these catalysts have poor solubility, which can be a drawback for the optical 3D printing process. Schlögl and co-workers have introduced organic phosphates and phosphonates as transesterification catalysts that were soluble in acrylate monomers and allowed efficient stress relaxation of the materials at higher temperatures, which is important for the reshaping and repair of 3D printed objects [15–17].

In the last five years, an increase in scientific publications with biobased vitrimers has been observed. Functionalized triglycerides, lignin, vanillin, tannin, polysaccharides, and furan derivatives have already been used as monomers for various vitrimer synthesis reactions [6]. This attracts the attention of the vitrimer researchers to the need to develop new biobased monomers for the synthesis of high-performance and sustainable materials. Biodiesel production from vegetable oils and animal fats generates approximately 10% (w/w) of glycerol as the main by-product, which has been used as a starting material for the synthesis of various glycerol-based monomers [18]. Glycerol is a low volatile, non-toxic, hygroscopic monomer compatible with a wide range of materials, miscible monomer with plasticizing effect [19]

and has even been used to produce biodegradable plastics already [20–22], which is attractive for vitrimer synthesis. Commercially available glycerol-based monomers, such as 2-hydroxy-2-phenoxypropyl acrylate (HPPA), glycerol 1,3-diglycerolate diacrylate, 3-(acryloyloxy)-2-hydroxypropyl methacrylate, have been used for the synthesis of vitrimers by optical 3D printing since they have hydroxyl and ester groups which are essential for transesterification reactions [15–17, 23, 24]. The obtained vitrimers had shape memory and self-healing properties, and were reprocessable. However, these glycerol monomers were cross-linked mainly with petroleum-based monomers. Moreover, the lack of bio-based resins suitable for digital light processing (DLP) 3D printing of vitrimers led to the development of a novel vitrimer based on glycerol and soybean oil for DLP 3D printing. At the same time, the novel plant-based resins offer a high renewable carbon content and can be used for various optical lithography setups enabling 3D printing on multiple scales [25]. Vegetable oils and their derivatives, such as fatty acids, have been used for vitrimer synthesis, because their price is low, they are easily modifiable, and vitrimers can have properties such as flexibility, resistance to chemicals, low toxicity, and biodegradability [26–30]. Most of the time, epoxidized vegetable oils with carboxylic acids were used for vitrimer synthesis, as carboxylic acid groups act as catalysts for transesterification [31–34]. Acrylated epoxidized soybean oil (AESO) was thermally cross-linked with a dithiol with a boronic ester linkage as a dynamic bond [11]. The synthesized vitrimer was prepared by an environmentally friendly strategy and had self-healing and reprocessability properties.

The aim of this work was to develop and investigate new vitrimers based on glycerol and soybean oil suitable for optical 3D printing. Vitrimers were synthesized using an environmentally friendly strategy by mixing the monomers at different ratios with a photoinitiator and transesterification catalyst and applying irradiation under solvent-free conditions. 2-Hydroxy-2-phenoxypropyl acrylate (HPPA) (Figure 1) was chosen as a monomer as has the glycerol fragment in the structure with hydroxyl and ester groups that are essential for the transesterification reaction. Acrylated epoxidized soybean oil (AESO) was chosen as a cross-linker because of the functional groups of hydroxyl and ester and is reported here for the first time in UV-curable resins for the synthesis of vitrimers.

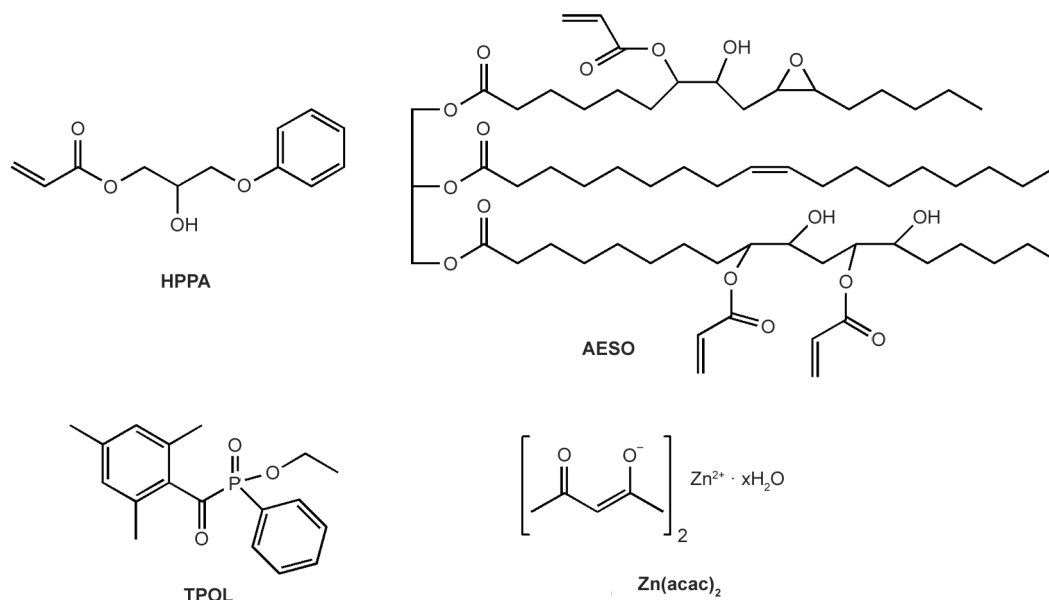


Figure 1. Chemical structures of 2-hydroxy-2-phenoxypropyl acrylate (HPPA), acrylated epoxidized soybean oil (AESO), ethyl(2,4,6-trimethylbenzoyl) phenylphosphinate (TPOL) and zinc acetylacetonate hydrate ($\text{Zn}(\text{acac})_2$).

Ethyl(2,4,6-trimethylbenzoyl) phenylphosphinate (TPOL) was used as a photoinitiator as allows to get transparent coatings due to the photobleaching effect [35, 36]. Zinc acetylacetonate hydrate ($\text{Zn}(\text{acac})_2$) was used as a transesterification catalyst, which is one of the most commonly used catalysts and is soluble in the selected acrylate monomers. The rheological properties and photocuring kinetics of the resins based on glycerol and soybean oil were monitored for the first time. The experiments showed the influence of the amount of functionalized glycerol monomer on the viscosity and rheological properties. AESO was found to be a suitable cross-linker in the UV-curing reactions with HPPA because after UV-curing, the dynamic networks were able to rapidly undergo thermoactivated rearrangements of the network topology, as shown by stress relaxation experiments. Incorporation of AESO in the resins with HPPA led to self-healing, shape memory properties, reprocessability, and recyclability. The novel resin based on glycerol and soybean oil was used to form vitrimeric 3D structures by DLP 3D printing.

2. Experimental

2.1. Materials

2-Hydroxy-2-phenoxypropyl acrylate (HPPA, $\geq 80\%$), soybean oil, epoxidized acrylate (AESO, $\leq 100\%$), and zinc acetylacetonate hydrate ($\text{Zn}(\text{acac})_2$, $\leq 100\%$) were purchased from Merck, Darmstadt, Germany. Ethyl(2,4,6-trimethylbenzoyl) phenylphosphinate (TPOL, $>95\%$) was purchased from Fluorochem,

Hadfield, Derbyshire, United Kingdom. All chemicals were used as received.

2.2. Preparation of UV-curable resins

The resins were prepared by dissolving 5 mol% of transesterification catalyst $\text{Zn}(\text{acac})_2$ in HPPA at 70°C . After the resin was cooled down to room temperature, different amounts of AESO and 3 mol% of TPOL were added as the photoinitiator with respect to the total amount of both monomers and stirred at room temperature. The resin codes consist of a number that expresses the amount of HPPA (0–100 wt%) and the abbreviation of 2-hydroxy-2-phenoxypropyl acrylate (HPPA), e.g., 9HPPA is a resin with the weight ratio of 9:1 of monomer HPPA and cross-linker AESO. 9HPPAV is a post-cured vitrimer at 200°C for 4 h.

The viscosity of the resins based on glycerol and soybean oil was measured with an Anton Paar rheometer MCR302 (Graz, Austria) with a plate/plate accessory (15 mm diameter of the top plate) using a shear rate of 0.001 to 50 s^{-1} at 25°C .

Resins were cross-linked in a Teflon mold of size of $(70 \times 10 \times 1) \pm 0.01$ mm under a 500 W Helios Italquartz GR.E UV lamp (Milano, Italy) at a wavelength of 250–450 nm and an intensity of $310\text{ mW} \cdot \text{cm}^{-2}$ for 2 min until a solid polymer was obtained.

2.3. Characterization techniques

The photocuring kinetics of the resins was studied using an Anton Paar MCR302 (Graz, Austria)

Table 1. Composition of resins based on glycerol and soybean oil.

Resin	Amount of HPPA [wt%]	Amount of AESO [wt%]	Amount of TPOL [mol%]	Amount of Zn(acac) ₂ [mol%]	Viscosity [mPa·s]
0HPPA	–	100	3	5	2486±240
1HPPA	10	90			11650±137
2HPPA	20	80			7969±135
3HPPA	30	70			6210±66
4HPPA	40	60			3998±35
5HPPA	50	50			1885±14
6HPPA	60	40			1633±3
7HPPA	70	30			1403±29
8HPPA	80	20			423±11
9HPPA	90	10			332±7
10HPPA	100	–			184±4

rheometer with plate/plate accessory and the Omni-Cure S2000 curing system from Lumen Dynamics Group Inc. (Mississauga, Ontario, Canada). The diameter of the bottom glass plate and the top steel plate was 38 and 15 mm, respectively. The tests were carried out at a temperature of 25 °C and a resin thickness of 0.1 mm. The resins were irradiated with UV/VIS radiation with a wavelength of 250–450 nm and an intensity of 9.3 W·cm⁻² through a bottom glass plate. A shear test was performed using a frequency of 10 Hz and a strain of 0.5%. The values of the storage modulus G' , loss modulus G'' , and the complex viscosity η^* of the resins were determined after 120 s of irradiation. The gel point t_{gel} was identified as the crossover point of the G' and G'' modulus curves. The shrinkage was defined as the difference between the gap before and after photocuring.

Fourier transformation infrared (FT-IR) reflection spectra were recorded using a Spectrum BX II FT-IR spectrometer (Perkin Elmer, Llantrisant, UK) in the wavenumber range of (650–4000) cm⁻¹.

The insoluble fraction was determined by extracting polymer samples (0.2 g) with acetone for 24 h in a Soxhlet extractor. The samples were dried until a constant weight was reached, and the yield of the insoluble fraction was calculated as the ratio between the weight of the polymer before and after extraction and drying.

The elongation at break, tensile strength, and elastic modulus was estimated by a tensile test on a Testometric M500-50CT machine (Testometric Co Ltd, Rochdale, UK) with HDFF100 grips according to the standard ISO 527-3. Samples with dimensions of (70×10×1)±0.01 mm were tested with a crosshead speed of 5 mm·min⁻¹. Average values were calculated from 5 parallel measurements. The variation in

the experimental results did not exceed 5% within the group.

The topology freezing temperature (T_v) was determined by stress relaxation experiments on an MCR302 rheometer from Anton Paar (Graz, Austria). The samples were equilibrated with the selected measurement temperature (140–200 °C) for 20 min and a 5% step strain was applied and the decreasing stress was recorded over time.

The glass transition temperature (T_g) was determined by dynamic mechanical thermal analysis (DMTA) with an Anton Paar MCR302 rheometer (Graz, Austria). Samples with dimensions of (10×10×1)±0.01 mm were tested in a shear mode from -20 to 130 °C at a rate of 2 °C·min⁻¹. T_g was defined as the maximum of the tan δ curve peak.

The thermal stability of the polymers was determined with a Perkin–Elmer TGA 4000 thermogravimetric analyzer (TGA) (Llantrisant, UK) with a heating rate of 20 °C·min⁻¹ and a nitrogen flow rate of 100 ml·min⁻¹.

2.4. DLP 3D printing

DLP 3D printing was performed on an Asiga PICO2 39 UV (Sydney, Australia) printer with a 385 nm LED UV light source. The first layer of 220 μ m was exposed for 8 s and the other layers with a height of 100 μ m were irradiated for 1 s. The structures of ‘Benchy’ and ‘Marvin’ were printed as they are specifically designed to test the accuracy and capabilities of 3D printers and photo-resins [25].

2.5. Self-healing experiments

UV-cured samples with (70×10×1)±0.01 mm dimensions were cut into two equal pieces, then brought in contact with each other, and heated at 200 °C for

1 h. Rejoined samples were mechanically tested with a Testometric M500-50CT machine (Testometric Co Ltd, Rochdale, UK).

The scratch repairing tests were performed by scratching the UV-cured vitrimer sample with a razor blade and curing at 200 °C for 1 h and monitoring with an Olympus BX41 optical microscope (Microscope Central, Feasterville, PA, USA).

2.6. Shape memory experiments

For shape memory experiments, the ‘butterfly’ sample ($27 \times 18 \times 1 \pm 0.01$ mm) was prepared by DLP printing of the 9HPPA resin on an Asiga PICO2 39 UV printer (Sydney, Australia). Two-way shape memory experiments were carried out with a UV-cured sample with the dimensions of ($70 \times 10 \times 1 \pm 0.01$ mm) and a ‘butterfly’ sample. The first shape was obtained by heating the sample at 80 °C (above T_v), transforming it into the desired shape, and cooling it to 40 °C (above T_g). The second shape was obtained by heating the sample at 80 °C (above T_v) due to transforming and cooling the sample below room temperature with an ice bath. By heating again, the permanent shape was regained.

The shape recovery ratio was calculated as the ratio between the lengths of the polymer in different stages of shape memory [37]. First, the sample was heated at 80 °C (above T_v) and elongated by applying force. When in the fixing stage, the sample was cooled down to room temperature with the load applied and the tensile load was released. Finally, the deformed sample was heated to 80 °C to allow the length to recover (Equation (1)).

$$RR = \frac{L_f - L}{L_f - L_0} \cdot 100 \quad (1)$$

where RR is the shape recovery ratio [%], L_0 is the original sample length [cm], L_f is the length of the sample in the fixing stage when the tensile load is released [cm], L is the length of the sample in the recovery stage when heated at 80 °C [cm].

2.7. Recyclability experiments

The chemical degradable property was tested by immersing the samples (0.1 g) in vials with ethylene glycol (5 ml) at 200 °C. Samples were taken every hour, dried and weighed. The relative weight was calculated as the difference between the mass before and after degradation.

2.8. Reprocessability experiments

The UV-cured samples were ground into a fine powder, placed between stainless steel plates with a size of ($400 \times 400 \pm 0.01$ mm) (Labtech Engineering Company Ltd, Thailand) and heated at 180 °C for 1 h at a pressure of 5 MPa. After being cooled to room temperature, the recycled samples were trimmed into a rectangular shape of ($70 \times 10 \times 1 \pm 0.01$ mm). The remolded samples were mechanically tested with a Testometric M500-50CT machine (Testometric Co Ltd, Rochdale, UK). Average values were calculated from 5 parallel measurements. The variation in the experimental results did not exceed 5% within the group.

3. Results and discussions

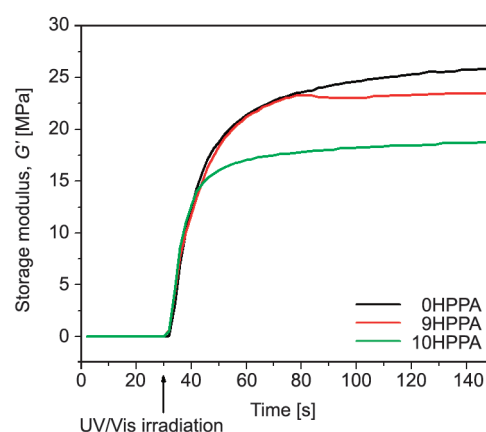
3.1. Selection of the resin for vitrimer synthesis

The rheological parameters are important in the optical 3D printing process as they describe the curing rate, viscosity, and shrinkage when the resin transits from liquid to solid, and the rigidity of the final 3D printed object [38]. Thus, real-time photorheometry is now being investigated as a tool for understanding the behavior of the resin during the curing process. Viscosity determines the capacity of the resin to renew the feedstock material once the platform moves to form a new layer, and conventional 3D printing resins generally have a viscosity in the range of (200–1500) mPa·s [39]. While the viscosity determined for the glycerol and soybean oil-based resins was in the range of (184–24 862) mPa·s (Table 1) and was reduced with increasing the amount of HPPA. Importantly, the viscosities of the resins showed no significant changes after 3 months of storage in the dark. Rheological parameters such as the storage modulus (G'), the loss modulus (G''), the complex viscosity (η^*), and the shrinkage of the glycerol and soybean oil-based resins are collected in Table 2. The G' modulus of 0HPPA containing only AESO was 26.57 MPa and the G' modulus of 10HPPA containing only HPPA was 19.35 MPa, while the values of the other resins were similar to that of 9HPPA and no significant influence related to the amount of HPPA was observed. This was due to the plastification effect of HPPA that predetermined that the G' modulus that corresponds to the rigidity of 10HPPA was the lowest. Although the G'' modulus, which corresponds to the energy dissipated as heat, representing

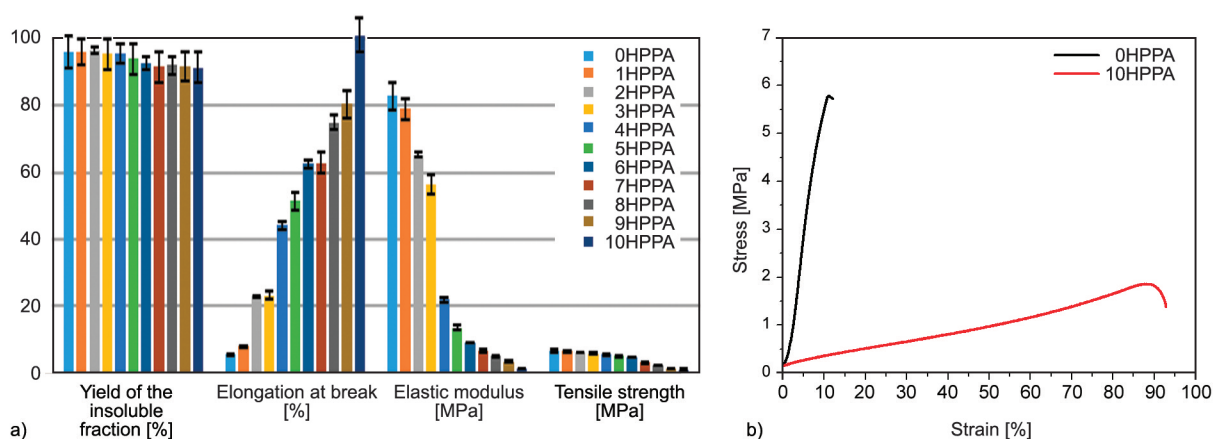
Table 2. Real-time photorheometry data of glycerol- and soybean oil-based resins.

Resin	Storage modulus, G' [MPa]	Loss modulus, G'' [MPa]	Complex viscosity, η^* [MPa·s]	Shrinkage [%]
0HPPA	26.57±2.19	4.87±0.85	0.45±0.01	3.0±0.0
1HPPA	23.85±2.95	6.19±2.18	0.39±0.05	6.5±0.5
2HPPA	27.60±1.10	8.36±0.63	0.46±0.01	6.5±0.5
3HPPA	25.45±1.25	6.39±0.18	0.42±0.02	7.5±0.5
4HPPA	25.60±0.60	11.23±2.48	0.45±0.01	7.5±0.5
5HPPA	23.75±0.65	12.40±0.40	0.43±0.01	9.5±1.0
6HPPA	22.10±0.60	11.30±0.60	0.40±0.01	6.5±0.5
7HPPA	23.45±0.85	12.90±1.20	0.35±0.00	7.5±0.5
8HPPA	24.40±1.30	14.20±4.41	0.46±0.02	6.5±0.5
9HPPA	23.25±1.55	13.34±3.56	0.43±0.01	6.5±0.5
10HPPA	19.35±0.45	16.00±2.00	0.40±0.02	7.5±0.5

the viscous part [38] showed the opposite results, as the resin 10HPPA had the highest G'' modulus of 16 MPa. η^* values which represent the resistance to flow as a function of the angular frequency of all resins based on glycerol and soybean oil were in the same range (0.35–0.45 mPa·s), while the shrinkage of the resin 10HPPA (7.5%) resin was greater compared to the AESO resin 0HPPA (3.0%) due to the lower viscosity and the tgel values did not influence since the gelation of all resin began after 2 s of irradiation. Based on data from the published literature, resins for vitrimer synthesis by optical 3D printing frequently consist of the ratio of 9:1 from the monomer and the cross-linker [23, 24], therefore, the storage modulus G' describes the rigidity versus the irradiation time of resins without HPPA (0HPPA), with 90 wt% of HPPA (9HPPA), and without AESO (10HPPA) are presented in Figure 2. The resin 9HPPA exhibited the intermediate G' modulus value after 2 min of irradiation (23.25 MPa).

**Figure 2.** Curves of the storage modulus G' versus irradiation time of resins without HPPA (0HPPA), with 90 wt% of HPPA (9HPPA), and without AESO (10HPPA).

Tensile testing and extraction of polymer samples were performed to investigate the mechanical properties and the yield of the insoluble fraction of the UV-cured resins (Figure 3). Polymer rigidity is

**Figure 3.** Yield of the insoluble fraction and mechanical characteristics of the polymers based on glycerol and soybean oil (a) and stress-strain curves of the polymers 0HPPA and 10HPPA (b).

important when planning applications in the industry, and rigid as well as flexible polymers are used in various areas depending on the needs of the 3D printed structure. The HPPA monomer with the glycerol fragment was determined to act as a plasticizer [19] as it lowered the values of tensile strength, elastic modulus, of the insoluble fraction and increased the values of elongation at break. The polymer yield having the highest amount of HPPA had the lowest values of tensile strength, yield of the insoluble fraction and elastic modulus (1.39 MPa, 91.79% and 3.45 MPa) and the highest value of elongation at break (80.47%).

After evaluation of the rheological and mechanical characteristics of the polymers, it was decided to select the resin 9HPPA for vitrimer synthesis with the lowest amount of AESO and the highest amount of HPPA, which ensures the highest amount of hydroxyl and ester groups that are beneficial for transesterification reactions. Furthermore, the viscosity of the resin (332 mPa·s) (Table 1) was suitable for the formation of 3D structures using DLP. The chemical structure of the 9HPPA uncured, photocured, and thermally post-cured resin at 200 °C was confirmed by FT-IR spectroscopy (Figure 4). The intensities of the OH and C=O groups at 3434 and 1732 cm⁻¹ remain constant in the photocured polymer spectrum in comparison with the spectra of the uncured resin, which is essential for the transesterification reaction. The intensity of the C=C group signal, which was present at 1599 cm⁻¹ was reduced after photopolymerization. After post-curing at 200 °C, a decrease in OH groups was observed due to hydrogen bonding formation. Stress relaxation experiments were performed to determine the topology freezing temperature (T_v) of the resin 9HPPA. The thermal properties

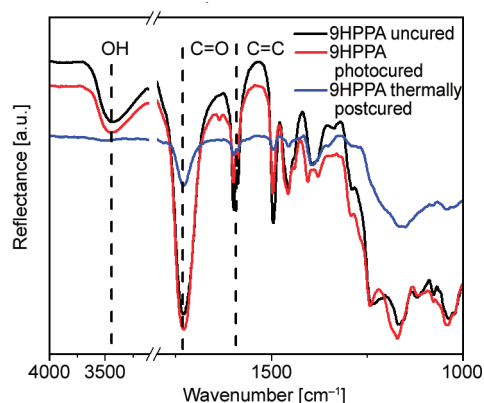


Figure 4. FTIR spectra of the uncured, photocured, and thermally postcured resin 9HPPA.

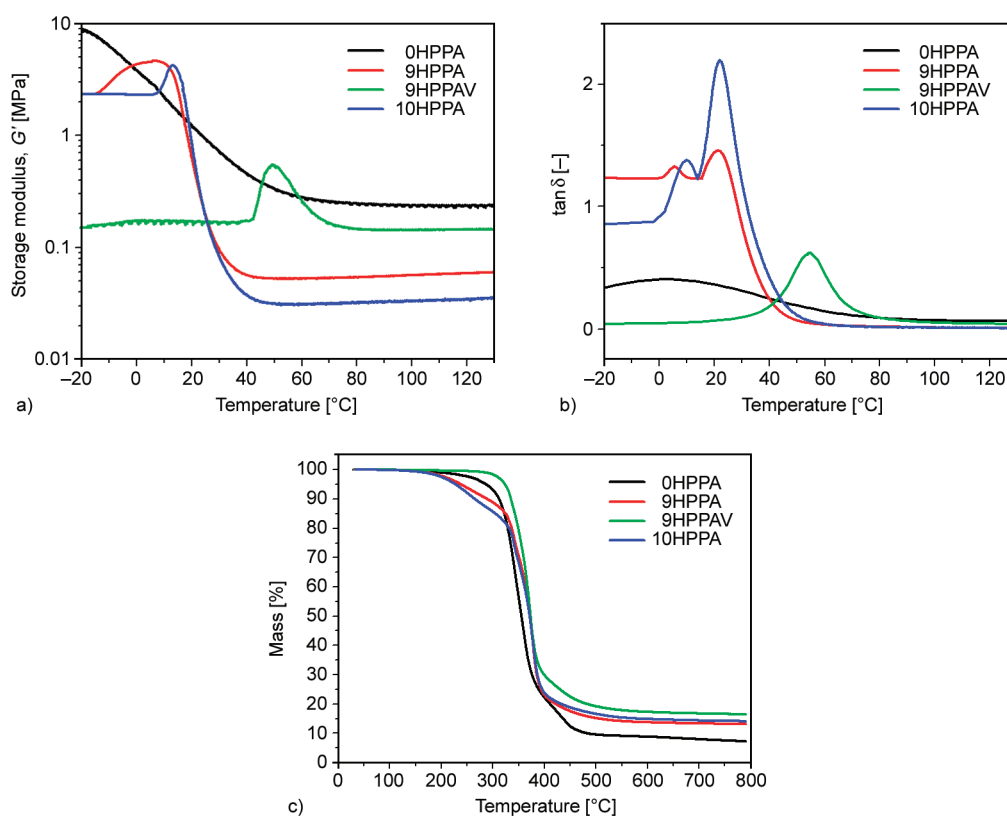
of the polymer 9HPPA and the post-cured vitrimer 9HPPAV at 200 °C were compared with the neat AESO polymer and the neat HPPA polymer (0HPPA and 10HPPA, respectively). Vitrimeric abilities, such as shape memory, self-healing, recycling, and reprocessing properties, were investigated.

3.2. Thermal properties

The thermal characteristics obtained by DMTA and TGA analysis of polymers based on glycerol and soybean oil are summarized in Table 3. The thermal properties of the UV-cured polymer 9HPPA were compared with the polymer 0HPPA only with the fragments of AESO in the structure, polymer 10HPPA containing the fragments of HPPA, and the vitrimer 9HPPAV, which was obtained by post-curing the 9HPPA at 200 °C for 4 h. The incorporation of HPPA into the network led to the obtainment of the polymer with a higher T_g temperature (23 °C) compared to the polymer with flexible AESO chains (0 °C). However, the highest values of T_g , G_r , $T_{dec-10\%}$, and char yield (53 °C, 0.15 MPa, 335 °C, and 16.5%, respectively) were obtained when the UV-cured 9HPPA polymer was post-cured at 200 °C. This was due to the highest yield of the insoluble fraction (99.5%) after extraction with acetone, which was chosen as a solvent due to its ability to dissolve both polar and minor polar substances, while other solvents can only dissolve one or the other [40]. The curves of the storage modulus G' versus temperature obtained from the DMTA analysis are presented in Figure 5a. It can be seen that the UV-cured polymer 10HPPA has a peak at about 20 °C meaning that the monomer HPPA provides crystallinity to the network due to the presence of benzene rings [41], however, the polymer is more amorphous as it gradually softened and did not melt with increasing temperature. Although glycerol is one of the most studied glass formers, it also has an extremely low tendency to crystallize [42]. The more clearly apparent peak can be seen in the curve of post-cured vitrimer 9HPPAV and the G' modulus remained the same as the temperature increased, meaning the network of vitrimer is more semicrystalline when amorphous with more uniformly packed molecules. Two peaks have been observed in the curves of $\tan\delta$ versus temperature (Figure 5b). The lower temperature peak contributes to the β -relaxation process observed below T_g , which is associated with the polymer backbone and involves local motions of the polymer chain backbone that do not

Table 3. Yield of the insoluble fraction, thermal, and thermomechanical characteristics of polymers.

Polymer	The yield of the insoluble fraction ¹ [%]	DMTA		TGA	
		T_g^2 [°C]	$G_r'^3$ [MPa]	$T_{dec-10\%}^4$ [°C]	Char yield ⁵ [%]
0HPPA	96.3±0.2	0	0.24	312	7.3
9HPPA	91.8±0.1	23	0.06	289	13.1
9HPPAV	99.5±0.8	53	0.15	335	16.5
10HPPA	91.4±0.2	23	0.04	265	14.1

¹After 24 h of Soxhlet extraction with acetone,²Glass transition temperature determined by DMTA,³Storage shear modulus of cured resins in the rubbery plateau region,⁴Temperature at a weight loss of 10% obtained from TGA curves,⁵From TGA curves.**Figure 5.** Curves of the storage modulus G' versus temperature (a), curves of $\tan \delta$ versus temperature (b), and thermogravimetric curves of polymers based on glycerol and soybean oil (c).

require cooperative motion of the surrounding chains and is a precursor for the primary α -relaxation process (T_g) [43]. The thermal decomposition of the UV-cured polymer 9HPPA proceeded in two steps, while the thermal degradation of the vitrimer 9HPPAV proceeded in one step (Figure 5c), which confirmed a densely cross-linked network.

3.3. Relaxation of the stress of the vitrimer

Thermosets have permanent covalent bonds in their network, which leads to difficulties in stress relaxation. While vitrimers with dynamic bonds can rearrange the network and alleviate the relaxation of

internal stress caused by deformation [44]. Therefore, topology rearrangements were investigated by measuring the stress relaxation of sample 9HPPA (Figure 6) and a topology freezing transition temperature (T_v) was determined at which the transition from viscoelastic solid to viscoelastic liquid occurs. Stress relaxation experiments were carried out at temperatures (160–200 °C) and thermal degradation was avoided, as the thermal stability of the 9HPPA sample is above 200 °C (Figure 5c). The relaxation time (τ^*) is the time the modulus relaxes to 1/e of its value [45]. With increasing temperature, the relaxation time of the 9HPPA decreased from 172.45 to 11.5 min

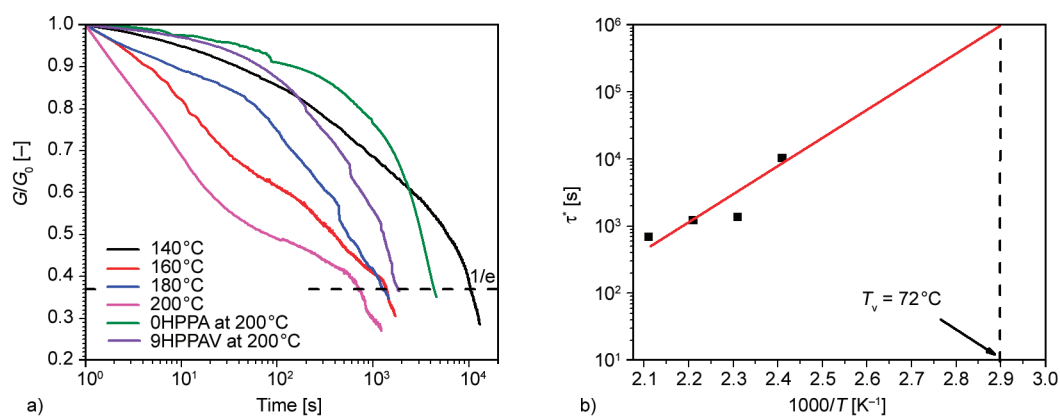


Figure 6. Stress relaxation curves versus the time of 9HPPA, 0HPPA, and the 9HPPAV (a) and Arrhenius plot of relaxation times (b).

due to dynamic bond exchange and chain diffusion. The relaxation time of 0HPPA at 200°C was 71.12 min, which shows that more ester groups need more time to relax. Furthermore, 9HPPAV at 200°C needed 30.18 min to relax, which is more compared to photocured 9HPPA showing the additional formation of hydrogen bonds during curing at 200°C that results in a decrease in OH groups that could not participate in transesterification reactions (Figure 4). The topology freezing temperature (T_v) can be determined from the Arrhenius curves for relaxation times of 10^6 s [9]. Therefore, the T_v value of 9HPPA was obtained by extrapolating the data to a relaxation time of 10^6 s and was 72°C (Figure 6b).

3.4. DLP 3D printing and shape memory properties

DLP 3D printing has advantages such as high resolution and accuracy, good surface finish, high fabrication speed, and is attractive for the formation of objects that need to have the mentioned properties [46]. Therefore, the accurate structures ‘Benchy’ and ‘Marvin’ with small details and smooth surface finishing were formed to show the suitability of the resin 9HPPA for DLP 3D printing (Figure 7a).

Two-way shape memory polymers can be used in the application of reversible actuation as artificial muscles and actuators, as they can transit between two different shapes spontaneously and reversibly when heating or cooling is applied [47]. Flexible AESO chains and free hydroxyl groups of the UV-cured polymer 9HPPA provide plasticity that could impart shape memory properties [48]. Therefore, the two-way shape memory cycle of the DLP 3D printed ‘butterfly’ sample and the UV-cured rectangular sample is shown in Figures 7b and 7c. The procedure

consisted of transforming the samples above T_v and fixing above and below T_g . The permanent shape of the printed and UV-cured samples was changed by heating above T_v at 80°C and applying the external force for deformation. The first shape was fixed by cooling the sample down above T_g to 40°C . The second shape of a ‘butterfly’ was obtained by cooling down the sample below T_g to 0°C and fixing the wings to the desired shape. The rectangular shape obtained the second desired ‘spiral’ shape only by transforming at above T_v and cooling down the sample below T_g . After being heated above the T_v , the samples completely recovered to the permanent shape, indicating an excellent shape memory property. Both the UV-cured rectangular and DLP 3D printed ‘butterfly’ sample showed a shape recovery ratio (RR) of 100% meaning that the samples are able to recover their original length.

3.5. Self-healing properties

To investigate the self-healing properties of vitrimer 9HPPAV, the UV-cured sample 9HPPA was cut and rejoined at 200°C for 1 h, and the stress-strain curves of the samples are presented in Figure 8. Mechanical properties were improved after a thermal treatment, indicating excellent repairability and weldability of the cured sample. The elastic modulus of the thermally treated sample 9HPPAV was 134 MPa, which is 38 times higher compared to the UV-cured sample 9HPPA, and elongation at break was reduced by approximately 3 times to 30%. This was due to topological rearrangements and additional formation of hydrogen bonding during prolonged treatment at 200°C that resulted in a decrease in OH groups (Figure 4). Scratch-repairing test was performed to verify the repairability as self-healing of the UV-cured sample

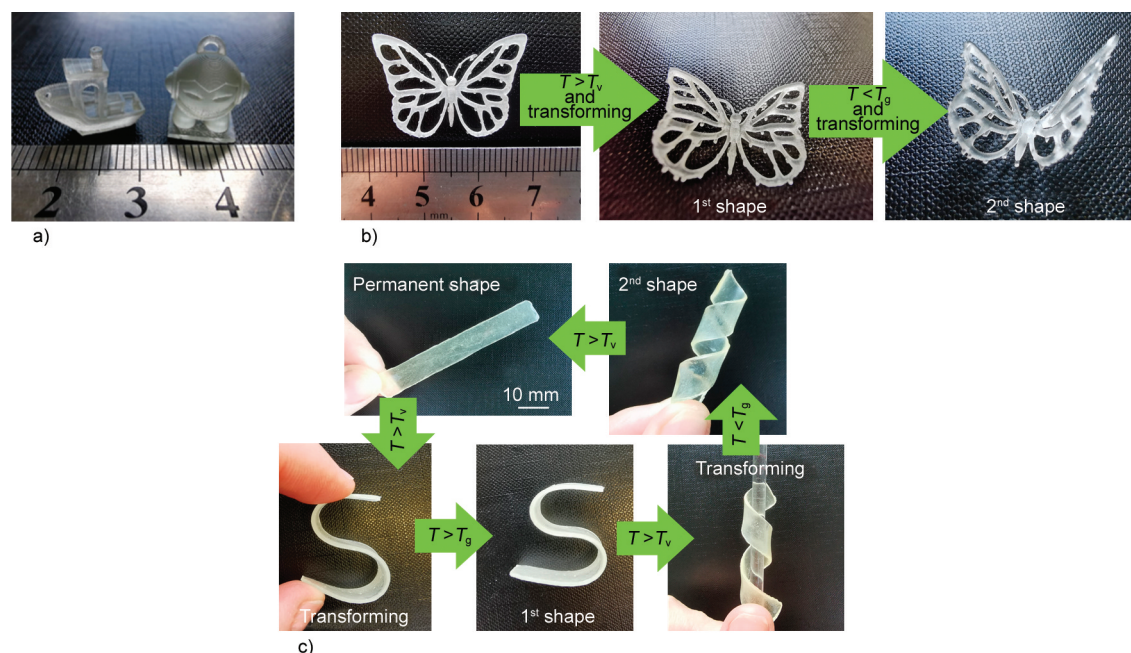


Figure 7. Photographs expressing DLP printing of ‘Benchy’ and ‘Marvin’ structures (a) and monitoring the shape memory behavior of 9HPPA: of DLP printed ‘butterfly’ sample (b) and UV-cured rectangular sample (c).

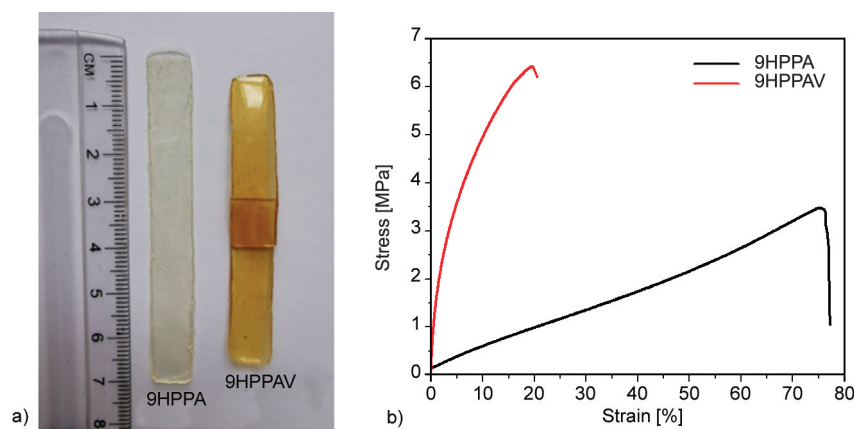


Figure 8. Photograph (a) and stress-strain curves (b) of the UV-cured 9HPPA sample and the vitrimer 9HPPAV after repair at 200 °C for 1 h.

9HPPA at high temperatures should occur due to dynamic transesterification reactions. Images of the scratched UV-cured sample 9HPPA with a razor blade and repaired at 200 °C for 1 h are shown in Figure 9. Self-healing with an efficiency of 47% was obtained as the ratio between the width of the repaired sample and the width of the initial sample. The sufficiently low T_g value provided active chain mobility at a temperature of 200 °C [44].

3.6. Recyclability

Polymeric products need to be degraded after the end of their use when they do not have useful properties. This would reduce the negative impact on environmental health, which is the main idea of green chemistry and chemical engineering [49]. The chemical

recycling of thermosets into soluble products is usually carried out by catalysis at high temperatures using pressure to recycle the network [50]. While the chemical recycling of vitrimers at elevated temperatures is carried out more simply through alcoholysis due to dynamic bond exchange reactions [13]. Therefore, the chemical degradation of the sample 9HPPA was performed with ethylene glycol (Figure 10a) and the curve of weight loss of 9HPPA versus temperature is presented in Figure 10b. After recyclability testing, the color of ethylene glycol changed from transparent to brown and the 9HPPA sample shrank, indicating that the transesterification reaction between the ester bonds of the sample 9HPPA and hydroxyl groups of ethylene glycol occurred as the cross-linked network was deconstructed and the

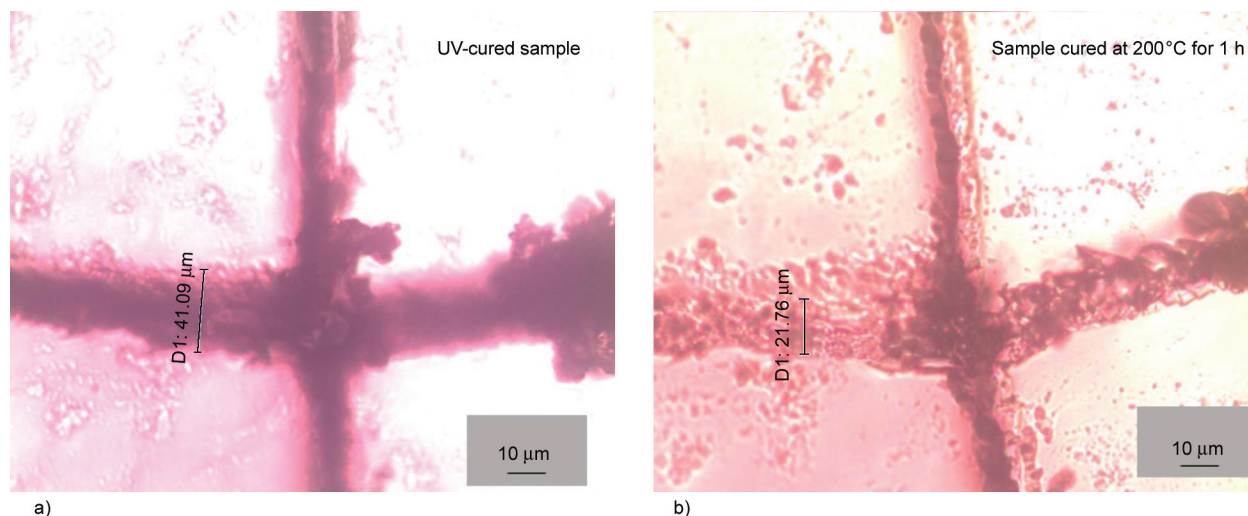


Figure 9. Scratch repair images of the UV-cured sample 9HPPA. a) UV-cured sample, b) Sample cured at 200°C for 1 h

degraded product was dissolved in ethylene glycol. The weight of the sample decreased rapidly to 50% during the first 6 h and gradually to 10% during the 17 h and stabilized. The permanent linkages of the sample had an impact on the residue after chemical degradation. The intensities of the OH, C=C and

C=O group signals at 3434, 1599 and 1732 cm^{-1} remained the same in the spectra of the sample 9HPPA residue after alcoholysis and dissolved in ethylene glycol, since the rearrangement of the cross-linked network occurred via dynamic transesterification (Figure 10c).

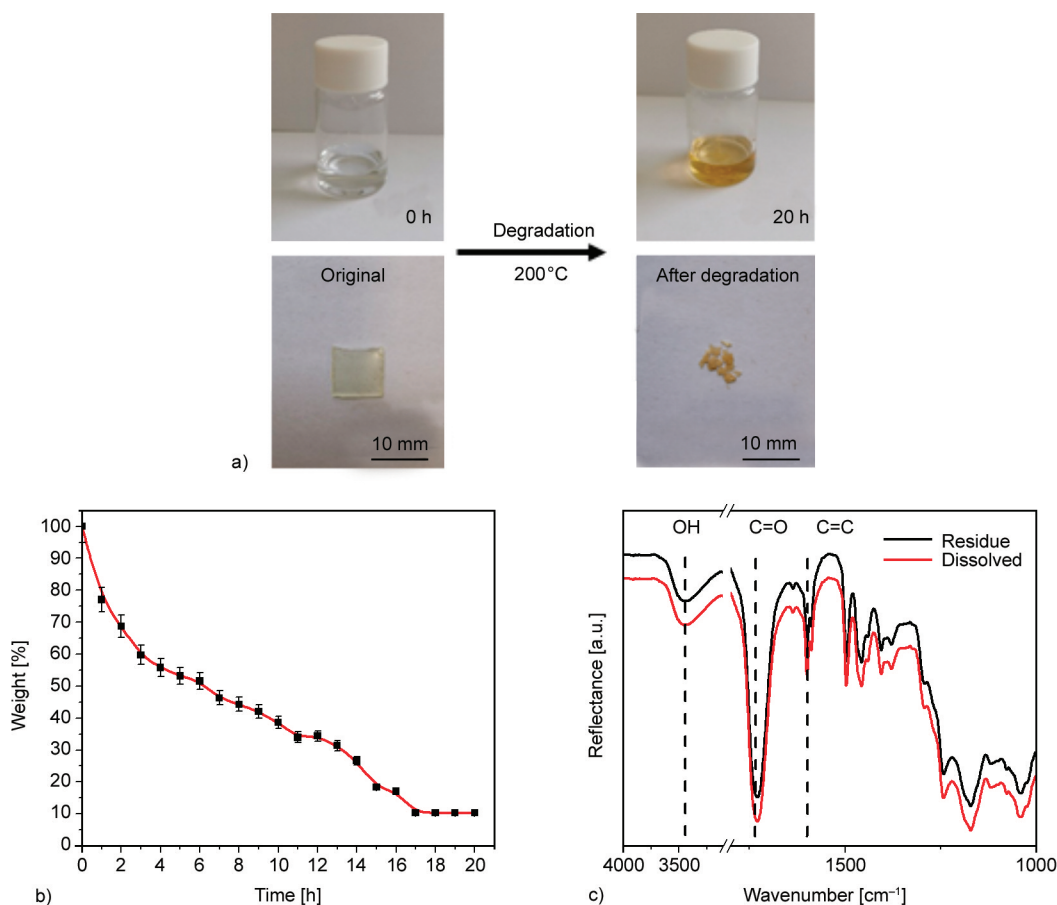


Figure 10. Photograph expressing the chemical degradation experiment (a), the weight loss of 9HPPA versus temperature (b), and the FTIR spectra of the sample residue after alcoholysis and dissolved in ethylene glycol (c).

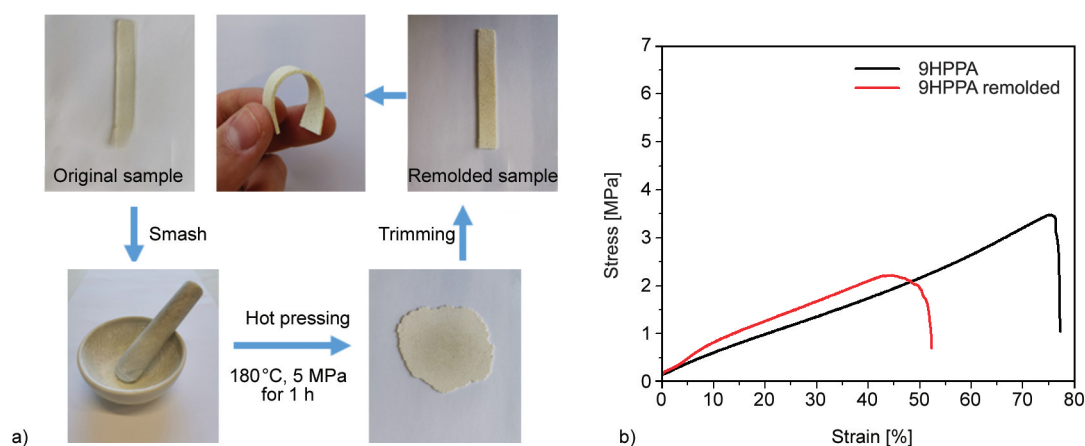


Figure 11. Photograph expressing the reprocessability experiment (a) and stress-strain curves of the UV-cured and remolded sample 9HPPA (b).

3.7. Reprocessability

To demonstrate the reprocessability of the UV-cured sample 9HPPA, the grounded fine powder was heated at 180 °C for 1 h under a pressure of 5 MPa and the remolded samples were obtained (Figure 11a). After reprocessing, the sample retained its elasticity. The stress-strain curves of the UV-cured sample 9HPPA and the remolded sample are shown in Figure 11b. The remolded sample exhibited a higher elastic modulus of 6.86 MPa compared to the original sample with an elastic modulus of 3.45 MPa. However, the sample could not be fully restored as it showed lower values of tensile strength and elongation at break compared to the original sample (0.43 MPa, 48.10% and 1.39 MPa, 80.47%, respectively). A recycling efficiency of 31% was calculated as the ratio of the tensile strength of the recycled and original samples.

4. Conclusions

Glycerol- and soybean oil-based resins were designed using an environmentally friendly strategy by mixing the monomers in different ratios with a photoinitiator and a transesterification catalyst and applying irradiation under solvent-free conditions. Acrylated epoxidized soybean oil was used in UV-curable resins for the synthesis of vitrimer for the first time. The resin containing the highest amount of functionalized glycerol was selected for the vitrimer synthesis and DLP 3D printing as a real-time photorheometric study showed that the rigidity and viscosity of the resins were reduced with increasing amount of glycerol-based monomer and the selected resin contained the highest amount of hydroxyl and ester groups that are beneficial for transesterification reactions. The dynamic network of UV-cured material showed stress

relaxation at elevated temperatures and a topology freezing temperature of 72 °C. Acrylated epoxidized soybean oil was found to be a suitable cross-linker in the UV-curing reactions with 2-hydroxy-2-phenoxypropyl acrylate as it led to reach shape memory, self-healing, reprocessability, and recyclability properties. Flexible chains of acrylated epoxidized soybean oil and free hydroxyl groups of the UV-cured sample imparted shape memory properties. Thermal and mechanical properties after vitrimer welding were improved due to the additional formation of hydrogen bonds during prolonged treatment at 200 °C. The synthesized vitrimer showed self-healing and reprocessability with an efficiency of 47 and 31 %, respectively, and was degraded by alcoholysis. The vitrimeric abilities of the synthesized vitrimer could contribute to recyclability and decrease production costs because the vitrimer could partially repair cracks and defects, change the permanent shape to the new one, and, because of weldability, could have a complex design from several parts. The synthesized vitrimer could be applied in reversible actuation as artificial muscles and actuators, where transits between two shapes are required.

Acknowledgements

This project has received funding from European Social Fund (project No. 09.9.9-LMT-K-712-23-0088) under grant agreement with the Research Council of Lithuania (LMTLT).

References

- [1] Guerre M., Taplan C., Winne J. M., du Prez F. E.: Vitrimers: Directing chemical reactivity to control material properties. *Chemical Science*, **11**, 4855–4870 (2020). <https://doi.org/10.1039/d0sc01069c>








- [2] Huang S., Kong X., Xiong Y., Zhang X., Chen H., Jiang W., Niu Y., Xu W., Ren C.: An overview of dynamic covalent bonds in polymer material and their applications. *European Polymer Journal*, **141**, 110094 (2020). <https://doi.org/10.1016/j.eurpolymj.2020.110094>
- [3] Zheng J., Png Z. M., Ng S. H., Tham G. X., Ye E., Goh S. S., Loh X. J., Li Z.: Vitrimers: Current research trends and their emerging applications. *Materials Today*, **51**, 586–625 (2021). <https://doi.org/10.1016/j.mattod.2021.07.003>
- [4] Memon H., Wei Y., Zhu C.: Recyclable and reformable epoxy resins based on dynamic covalent bonds – Present, past, and future. *Polymer Testing*, **105**, 107420 (2022). <https://doi.org/10.1016/j.polymertesting.2021.107420>
- [5] Alabiso W., Schlögl S.: The impact of vitrimers on the industry of the future: Chemistry, properties and sustainable forward-looking applications. *Polymers*, **12**, 1660 (2020). <https://doi.org/10.3390/polym12081660>
- [6] Lucherelli M. A., Duval A., Avérous L.: Biobased vitrimers: Towards sustainable and adaptable performing polymer materials. *Progress in Polymer Science*, **127**, 101515 (2022). <https://doi.org/10.1016/j.progpolymsci.2022.101515>
- [7] Winne J. M., Leibler L., du Prez F. E.: Dynamic covalent chemistry in polymer networks: A mechanistic perspective. *Polymer Chemistry*, **10**, 6091–6108 (2019). <https://doi.org/10.1039/c9py01260e>
- [8] Montarnal D., Capelot M., Tournilhac F., Leibler L.: Silica-like malleable materials from permanent organic networks. *Science*, **334**, 965–968 (2011). <https://doi.org/10.1126/science.1212648>
- [9] Capelot M., Unterlass M. M., Tournilhac F., Leibler L.: Catalytic control of the vitrimer glass transition. *ACS Macro Letters*, **1**, 789–792 (2012). <https://doi.org/10.1021/mz300239f>
- [10] Tellers J., Pinalli R., Soliman M., Vachon J., Dalcanale E.: Reprocessable vinylous urethane cross-linked polyethylene *via* reactive extrusion. *Polymer Chemistry*, **10**, 5534–5542 (2019). <https://doi.org/10.1039/C9PY01194C>
- [11] Zych A., Tellers J., Bertolacci L., Ceseracciu L., Marini L., Mancini G., Athanassiou A.: Biobased, biodegradable, self-healing boronic ester vitrimers from epoxidized soybean oil acrylate. *ACS Applied Polymer Materials*, **3**, 1135–1144 (2021). <https://doi.org/10.1021/acsapm.0c01335>
- [12] Freed K. F.: The descent into glass formation in polymer fluids. *Accounts of Chemical Research*, **44**, 194–203 (2011). <https://doi.org/10.1021/ar100122w>
- [13] Liu T., Zhao B., Zhang J.: Recent development of repairable, malleable and recyclable thermosetting polymers through dynamic transesterification. *Polymer*, **194**, 122392 (2020). <https://doi.org/10.1016/j.polymer.2020.122392>
- [14] Lossada F., Guo J., Jiao D., Groeer S., Bourgeat-Lami E., Montarnal D., Walther A.: Vitrimer chemistry meets cellulose nanofibrils: Bioinspired nanopapers with high water resistance and strong adhesion. *Biomacromolecules*, **20**, 1045–1055 (2018). <https://doi.org/10.1021/acs.biomac.8b01659>
- [15] Moazzen K., Rossegger E., Alabiso W., Shaukat U., Schlögl S.: Role of organic phosphates and phosphonates in catalyzing dynamic exchange reactions in thiol-click vitrimers. *Macromolecular Chemistry and Physics*, **222**, 2100072 (2021). <https://doi.org/10.1002/macp.202100072>
- [16] Rossegger E., Höller R., Reisinger D., Fleisch M., Strasser J., Wieser V., Griesser T., Schlögl S.: High resolution additive manufacturing with acrylate based vitrimers using organic phosphates as transesterification catalyst. *Polymer*, **221**, 123631 (2021). <https://doi.org/10.1016/j.polymer.2021.123631>
- [17] Rossegger E., Höller R., Reisinger D., Strasser J., Fleisch M., Griesser T., Schlögl S.: Digital light processing 3D printing with thiol–acrylate vitrimers. *Polymer Chemistry*, **12**, 639–644 (2021). <https://doi.org/10.1039/d0py01520b>
- [18] Yang F., Hanna M. A., Sun R.: Value-added uses for crude glycerol – A byproduct of biodiesel production. *Biotechnology for Biofuels*, **5**, 13 (2012). <https://doi.org/10.1186/1754-6834-5-13>
- [19] Monteiro M. R., Kugelmeier C. L., Pinheiro R. S., Batalha M. O., da Silva César A.: Glycerol from biodiesel production: Technological paths for sustainability. *Renewable and Sustainable Energy Reviews*, **88**, 109–122 (2018). <https://doi.org/10.1016/j.rser.2018.02.019>
- [20] Kasetaitė S., Ostrauskaitė J., Gražulevičienė V., Svedienė J., Bridziuvienė D.: Photocross-linking of glycerol diglycidyl ether with reactive diluents. *Polymer Bulletin*, **72**, 3191–3208 (2015). <https://doi.org/10.1007/s00289-015-1461-x>
- [21] Kasetaitė S., Ostrauskaitė J., Gražulevičienė V., Bridziuvienė D., Rainosaló E.: Biodegradable glycerol-based polymeric composites filled with industrial waste materials. *Journal of Composite Materials*, **51**, 4029–4039 (2017). <https://doi.org/10.1177/0021998317697809>
- [22] Kasetaitė S., Ostrauskaitė J., Gražulevičienė V., Bridziuvienė D., Budreckienė R., Rainosaló E.: Biodegradable photocross-linked polymers of glycerol diglycidyl ether and structurally different alcohols. *Reactive and Functional Polymers*, **122**, 42–50 (2018). <https://doi.org/10.1016/j.reactfunctpolym.2017.11.005>
- [23] Zhang B., Kowsari K., Serjouei A., Dunn M. L., Ge Q.: Reprocessable thermosets for sustainable three-dimensional printing. *Nature Communications*, **9**, 1831 (2018). <https://doi.org/10.1038/s41467-018-04292-8>

- [24] Li H., Zhang B., Wang R., Yang X., He X., Ye H., Cheng J., Yuan C., Zhang Y-F., Ge Q.: Solvent-free up-cycling vitrimers through digital light processing-based 3D printing and bond exchange reaction. *Advanced Functional Materials*, **32**, 2111030 (2022).
<https://doi.org/10.1002/adfm.202111030>
- [25] Skliutas E., Lebedevaite M., Kasetaitė S., Rekštytė S., Lileikis S., Ostrauskaite J., Malinauskas M.: A bio-based resin for a multi-scale optical 3D printing. *Scientific Reports*, **10**, 9758 (2020).
<https://doi.org/10.1038/s41598-020-66618-1>
- [26] Tremblay-Parrado K-K., García-Astrain C., Avérous L.: Click chemistry for the synthesis of biobased polymers and networks derived from vegetable oils. *Green Chemistry*, **23**, 4296–4327 (2021).
<https://doi.org/10.1039/D1GC00445J>
- [27] Mustapha R., Rahmat A. R., Majid R. A., Mustapha S. N. H.: Vegetable oil-based epoxy resins and their composites with bio-based hardener: A short review. *Polymer-Plastics Technology and Materials*, **58**, 1311–1326 (2019).
<https://doi.org/10.1080/25740881.2018.1563119>
- [28] Güner F. S., Yağci Y., Erciyes A. T.: Polymers from triglyceride oils. *Progress in Polymer Science*, **31**, 633–670 (2006).
<https://doi.org/10.1016/j.progpolymsci.2006.07.001>
- [29] Lebedevaite M., Talacka V., Ostrauskaite J.: High biorenewable content acrylate photocurable resins for DLP 3D printing. *Journal of Applied Polymer Science*, **138**, e50233 (2021).
<https://doi.org/10.1002/app.50233>
- [30] Lebedevaite M., Gineika A., Talacka V., Baltakys K., Ostrauskaite J.: Development and optical 3D printing of acrylated epoxidized soybean oil-based composites with functionalized calcium silicate hydrate filler derived from aluminium fluoride production waste. *Composites Part A: Applied Science and Manufacturing*, **157**, 106929 (2022).
<https://doi.org/10.1016/j.compositesa.2022.106929>
- [31] Tran T-N., Di Mauro C., Graillot A., Mija A.: Chemical reactivity and the influence of initiators on the epoxidized vegetable oil/dicarboxylic acid system. *Macromolecules*, **53**, 2526–2538 (2020).
<https://doi.org/10.1021/acs.macromol.9b02700>
- [32] Di Mauro C., Malburet S., Genua A., Graillot A., Mija A.: Sustainable series of new epoxidized vegetable oil-based thermosets with chemical recycling properties. *Biomacromolecules*, **21**, 3923–3935 (2020).
<https://doi.org/10.1021/acs.biomac.0c01059>
- [33] Altuna F. I., Pettarin V., Williams R. J. J.: Self-healable polymer networks based on the cross-linking of epoxidized soybean oil by an aqueous citric acid solution. *Green Chemistry*, **15**, 3360–3366 (2013).
<https://doi.org/10.1039/C3GC41384E>
- [34] Wu J., Yu X., Zhang H., Guo J., Hu J., Li M-H.: Fully biobased vitrimers from glycyrrhizic acid and soybean oil for self-healing, shape memory, weldable, and recyclable materials. *ACS Sustainable Chemistry and Engineering*, **8**, 6479–6487 (2020).
<https://doi.org/10.1021/acssuschemeng.0c01047>
- [35] Green W. A.: *Industrial photoinitiators: A technical guide*. CRC Press, Boca Raton (2010).
- [36] Navaruckiene A., Bridziuviene D., Raudoniene V., Rainosalto E., Ostrauskaite J.: Vanillin acrylate-based thermo-responsive shape memory antimicrobial photopolymers. *Express Polymer Letters*, **16**, 279–295 (2022).
<https://doi.org/10.3144/expresspolymlett.2022.22>
- [37] Gu S., Jana S.: Effects of polybenzoxazine on shape memory properties of polyurethanes with amorphous and crystalline soft segments. *Polymers*, **6**, 1008–1025 (2014).
<https://doi.org/10.3390/polym6041008>
- [38] Mezger T. G.: *The rheology handbook*. Vincentz Network, Hannover (2011).
- [39] Pugh R. J., Bergstrom L.: *Surface and colloid chemistry in advanced ceramics processing*. CRC Press, Boca Raton (2017).
- [40] Eloff J. N.: Which extractant should be used for the screening and isolation of antimicrobial components from plants? *Journal of Ethnopharmacology*, **60**, 1–8 (1998).
[https://doi.org/10.1016/s0378-8741\(97\)00123-2](https://doi.org/10.1016/s0378-8741(97)00123-2)
- [41] Zhang Z. P., Rong M. Z., Zhang M. Q.: Polymer engineering based on reversible covalent chemistry: A promising innovative pathway towards new materials and new functionalities. *Progress in Polymer Science*, **80**, 39–93 (2018).
<https://doi.org/10.1016/j.progpolymsci.2018.03.002>
- [42] Roed L. A., Gundermann D., Dyre J. C., Niss K.: Communication: Two measures of isochronal superposition. *The Journal of Chemical Physics*, **139**, 101101 (2013).
<https://doi.org/10.1063/1.4821163>
- [43] Smith G. D., Bedrov D.: Relationship between the α - and β -relaxation processes in amorphous polymers: Insight from atomistic molecular dynamics simulations of 1,4-polybutadiene melts and blends. *Journal of Polymer Science Part B: Polymer Physics*, **5**, 627–643 (2007).
<https://doi.org/10.1002/polb.21064>
- [44] Zhang J., Huang J., Zhu G., Yu X., Cheng J., Liu Z., Hu Y., Shang Q., Liu C., Hu L., Zhou Y.: Self-healing, recyclable, and removable UV-curable coatings derived from tung oil and malic acid. *Green Chemistry*, **23**, 5875–5886 (2021).
<https://doi.org/10.1039/D1GC01726H>
- [45] Qiu M., Wu S., Fang S., Tang Z., Guo B.: Sustainable, recyclable and robust elastomers enabled by exchangeable interfacial cross-linking. *Journal of Materials Chemistry A*, **6**, 13607–13612 (2018).
<https://doi.org/10.1039/C8TA04173C>

- [46] González-Henríquez C. M., Sarabia-Vallejos M. A., Rodríguez-Hernández J.: Polymers for additive manufacturing and 4D-printing: Materials, methodologies, and biomedical applications. *Progress in Polymer Science*, **94**, 57–116 (2019).
<https://doi.org/10.1016/j.progpolymsci.2019.03.001>
- [47] Jin B., Song H., Jiang R., Song J., Zhao Q., Xie T.: Programming a crystalline shape memory polymer network with thermo- and photo-reversible bonds toward a single-component soft robot. *Science advances*, **4**, eaao3865 (2018).
<https://doi.org/10.1126/sciadv.aao3865>
- [48] Liang R., Yu H., Wang L., Amin B. U., Wang N., Fu J., Xing Y., Shen D., Ni Z.: Triple and two-way reversible shape memory polymer networks with body temperature and water responsiveness. *Chemistry of Materials*, **33**, 1190–1200 (2021).
<https://doi.org/10.1021/acs.chemmater.0c03860>
- [49] Zhang Y.: Discussion on the development of green chemistry and chemical engineering. in ‘Proceedings of the IOP Conference Series: Earth and Environmental Science, 3rd International Conference on Energy, Environment and Materials Science (EEMS 2017). Singapore’ Vol. 94, 012136 (2017).
<https://doi.org/10.1088/1755-1315/94/1/012136>
- [50] Liu T., Zhang M., Guo X., Liu C., Liu T., Xin J., Zhang J.: Mild chemical recycling of aerospace fiber/epoxy composite wastes and utilization of the decomposed resin. *Polymer Degradation and Stability*, **139**, 20–27 (2017).
<https://doi.org/10.1016/j.polymdegradstab.2017.03.017>

Research article

Use of modified deep eutectic solvent as an additional chemical in a flexible conductive natural rubber sensor for motion analysis

Boripat Sripornsawat^{1,2}, Antonia Georgopoulou^{2,3}, Sarttrawut Tulaphol¹,
Anoma Thitithammawong⁴, Jobish Johns⁵, Yeampon Nakaramontri^{1*}, Frank Clemens²

¹Sustainable Polymer & Innovative Composite Materials Research Group, Department of Chemistry, Faculty of Science, King Mongkut's University of Technology Thonburi, Bangkok, Thailand

²Department of Functional Materials, Empa-Swiss Federal Laboratories for Materials Science and Technology, Überlandstrasse 129, 8600 Dübendorf, Switzerland

³Department of Mechanical Engineering (MECH), Vrije Universiteit Brussel (VUB), and Flanders Make Pleinlaan 2, B-1050 Brussels, Belgium

⁴Department of Rubber Technology and Polymer Science, Faculty of Science and Technology, Prince of Songkla University, Pattani Campus, Pattani, Thailand

⁵Department of Physics, Rajarajeswari College of Engineering, Bangalore, India

Received 13 June 2022; accepted in revised form 22 August 2022

Abstract. The strain sensors based on conductive natural rubber (NR) composite, filled with carbon nanotubes (CNT) and conductive carbon black (CCB), are developed due to their superior elasticity and sensitivity. To encourage electron tunneling, ionic pathway for electron moving was achieved by modified deep eutectic solvent (mDES) synthesized in-house. It was found that the incorporation of mDES impacts the curing, mechanical and electrical properties of the composites due to the interconnected CNT/CCB-mDES networks. It is demonstrated that the electrical signal sensation of conductive NR composite was improved by adding mDES, and the inconsistent sensor behavior under cyclic and quasi-static loadings was eliminated. The mDES not only improves the movement of electrons, but it also promotes the crosslinking of NR molecules without adding ZnO. In addition, for analyzing the object motion, the piezoresistive rubber sensors were tested on a soft printing structure through the cyclic motion analysis of a soft tendon-based actuator. The obtained electrical signals showed the smooth signal with noise and un-prediction electrical peaks after the combination of the mDES into the conductive NR composites. This clarifies the flexible movement of the CNT/CCB structure into the NR matrix following the specific designed objects' motion. The present work indicates the different core novel technologies based on the use of mDES in the conductive composites matching with the acceptable electrical signal for applying as the promising motion sensor materials for soft structures.

Keywords: rubber, polymer composites, material testing, mechanical properties

1. Introduction

Resistive sensors typically convert mechanical, thermal, or chemical stimuli into an electrical signal and are generally fabricated from various materials, selective from metallic to semiconductors and inorganics

to organics [1]. In recent years, the demand for flexible and stretchable strain sensors based on polymer matrix has received enormous attention in wearable electronics, soft robotics, and stretchable devices due to the potential of expressing flexibility, processability,

*Corresponding author, e-mail: yeampon.nak@kmutt.ac.th

© BME-PT

and lightweight [1]. Several research groups have succeeded in fabricating stretchable strain sensors by using various forms of thermoplastic elastomer (TPE), *i.e.*, thermoplastic polyurethane (TPU) [2–5], thermoplastic styrene co-block polymers (TPS) [6, 7] and styrenic block copolymers (SBC) [8, 9]. However, it was found that the use of TPE is difficult in highly dynamic strain sensors since the material requires a superior capacity for original shape recovery. It is known that the TPE has both elastic and plastic deformation behaviors. In particular, at high strain monitoring over 20% of extension ratio, plastic deformation occurs. Therefore, it is a new challenge for the development of elastomeric sensors by incorporating synthetic and natural rubbers. Two different hypotheses for using rubber sensors are (i) the lowest hardness of crosslinked rubber [10, 11] and (ii) appropriate elastic properties for reasonable shape recovering time are needed [12]. According to our previous work, we found that the use of pure natural rubber (NR) for applying as the sensor monitor is needed to be developed. With the superior elasticity of NR and its lower plastic deformation during applied stress in comparison to TPE, the cumulative stress originated during stretching and caused strong deformation inside the rubber structure. As a result, the incorporation of hard filler particles into the NR matrix is considered; in particular, the conductive filler helps the NR composites respond to the electrical signals. Among the reinforcing fillers, conductive carbon black (CCB), carbon nanotubes (CNT), and graphene (GP) deliver excellent electrical performances based on their sp^2 hybridized carbon structure pathway of the filler network in the NR matrix [13]. The geometry and morphology of the conductive fillers inevitably influence the formation of conductive networks [14, 15]. Carbon nanoparticles have a strong tendency to agglomerate, which results in high percolation threshold concentration, poor electrical conductivity, and poor electron tunneling across the gaps between adjacent nano-carbon particles in NR composites [16]. Hence, the hybrid filler concept by the combination of CCB and CNT to improve electrical conductivity has been explored [17, 18]. Furthermore, CCB also improves the sensitivity to stress and strain due to its spherical shape that eases the disconnection of conductive particles by strain, while the long cylindrical CNT particles have sliding contact [19, 20]. However, mechanical deformation often results in additional peaks of sensor

signal upon releasing the load and strain [20, 21]. With these drawbacks, using NR in sensor applications is still limited and promising. Finding eco-friendly and cost-effective materials with sensitivity has been proposed, and there are no prior reports available in the literature.

To overcome this problem, the conductive liquid phase inside the NR matrix might organize the transfer of an electron from end-to-end of the filler particles since the liquid will be wetted on filler surface and serves as a better electron bridge between the conductive filler particles [22–24]. Based on the context of green chemistry, the ionic liquid was synthesized by deep eutectic solvent (DES) with free cationic and anionic movements as reported by Azizi *et al.* [25], where DES is a mixture of hydrogen bond donor (HBD, *i.e.* urea, carboxylic acid and polyalcohol) and hydrogen bond acceptor (HBA, *i.e.* choline chloride and quaternary ammonium salt). The preparation of DES in a pure state is simple and economically viable as it shows a 100% atom economy with no need for post-synthesis purification like other ionic liquids. In this case, choline chloride (ChCl) and urea are both naturally biocompatible chemicals that are not hazardous if they are released back into nature separately. The incorporation of DES and modified DES (mDES) into NR and epoxidized NR (ENR) affects vulcanization and mechanical properties and enhances the conductivity of NR and ENR by the formation of intermolecular attraction between rubber molecules [26]. However, DES and mDES in combination with NR composites filled with CNT and CCB, have not been investigated so far. Therefore, it is a new system for the investigation of NR-based sensors.

In the present article, the fabrication of conductive NR composites using CNT-CCB as conductive hybrid filler is reported. To improve the dispersion and conductivity, mDES was prepared by dissolving active ZnO in DES with various DES loadings and added to the conductive NR composite (CNRC). The nature of dispersion was assessed from Payne effect and morphological studies. The chemical crosslinking, mechanical properties, and electrical conductivity of the composites were investigated in detail. Piezoresistivity of the CNRC (strain sensitivity of electrical resistance) was investigated in terms of relative change in resistance, $\Delta R/R_0$ (ΔR and R_0 are the change in resistance with and without the strain of the composite) [27, 28]. Also, both dynamic and

quasi-static deformations were investigated by cyclic tensile testing methods. Finally, the performance of the resulting NR-based sensor was investigated on tendon-based 3D printed actuators to confirm its use in the field of soft robotics. It has to be noted that the uses of DES for improving the sensitivity of the conductive composites are a challenge and promising; the pairing among ChCl and urea was first chosen to modify with the ZnO and apply to the CNRC for studying and examining the sensitivity of the hyper-elastic material.

2. Experimental

2.1. Materials

For the fabrication of conductive rubber with hybrid filler and ionic liquid concept, natural rubber (NR) was mixed with multi-walled carbon nanotubes (CNT), conductive carbon black (CCB), and modified deep eutectic solvent (mDES). All chemicals used in this study are listed in Table 1, along with their functions and suppliers.

2.2. Preparation of modified deep eutectic solvents (mDES)

The mDES was synthesized using ChCl (hydrogen bond acceptor) and urea (hydrogen bond donor) at the molar ratio ChCl: urea of 1:2 [27]. ChCl and urea were mixed at 80 °C for 6 h or until the formation of a homogeneous transparent liquid called DES. Then, active zinc oxide (aZnO) was added in DES at four different weight ratios, namely 1:0.5, 1:1, 1:2 and

1:4 (aZnO:DES) at 80 °C for 24 h. The resulting mDES samples were kept in a desiccator to avoid moisture absorption. The detailed synthesis of DES and mDES has been described elsewhere [26].

2.3. Fabrication of NR composites

The NR/CNT-CCB composites with and without mDES were prepared using an internal mixer (model MX75; Charoen tut Co., Ltd., Samutprakarn, Thailand) at a mixing temperature of 80 °C, a rotor speed of 60 rpm, and 75% fill factor of the chamber volume. The mixing process was started by masticating NR in an internal mixer for 1 min at 80 °C and an additional mixing of 5 min after adding the CNT-CCB hybrid nanofillers. Then, the stearic acid and ZnO were incorporated stepwise for min and later mDES for 2 min. Finally, the accelerator and sulfur were consecutively added to the conductive NR compound with continued mixing until reaching 13 min. As a reference, the pure NR and NR/CNT-CCB without mDES were prepared following the same procedure. All compounds were rapidly passed through the 1 mm nip of the two-roll mill continuously 5 times (1 min/time) under the controlled rolling speed of 60 rpm to achieve homogeneous dispersion of CNT-CCB in the NR matrix before conditioning at room temperature in a desiccator for at least 24 h. NR composite sheets with 2 mm thickness were fabricated by using compression molding at 160 °C with the cure times based on rheometer tests. It is noted that the composites with CNT-CCB without and with

Table 1. List of chemicals used in the preparation of NR composites with and without mDES along with their functions and suppliers.

Materials	Functions	Suppliers
Natural rubber (Standard Thai Rubber, STR 5L)	Matrix	Nabon Rubber Co., Ltd., Nakorn Si Thammarat, Thailand
Stearic acid	Co-activator in sulfur curing systems	Imperial Chemical Co., Ltd., Pathumthani, Thailand
Active zinc oxide (aZnO)	Modifying agent of DES and activator in sulfur curing systems	Global Chemical Co., Ltd., Samutprakarn, Thailand
Multi-walled carbon nanotubes (CNT; NC7000)	Cylindrical conductive reinforcing filler in rubber	Nanocyl S. A. Sambreville, Belgium
Conductive carbon black (CCB; Vulcan XC72)	Spherical conductive reinforcing filler in rubber	Cabot China Ltd., Shanghai, China
2,2'-Dithiobis-(benzothiazole) (MBTS)	Accelerator in sulfur curing systems	Flexsys Inc., Termoli, Italy
Sulfur	Curing agent	Ajax Chemical Co. Ltd., Samutprakarn, Thailand
Choline chloride (ChCl)	Reactant of DES	Loba Chemie Pvt. Ltd., Maharashtra, India
Urea	Reactant of DES	Elago Enterprises Pty. Ltd., Cherrybrook, Australia

Table 2. Composition of all conductive pure NR and NR composites.

Ingredients	Contents [phr]					
	Pure NR	NR-C/mDES _x				
		0.0	2.5	5.0	10.0	20.0
NR	100.0	100.0	100.0	100.0	100.0	100.0
Stearic acid	1.0	1.0	1.0	1.0	1.0	1.0
aZnO	5.0	5.0	–	–	–	–
CNT-CCB*	–	5.0/7.5	5.0/7.5	5.0/7.5	5.0/7.5	5.0/7.5
MBTS	1.0	1.0	1.0	1.0	1.0	1.0
Sulfur	2.5	2.5	2.5	2.5	2.5	2.5
mDES			7.5	10.0	15.0	25.0
(aZnO:DES)	–	–	(1:0.5)	(1:1.0)	(1:2.0)	(1:4.0)

*CNT-CCB ratio is clarified from the previous work [16]

mDES were labeled as ‘NR-C/mDES_x’, where x refers to the DES content existing in mDES following the unit of part per hundred rubbers [phr]. The recipes of all composite samples are shown in Table 2.

3. Characterizations

3.1. Cure characteristic

Cure characteristics of pure NR and NR/CNT-CCB composites with various mDES loadings were determined using a rubber process analyzer (RPA 2000, Alpha Technologie, Hudson, Ohio, USA). Each sample (1 sample of each formulation) was investigated at a fixed oscillation frequency (1.66 Hz) and amplitude (0.5° arc) at 160 °C. The curing properties were reported as scorch time (t_{s2}) (the time at which the torque has increased by 2 dN·m from the minimum torque *i.e.* the initiation of chemical crosslinking), curing time (t_{c90}) (the time at which the molecular chains have reached 90% of chemical crosslinking propagation) and the torque difference ($M_H - M_L$) (the different of maximal (M_H) and minimal (M_L) torques).

3.2. Payne effect

To investigate the Payne effect of pure and conductive NR composites, a rubber process analyzer (RPA 2000, Alpha Technologies, Hudson, Ohio, USA) at 100 °C was used. The test was performed under shear deformation with strain amplitudes in the range of 0.56–100% at a fixed oscillation frequency (1 Hz) to analyze the storage shear modulus (G') of each sample (1 sample of each formulation). The Payne effect was calculated by Equation (1):

$$\text{Payne effect: } \Delta G = G'_{0.56} - G'_{100} \quad (1)$$

where $G'_{0.56}$ and G'_{100} are the storage moduli at 0.56 and 100% strain amplitudes, respectively. It is noted that the high Payne effect value indicates the reduction in strength of the filler network.

3.3. Electrical properties

The electrical properties of the samples in terms of resistance (R_p) were measured at room temperature using an LCR meter (E4980A, Keysight Technologies, Inc., Santa Rosa, California, USA). Approximately 2 mm thick samples were placed between two parallel plates of a dielectric test fixture (16451B dielectric test fixture, Keysight Technologies, Inc., Santa Rosa, California, USA) with a 38 mm electrode diameter. The analysis was performed over the frequency range from 20 to 100 kHz, and 5 different points of each sample were tested. The electrical conductivity (σ) was calculated using Equation (2) [29]:

$$\sigma = \frac{1}{\rho} = \frac{d}{(R_p)A} \quad (2)$$

The parameters d and A refer to the sample thickness and the area of an electrode, respectively. The factor ρ is the volume resistivity, *i.e.*, the reciprocal of conductivity.

3.4. Tensile properties

Tensile testing was performed using the dumbbell-shaped specimens of composites according to ISO 527 (type 5A) using 5 different samples for each formulation. The stress-strain behavior of the composites was then studied using universal testing machines (Model 3365, Instron® Inc., Norwood, Massachusetts, USA) operated at a crosshead speed of 200 mm/min at room temperature (25±3 °C).

3.5. Piezoresistive properties

The piezoresistivity was investigated using a universal testing machine ZwickRoell Z005, (ZwickRoell, Ulm, Germany), with an integrated source meter Keithley 2450 (Keithley Instruments, Solon, USA) with 3 different samples for each formulation. To record the electrical signal during mechanical test, the source meter was connected to a computer, and KickStart software (Keithley Instruments, Solon, USA) was used for data storage. The electrical resistance was calculated by the measured current, while the voltage was held constant at 1 V, as seen in the setup instrument in Figure 1. From the resistance analysis, the relative resistance (R_{rel}) was calculated following Equation (3), where R is the measured resistance and R_0 is the initial resistance, measured after fixing the sample inside the universal testing machine. The 5 bar pneumatic pressure was applied on the insulation grips to avoid slippage.

$$R_{rel} = \frac{R - R_0}{R_0} \quad (3)$$

In addition to the tensile test, cycling and quasi-static tests were performed to investigate the sensor behavior of conductive NR composites (CNRC) in detail. All the tests were performed at room temperature with a crosshead speed of 50 mm/min. The

dumbbell-shaped specimen (ISO 527, type 5A) was inserted between the grips aligned with the direction of extension. The dynamic tests were performed with 20 cycles (strain loading and releasing). The quasi-static tests were performed by stretching and releasing the samples with a dwell time of 60 s at minimal and maximal strain. Both dynamic and quasi-static tests were performed between 0–50 and 50–100% strain levels. Further details on the dynamic and quasi-static analysis of soft sensor materials are reported elsewhere [30–34].

4. Results and discussion

4.1. Processability and network formation in NR composites with DES

Ability to perform NR product

Figure 2 shows the crosslinking propagation of NR composites with various mDES (aZnO:DES) ratios. The vulcanization properties in terms of M_L , M_H , $M_H - M_L$, t_{s2} , and t_{c90} are summarized in Table 3. The NR composites with mDES at the aZnO:DES ratio 1:1 exhibited the highest M_H due to improvement of filler dispersion with using mDES. The M_H steadily decreased with increasing aZnO:DES ratios because the excess of mDES considerably acts like a lubricating plasticizer in the NR compound [35]. A higher amount of DES in mDES reduces NR

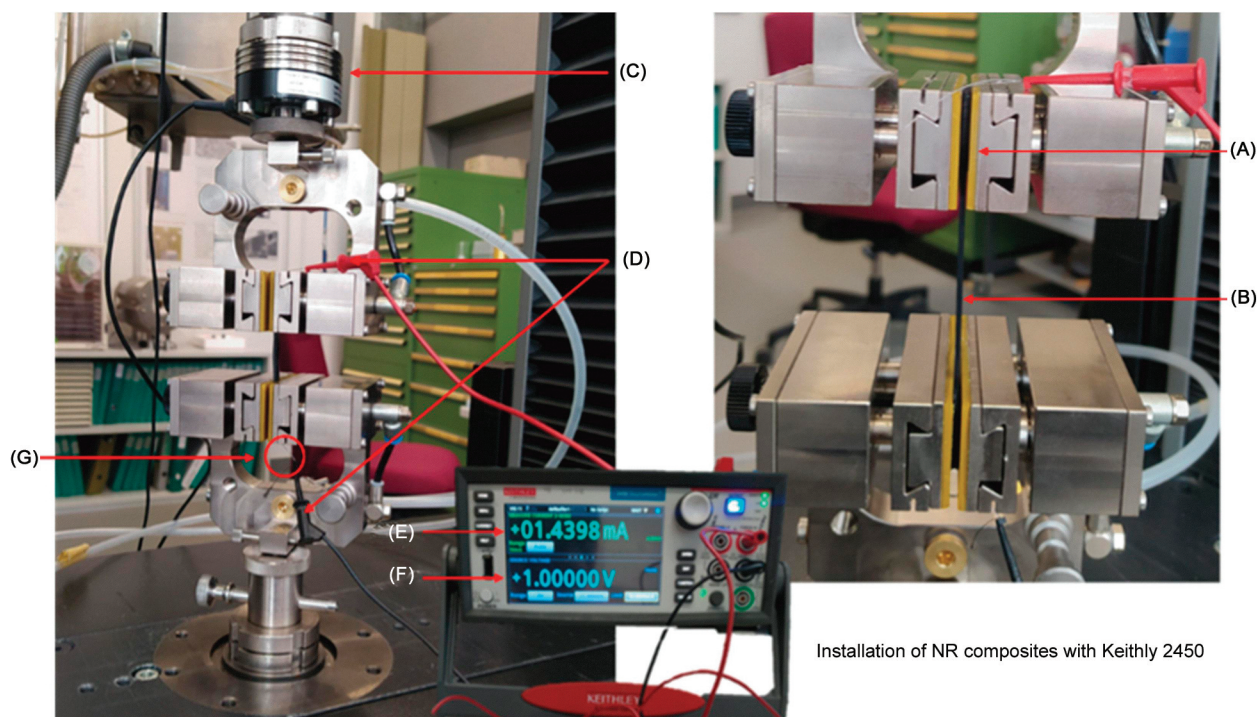


Figure 1. Universal testing machine with integrated piezoresistive analysis, pneumatic clamping and electrical connection of the conductive NR composite samples, where (A) – Insulation clamp, (B) – Rubber sample, (C) – Load cell, (D) – Conduction clamp, (E) – Electrical/Resistance detection, (F) – Applied voltages and (G) – Conduction wire.

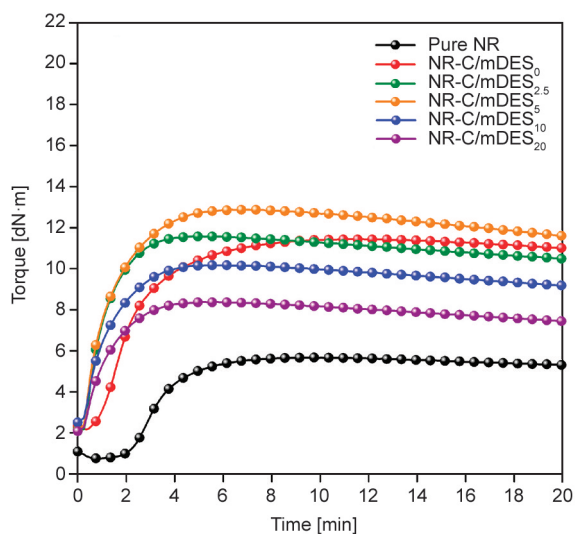


Figure 2. Vulcanization curves of pure NR and conductive NR composites (CNRC) with various mDES ratios. Up to 5 phr of mDES, the torque and the value of $M_H - M_L$ are increased. This can be correlated with the increased crosslink density. A further increase results in lowering torque value and crosslinking density.

chain entanglement, which develops strong molecular chain slippages and higher mobilities in the composite; hence it lowers the value of M_H . Considering the t_{s2} and t_{c90} of the NR composites in Table 3, both properties are significantly decreased upon increasing the amount of mDES. This is due to the formation of ionic interaction between NR and DES molecules [16]. Molecular chain degradation of NR occurs during compression molding, which results in the formation of ketone functional groups at the terminal chain of NR [36, 37] and the promotion of new ionic linkages between NR and DES molecules. Thus, active C=C bonds in NR are decreased and accelerate the vulcanization of conductive NR composites. Additionally, it can be observed that up to 5 phr of mDES in NR compounds, the value of $M_H - M_L$ dramatically increased. This is related to the enhancement of crosslink density (inferred from

Table 3. Crosslink properties of NR and CNRC with various mDES ratios.

Samples	Cure characteristics				
	M_L [dN·m]	M_H [dN·m]	$M_H - M_L$ [dN·m]	t_{s2} [min]	t_{c90} [min]
Pure NR	0.7	5.6	4.9	3.0	5.4
NR-C/mDES ₀	2.1	11.4	9.3	1.3	5.2
NR-C/mDES _{2.5}	2.1	11.6	9.5	0.5	3.5
NR-C/mDES ₅	2.1	12.9	10.8	0.4	3.3
NR-C/mDES ₁₀	2.5	10.2	7.7	0.5	2.9
NR-C/mDES ₂₀	2.1	8.5	6.4	0.6	2.7

$M_H - M_L$) based on the newly formed links of NR-mDES-CNT, NR-mDES-CCB, and NR-mDES-CNT-CCB. The proposed ionic interaction mechanisms in NR/CNT-CCB composites filled with DES are shown in Figure 3. At a higher loading level of mDES, the value of $M_H - M_L$ steadily decreased due to the formation of filler agglomerates or the micro-phase separation of mDES in the NR compounds, which resulted in a reduced force of attraction between the linkages. It can be concluded that the proper addition of mDES improves the processing of NR composites by reducing t_{c90} and increasing the estimated crosslink density based on $M_H - M_L$.

Formation of conductive network

The formation of CNT-CCB network in NR composites upon the addition of various mDES loading was examined from the electrical conductivity, which directly relates to the degree of filler dispersion [38]. Figure 4 shows the electrical conductivity as a function of frequency for the pure NR and CNRCs. As expected, the conductivity of the resulting material depends on the applied frequency. The electrical resistivity of pure NR and CNRC without mDES indicated poor transport of electric charges throughout the composites. For NR and CNRC, this is due to the insufficiently connected filler networks in the rubber matrix [38], as displayed in the proposed model (Figure 5a). In the case of CNRC without mDES, conductivity monotonically increases at a frequency below 10^4 Hz. This is attributed to the tunneling of electrons from end to end of CNT/CCB networks which increases with frequency. For the CNRC with mDES, conductivity is less dependent on the frequency because of the occurrence of electronic and ionic conduction inside the NR matrix. With the proper mDES, wetting of the liquid region on CNT/CCB surfaces helps to transport the electronic charges and improves the conductivity. Simultaneously, ionic charges move through the newly formed mDES pathway and can change the electrical behavior of the composites. Composites with 2.5–5.0 phr mDES, the partly wetted CNT-CCB surfaces by mDES, as seen proposed model in Figure 5b, accelerate the charge carriers through the CNT-CCB combination and support the network formation with narrow filler-filler contacts leading to an increase in conductivity of composites based on electron tunneling along the end-to-end of CNT-CCB [39]. This means that mDES develops a molecular chain bridge among the

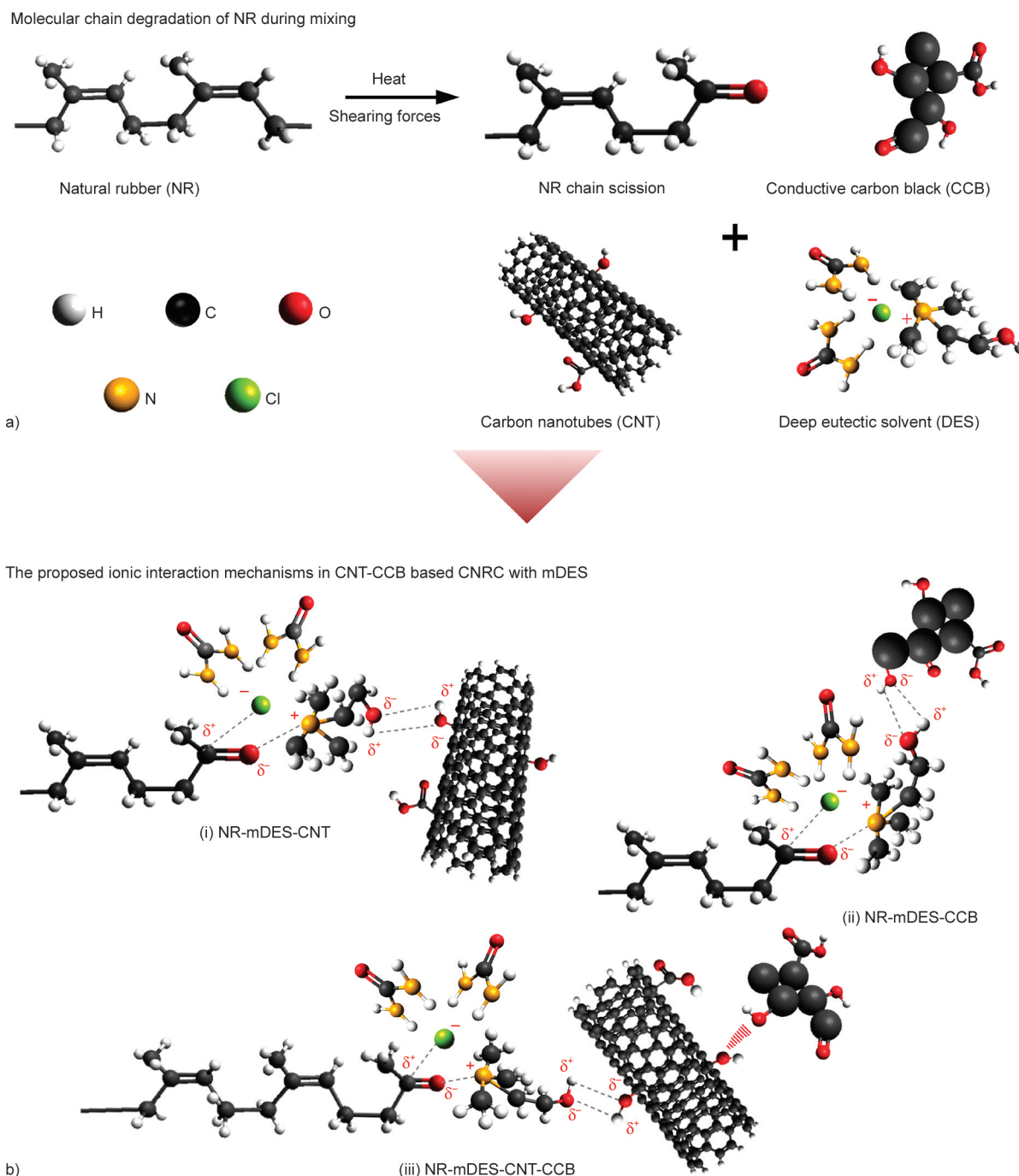


Figure 3 Proposed models of ionic interaction mechanisms in CNT-CCB based CNRC with mDES. a) Molecular chain degradation of NR during mixing generates ketone functional groups at the terminal chain of NR. b) The proposed ionic interaction mechanisms are shown as (i) NR, mDES, and CNT, (ii) NR, mDES, and CCB, and (iii) NR, mDES, and CNT/CCB.

filler particles. Hence, better electron transport takes place throughout the composites, resulting in the improved electrical conductivity of the composites. Below 5.0 phr of mDES, the effect of electronic conductivity is more predominant than the conductivity contributed by ionic charge transportation. However, beyond 5 phr of mDES (Figure 5c), the formation of mDES region occurs in the NR matrix. Thus, the conductivity arises in the composite due to two different

forms of networks. Generally, at higher frequencies, the electronic conductivity increases by reducing the ionic conductivity [40, 41]. The excess of mDES results in lowering the electrical conductivity. However, the excess of DES not only affected the conductivity but also imposed on the percolation threshold concentration of the composites. In this case, we have modified the percolation threshold theory for finding the critical DES concentration (ρ_{CX})

that enables the suitable electrical conductivity of NR composites. In general, the ρ_{CX} is examined from the plot of electrical conductivity and the varied chemical content (*i.e.*, amount of DES). With the curves, the ρ_{CX} of the composites can be evaluated using the classical percolation theory as Equation (4) [42]:

$$\sigma = \sigma_0(\rho - \rho_{CX})^t, \rho > \rho_{CX} \quad (4)$$

where σ_0 is a constant value, ρ is the DES ratio in mDES and t is the scaling exponent. As observed in the inset of Figure 4, the fitting results show that a low ρ_{CX} of DES ratio in mDES is found at 0.24 in conductive NR composites with mDES. This indicated the formation of an interconnected conductive network throughout the NR phases. It clarifies well that the addition of a little DES ratio in mDES improved well dispersion of CNT-CCB hybrid filler in the NR composites and consequently increased the electrical conductivity of the conductive NR composites.

The state of CNT-CCB dispersion and distribution in the NR matrix can also be observed from the relation of storage moduli of the composites at maximal and minimal strain amplitudes which is the so-called Payne effect [43]. The value is directly related to the degree of CNT-CCB agglomerates in the matrix and also related to the strength of CNT/CCB network deformation [43]. Figure 6 shows the storage

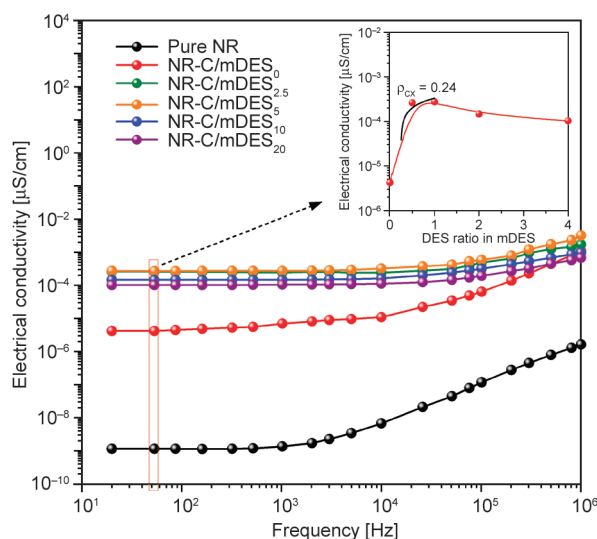


Figure 4. Electrical conductivity as a function of frequency for pure NR and their composites with various mDES ratios and the plot of electrical conductivity at a frequency of 50 Hz as a function of DES concentration in mDES to find the critical DES concentration (ρ_{CX}) from the applied percolation threshold theory.

modulus as a function of strain amplitude which demonstrates that the incorporation of mDES up to the ratio of 1:1 (aZnO:DES) increases the storage modulus of NR composites. It improves the CNT-CCB dispersion in the NR matrix, relating the concentration over the ρ_{CX} value. As expected, at mDES ratio higher than 1:1, the initial storage modulus steadily decreased due to the excess of liquid phases inside the NR, which reduces the physical interactions from bound rubber absorption of NR molecular chain on the CNT-CCB surfaces, allowing the NR chains slippage and disentanglement. It also affects the strength of the CNT/CCB network, which can be broken easily upon the addition of excess mDES. Considering the Payne effect in Figure 6, a reduction in their values is found for the NR composites with mDES relative to the ones without mDES. This is contributed by the improved dispersion of CNT-CCB in rubber matrices, as described in models in Figure 5. The use of mDES reduced the degree of CNT-CCB agglomeration in the NR matrix, relating to the reduced Payne effect value. It also helps the CNT-CCB interconnection and supports the strength of network formation with narrow filler-filler contacts (as seen in Figure 5b). However, the addition of excess mDES lowers the Payne effect, and it is reflected in the poor G' values. This means that the increase of liquid phase inside the NR matrix improves the filler dispersion, but the network strength is worth it due to the ease of breakages under strain. Thus, it summarizes that the addition of proper mDES improves the dispersion very well and supports the network formation of CNT-CCB hybrid filler in NR composites by increasing the electrical conductivity of NR composites.

Effect of DES on mechanical properties

Network formation of CNT-CCB also affected the tensile properties of CNRC upon the addition of mDES. Figure 7 shows the stress-strain curves of pure NR and NR composites with various mDES ratios. Also, properties in terms of 100 and 300% moduli, tensile strength, and elongation at break are shown in Table 4. Pure NR shows a dramatic increase in the modulus at high strain (500–700%) due to strain-induced crystallization of NR molecules. However, CNRC with various mDES displayed higher initial slopes (*i.e.*, Young’s modulus, the ability to resist the deformation of composites) and the moduli at 100 and 300% strains compared to pure

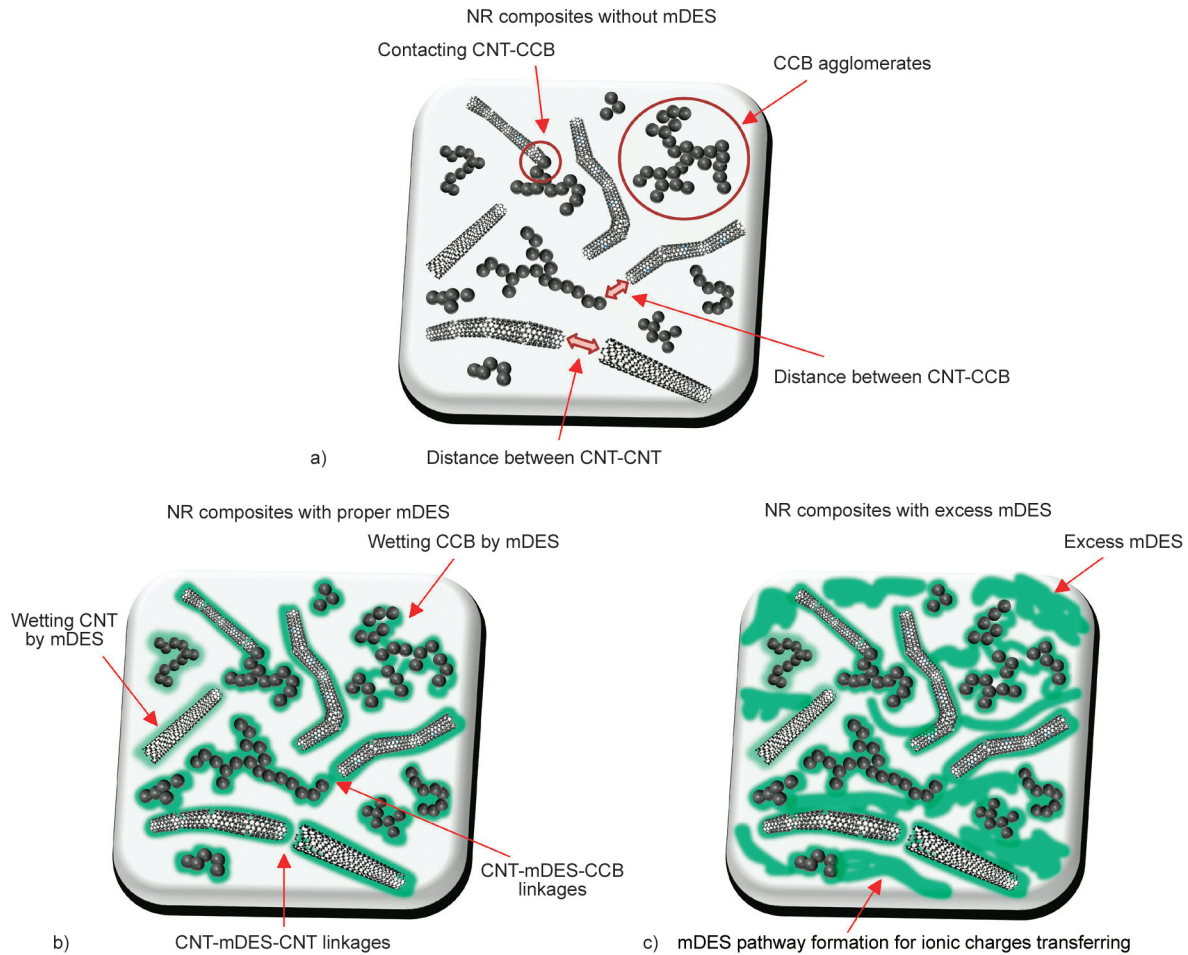


Figure 5. Proposed models of CNT-CCB dispersion inside the NR matrix; a) CNRC without mDES indicated poor electric transport due to a lack of connected filler networks in the rubber matrix, b) CNRC with proper mDES exhibited partly wetted CNT-CCB surfaces by mDES accelerates the network formation with narrow filler-filler contacts increases the conductivity and c) CNRC with the excess of mDES regions inside NR matrix.

NR. It is noted that the ‘modulus’ refers to the stiffness of a material that resists deformation. Thus, the addition of highly rigid filler particles into the NR matrix is expected to improve the stiffness of the composite. In contrast, higher stiffness leads to lower elasticity, and the composites exhibit lower strain at break. This can be explained by the surrounding CNT-CCB particles that strongly hinder the mobility of rubber chains [44]. Table 4 shows that the tensile strength of NR-C/mDES0 composites increases approximately 11% upon the addition of DES at the ratios 1:0.5 and 1:1 (aZnO:DES). The addition of sufficient mDES loading improved the dispersion of CNT-CCB in the NR matrix and increased the reinforcement efficiency of filler particles to rubber molecules. However, as seen in the proposed model of Figure 5c, increasing mDES above 5 phr increases the defect points inside the NR matrix and reduces the resistance of physical deformation during extension [45]. Thus, tensile strength is found to be strongly

lowered. In addition, the presence of excess liquid phases is observed in the morphologies of the composites, as seen in Figure 8. It is clearly noticed that the degree of filler agglomeration (*i.e.*, the purple area) is effectively increased upon increasing the loading level of mDES. Interestingly, in NR-C/mDES_{2.5} and NR-C/mDES₅, a homogenous dispersion of mDES in the NR composites filled with CNT-CCB is observed, especially the one with 5 phr of mDES compared to the one without mDES. A further increase in mDES results in a larger area of filler agglomeration.

According to the observed results of CNRC filled with various mDES loading, it is found that the addition of 5 phr mDES improves the processability of NR-C/mDES0 by reducing cure time and increasing tensile properties. However, excess DES from 10 and 20 phr reduces the properties of the composites owing to the existence of large defect regions. This leads the composites to break easily, and therefore,

R1
R2
R3
R4
R5
R6
R7
R8
R9
R10
R11
R12
R13
R14
R15
R16
R17
R18
R19
R20

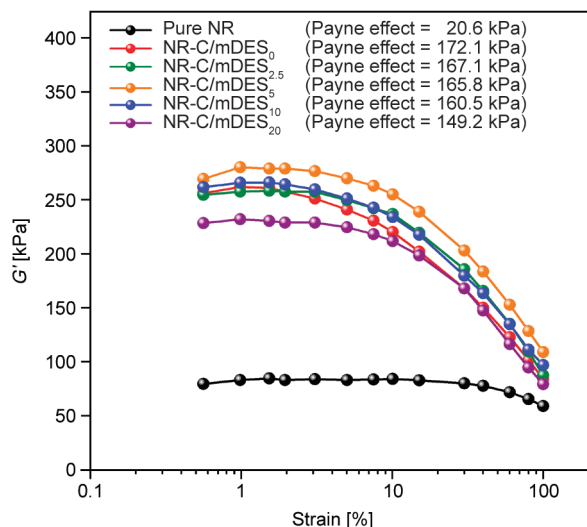


Figure 6. Relation of storage modulus and strain amplitude of pure NR and their composites with various mDES ratios. The test was performed under the shear deformation with strain amplitudes in the range of 0.56–100%. The obtained Payne effect from different storage moduli at 0.56 and 100% strain amplitudes, which refers to the strength of the filler network and filler dispersion inside the NR matrix, is also presented.

the tensile properties are decreased. Thus, the possibility of using the resulting composites as a motion sensor in soft actuators and piezoresistive properties

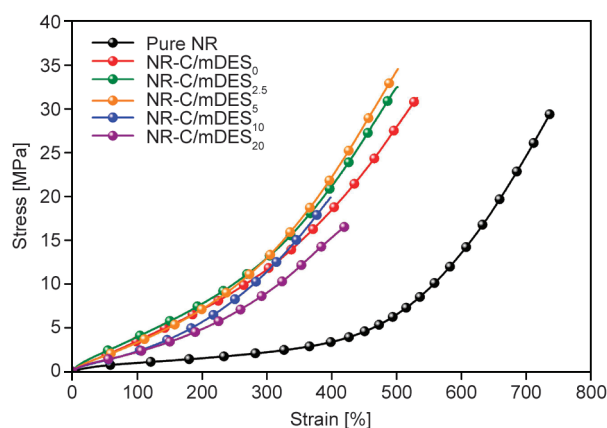


Figure 7. Stress-strain curves of pure NR and their composites with various mDES ratios.

Table 4. Tensile properties in terms of 100 and 300% moduli, tensile strength, and elongation at break of NR composites with various mDES ratios.

Samples	100% modulus [MPa]	300% modulus [MPa]	Tensile strength [MPa]	Elongation at break [%]
Pure NR	0.9±0.1	2.2±0.2	29.5±2.0	738.5±13.3
NR-C/mDES ₀	3.3±0.2	10.9±0.2	31.3±2.3	532.3±15.1
NR-C/mDES _{2.5}	3.9±0.3	12.8±0.3	32.4±1.7	503.8±22.6
NR-C/mDES ₅	3.5±0.3	12.8±0.3	34.6±1.9	502.7±20.1
NR-C/mDES ₁₀	2.4±0.2	11.9±0.2	19.9±2.5	419.1±17.8
NR-C/mDES ₂₀	2.1±0.2	8.6±0.3	16.5±1.2	398.2±16.7

in terms of the relative change of resistance (R_{rel}) by dynamic and quasi-static tests are investigated and further explained by matching with the proposed phenomena.

4.2. Piezoresistive properties of NR composites with mDES

Sensitivity of the composites

The piezoresistive properties of the CNRCs are measured based on the variation of conductivity upon the application of stress by using a universal tensile testing machine. On straining the CNRC samples, the distance between conductive fillers increases, and electron transport is reduced by a larger distance between the fillers (tunneling effect). As a result, only CNRC samples without mDES and with 5 phr mDES are selected for sensor studies. Due to the considerable difference in the initial conductivity of these two samples (see Figure 4), the R_{rel} during tensile testing of the samples is shown in Figure 9. Both the CNRC samples show positive piezoresistive behavior. This can be explained by the loss of contact between the filler particles that results in enlarged electron tunneling resistance [42, 46, 47]. For piezoresistive strain sensors, the estimation of sensitivity correlates with the estimation of the gauge factor (GF). It can be defined as the ratio of change in relative resistance to the change in strain. In this case, the correlation of both properties is linear; the GF is calculated from the slope of the plot of the relative resistance change and the applied strain of 0–50, 50–80, and 80–100% (see the estimated slope from the green line). A higher GF corresponds to a larger change in resistance at a given strain, and therefore it indicates good sensitivity [48]. In Figure 9, it is seen that the GF value of the CNRC with and without mDES had no significant differences relating to the applied strain of 0–50%. However, at 50–80 and 80–100% strain, the GF of the CNRC filled with mDES had approximately 2 and 4 times higher than

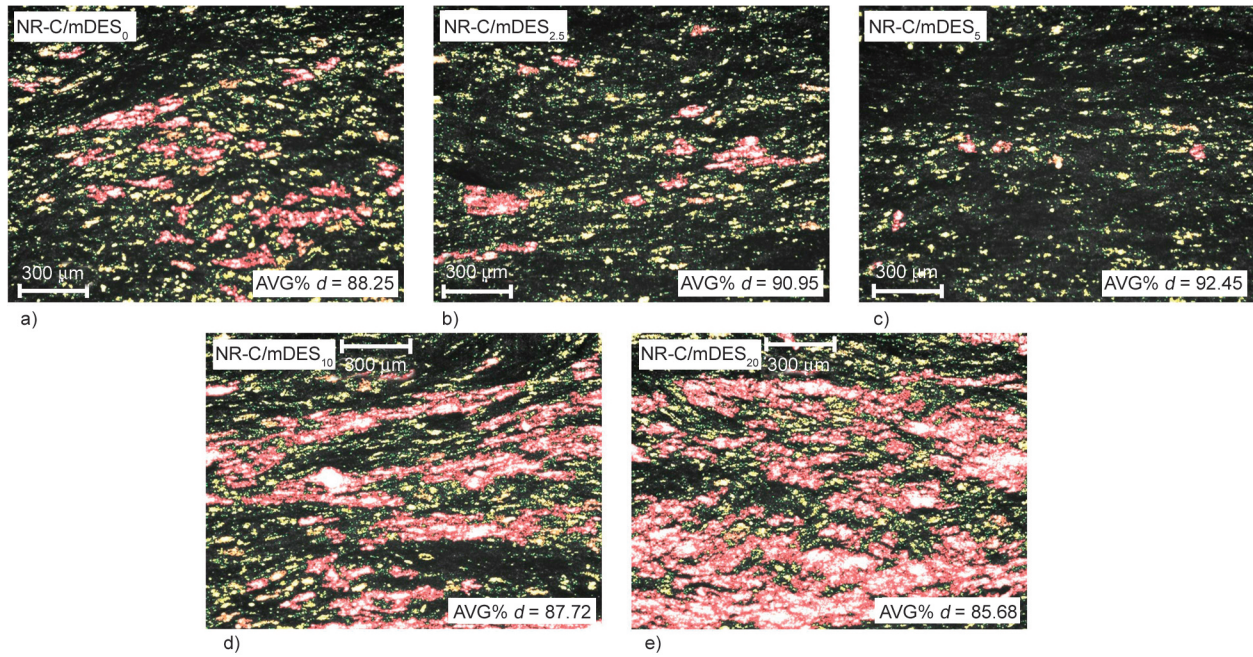


Figure 8. The morphologies based on optical microscope detection of the CNRCs with various mDES contents at 0, 2.5, 5, 10, and 20 phr, respectively, using a magnification of 100×. The purple area refers to the agglomeration areas of the fillers, whereas the AVG% d is the average% dispersion of the filler inside the NR matrix. a) NR-C/mDES₀, b) NR-C/mDES_{2.5}, c) NR-C/mDES₅, d) NR-C/mDES₁₀, e) NR-C/mDES₂₀.

that of one without mDES. This clarifies the fast responsibility of the composites due to the addition of the DES, reflecting good sensitivity at the applied strain. Thus, at 0–50% strain, similar GF is received and not applicable for interpreting the sensitivity of the CNRC. In addition, the sensitivity of the presented CNRC to other conductive composites is based on the TPU, SR, and PDMS matrices indicated in Table 5. It is clearly seen that the NR-C/mDES₅ had

the highest maximal GF value relative to the others used matrices. The two different reasons for the obtained results are related to (i) the high molecular weight of NR, which causes superior elasticity to the material, and (ii) the long molecular chain of NR, which provides a high degree of chain entanglement that resists breakage of the material. This is also the phenomenon for affirming the sensing performance of the CNRC owing to the addition of the mDES.

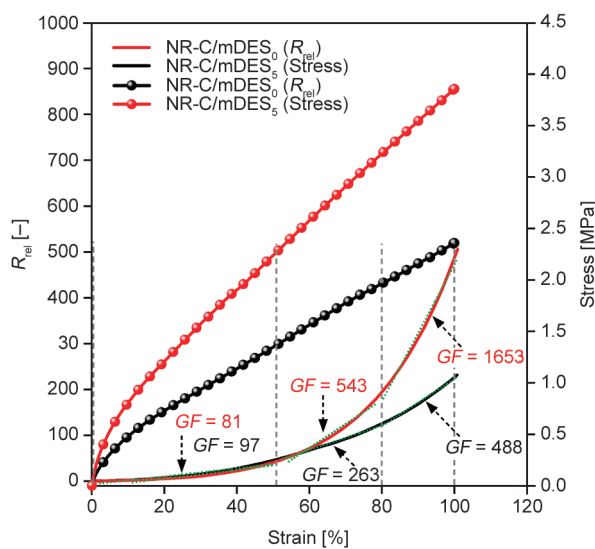


Figure 9. Relative resistance (R_{rel}) and stress as a function of strain together with the GF values calculated from the slope of the plot of R_{rel} changes at 80–100% strain.

Cyclic testing

Dynamic testing provides useful insights into the sensing behavior of the long-term performance of a composite sensor system [42]. Dynamic cyclic tests are performed to ensure the sensor signal's repeatability under the given strain [53]. This indicates the linearity of the sensor signal response during loading and unloading, the signal drift, and the reliability of the sensor in terms of how the signal response changes after many consequent cycles of loading and unloading. Figure 10 shows the variation of stress-strain curves in the case of pure NR and CNRC with and without mDES. The samples have been cycled 20 times from 0–50 and 50–100% strains. It is found that the CNRCs showed lower stress during 2nd cycle than the 1st cycle of the dynamic test when compared to pure NR. This is attributed to the detachment of rubber from filler surfaces as a result of poor filler

Table 5. Sensing performance comparison of the CNRC with and without the addition of DES relative to other referenced matrix composites, where ^{*a}, ^{*b}, ^{*c}, and ^{*d} are assigned to thermoplastic polyurethane (TPU), reduced graphene oxide (rGO), polydimethylsiloxane (PDMS) and silicone rubber (SR), respectively.

Samples	Sensor type	Stretchability	Linearity	Maximal GF
NR-C/mDES ₀	Resistive	100%	Three linear regions	488.0
NR-C/mDES ₅	Resistive	100%	Three linear regions	1653.0
TPU ^{*a} /rGO ^{*b} [50]	Resistive	100%	Two linear regions	79.0
PDMS ^{*c} /CNT [51]	Resistive	100%	Two linear regions	87.0
SR ^{*d} /GP [52]	Resistive	12%	Two linear regions	164.5

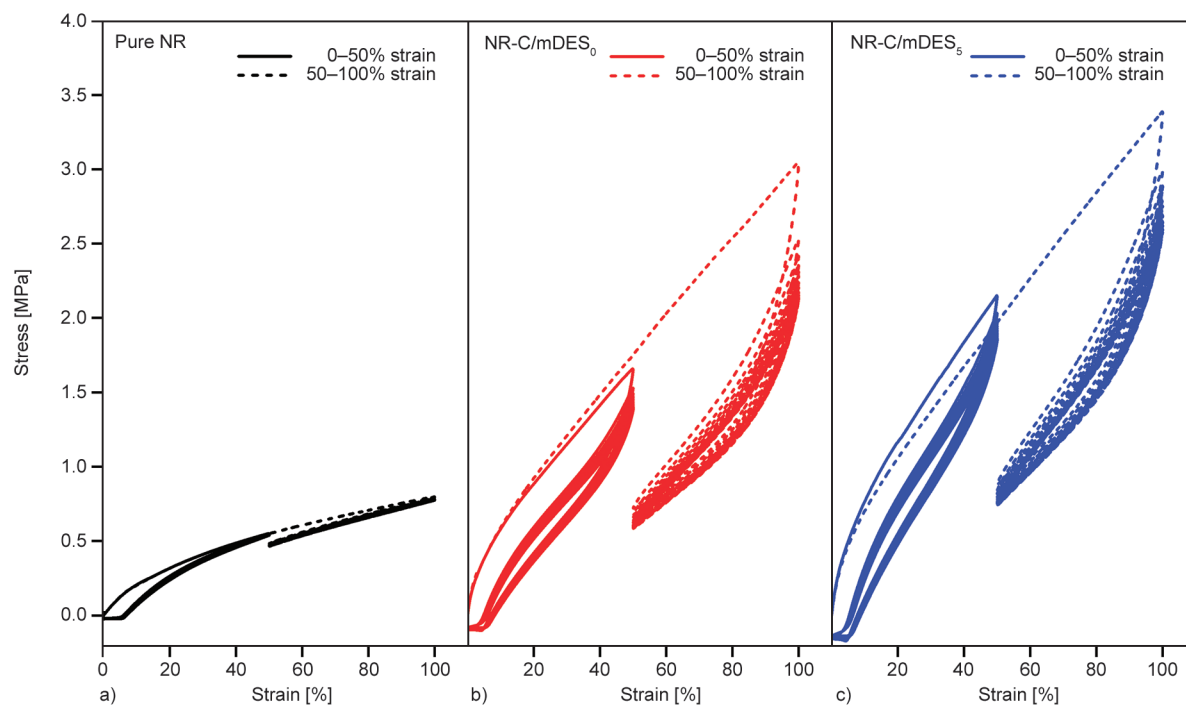


Figure 10. Stress-strain curves of pure NR and their composites without and with mDES during the 20 cycles of the dynamic tensile testing at 0–50 strain and 50–100% strain. a) Pure NR, b) NR-C/mDES₀, c) NR-C/mDES₅.

reinforcement efficiency. However, comparing the composites, the sample with mDES exhibited higher stress than without mDES. It is expected that the incorporation of mDES causes improvement in the dispersion of CNT-CCB hybrid fillers which subsequently increased the reinforcement efficiency in the NR matrix.

For the investigation of signal drift under strain, the maximum stress of each cycle ($\sigma_{\max-C_y}$) needs to be examined. Here, the difference in $\sigma_{\max-C_y}$ at the first cycle of the one without and with pre-straining is due to the detachment of NR molecules from the filler surface, which is increased with the degree of extension ratio. Based on the $\sigma_{\max-C_y}$ of the composites with and without mDES, it is found that the addition of mDES significantly helped the composites by lowering the % change of $\sigma_{\max-C_y}$ along with the cyclic testing. This correlated well to the relation of stress-time

curves at 0–50 and 50–100% indicated in Figures 11e–11h. In addition, to examine the effect of DES on the hysteresis of the NR composites, the difference of $\sigma_{\max-C_y}$ and $\sigma_{\min-C_y}$ (*i.e.* minimum stress of each cycle) is known as the correlation of the estimated hysteresis of the CNRC was interpreted. It is seen that the larger different values are found after the addition of DES. This means that the NR-C/DES₅ composite had higher energy dissipation than the one without DES during the help of DES phase, which causes improvement of reinforcement efficiency relating well dispersion and distribution of fillers throughout the NR matrix.

Considering the variation of R_{rel} value upon applying and releasing strain, the different R_{rel} behaviors of NR composites under loading and unloading cycles at 0–50 and 50–100% strains are shown in Figures 11a–11d. In Figure 11, the R_{rel} of the composites exhibited

a decreasing trend as the number of cycles increased, and this reduction in resistivity was more pronounced at the beginning of the test. A decrease in R_{rel} is

observed during the cyclic test caused by softening of the matrix due to the breakage of filler-filler contacts and the detachment of NR molecules from

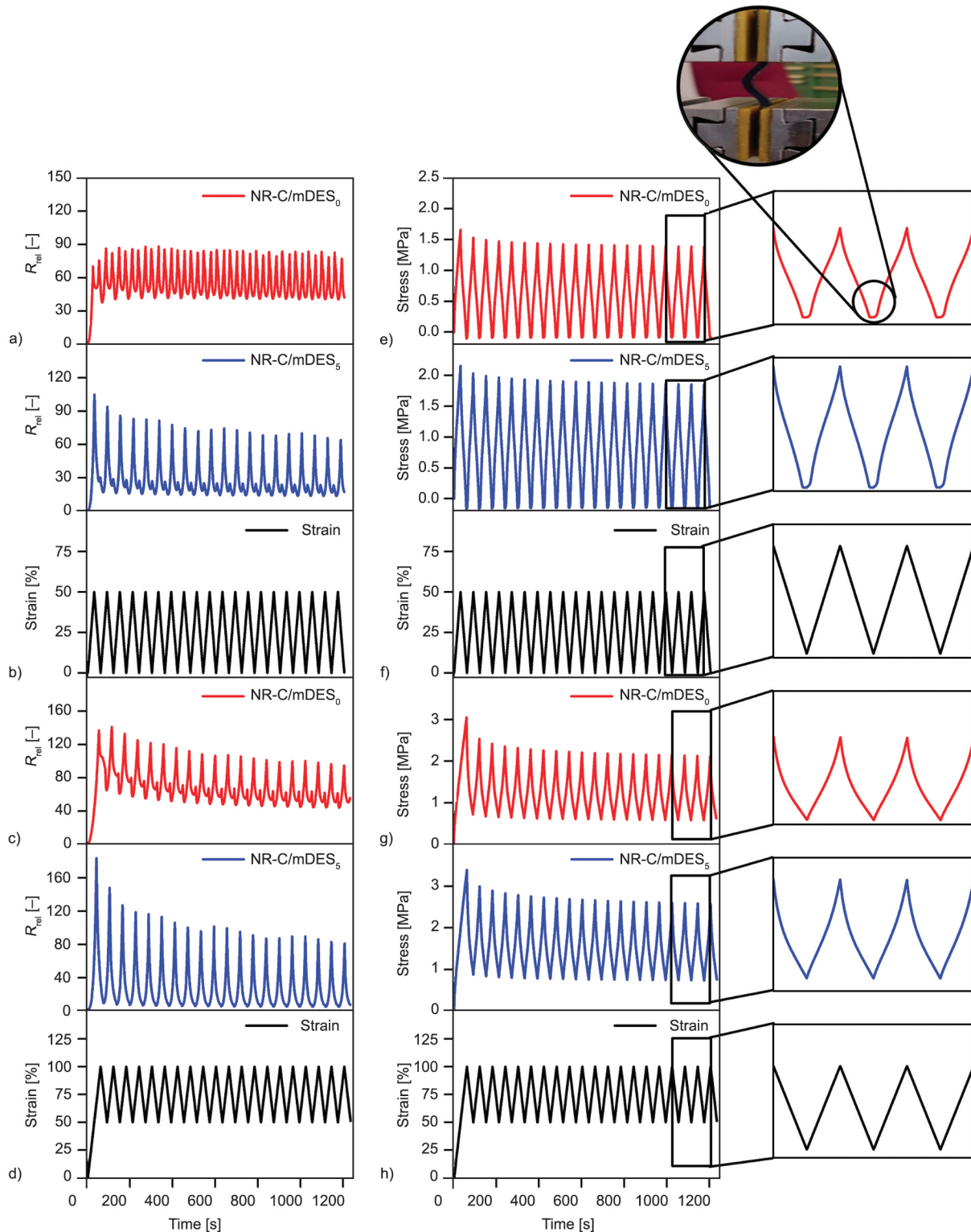


Figure 11. Variation of R_{rel} value upon applying and releasing strains of a) CNRC without mDES, b) CNRC with 5 phr mDES together with the relation of stress and time of e) CNRC without mDES and f) CNRC with 5 phr mDES on performing the dynamic tests in 20 cycles at 0–50% strain. Also, R_{rel} and stress changes as a function of time during the dynamic tests at 50–100% strain of CNRC without and with mDES 5 phr are shown in c), d), g), and h), respectively.

CNT/CCB surfaces [13, 41]. Repeated stretching and contracting during the cyclic strain test increase the contact surface areas of the existing conductive particles due to the occurrence of multiple contacts of each particle. At the same time, the additional conductive pathways established during stretching and releasing reduce the electrical resistance [42, 54]. In addition, it is also seen in Figure 11 that the resistivity of the composites increased upon the application of mechanical force because of the change in distance of separation between the particles, and further, the resistivity is found to be decreased with strain. This is typical behavior of piezoresistive composites known as the positive strain effect or positive response. However, the further contraction (*i.e.*, decreasing strain) results in increasing resistance, leading to an additional peak in each cycle. This peak exhibited a negative strain effect that has already been reported in the literature [2, 49]. The existence of a shoulder peak or a negative response during loading-unloading cycles indicates the formation of destruction and reconstruction of conductive pathways [55, 56]. Also, buckling of the sample, as shown in Figure 11e, was another reason for the more pronounced shoulder peak. However, in Figure 11b, the composites with mDES exhibited a smaller negative effect on the peak as compared to the composites without mDES (Figure 11a). This can be related to the

synergy of plasticizing by mDES that provides better dispersion of CNT-CCB hybrid fillers, originating infinite 3D CNT-CCB pathways inside the NR matrix. In addition, the partly wetted CNT by mDES accelerated the dispersion of CNT and supported the network formation with narrow filler-filler contacts that led to an increase in the conductivity of composites by reducing the shoulder peak. Figure 11d shows that the shoulder peak of NR composites at 50–100% strain was significantly decreased from the NR composites at 0–50% strain (Figures 11a and 11b). It can be related to the visco-elastic behavior of the composites upon changing the extension ratio and addition of mDES, as shown in the proposed mechanism (Figure 12). On increasing the extension ratio of the composites (Figure 12a), the detachment between NR molecules and filler surface has occurred, and therefore, the restriction of NR deformation is lowered. This phenomenon reduces the elastic nature of NR molecules to regain the original shape and finally decreases the buckling phenomena. Thus, the secondary peak of the electrical signal is found to be minimized. However, with no significant changes in the bending degree of the composites after releasing forces and the addition of DES eliminates the appearance of the unnecessary peak. In Figure 12c, it is seen that the wetting of DES on the surface of CNT-CCB indicates tunneling of current through the

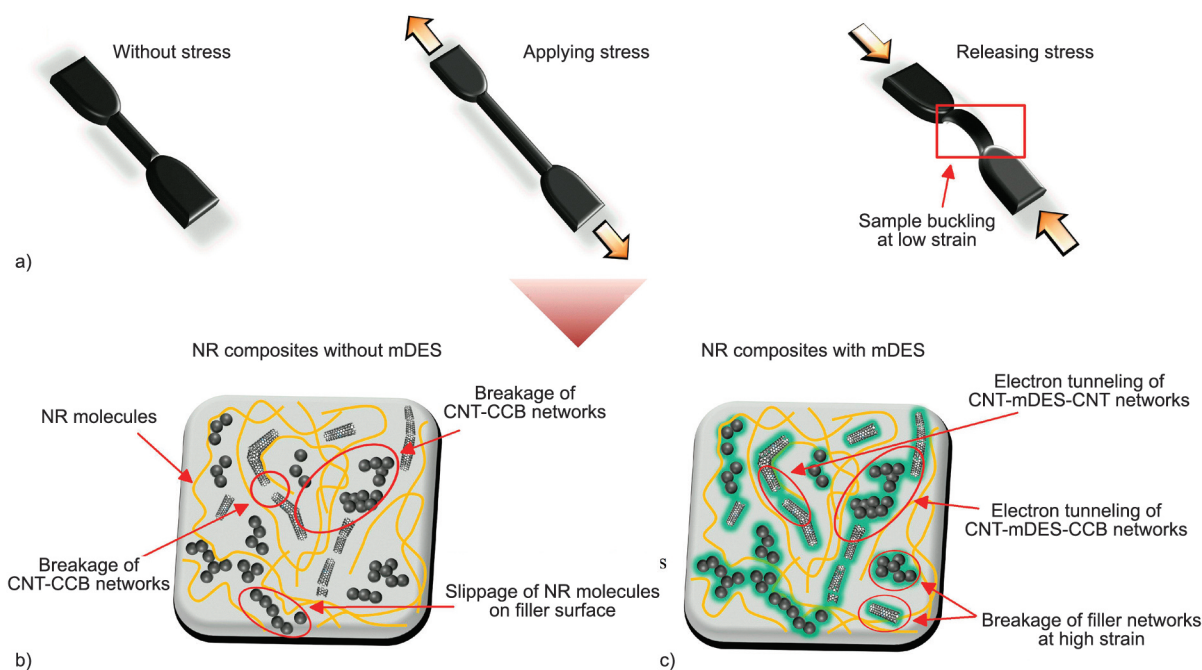


Figure 12. Proposed models of the CNRC without and with mDES during extension. a) Changes in the appearance of specimens during stretching and releasing. b) The proposed image of filler network formation of CNRC without mDES when applying stress. c) The schematic mechanism of mDES wetting on the CNT-CCB surfaces accelerated the CNT-mDES-CNT and CNT-mDES-CCB linkages in CNRC with mDES during extension.

linkages of CNT-DES-CNT and CNT-DES-CCB even though it consists of separation between them. Therefore, under dynamic conditions, the DES stabilized well the transport of electric current throughout the NR matrix and effectively minimized the signal errors.

Quasi-static testing

The applicability of CNRC with 5 phr mDES and without mDES has been studied in soft actuators. The sensor has to measure the same strain at different intervals of time. Rubber molecules are linked with stress relaxation phenomena that exhibit the effect of the piezoresistive response of the strain sensor [57]. Therefore, a quasi-static test can be conducted to study the effect of relaxation and drifts on the sensor performance due to the interconnection between the rubber-filler, where the stress is held constant with time [58]. Figure 13 shows the quasi-static results of NR composites with and without mDES focusing on stress and R_{rel} relaxation at constant strain and strain varying between 50–100%. In Figure 13a, it is seen that the stress relaxation is 6.9 and 7.5% in the cases of CNRC with and without mDES, respectively. This means that NR molecular chains and CNT-CCB particles with mDES build a more stable network, and it cannot be easily moved due to the better dispersion of filler in the NR matrix. The results correlated with the electrical relaxation represented in

Figure 13b. As expected, the value of R_{rel} increases on applying strain and decreases when the strain is lowered. When the strain is held at a constant ratio, the R_{rel} decreases to approximately 41.4% for the composite without mDES and 36.0% for the one with mDES. This reduction in relaxation of CNRC with mDES can be explained by molecular chain bridging among the filler particles by mDES, although the sample experiences buckling. As already mentioned, mDES helps the electron transport throughout the NR matrix by improving the electrical conductivity, and the CNRC composites with mDES₅ exhibited better sensor performance compared to others.

4.3 Use of CNRC filled with mDES₅ to detect motion of the soft tendon-based actuator

Fabrication of soft tendon-based actuator

A soft tendon-based actuator has been designed with one joint (flexible hinge), as can be seen in Figure 14. Here, the tendon-based actuator was fabricated by fused deposition modeling (FDM), a method of material extrusion additive manufacturing. For the fabrication, A Raise Pro 2 FDM 3D printer from Raise 3D (Irving, Texas, USA) was used. The material used for the actuator was 1.75 mm TPU filament with Shore hardness 90A, supplied by Spectrum (Pecice, Poland). The temperature used during printing was 230 °C for the printing head and 45 °C for the printing

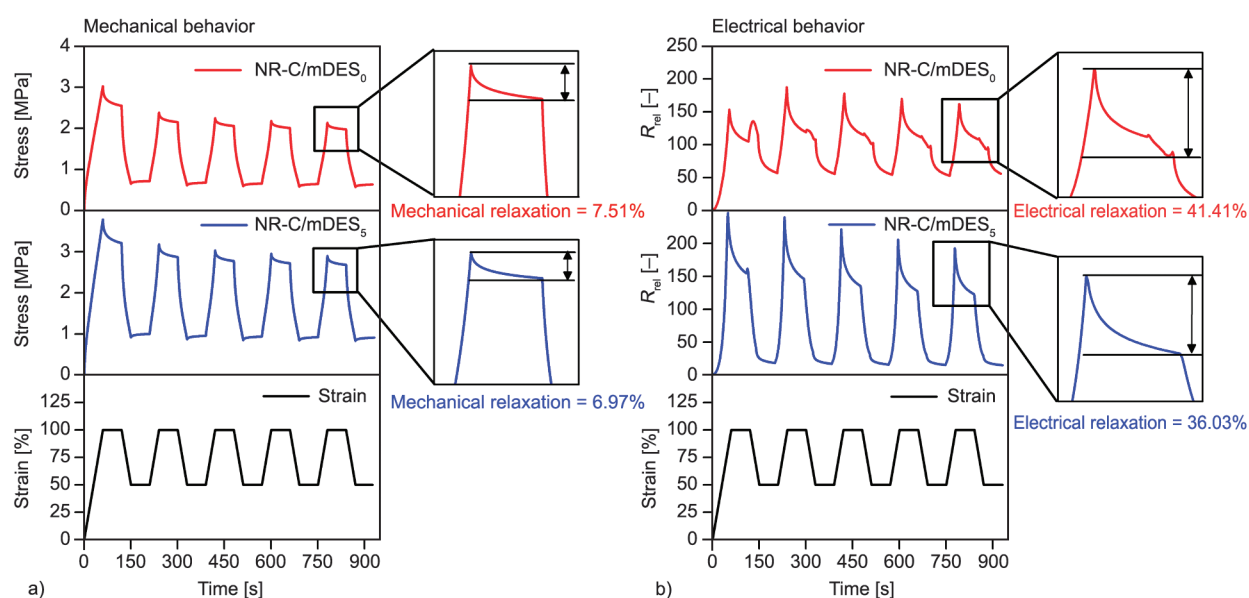


Figure 13. a) Mechanical behavior by means of stress as a function of time of the CNRC without mDES and with 5 phr mDES during the quasi-static testing. The tests were performed by stretching and releasing the CNRC in 50–100% strain together with a dwell time of 60 s at minimal and maximal strains. b) The R_{rel} signal relaxation behavior in a quasi-static strain cycling test of CNRC without mDES and with 5 phr mDES relative to time.

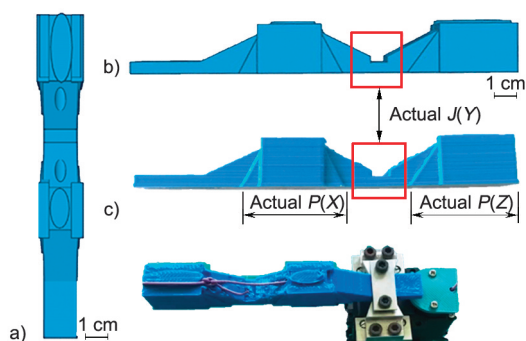


Figure 14. Computer-aided design (CAD design) of the soft tendon-based actuator for the top view (a) and side view of the design (b) and the printed material (c).

bed. The filament was printed with a speed of 20 mm/s and an extrusion multiplier of 1.2.

For the actuation, a tendon consisting of 0.3 mm copper wire coated with polytetrafluoroethylene was attached to a Dynamixel AX-12A servomotor from Robotis (Lake Forest, Illinois, USA). For the control of the servomotor, an Arduino Mega microcontroller with an external power supply was used. The actuator was programmed to move from open position to closed position with a 2 s delay in each position (Figure 14c).

Sensing the motion of the tendon-based actuator

To detect the motion of the tendon-based actuator, a dumbbell-shaped sensor was used, similar to the samples used in tensile testing experiments. The

CNRC was fixed on the actuator using Sil-Poxy glue from Smooth-On (Macungie, Pennsylvania, USA), as seen in the installation details (Figure 15). The CNRC sensor was connected with a multi-meter using electrical safety grippers to detect the motion of the actuator and the sensor signal, as shown in Figure 15 and Appendixes 1 and 2. It is seen that the monotonic sensor signal could be achieved. However, a significant drift could be observed owing to the breakage of filler networks and detachment of NR molecules from the CNT/CCB surfaces related to the extension of CNRC, as also found in the cyclic test displayed in Figure 11. Figure 15 shows no second peak even though it has been strained several times. Therefore, the bending motion of a soft tendon-based actuator can be detected by the CNRC with 5 phr mDES.

In an additional experiment, the actuator design and tendon material are changed, as shown in Figures 16. Based on these results, it can be proposed that the drift shown in Figure 15 is also affected by the actuator design and the tendon material. According to Figure 14, the design of the actuator is investigated by varying the thickness of the position at Actual $J(Y)$, which connects the Actual $P(X)$ and $P(Z)$ parts. Figure 16a shows the R_{rel} change of CNRC sensor fixed on the actuator with different thicknesses of Actual $J(Y)$, namely 2, 3, and 4 mm. It is seen that a similar monotonic sensor signal is represented for all different hinges, although the drifts are slightly

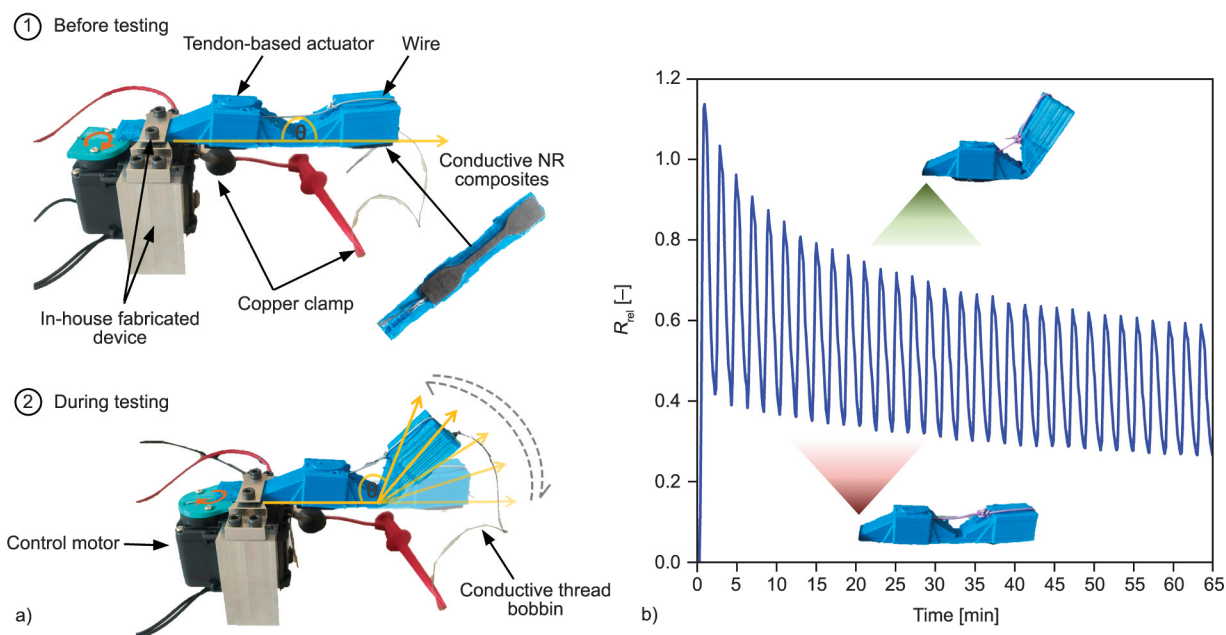


Figure 15. a) Steps of setting the tendon-based actuator with integrated CNRC sensor and b) the variation in resistance during the motion of the actuator.

different due to the difference in stress inside the hinge. Figure 16b shows the effect of the tendon cross section on the R_{rel} . The actuator with 3 mm of Actual $J(Y)$ was chosen for the test with different cross sections and cladding types of metal tendons such as 0.06 mm² (polytetrafluoroethylene, PTFE), 0.14 mm² (thermoplastic elastomer, TPE (styrene-ethylene-butylene-styrene copolymer)), 0.23 mm² (polyvinyl chloride, PVC) and 0.35 mm² (PVC). It is observed that the different tendon types exhibited slightly different drifts within the cyclic sensor signal. Also, in the case of PVCs with smaller tendon cross-sections, the greater R_{rel} changes of the CNRC sensors are observed. In addition, based on Figure 16, different drift values (DV) are represented where the different designs and tendons are shown. Here, the R_{rel} at 25 and 50 cycles are considered since the R_{rel} below 25 cycles is disturbed by filler-filler and rubber-filler attractions. The sensor with the lowest DV is recommended as the most stable sensor in the case

of the actuator with an actual $J(Y)$ of 3 mm by using a SEBS tendon with a 0.23 mm² area. It clarifies the possibility of the proposed CNRC to be used as a hyper-elastic sensor for a tendon-based actuator with a selected composite.

5. Conclusions

The processability, electrical conductivity, tensile properties, and piezoresistive behavior of the conductive NR/CNT-CCB composites (CNRC) filled with various mDES loadings were investigated in the presented work. The proper mDES (aZnO:DES) ratio in NR composite of 1:1 was obtained for achieving optimal elastic and electric properties. The combination of appropriate mDES promoted processability well with a shorter cure time and high tensile properties. Additional ionic linkages based on mDES-CNT and mDES-CCB with NR molecules under the proper mDES concentration were the reason behind the enhancement of composite properties. The wettability

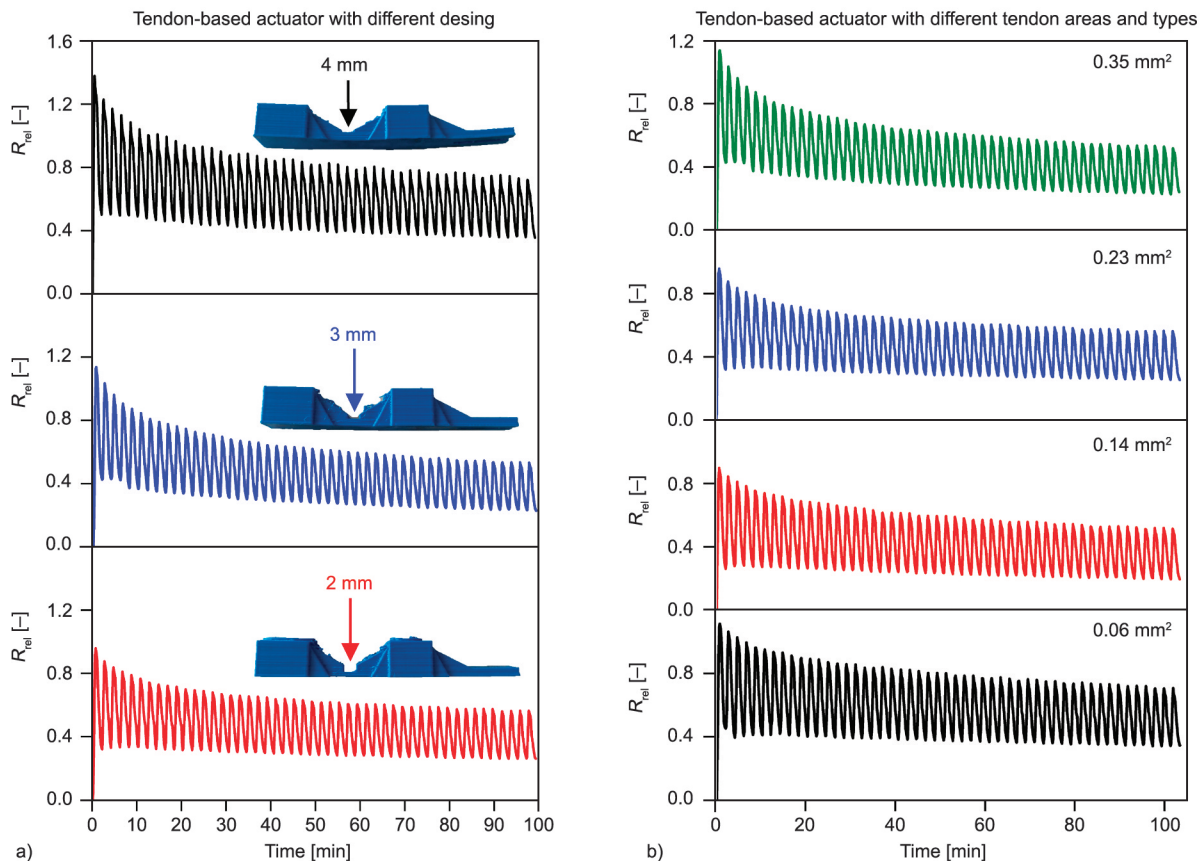


Figure 16. Variation in R_{rel} of CNRC sensor fixed on the actuator during the motion of actuator together with drift value (DV) calculated from $(C_{25} - C_{50}) \cdot 100 / C_{25}$. Where C_{25} and C_{50} refer to R_{rel} of the composites upon moving for 25 and 50 rounds, respectively. a) Different designs of the actuator by changing the thickness of the hinge at the position of Actual $J(Y)$ for 2 ($DV = 13.75$), 3 ($DV = 11.29$), and 4 ($DV = 12.20$) mm with the SEBS tendon area of 0.23 mm². b) Different tendon areas and types of PVC for 0.06 mm² ($DV = 13.25$) and 0.14 mm² ($DV = 10.86$), SEBS for 0.23 mm² ($DV = 11.63$) and PTFE for 0.35 mm² ($DV = 12.13$).

of mDES on the CNT-CCB surfaces provides the opportunity for electron movement even if it was bent from the un-proper relaxation degree of the rubber matrix. This causes CNRC in the presence of mDES to exhibit better sensing response with tunable positive piezoresistivity, while the negative result has occurred in the one without mDES. Under the virtual test of recoverability, reproducibility, and time dependence behavior, the present work demonstrates that the CNRC can be applied in strain sensor applications with balanced sensitivity of proper straining ratio, particularly for the monitoring tendon-based actuator motion. Tunable piezoresistive NR composite was identified as a functional material for newer applications in soft robotics and human body monitoring in the near future.

Acknowledgements

The authors gratefully acknowledge the financial support from the Post-doctoral Fellowship, King Mongkut's University of Technology Thonburi, and the Thailand Science Research and Innovation (TSRI) under Fundamental Fund 2022 (Project: Advanced Materials and Manufacturing for Applications in new S-curve industries). Also, the funding from the European Union's Horizon 2020 research and the Innovation Program under grant agreement No. 828818 (SHERO Project) and under Marie Skłodowska-Curie grant agreement No. 860108 (SMART PROJECT) are acknowledged.

References

- [1] Cetin M. S., Toprakci O., Toprakci H. A.: Flexible piezoresistive strain sensors based on carbonaceous filler/thermoplastic elastomer composites. in 'Theory and research in engineering II' (ed.: Kalkanci M.) Gece Publishing, Ankara, Vol. 1, 215–236 (2020).
- [2] Bilotti E., Zhang R., Deng H., Baxendale M., Peijs T.: Fabrication and property prediction of conductive and strain sensing TPU/CNT nanocomposite fibres. *Journal of Materials Chemistry A*, **20**, 9449–9455 (2010).
<https://doi.org/10.1039/C0JM01827A>
- [3] Zheng Y., Li Y., Dai K., Liu M., Zhou K., Zheng G., Liu C., Shen C.: Conductive thermoplastic polyurethane composites with tunable piezoresistivity by modulating the filler dimensionality for flexible strain sensors. *Composites Part A: Applied Science and Manufacturing*, **101**, 41–49 (2017).
<https://doi.org/10.1016/j.compositesa.2017.06.003>
- [4] Kumar S., Gupta T., Varadarajan K.: Strong, stretchable and ultrasensitive MWCNT/TPU nanocomposites for piezoresistive strain sensing. *Composites Part B: Engineering*, **177**, 107285 (2019).
<https://doi.org/10.1016/j.compositesb.2019.107285>
- [5] Sang Z., Ke K., Manas-Zloczower I.: Effect of carbon nanotube morphology on properties in thermoplastic elastomer composites for strain sensors. *Composites Part A: Applied Science and Manufacturing*, **121**, 207–212 (2019).
<https://doi.org/10.1016/j.compositesa.2019.03.007>
- [6] Melnykowycz M., Koll B., Scharf D., Clemens F.: Comparison of piezoresistive monofilament polymer sensors. *Sensors*, **14**, 1278–1294 (2014).
<https://doi.org/10.3390/s140101278>
- [7] Georgopoulou A., Sebastian T., Clemens F.: Thermoplastic elastomer composite filaments for strain sensing applications extruded with a fused deposition modelling 3D printer. *Flexible and Printed Electronics*, **5**, 035002 (2020).
<https://doi.org/10.1088/2058-8585/ab9a22>
- [8] Duan L., Fu S., Deng H., Zhang Q., Wang K., Chen F., Fu Q.: The resistivity-strain behavior of conductive polymer composites: Stability and sensitivity. *Journal of Materials Chemistry A*, **2**, 17085–17098 (2014).
<https://doi.org/10.1039/C4TA03645J>
- [9] Yang X., Sun L., Zhang C., Huang B., Chu Y., Zhan B.: Modulating the sensing behaviors of poly(styrene-ethylene-butylene-styrene)/carbon nanotubes with low-dimensional fillers for large deformation sensors. *Composites Part B: Engineering*, **160**, 605–614 (2019).
<https://doi.org/10.1016/j.compositesb.2018.12.119>
- [10] Amjadi M., Pichitpajongkit A., Lee S., Ryu S., Park I.: Highly stretchable and sensitive strain sensor based on silver nanowire-elastomer nanocomposite. *ACS Nano*, **8**, 5154–5163 (2014).
<https://doi.org/10.1021/nn501204t>
- [11] Zhang B., Li B., Jiang S.: Noncovalently functionalized multi-walled carbon nanotube with core-dualshell nanostructure for improved piezoresistive sensitivity of poly(dimethyl siloxane) nanocomposites. *Composites Part A: Applied Science and Manufacturing*, **94**, 124–132 (2017).
<https://doi.org/10.1016/j.compositesa.2016.12.008>
- [12] Nakaramontri Y., Kummerlöwe C., Nakason C., Pichaiyut S., Wisunthon S., Clemens F.: Piezoresistive carbon-based composites for sensor applications: Effects of polarity and non-rubber components on shape recovery. *Express Polymer Letters*, **14**, 970–988 (2020).
<https://doi.org/10.3144/expresspolymlett.2020.79>
- [13] Salaeh S., Das A., Stöckelhuber K. W., Wiessner S.: Fabrication of a strain sensor from a thermoplastic vulcanizate with an embedded interconnected conducting filler network. *Composites Part A: Applied Science and Manufacturing*, **130**, 105763 (2020).
<https://doi.org/10.1016/j.compositesa.2020.105763>
- [14] Iijima S.: Helical microtubules of graphitic carbon. *Nature*, **345**, 56–58 (1999).
<https://doi.org/10.1038/354056a0>

- [15] Nakaramontri Y., Nakason C., Kummerlöwe C., Vennemann N.: Influence of modified natural rubber on properties of natural rubber–carbon nanotube composites. *Rubber Chemistry and Technology*, **88**, 199–218 (2015).
<https://doi.org/10.5254/rct.14.85949>
- [16] Nakaramontri Y., Pichaiyut S., Wisunthorn S., Nakason C.: Hybrid carbon nanotubes and conductive carbon black in natural rubber composites to enhance electrical conductivity by reducing gaps separating carbon nanotube encapsulates. *European Polymer Journal*, **90**, 467–484 (2017).
<https://doi.org/10.1016/j.eurpolymj.2017.03.029>
- [17] Sumfleth J., Adroher X. C., Schulte K.: Synergistic effects in network formation and electrical properties of hybrid epoxy nanocomposites containing multi-wall carbon nanotubes and carbon black. *Journal of Materials Science*, **44**, 3241–3247 (2009).
<https://doi.org/10.1007/s10853-009-3434-7>
- [18] Ma P-C., Liu M-Y., Zhang H., Wang S-Q., Wang R., Wang K., Wong Y-K., Tang B-Z., Hong S-H., Paik K-W., Kim J-K.: Enhanced electrical conductivity of nanocomposites containing hybrid fillers of carbon nanotubes and carbon black. *ACS Applied Materials and Interfaces*, **1**, 1090–1096 (2009).
<https://doi.org/10.1021/am9000503>
- [19] Szeluga U., Kumanek B., Trzebicka B.: Synergy in hybrid polymer/nanocarbon composites. A review. *Composites Part A: Applied Science and Manufacturing*, **73**, 204–231 (2015).
<https://doi.org/10.1016/j.compositesa.2015.02.021>
- [20] Natarajan T. S., Eshwaran S. B., Stöckelhuber K. W., Wießner S., Pötschke P., Heinrich G., Das A.: Strong strain sensing performance of natural rubber nanocomposites. *ACS Applied Materials and Interfaces*, **95**, 4860–4872 (2017).
<https://doi.org/10.1021/acsami.6b13074>
- [21] Zhang X. W., Pan Y., Zheng Q., Yi X. S.: Piezoresistance of conductor filled insulator composites. *Polymer International*, **50**, 229–236 (2001).
[https://doi.org/10.1002/1097-0126\(200102\)50:2<229::AID-PI612>3.0.CO;2-U](https://doi.org/10.1002/1097-0126(200102)50:2<229::AID-PI612>3.0.CO;2-U)
- [22] Das A., Stöckelhuber K. W., Jurk R., Fritzsche J., Klüppel M., Heinrich G.: Coupling activity of ionic liquids between diene elastomers and multi-walled carbon nanotubes. *Carbon*, **47**, 3313–3321 (2009).
<https://doi.org/10.1016/j.carbon.2009.07.052>
- [23] Subramaniam K., Das A., Stöckelhuber K. W., Heinrich G.: Elastomer composites based on carbon nanotubes and ionic liquid. *Rubber Chemistry and Technology*, **86**, 367–400 (2013).
<https://doi.org/10.5254/rct.13.86984>
- [24] Maciejewska M., Zaborski M.: Effect of ionic liquids on the dispersion of zinc oxide and silica nanoparticles, vulcanisation behaviour and properties of NBR composites. *Express Polymer Letters*, **8**, 932–940 (2014).
<https://doi.org/10.3144/expresspolymlett.2014.94>
- [25] Azizi N., Dezfooli S., Hashemi M. M.: A sustainable approach to the Ugi reaction in deep eutectic solvent. *Comptes Rendus Chimie*, **16**, 1098–1102 (2013).
<https://doi.org/10.1016/j.crci.2013.05.013>
- [26] Sripornsawat B., Thitithammawong A., Tulaphol S., Johns J., Nakaramontri Y.: Positive synergistic effects on vulcanization, mechanical and electrical properties of using deep eutectic solvent in natural rubber vulcanizates. *Polymer Testing*, **96**, 107071 (2021).
<https://doi.org/10.1016/j.polymertesting.2021.107071>
- [27] Culha U., Nurzaman G., Clemens F., Lida F.: SVAS(3): Strain vector aided sensorization of soft structures. *Sensors*, **14**, 12748–12770 (2014).
<https://doi.org/10.1088/2058-8585/ab9a22>
- [28] Abbott A. P., Capper G., Davies D. L., Rasheed R. K., Tambyrajah V.: Novel solvent properties of choline chloride/urea mixtures. *Chemical Communications*, **1**, 70–71 (2003).
<https://doi.org/10.1039/B210714G>
- [29] Guggilla P., Batra A. K., Edwards M. E.: Electrical characterization of LiTaO₃:P(VDF–TrFE) composites. *Journal of Materials Science*, **44**, 5469–5474 (2009).
<https://doi.org/10.1007/s10853-009-3753-8>
- [30] Xiang D., Zhang X., Li Y., Harkin-Jones E., Zheng Y., Wang L., Zhao C., Wang P.: Enhanced performance of 3D printed highly elastic strain sensors of carbon nanotube/thermoplastic polyurethane nanocomposites via non-covalent interactions. *Composites Part B: Engineering*, **176**, 107250 (2019).
<https://doi.org/10.1016/j.compositesb.2019.107250>
- [31] Liu J., Liu Z., Li M., Zhao Y., Shan G., Hu M., Zheng D.: Polydimethylsiloxane nanocomposite filled with 3D carbon nanosheet frameworks for tensile and compressive strain sensors. *Composites Part B: Engineering* **168**, 175–182 (2019).
<https://doi.org/10.1016/j.compositesb.2018.12.089>
- [32] Georgopoulou A., Vanderborcht B., Clemens F.: Fabrication of a soft robotic gripper with integrated strain sensing elements using multi-material additive manufacturing. *Frontiers in Robotics and AI*, **8**, 615991 (2021).
<https://doi.org/10.3389/frobt.2021.615991>
- [33] Georgopoulou A., Michel S., Clemens F.: Sensorized robotic skin based on piezoresistive sensor fiber composites produced with injection molding of liquid silicone. *Polymers*, **13**, 1226 (2021).
<https://doi.org/10.3390/polym13081226>
- [34] Georgopoulou A., Bosman A. W., Brancart J., Vanderborcht B., Clemens F.: Supramolecular self-healing sensor fiber composites for damage detection in piezoresistive electronic skin for soft robots. *Polymers*, **13**, 2983 (2021).
<https://doi.org/10.3390/polym13172983>
- [35] Marzec A., Laskowska A., Boiteux G., Zaborski M., Gain O., Serghei A.: The impact of imidazolium ionic liquids on the properties of nitrile rubber composites. *European Polymer Journal*, **53**, 139–146 (2014).
<https://doi.org/10.1016/j.eurpolymj.2014.01.035>

- [36] Bevilacqua E. M., English E. S.: The scission step in hevea oxidation. *Journal of Polymer Science*, **49**, 495–505 (1961).
<https://doi.org/10.1002/pol.1961.1204915229>
- [37] Zheng W., Jia Z., Zhang Z., Yang W., Zhang L., Wu S.: Improvements of lanthanum complex on the thermal-oxidative stability of natural rubber. *Journal of Materials Science*, **51**, 9043–9056 (2016).
<https://doi.org/10.1007/s10853-016-0157-4>
- [38] Nakaramontri Y., Kummerlöwe C., Vennemann N., Wisunthorn S., Pichaiyut S., Nakason C.: Effect of bis(triethoxysilylpropyl) tetrasulfide (TESPT) on properties of carbon nanotubes and conductive carbon black hybrid filler filled natural rubber nanocomposites. *Express Polymer Letters*, **12**, 867–884 (2018).
<https://doi.org/10.3144/expresspolymlett.2018.75>
- [39] Le H. H., Pham T., Henning S., Klehm J., Wießner S., Stöckelhuber K.-W., Das A., Hoang X. T., Do Q. K., Wu M., Vennemann N., Heinrich G., Radusch H.-J.: Formation and stability of carbon nanotube network in natural rubber: Effect of non-rubber components. *Polymer*, **73**, 111–121 (2015).
<https://doi.org/10.1016/j.polymer.2015.07.044>
- [40] Chandra A., Bagchi B.: Frequency dependence of ionic conductivity of electrolyte solutions. *The Journal of Chemical Physics*, **112**, 1876–1886 (2000).
<https://doi.org/10.1063/1.480751>
- [41] Suzuki K., Yataka K., Okumiya Y., Sakakibara S., Sako K., Mimura H., Inoue Y.: Rapid-response, widely stretchable sensor of aligned MWCNT/elastomer composites for human motion detection. *ACS Sensors*, **1**, 817–825 (2016).
<https://doi.org/10.1021/acssensors.6b00145>
- [42] Duan L., D’Hooge D. R., Cardon L.: Recent progress on flexible and stretchable piezoresistive strain sensors: From design to application. *Progress in Materials Science*, **144**, 100617 (2020).
<https://doi.org/10.1016/j.pmatsci.2019.100617>
- [43] Sarkawi S. S., Dierkes W. K., Noordermeer J. W. M.: Morphology of silica-reinforced natural rubber: The effect of silane coupling agent. *Rubber Chemistry and Technology*, **88**, 359–372 (2015).
<https://doi.org/10.5254/rect.15.86936>
- [44] Matchawet S., Nakason C., Kaesaman A.: Electrical and mechanical properties of conductive carbon black filled epoxidized natural rubber. *Advanced Materials Research*, **844**, 255–258 (2014).
<https://doi.org/10.4028/www.scientific.net/AMR.844.255>
- [45] Matchawet S., Kaesaman A., Vennemann N., Kumerlöwe C., Nakason C.: Effects of imidazolium ionic liquid on cure characteristics, electrical conductivity and other related properties of epoxidized natural rubber vulcanizates. *European Polymer Journal*, **87**, 344–359 (2017).
<https://doi.org/10.1016/j.eurpolymj.2016.12.037>
- [46] Zhai W., Zhao S., Wang Y., Zheng G., Dai K., Liu C., Shen C.: Segregated conductive polymer composite with synergistically electrical and mechanical properties. *Composites Part A: Applied Science and Manufacturing*, **105**, 68–77 (2018).
<https://doi.org/10.1016/j.compositesa.2017.11.008>
- [47] Yu S., Wang X., Xiang H., Zhu L., Tebyetekerwa M., Zhu M.: Superior piezoresistive strain sensing behaviors of carbon nanotubes in one-dimensional polymer fiber structure. *Carbon*, **140**, 1–9 (2018).
<https://doi.org/10.1016/j.carbon.2018.08.028>
- [48] Georgopoulou A., Clemens F.: Piezoresistive elastomer-based composite strain sensors and their applications. *ACS Applied Electronic Material*, **2**, 1826–1842 (2020).
<https://doi.org/10.1021/acsaelm.0c00278>
- [49] Souri H., Banerjee H., Jusufi A., Radacsi N., Stokes A., Park I., Sitti M., Amjadi M.: Wearable and stretchable strain sensors: Materials, sensing mechanisms, and applications. *Advanced Intelligent Systems*, **8**, 2000039 (2020).
<https://doi.org/10.1002/aisy.202000039>
- [50] Wang Y., Wang Y., Yang Y.: Graphene–polymer nanocomposite-based redox-induced electricity for flexible self-powered strain sensors. *Advanced Energy Materials*, **8**, 1800961 (2018).
<https://doi.org/10.1002/aenm.201800961>
- [51] Sun J., Kormakov S., Liu Y., Huang Y., Wu D., Yang Z.: Recent progress in metal-based nanoparticles mediated photodynamic therapy. *Molecules*, **23**, 1704–1727 (2018).
<https://doi.org/10.3390/molecules23071704>
- [52] Shi J., Li X., Cheng H., Liu Z., Zhao L., Yang T., Dai Z., Cheng Z., Shi E., Yang L., Zhang Z., Cao A., Zhu H., Fang Y.: Graphene reinforced carbon nanotube networks for wearable strain sensors. *Advanced Functional Materials*, **26**, 2078–2084 (2016).
<https://doi.org/10.1002/adfm.201504804>
- [53] Hempel M., Nezhich D., Kong J., Hofmann M.: A novel class of strain gauges based on layered percolative films of 2D materials. *Nano Letters*, **12**, 5714–5718 (2012).
<https://doi.org/10.1021/nl302959a>
- [54] Lin L., Liu S., Zhang Q., Li X., Ji M., Deng H., Fu Q.: Towards tunable sensitivity of electrical property to strain for conductive polymer composites based on thermoplastic elastomer. *ACS Applied Materials and Interfaces*, **5**, 5815–5824 (2013).
<https://doi.org/10.1021/am401402x>
- [55] Zhou Y., Zhou Y., Deng H., Fu Q.: A novel route towards tunable piezoresistive behavior in conductive polymer composites: Addition of insulating filler with different size and surface characteristics. *Composites Part A: Applied Science and Manufacturing*, **96**, 99–109 (2017).
<https://doi.org/10.1016/j.compositesa.2017.02.002>

- [56] Zheng Y., Li Y., Dai K., Wang Y., Zheng G., Liu C., Shen C.: A highly stretchable and stable strain sensor based on hybrid carbon nanofillers/polydimethylsiloxane conductive composites for large human motions monitoring. *Composites Science and Technology*, **B**, 276–286 (2018).
<https://doi.org/10.1016/j.compscitech.2018.01.019>
- [57] Yamaguchi K., Thomas A. G., Busfield J. J. C.: Stress relaxation, creep and set recovery of elastomers. *International Journal of Non-Linear Mechanics*, **68**, 66–70 (2015).
<https://doi.org/10.1016/j.ijnonlinmec.2014.07.004>
- [58] Wang L., Ding T., Wang P.: Research on stress and electrical resistance of skin-sensing silicone rubber/carbon black nanocomposite during decompressive stress relaxation. *Smart Materials and Structures*, **18**, 065002 (2009).
<https://doi.org/10.1088/0964-1726/18/6/065002>

Research article

Optimizing interfacial interactions between functionalized graphene and chitosan for enhanced strength and toughness of composite films

Tengxin Zhang^{1,2}, Han Wang^{1,2}, Yabin Hao^{1,2}, Chang Liu^{1,2}, Yan Zhao³, You Zeng^{1,2*}

¹Shenyang National Laboratory for Materials Science, Institute of Metal Research, Chinese Academy of Sciences, 110016 Shenyang, P. R. China;

²School of Materials Science and Engineering, University of Science and Technology of China, 110016 Shenyang, P.R. China

³Ji Hua Laboratory, 528200 Foshan, P. R. China

Received 3 May 2022; accepted in revised form 25 August 2022

Abstract. Remarkable mechanical reinforcement of chitosan films using graphene is extremely important to greatly widen the practical application of chitosan (CS) in many fields, but there still exist challenges to regulating graphene-CS interactions for both enhanced strength and toughness. In this work, we functionalized graphene oxide (GO) with carboxyl (G-COOH) and amino groups (G-NH₂), and investigated the effects of interfacial interactions on the mechanical properties of graphene/CS composite films in detail. We found that the G-NH₂/CS composites exhibited the most remarkable reinforcement in both tensile strength and toughness than the GO/CS and G-COOH/CS composites, even different from a theoretical prediction on graphene-CS interactions. Such remarkable reinforcement is mainly attributed to the moderate graphene-CS interaction, uniform dispersion, and high alignment of G-NH₂ in CS films.

Keywords: nanocomposites, polymer composites, mechanical properties, graphene, interfacial interaction

1. Introduction

Chitosan (CS) is one of the most abundant natural macromolecules on the earth [1–3], and it has been widely used as a multi-functional film in the fields of food packaging, water treatment, and biomedical materials because of its good biocompatibility, bacterial resistance, adsorption capability, and biological degradability [4–7]. However, CS films generally possess unsatisfactory mechanical strength due to weak intermolecular interactions, which cannot meet gradually-increasing requirements of high strength and toughness for high-performance films such as medical bandages, wound dressing, and packaging materials [8, 9]. Recently, many methods of chemical cross-linkage, graft copolymerization, and functionalized

modification have been developed to improve the mechanical performance of CS films [10–12], but these chemical synthesis processes are rather complicated and time-consuming [13]. By contrast, directly adding nanofillers into the CS matrix has been proved to be an effective method for mechanical reinforcement in a simple way [14, 15].

For the achievement of remarkable mechanical reinforcement, high-level dispersion and strong nanofiller-CS interactions are two critical influencing factors [14]. It has been reported that nanofillers such as clay, montmorillonite, zeolite, and carbon nanotubes (CNTs) can be used to effectively improve the mechanical strength of CS matrix, but there still exist some problems of poor dispersion, severe aggregation,

*Corresponding author, e-mail: yuzeng@imr.ac.cn

© BME-PT

or entanglement of CNTs, resulting in unsatisfactory mechanical reinforcement [16, 17]. Graphene possesses unique two-dimensional graphitic structures, excellent mechanical performance, low density, and large diameter/thickness ratio, making it much easier to be well dispersed throughout the matrix than the entangled CNTs [18–20]. In addition, graphene can be further chemically modified to graft various chemical functional groups for forming good compatibility and strong interfacial interactions with CS [21, 22]. Graphene oxide (GO), as one derivative of graphene, possesses plenty of oxygen-containing functional groups to form strong interactions with CS through electrostatic attraction and hydrogen bonding [23, 24], greatly improving tensile strength and Young's modulus of CS films. Furthermore, grafting functional groups onto GO can effectively regulate interfacial interactions between graphene and CS for desired mechanical reinforcement [23, 25, 26]. Huang *et al.* [27] have prepared tea polyphenol-modified GO (TPG) and obtained TPG/CS composite films with improved mechanical strength due to homogeneous dispersion and strong interfacial interactions. In addition, trimethyl silane, phosphoric acid, and sulfonic acid have been grafted onto GO surfaces to increase the mechanical strength of CS films [28, 29]. On the other hand, graphene orientation, similar to biomimetic nacre structures, is also beneficial to realizing enhancement in both tensile strength and toughness of CS films [30, 31]. Although mechanical reinforcement of graphene/CS composites has been widely investigated, the intrinsic reinforcement mechanism based on graphene-CS interactions has not been clearly demonstrated. Zhang *et al.* [25] have theoretically calculated interaction energy between functionalized graphene (FG) and CS and reported that carboxyl groups of FG were much more beneficial to forming strong interfacial interactions with CS for remarkable reinforcement than hydroxyl and amino groups. It is worth pointing out that the ultimate mechanical properties of graphene/CS composites depend on not only the graphene-CS interactions but also the microstructures of composites. There still exist challenges to regulate graphene-CS interactions and microstructures for the high tensile strength and toughness of graphene/CS composites.

This work aims to fabricate high-performance graphene/CS composite films with high strength and toughness. It is the first time to clearly clarify interfacial interactions between functionalized graphene

(FG) and CS and to build a relationship of interfacial interactions with microstructures and ultimate mechanical properties for the fabrication of high-performance composites. We used GO as a precursor and prepared functionalized graphene with carboxyl groups (G-COOH) or amino groups (G-NH₂). Dispersion stability and rheological behavior of FG/CS solutions were measured to evaluate FG-CS interactions. The FG/CS composite films were fabricated using a solution-casting method, and their microstructures and mechanical properties were investigated in detail to establish a relationship between FG-CS interactions with mechanical reinforcement. We found that the G-COOH could form the strongest interactions with CS than the GO and G-NH₂ as theoretical prediction, but the G-NH₂/CS composites exhibited the highest tensile strength and toughness among all the composites. It reveals that the interfacial interaction plays an important role in greatly influencing the dispersion stability of FG/CS solutions, but the ultimate performance of FG/CS composites strongly depends on the microstructure and FG alignment. Comprehensive consideration of both interfacial interactions and resultant microstructures is extremely essential to designing and fabricating high-performance graphene/CS composite films with enhanced strength and toughness.

2. Experimental

2.1. Materials

Chitosan (CS, deacetylation degree of 88%, $M_w = 8000-20000$) was obtained from Sinopharm Chemical Reagent Co. Ltd in China. Graphene oxide (GO) was purchased from Sixth Element Materials Technology Co. Ltd. (Changzhou, China), and its layer numbers and lateral size were less than 10 graphitic layers and 5–15 μm , respectively. The GO possessed plenty of oxygen-containing functional groups, showing good aqueous dispersibility and high chemical activity. Analytic reagents of 65% nitric acid, 98% sulfuric acid, ethylenediamine (EDA), dimethylformamide (DMF), and glacial acetic acid were purchased from Sinopharm Chemical Reagent Co. Ltd. in China.

2.2. Synthesis of functionalized graphene

GO was used as a precursor to prepare functionalized graphene with carboxyl or amino groups. Carboxyl-functionalized graphene (G-COOH) was prepared as follows [32]: GO of 100 mg was weighed

and poured into a 40 ml mixed acid solution of HNO₃ and H₂SO₄ (volume ratio of 1:3). The GO-containing suspension was heated up to 80 °C and refluxed for 8 h. With the increment of carboxyl groups, the GO was further chemically oxidized into G-COOH. Thereafter, the obtained suspension was diluted and repeatedly washed with deionized water to remove residuals. After being freeze-dried at –55 °C for 24 h, G-COOH nanosheets were prepared. As for the preparation of amino-functionalized graphene (G-NH₂), 80 mg GO was put into 40 ml DMF and ultrasonically treated for 30 min, then 1.5 ml EDA was added to chemically react with GO in a sealed vessel at 80 °C for 8 h. The EDA could react with GO through nucleophilic substitution and amidation reaction, consequently introducing amino groups onto GO and obtaining G-NH₂ [33]. Thereafter, the G-NH₂-containing suspension was vacuum-filtrated and repeatedly washed out with deionized water for the removal of residuals. After freeze-drying at –55 °C for 24 h, G-NH₂ nanosheets were obtained.

2.3. Fabrication of FG/CS composite films

The GO, G-COOH, and G-NH₂ were weighed respectively and dispersed ultrasonically in deionized water to prepare 2 mg/ml FG suspensions. The obtained suspensions were poured into 2 wt% chitosan solutions which were prepared by dissolving chitosan into 1 vol% acetic acid solutions. The mixtures were mechanically stirred for 4 h to obtain a homogeneous dispersion of FG. Thereafter, the FG/CS mixtures were cast into plastic Petri dishes and dried in an oven at 37 °C for 48 h. As a result, FG/CS composite films with 1.5 wt% FG loadings and 0.06 mm thickness were obtained.

2.4. Characterization

Fourier transform infrared (FT-IR) and X-ray photoelectron (XPS) spectra of samples were recorded on Bruker Tensor 27 (Germany) and Escalab 250 (Thermo Scientific, USA), respectively for analyzing functional groups and elemental compositions. Raman spectra were measured to evaluate the structural integrity of samples by using Jobin Yvon LabRam HR800 (Horiba, France). An X-ray diffractometer (XRD, D/max 2400 with Cu K_α radiation, Japan) was used to characterize the crystalline structures of the samples. Optical microscopic images of FG/CS solutions were observed using Nikon Eclipse

LV100ND (Japan) at room temperature for evaluation of dispersion stability. Surface charges of FG in aqueous and CS solutions were measured using a Zeta potential analyzer (Malvern Zetasizer Nano-ZS90, UK). Particle size distribution of the FG and FG/CS clusters in aqueous solutions was measured using a laser particle size analyzer (Malvern Mastersizer 2000, UK). Microstructures of FG/CS composite films were observed using a scanning electron microscope (SEM, NavoSEM430, FEI, USA) at 10 kV.

2.5. Performance testing

The rheological behavior of FG/CS solutions was measured using a Pin's viscometer and a rotational rheometer (Haake Mars II, USA) equipped with a cone-partitioned plate fixture at shear rates ranging from 0.1 to 10 s⁻¹. Thermogravimetric analysis (TGA) was conducted on Netzsch STA-499C (Germany) at a heating rate of 10 °C/min from 30 to 700 °C in an argon atmosphere to evaluate the effect of FG-CS interactions on the thermal stability of composites. Mechanical properties of composite films were measured with a dynamic mechanical analyzer (DMA Q800, TA Instrument, USA) in a tensile mode at a force-loading speed of 1 N/min at room temperature, and the specimen size was 40 mm × 3 mm × 0.06 mm.

3. Results and discussion

3.1. Preparation and characterization of functionalized graphene

Functionalized graphene with carboxyl or amino groups was prepared using GO as a precursor. The preparation mechanism and chemical compositions of the GO, G-COOH, and G-NH₂ were shown in Figure 1. As shown in Figure 1a, the GO prepared by Hummers' method possesses numerous hydroxyl, epoxy, and carboxyl groups, and they can be easily modified into various functionalized graphene [34]. In this work, the G-COOH was prepared by chemically oxidizing GO with increased contents of carboxyl groups [35], and the G-NH₂ was obtained through nucleophilic substitution and amidation reaction between GO and EDA [33]. These above-mentioned reactions are mild and easily operated without severely destroying graphitic structures of GO, and all the FG show a similar particle size distribution in Figure 1b. The changes in functional groups before and after modification can be confirmed from FT-IR analysis (see Figure 1c). The GO shows characteristic peaks at 1720, 1230, and 1050 cm⁻¹, corresponding

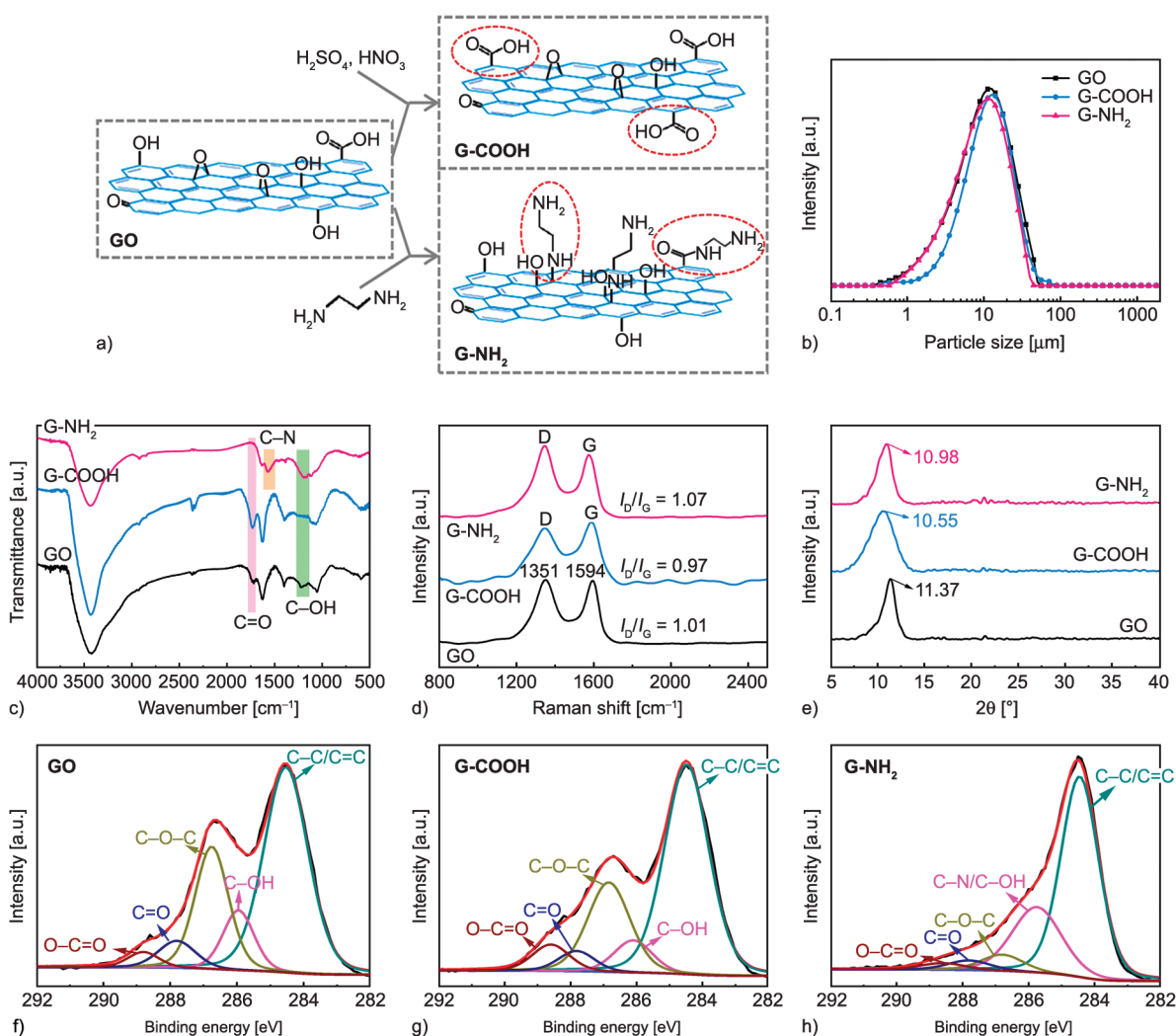


Figure 1. (a) Preparation schematic of functionalized graphene with carboxyl and amino groups. (b) Particle size distribution, (c) FT-IR spectra, (d) Raman spectra, (e) XRD patterns, and (f–h) C1s XPS spectra of the GO, G-COOH, and G-NH₂.

to stretching vibrations of C=O from COOH, C–OH, and C–O–C, respectively [36, 37]. The G-COOH exhibits an enhanced relative intensity at 1720 cm⁻¹ and a weakened vibration peak at 1230 cm⁻¹, revealing that the C–OH was chemically oxidized into COOH [36]. For the G-NH₂, its characteristic peaks at 1720 and 1050 cm⁻¹ were weakened with increased intensities at 1564 and 1230 cm⁻¹, implying that the amino groups were covalently grafted onto GO nanosheets [33].

Microstructures of the FG were determined by Raman and XRD (see Figures 1d–1e). It can be seen that all the FG show Raman characteristic peaks with D and G bands at 1351 and 1594 cm⁻¹, and similar XRD diffraction peaks at about 11°, implying that the chemical modification has not severely destroyed the graphitic structures of graphene. We can still find slight changes in the intensity ratio of the D band to G band (I_D/I_G) due to the introduction of edge defects

during modification [38]. In addition, slight shifts of the diffraction peak towards low degree after modification indicate enlarged lamellar spacing from lamellar repulsion and steric hindrance caused by carboxyl and amino groups [39]. Figures 1f–1h show XPS spectra of FG for the characterization of chemical compositions. The increased intensities of the O–C=O peak at 288.6 eV for G-COOH and the C–N peak at 285.8 eV for G-NH₂ also confirm the presence of carboxyl and amino groups [37], which is consistent with the FT-IR analysis. Therefore, the functionalized graphene with carboxyl or amino groups was obtained by chemical modification without severely destroying the microstructure of graphene.

3.2. Dispersion of FG in CS solutions

These FG with various functional groups can form different interactions with CS, greatly influencing the dispersion of FG in CS solutions. Figure 2 shows

dispersion stability, surface charge (zeta potential), and size distribution of FG/CS solutions. It can be seen from Figure 2a that the GO, G-COOH, and G-NH₂ show distinct dispersion stability in CS solutions after 12 h settlement. The G-COOH exhibits the poorest stability in the CS solution accompanied by obvious aggregation, while the GO and G-NH₂ show satisfactory dispersion stability. Such phenomena can also be observed from optical microscopic images in Figures 2b–2e. We can see several aggregations of large-size clusters in the G-COOH/CS solution, followed by the GO/CS solution. By contrast, the G-NH₂ shows homogenous dispersion in the CS solution without apparent aggregation. Notably, all these FG possess nearly the same particle size and distribution shown in Figure 1b, but they exhibit distinct aggregation and particle sizes in CS solutions, which is closely associated with interfacial interactions of FG with CS.

We measured the Zeta potentials of the CS, FG, and FG/CS solutions for elucidation of the surface charges and FG-CS interactions (see Figure 2f). We can see that the CS exhibits a typical positive-charge characteristic with a Zeta potential of 66.6 mV due to amine protonation of CS in weak acid conditions [40]. The GO and G-COOH show negative surface charges with Zeta potentials of -40.9 and -54.8 mV in the presence of carboxyl groups respectively, while the G-NH₂ exhibits typical positive surface charges with a 14.2 mV potential. These diverse surface charges of FG can form distinct interactions with positive-charge CS. First of all, the G-COOH possesses plenty of carboxyl groups and exhibits much more negative charges than the GO, and it can form stronger interactions with CS through electrostatic attraction. By contrast, the G-NH₂ shows the same positive charges with CS, and its interactions with CS are much lower than that of the G-COOH and GO. Notably, we can

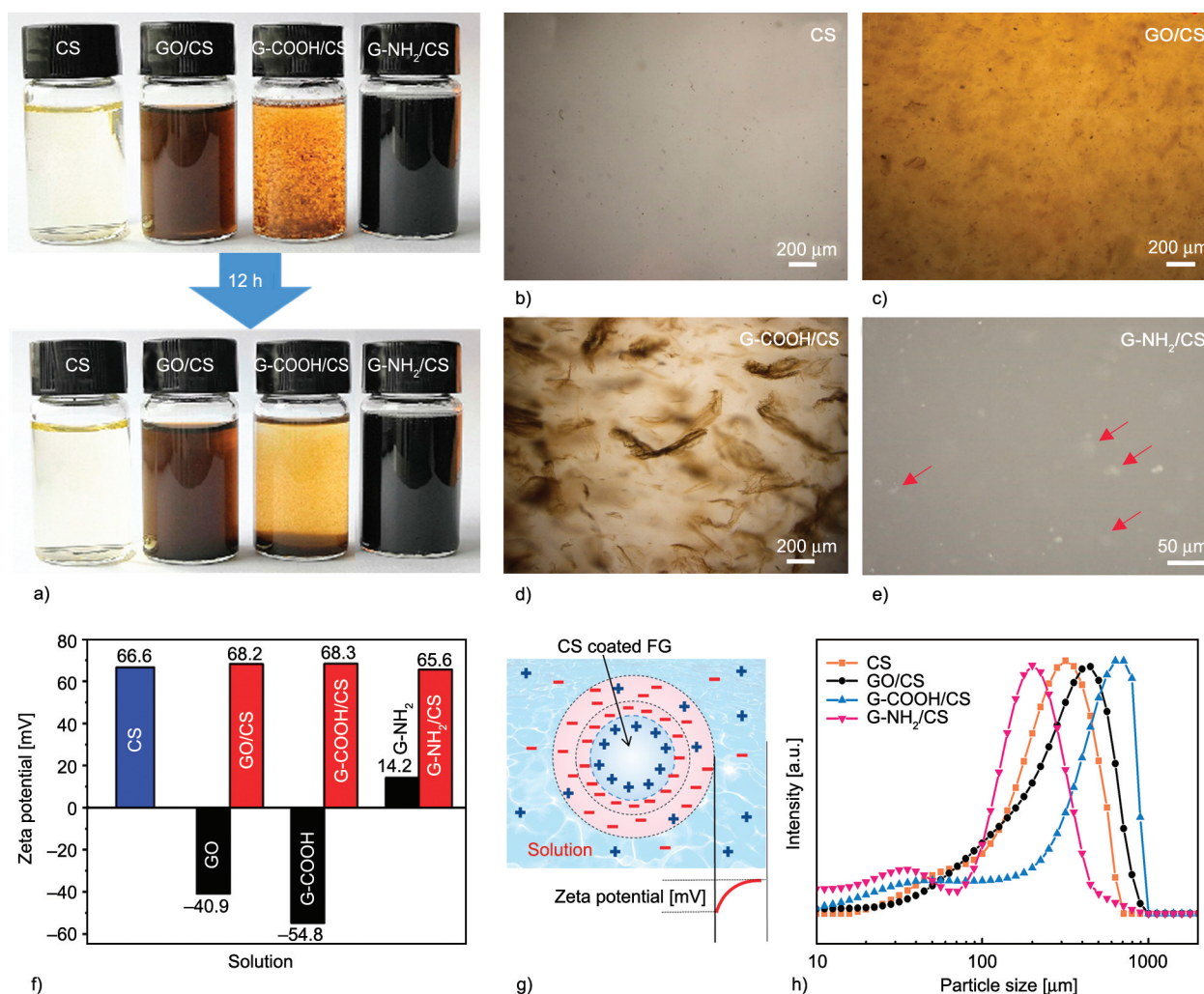


Figure 2. (a) Dispersion stability of FG/CS solutions. Optical micrographs of the (b) CS, (c) GO/CS, (d) G-COOH/CS, (e) G-NH₂/CS solutions. (f) Zeta potentials of the FG and FG/CS solutions. (g) Schematic of surface charges of FG in CS solutions. (h) Particle size distribution of the CS and FG/CS solutions.

see in Figure 2f that all the FG/CS solutions exhibit nearly the same potential of about 67 mV as the CS solution, implying that the FG surfaces were covered with positive-charge CS. It is because the FG possesses high surface energy and spontaneously adsorb CS onto its surfaces for charge balance, as shown in Figure 2g, resulting in the formation of CS-coated FG clusters and resultant positive Zeta potentials.

We further measured the particle size distribution of FG/CS solutions using a laser particle size analyzer (see Figure 2h). It can be seen clearly that the G-COOH/CS exhibits the largest average particle size of about 700 μm , much higher than that for the GO/CS and G-NH₂/CS. The G-COOH possesses plenty of negative surface charges, and it can form extremely strong interactions with CS and adsorb much more CS onto G-COOH surfaces, resulting in the formation of large-size GOOH/CS clusters, severe aggregation, and poor dispersion stability (see Figure 2d). Compared with the G-COOH/CS solution, the GO/CS solution exhibits a smaller cluster size and better dispersion stability due to the weaker interactions. For the G-NH₂ with positive surface charges, it can form the weakest interactions with CS, consequently resulting in the smallest size of clusters and the best dispersion stability. Therefore, the FG with various functional groups can form distinct interactions with CS, strongly influencing the aggregation and dispersion stability of FG/CS solutions.

3.3. Rheological behavior of FG/CS solutions

We measured the rheological behavior of FG/CS solutions to investigate the effect of FG-CS interactions on solution viscosity, as shown in Figure 3. It can be seen from Figure 3a that all the FG/CS solutions exhibit higher dynamic viscosity than the CS solution, indicating that the presence of FG can result in increased viscosity by hindering the motion of CS chains to some extent. Among all the FG/CS solutions, the G-NH₂/CS solution exhibits the lowest viscosity, followed by the G-COOH and GO/CS solutions. Such the same tendency can also be observed from kinematic viscosity measured using Pin's viscometers (see Figure 3b). The viscosity of fluid generally reflects the resistance to gradual deformation by shear or tensile stress, which is closely associated with inter-molecular friction and interactions between particles [8]. Figure 3c illustrates the FG-CS interactions and FG aggregation (FG/CS cluster) in CS solutions. As mentioned above, the GO and

G-COOH with negative charges can form strong electrostatic attractions with the CS and result in the formation of large-size clusters, consequently causing increased friction resistance and high viscosity. By contrast, the G-NH₂ with positive charges possesses moderate interactions with CS, and they can form small-size G-NH₂/CS clusters, resulting in decreased resistance and low viscosity for high dispersion stability. Therefore, the rheological behavior of FG/CS solutions strongly depends on the FG-CS interaction, friction resistance, and cluster size. The low viscosity of G-NH₂/CS solutions is beneficial to realizing homogenous dispersion and high orientation of the G-NH₂ in the CS matrix for remarkable mechanical reinforcement.

3.4. Fabrication and microstructures of FG/CS composite films

The FG/CS composite films were prepared using the solution-casting technique, and their SEM images are shown in Figure 4. In comparison with smooth fracture surfaces of the CS film, the FG/CS composites exhibit coarse and rough surfaces, and some FG aggregation can be observed. Among all the composites, the G-COOH/CS composites show the most severe aggregation in Figure 4c, mainly attributed to the large size of G-COOH/CS clusters and inhomogeneous dispersion. By contrast, the GO/CS and G-NH₂/CS composites show homogenous dispersion due to their small-size clusters and slight aggregation. Notably, we can see highly-aligned G-NH₂ in CS matrix along in-plane directions (see Figure 4d), which is closely associated with the high motion ability of the small-size clusters. During the fabrication of composite films, the G-NH₂ can be easily dispersed and aligned along the in-plane direction under interlaminar shearing forces. Such alignment of G-NH₂ in CS matrix is beneficial to improving both strength and toughness of composite films.

3.5. Interfacial interactions and thermal stability of FG/CS composites

Interfacial interactions between FG and CS in composite films were characterized using FT-IR and Raman techniques, as shown in Figure 5. It can be seen from Figure 5a that the CS films show typical characteristic peaks at 1630, 1402, and 1560 cm^{-1} , corresponding to vibrations of the C=O from amide I, C–N from amide III, and the N–H bending, respectively [41]. After adding GO into CS films, the adsorption

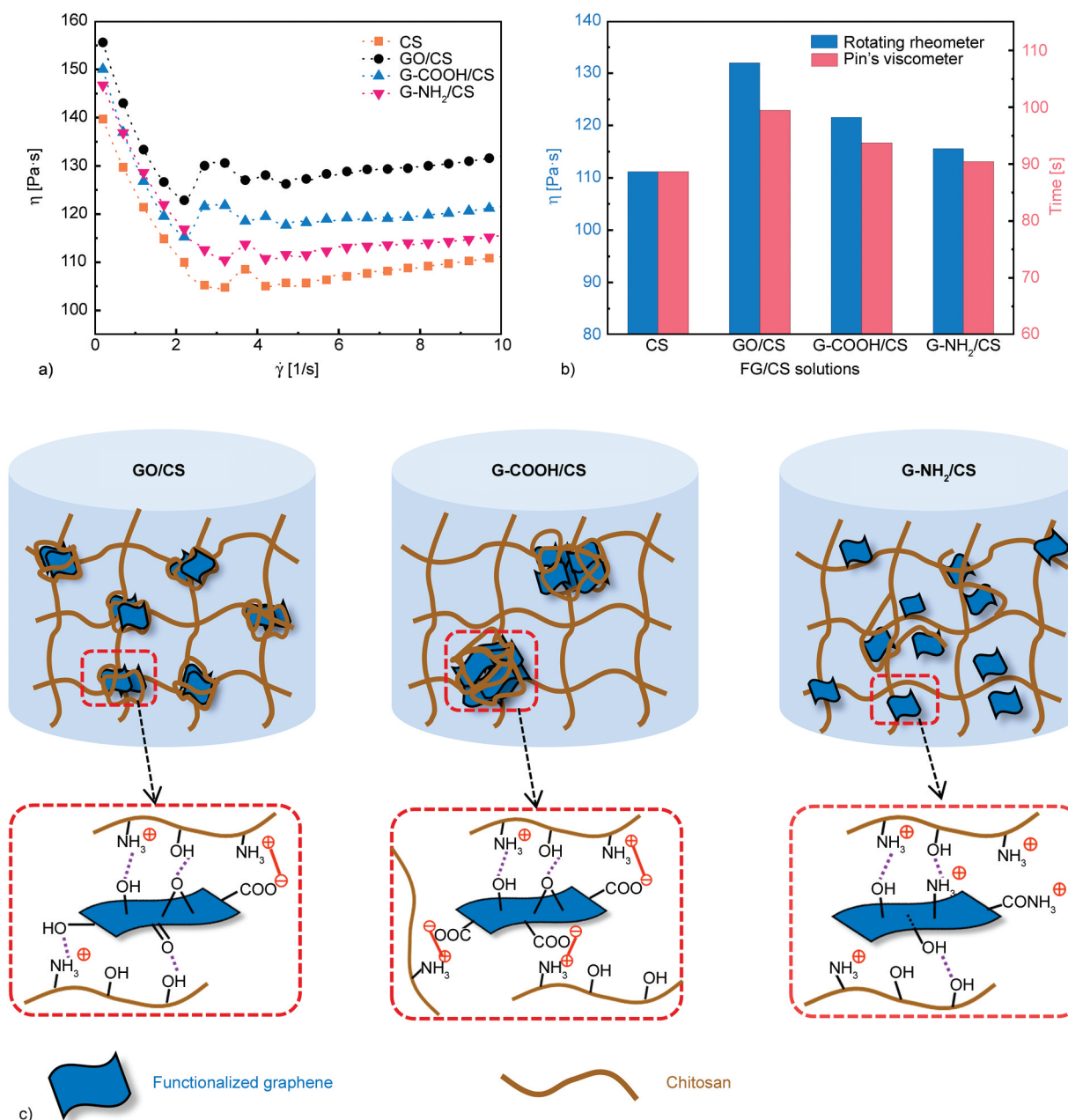


Figure 3. Viscosity of FG/CS solutions measured using (a) rotational rheometer and (b) Pin's viscometer. (c) Schematics of interaction and aggregation of the GO/CS, G-COOH/CS, and G-NH₂/CS solutions.

bands for C=O and C–N shift to 1635 and 1397 cm⁻¹, respectively, more susceptible to that for N–H, which is consistent with that reported in the literature [41, 42]. These shifts of characteristic peaks are mainly attributed to the graphene-CS interactions through hydrogen bonds and electrostatic attractions. In our work, the G-COOH/CS composites exhibit the largest shift, followed by the GO/CS and G-NH₂/CS, indicating that the G-COOH can form stronger interactions with CS than the GO and G-NH₂. Such strong interactions can also be confirmed through Raman analysis shown in Figure 5b. The G-COOH/CS composites exhibit the I_D/I_G value of 1.05, higher

than 0.97 for the corresponding G-COOH shown in Figure 1d. Such increased values imply additional defects caused by electrostatic attractions with CS [43]. In our work, the G-COOH/CS composites exhibit the largest I_D/I_G increment than the GO/CS and G-NH₂/CS composites, revealing that the G-COOH can form the strongest interactions with CS, followed by the GO and G-NH₂.

The thermal stability of the FG/CS composites was investigated and shown in Figures 5c–5d. It can be seen that all the FG/CS composites exhibit higher thermal stability than the CS because the presence of FG can effectively hinder the motion of CS chains at

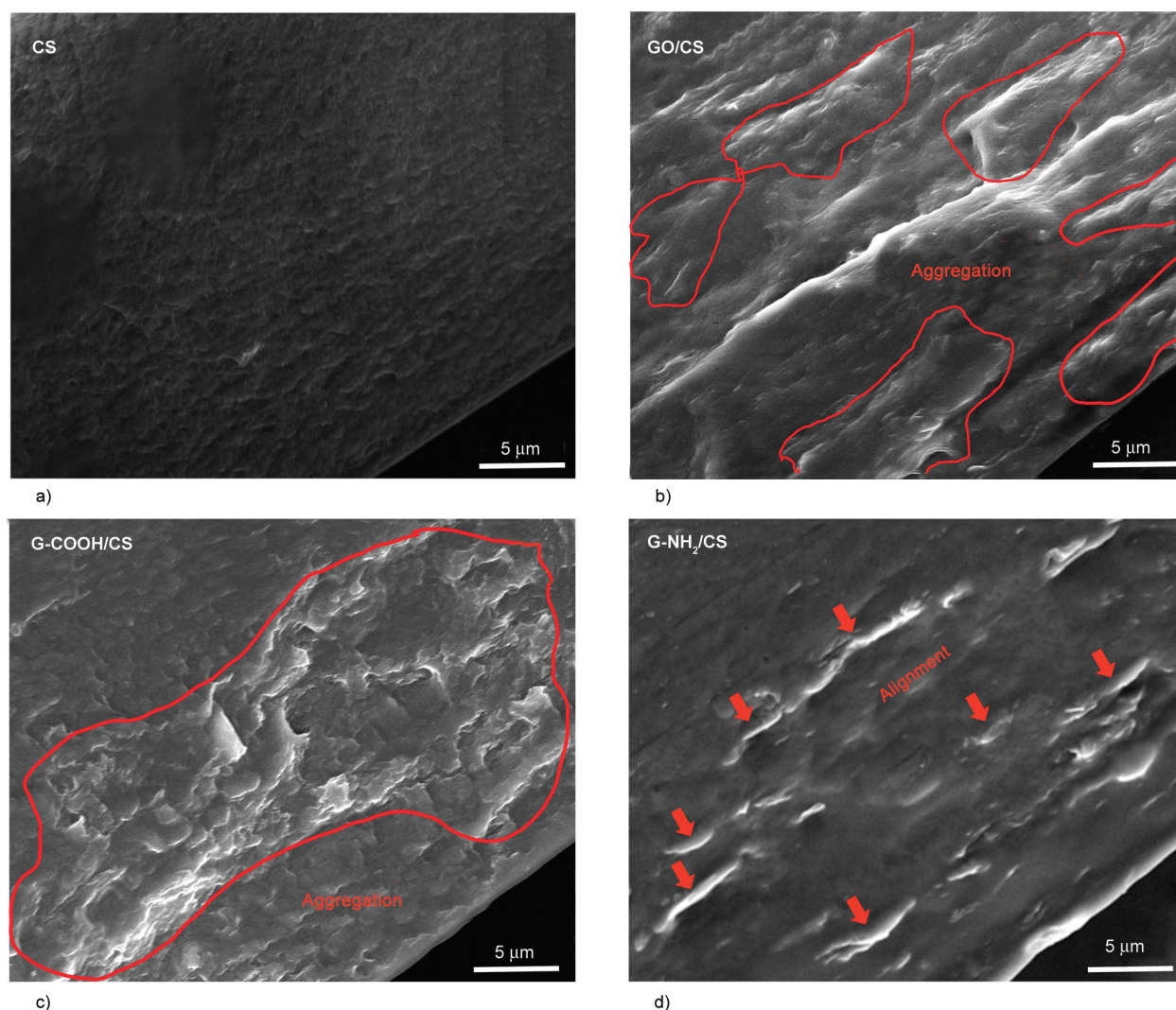


Figure 4. SEM images of (a) the CS, (b) GO/CS, (c) G-COOH/CS, and (d) G-NH₂/CS composite films.

elevated temperatures. Among all the FG/CS composites, the GO/CS and G-COOH/CS composites show higher thermal stability than the G-NH₂/CS composites because of their stronger interactions with CS. Notably, the GO/CS composites show much higher stability than the G-COOH/CS composites, although the GO possesses weaker interactions with CS than the G-COOH. It is mainly attributed to the better dispersion of GO in CS matrix (see Figure 4), effectively restricting CS chain motions and resulting in high thermal stability of composites [41]. Therefore, the FG/CS composites exhibit improved thermal stability of CS, which is closely associated with strong interfacial interactions.

3.6. Mechanical properties of FG/CS composite films

Tensile properties of the FG/CS composites were measured to evaluate the reinforcing effect of the FG with various functional groups, as shown in Figure 6.

It can be seen from Figure 6a that the G-NH₂/CS and GO/CS composites exhibit much higher tensile strength and elastic modulus (slopes of the initial linear region) than the CS, indicating that the presence of FG can significantly enhance the mechanical properties of CS films. As shown in Figure 6b, the tensile strength of the G-NH₂/CS and GO/CS composites is up to 81.8 and 75.8 MPa, respectively, increasing by 24.7 and 15.5% in comparison with 65.6 MPa for the CS films. It is notable that the G-COOH/CS composites show even lower tensile strength than the CS films despite the extremely strong interactions between G-COOH and CS, which is mainly attributed to the poor dispersion of the large-size clusters shown in Figure 4c. In comparison with satisfactory dispersion of the GO and G-NH₂ in the CS matrix, the G-COOH is prone to severely aggregate with CS through excessive interactions and form large-size clusters, consequently resulting in poor dispersion and unsatisfactory reinforcement.

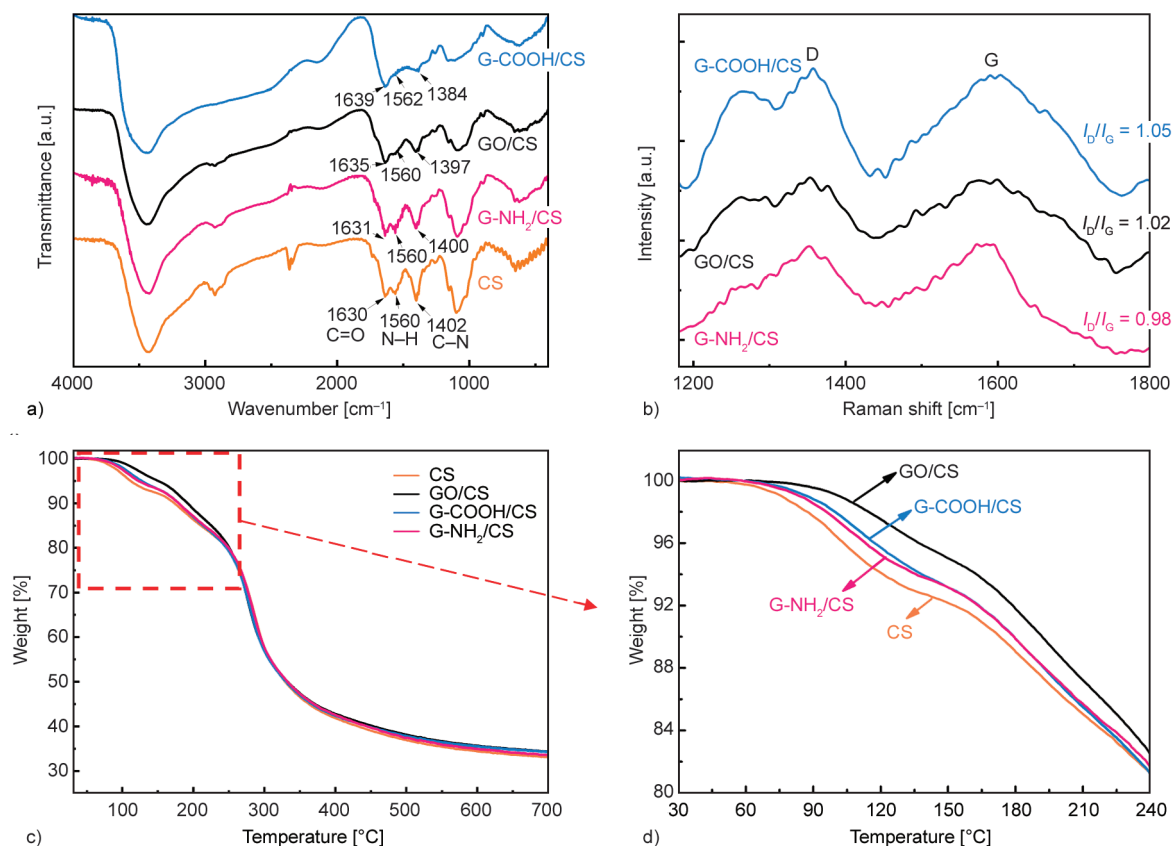


Figure 5. (a) FT-IR and (b) Raman spectra, and (c, d) thermogravimetric curves of FG/CS composite films.

We further compared the elongation at break and tensile toughness of FG/CS composites. It can be seen from Figures 6c–6d that the G-NH₂/CS composites exhibit the maximum elongation at break (22.4%) and highest tensile toughness (16.2 MJ/m³) among all the composites. It means that the presence of G-NH₂ can increase not only the tensile strength but also the tensile toughness of CS. Such remarkable reinforcement is mainly attributed to the uniform dispersion and highly-aligned structure along tensile directions. It has been reported that the alignment of graphene is beneficial to effectively transferring stress and dissipating fracture energy through interfacial friction slipping [31], consequently resulting in enhanced strength and toughness of composites. In our work, the G-NH₂ possesses moderate interactions with CS and forms small-size G-NH₂/CS clusters, and it is much easier to be well dispersed and form highly-aligned structures during the fabrication process. Such high alignment of G-NH₂ plays an important role in greatly improving the tensile strength and toughness of composites. By contrast, the G-COOH/CS and GO/CS composites exhibit even lower elongation at break and tensile toughness than the CS films in spite of their strong FG-CS interactions,

mainly attributed to the unsatisfactory dispersion and random orientation. Therefore, the mechanical reinforcement of FG/CS composites depends on not only the strong interfacial interactions but also the uniform dispersion and aligned microstructures.

We further compared the mechanical reinforcement in our work with that of other graphene/CS composites reported in the literature. It has been reported that graphene can increase tensile strength and elastic modulus of CS, but sacrifice the tensile toughness with reduced elongation at break by 30, 55, 71, 11, and 10% for GO/CS [27], tea polyphenols-GO/CS [44], sulphonated graphene/CS [28], RGO/CS [45], trimethyl silane-GO/CS [29], respectively. In our work, the G-COOH/CS and GO/CS composites also show reduced toughness and elongation at break than the CS films, consistent with that reported in the literature. It is worth pointing out that the 1.5 wt% G-NH₂/CS composites exhibit remarkable reinforcement in both the tensile strength and toughness, respectively increasing by 24.7 and 37.3% in comparison with the CS films. Such remarkable enhancement is mainly attributed to the uniform dispersion and high alignment of G-NH₂ in CS matrix.

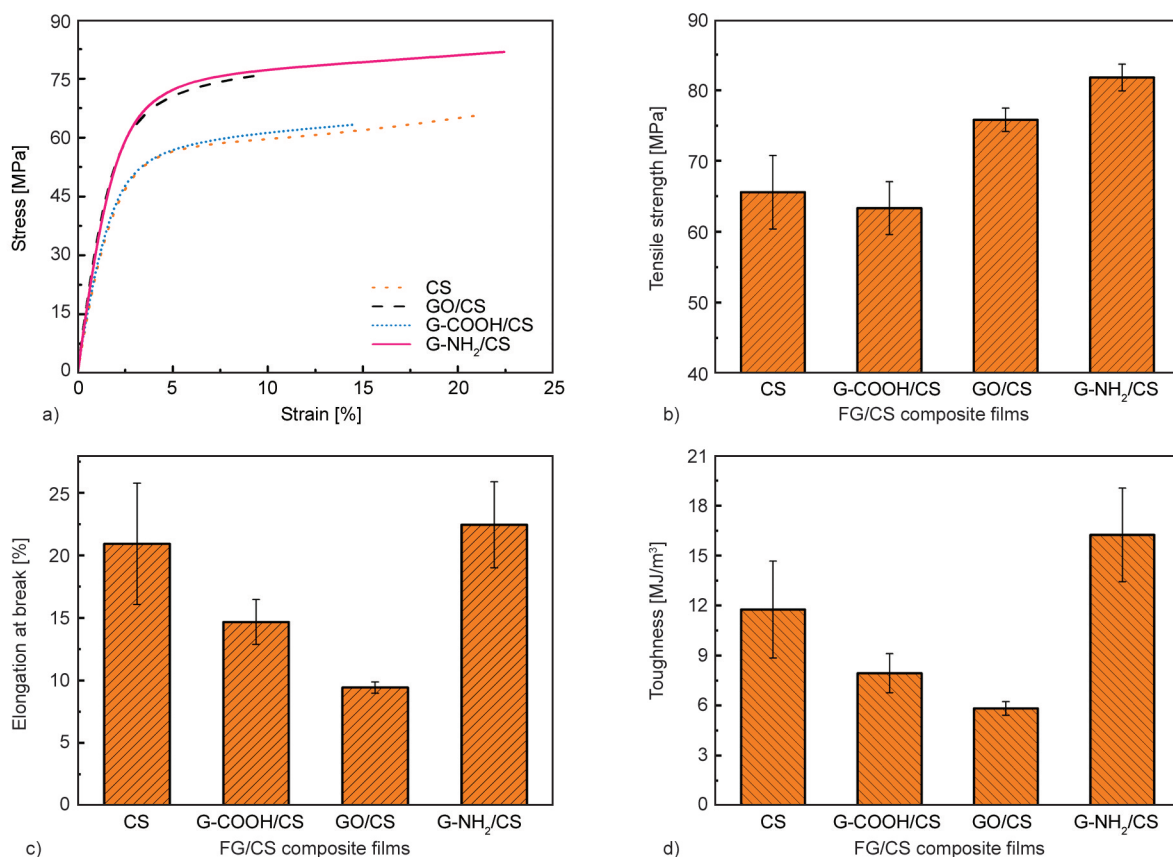


Figure 6. (a) Stress-strain curves, (b) ultimate tensile strength, (c) elongation at break, and (d) tensile toughness of FG/CS composite films.

3.7. Mechanism on improved strength and toughness of FG/CS composites

Figure 7 illustrates the reinforcing mechanism of FG/CS composites. It reveals that the FG with various functional groups can form distinct FG-CS interactions and diverse-size FG/CS clusters, greatly influencing the mechanical strength and toughness of composites. We can see from Figure 7a that the G-COOH can form the strongest interactions with CS as the theoretical prediction but causes severe aggregation, poor dispersion, and decreased mechanical performance (see Figure 7b). For the GO/CS composites, their GO-CS interactions are lower than that of the G-COOH/CS composites, and the GO can be well dispersed throughout the CS matrix, resulting in increased tensile strength (see Figure 7b). Notably, the GO/CS composites still exhibit lower elongation at break, and tensile toughness than the CS, which is because the medium-size GO/CS clusters are still rather difficult to be highly aligned in high-viscosity GO/CS solutions during fabrication. As a result, the random orientation of GO in the CS matrix improves the tensile strength of CS by sacrificing the tensile

toughness, which is consistent with that reported in the literature [8, 27, 44].

As for the G-NH₂/CS composites, the G-NH₂ can form moderate interactions with CS through hydrogen bonds [46], and it can be uniformly dispersed in the CS solution without obvious aggregation. The small-size G-NH₂/CS clusters can be easily aligned in the CS matrix during the fabrication of composite films (see Figure 7a). Such alignment of the G-NH₂ plays an important role in greatly increasing the pulling force of graphene out of the matrix and dissipating fracture energy [31, 47]. Therefore, the G-NH₂/CS composites exhibit remarkable enhancement in tensile strength and toughness, which is mainly attributed to the moderate interfacial interaction, small-size cluster, and high alignment of G-NH₂ in CS matrix. As mentioned above, theoretical calculation predicted that carboxyl groups could form much stronger interfacial interactions with CS than the hydroxyl and amino groups for remarkable mechanical reinforcement [25]. But, in our work, the G-COOH/CS composites exhibit the lowest tensile strength and toughness among all the composites. It

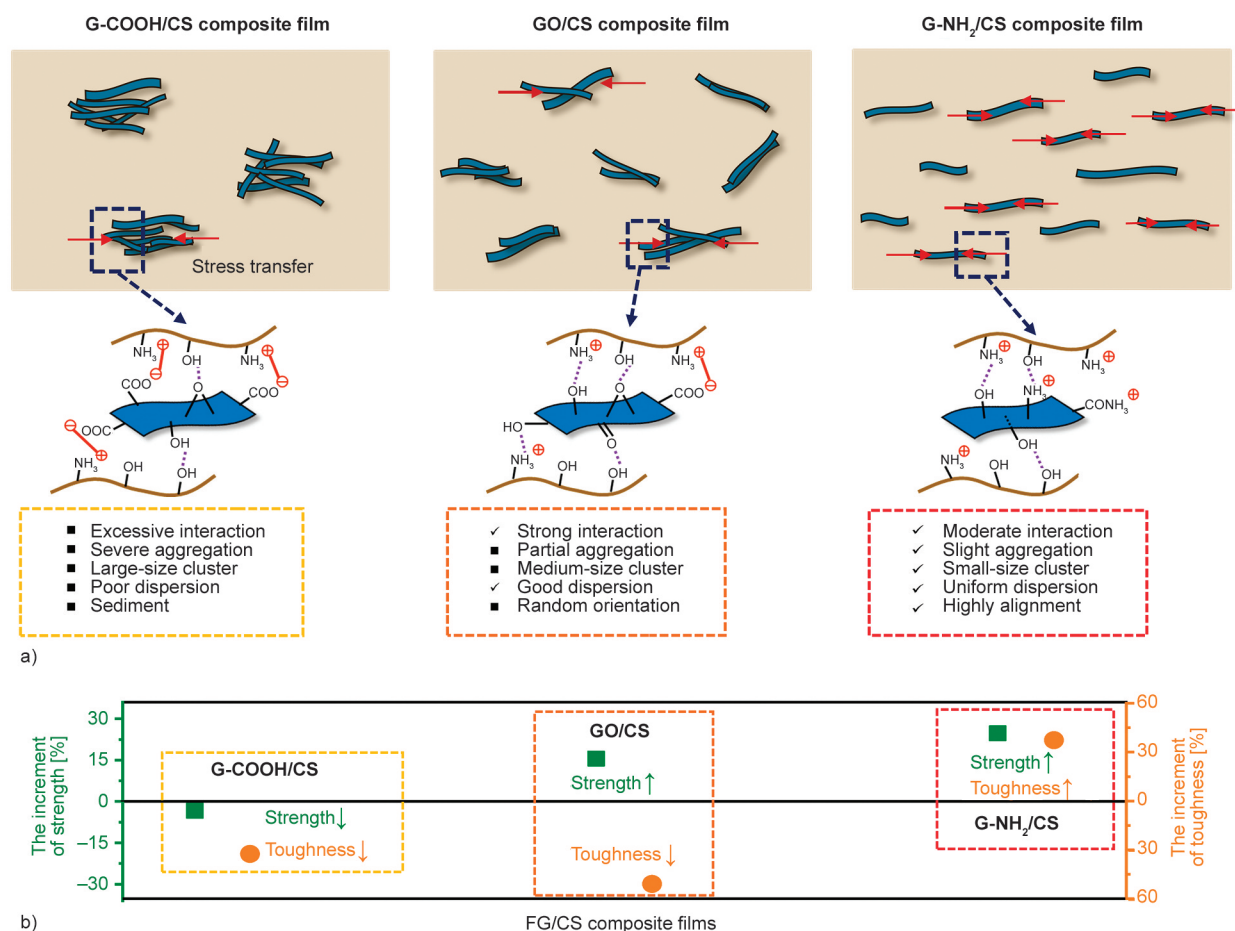


Figure 7. (a) Schematic of FG aggregation based on FG-CS interactions, and (b) the resultant mechanical reinforcement in tensile strength and toughness of FG/CS composites.

indicates that the mechanical reinforcement of graphene/CS composites depends on not only the graphene-CS interactions but also the dispersion stability, rheological behavior, microstructure, and alignment of graphene in the CS matrix. Notably, some influencing factors, such as molecular weight, deacetylation degree, preparation condition, and crystallinity degrees, should be comprehensively considered for the fabrication of high-performance graphene/CS composite films.

4. Conclusions

In this work, the interfacial interactions between CS and functionalized graphene of GO, G-COOH, and G-NH₂ were investigated to clarify the effect of FG-CS interactions on the mechanical properties of FG/CS composite films. The chemical compositions, dispersion stability, rheological behavior, microstructure, thermal stability, tensile strength and toughness of composites were measured in detail. Although theoretical calculation predicted that the G-COOH could form extremely strong interactions with CS for

remarkable mechanical reinforcement, we found that the excessive interactions could inevitably result in severe G-COOH aggregation in solutions, inhomogeneous dispersion, and decreased mechanical performance of composites. By contrast, the G-NH₂/CS composites exhibit remarkable enhancement in both tensile strength and toughness, which is mainly attributed to the moderate interaction, uniform dispersion, and highly-aligned structures. By virtue of their high strength and toughness, the G-NH₂/CS composites show great potential to be used as high-performance films in the field of packaging and biomedical materials.

Acknowledgements

This work was supported by the National Natural Science Foundation of China (Nos. 51802317, 52130209), Liaoning Natural Science Foundation (No. 2019JH3/30100008), and the Opening Foundation of Shanxi Key Laboratory of Nano & Functional Composite Materials (NFCM202102), Shenyang National Laboratory for Materials Science (2021-FP31), and IMR Innovation Fund (2022-PY07).

References





- [1] Pillai C. K. S., Paul W., Sharma C. P.: Chitin and chitosan polymers: Chemistry, solubility and fiber formation. *Progress in Polymer Science*, **34**, 641–678 (2009). <https://doi.org/10.1016/j.progpolymsci.2009.04.001>
- [2] Rinaudo M.: Chitin and chitosan: Properties and applications. *Progress in Polymer Science*, **31**, 603–632 (2006). <https://doi.org/10.1016/j.progpolymsci.2006.06.001>
- [3] Hejazi M., Behzad T., Heidarian P., Nasri-Nasrabadi B.: A study of the effects of acid, plasticizer, cross-linker, and extracted chitin nanofibers on the properties of chitosan biofilm. *Composites Part A: Applied Science and Manufacturing*, **109**, 221–231 (2018). <https://doi.org/10.1016/j.compositesa.2018.02.038>
- [4] Sirajudheen P., Poovathumkuzhi N. C., Vigneshwaran S., Chelaveettil B. M., Meenakshi S.: Applications of chitin and chitosan based biomaterials for the adsorptive removal of textile dyes from water – A comprehensive review. *Carbohydrate Polymers*, **273**, 118604 (2021). <https://doi.org/10.1016/j.carbpol.2021.118604>
- [5] Wang H., Qian J., Ding F.: Emerging chitosan-based films for food packaging applications. *Journal of Agricultural and Food Chemistry*, **66**, 395–413 (2018). <https://doi.org/10.1021/acs.jafc.7b04528>
- [6] Yang S., Lei P., Shan Y., Zhang D.: Preparation and characterization of antibacterial electrospun chitosan/poly(vinyl alcohol)/graphene oxide composite nanofibrous membrane. *Applied Surface Science*, **435**, 832–840 (2018). <https://doi.org/10.1016/j.apsusc.2017.11.191>
- [7] Liu Z., Wang K., Peng X., Zhang L.: Chitosan-based drug delivery systems: Current strategic design and potential application in human hard tissue repair. *European Polymer Journal*, **166**, 110979 (2022). <https://doi.org/10.1016/j.eurpolymj.2021.110979>
- [8] Han D., Yan L., Chen W., Li W.: Preparation of chitosan/graphene oxide composite film with enhanced mechanical strength in the wet state. *Carbohydrate Polymers*, **83**, 653–658 (2011). <https://doi.org/10.1016/j.carbpol.2010.08.038>
- [9] Jayakumar R., Prabakaran M., Kumar P. T. S., Nair S. V., Tamura H.: Biomaterials based on chitin and chitosan in wound dressing applications. *Biotechnology Advances*, **29**, 322–337 (2011). <https://doi.org/10.1016/j.biotechadv.2011.01.005>
- [10] Negm N. A., Hefni H. H. H., Abd-Elaal A. A. A., Badr E. A., Abou Kana M. T. H.: Advancement on modification of chitosan biopolymer and its potential applications. *International Journal of Biological Macromolecules*, **152**, 681–702 (2020). <https://doi.org/10.1016/j.ijbiomac.2020.02.196>
- [11] Bakshi P. S., Selvakumar D., Kadirvelu K., Kumar N. S.: Chitosan as an environment friendly biomaterial – A review on recent modifications and applications. *International Journal of Biological Macromolecules*, **150**, 1072–1083 (2020). <https://doi.org/10.1016/j.ijbiomac.2019.10.113>
- [12] Shukla S. K., Mishra A. K., Arotiba O. A., Mamba B. B.: Chitosan-based nanomaterials: A state-of-the-art review. *International Journal of Biological Macromolecules*, **59**, 46–58 (2013). <https://doi.org/10.1016/j.ijbiomac.2013.04.043>
- [13] Khan Y. H., Islam A., Sarwar A., Gull N., Khan S. M., Munawar M. A., Zia S., Sabir A., Shafiq M., Jamil T.: Novel green nano composites films fabricated by indigenously synthesized graphene oxide and chitosan. *Carbohydrate Polymers*, **146**, 131–138 (2016). <https://doi.org/10.1016/j.carbpol.2016.03.031>
- [14] Yang X., Tu Y., Li L., Shang S., Tao X.-M.: Well-dispersed chitosan/graphene oxide nanocomposites. *ACS Applied Materials and Interfaces*, **2**, 1707–1713 (2010). <https://doi.org/10.1021/am100222m>
- [15] Wahba M. I.: Enhancement of the mechanical properties of chitosan. *Journal of Biomaterials Science, Polymer Edition*, **31**, 350–375 (2020). <https://doi.org/10.1080/09205063.2019.1692641>
- [16] Liu M., Zhang Y., Wu C., Xiong S., Zhou C.: Chitosan/halloysite nanotubes bionanocomposites: Structure, mechanical properties and biocompatibility. *International Journal of Biological Macromolecules*, **51**, 566–575 (2012). <https://doi.org/10.1016/j.ijbiomac.2012.06.022>
- [17] Wang S-F., Shen L., Zhang W-D., Tong Y-J.: Preparation and mechanical properties of chitosan/carbon nanotubes composites. *Biomacromolecules*, **6**, 3067–3072 (2005). <https://doi.org/10.1021/bm050378v>
- [18] Geim A. K.: Graphene: Status and prospects. *Science*, **324**, 1530–1534 (2009). <https://doi.org/10.1126/science.1158877>
- [19] Lee C., Wei X., Kysar J. W., Hone J.: Measurement of the elastic properties and intrinsic strength of monolayer graphene. *Science*, **321**, 385–388 (2008). <https://doi.org/10.1126/science.1157996>
- [20] Pan Y., Bao H., Li L.: Noncovalently functionalized multiwalled carbon nanotubes by chitosan-grafted reduced graphene oxide and their synergistic reinforcing effects in chitosan films. *ACS Applied Materials and Interfaces*, **3**, 4819–4830 (2011). <https://doi.org/10.1021/am2013135>
- [21] Kuila T., Bose S., Mishra A. K., Khanra P., Kim N. H., Lee J. H.: Chemical functionalization of graphene and its applications. *Progress in Polymer Science*, **57**, 1061–1105 (2012). <https://doi.org/10.1016/j.pmatsci.2012.03.002>

- [22] Zhang Y., Zhang M., Jiang H., Shi J., Li F., Xia Y., Zhang G., Li H.: Bio-inspired layered chitosan/graphene oxide nanocomposite hydrogels with high strength and pH-driven shape memory effect. *Carbohydrate Polymers*, **177**, 116–125 (2017).
<https://doi.org/10.1016/j.carbpol.2017.08.106>
- [23] Geng L., Lin Y., Chen S., Shi S., Cai Y., Li L., Peng X.: Superior strength and toughness of graphene/chitosan fibers reinforced by interfacial complexation. *Composites Science and Technology*, **194**, 108174 (2020).
<https://doi.org/10.1016/j.compscitech.2020.108174>
- [24] Huang Y., Zeng M., Chen J., Wang Y., Xu Q.: Multi-structural network design and mechanical properties of graphene oxide filled chitosan-based hydrogel nanocomposites. *Materials and Design*, **148**, 104–114 (2018).
<https://doi.org/10.1016/j.matdes.2018.03.055>
- [25] Zhang H-P., Luo X-G., Lin X-Y., Lu X., Tang Y.: The molecular understanding of interfacial interactions of functionalized graphene and chitosan. *Applied Surface Science*, **360**, 715–721 (2016).
<https://doi.org/10.1016/j.apsusc.2015.11.051>
- [26] Zhang H-P., Yang B., Wang Z. M., Xie C., Tang P., Bian L., Dong F., Tang Y.: Porous graphene oxide/chitosan nanocomposites based on interfacial chemical interactions. *European Polymer Journal*, **119**, 114–119 (2019).
<https://doi.org/10.1016/j.eurpolymj.2019.07.032>
- [27] Huang Q., Hao L., Xie J., Gong T., Liao J., Lin Y.: Tea polyphenol-functionalized graphene/chitosan as an experimental platform with improved mechanical behavior and bioactivity. *ACS Applied Materials and Interfaces*, **7**, 20893–20901 (2015).
<https://doi.org/10.1021/acsami.5b06300>
- [28] Layek R. K., Samanta S., Nandi A. K.: Graphene sulphonic acid/chitosan nano biocomposites with tunable mechanical and conductivity properties. *Polymer*, **53**, 2265–2273 (2012).
<https://doi.org/10.1016/j.polymer.2012.03.048>
- [29] Wrońska N., Anouar A., El Achaby M., Zawadzka K., Kędzierska M., Milowska K., Katir N., Draoui K., Różalska S., Piwoński I., Bryszewska M., El Kadib A., Lisowska K.: Chitosan-functionalized graphene nanocomposite films: Interfacial interplay and biological activity. *Materials (Basel)*, **13**, 998 (2020).
<https://doi.org/10.3390/ma13040998>
- [30] Wang J., Jin X., Li C., Wang W., Wu H., Guo S.: Graphene and graphene derivatives toughening polymers: Toward high toughness and strength. *Chemical Engineering Journal*, **370**, 831–854 (2019).
<https://doi.org/10.1016/j.cej.2019.03.229>
- [31] Wan S., Peng J., Li Y., Hu H., Jiang L., Cheng Q.: Use of synergistic interactions to fabricate strong, tough, and conductive artificial nacre based on graphene oxide and chitosan. *ACS Nano*, **9**, 9830–9836 (2015).
<https://doi.org/10.1021/acs.nano.5b02902>
- [32] Zhang J., Zou H., Qing Q., Yang Y., Li Q., Liu Z., Guo X., Du Z.: Effect of chemical oxidation on the structure of single-walled carbon nanotubes. *Journal of Physical Chemistry B*, **107**, 3712–3718 (2003).
<https://doi.org/10.1021/jp027500u>
- [33] Che J., Shen L., Xiao Y.: A new approach to fabricate graphene nanosheets in organic medium: Combination of reduction and dispersion. *Journal of Materials Chemistry*, **20**, 1722–1727 (2010).
<https://doi.org/10.1039/b922667b>
- [34] Hummers W. S., Offeman R. E.: Preparation of graphitic oxide. *American Chemical Society*, **208**, 1334–1339 (1958).
<https://doi.org/10.1021/ja01539a017>
- [35] Tu X., Luo X., Luo S., Yan L., Zhang F., Xie Q.: Novel carboxylation treatment and characterization of multi-walled carbon nanotubes for simultaneous sensitive determination of adenine and guanine in DNA. *Microchimica Acta*, **169**, 33–40 (2010).
<https://doi.org/10.1007/s00604-010-0307-3>
- [36] Liu Y., Deng R., Wang Z., Liu H.: Carboxyl-functionalized graphene oxide–polyaniline composite as a promising supercapacitor material. *Journal of Materials Chemistry*, **22**, 13619–13624 (2012).
<https://doi.org/10.1039/c2jm32479b>
- [37] Wang Z., Dong Y., Li H., Zhao Z., Wu H. B., Hao C., Liu S., Qiu J., Lou X. W.: Enhancing lithium-sulphur battery performance by strongly binding the discharge products on amino-functionalized reduced graphene oxide. *Nature Communications*, **5**, 5002 (2014).
<https://doi.org/10.1038/ncomms6002>
- [38] Park K-W.: Carboxylated graphene oxide-Mn₂O₃ nanorod composites for their electrochemical characteristics. *Journal of Materials Chemistry A*, **2**, 4292–4298 (2014).
<https://doi.org/10.1039/C3TA14223J>
- [39] Navaee A., Salimi A.: Efficient amine functionalization of graphene oxide through the bucherer reaction: An extraordinary metal-free electrocatalyst for the oxygen reduction reaction. *RSC Advances*, **5**, 59874–59880 (2015).
<https://doi.org/10.1039/c5ra07892j>
- [40] Ding L., Huang Y., Cai X., Wang S.: Impact of pH, ionic strength and chitosan charge density on chitosan/casein complexation and phase behavior. *Carbohydrate Polymers*, **208**, 133–141 (2019).
<https://doi.org/10.1016/j.carbpol.2018.12.015>
- [41] Cobos M., González B., Fernández M. J., Fernández M. D.: Chitosan-graphene oxide nanocomposites: Effect of graphene oxide nanosheets and glycerol plasticizer on thermal and mechanical properties. *Journal of Applied Polymer Science*, **134**, 45092 (2017).
<https://doi.org/10.1002/app.45092>

- [42] Rodríguez-González C., Martínez-Hernández A. L., Castaño V. M., Kharissova O. V., Ruoff R. S., Velasco-Santos C.: Polysaccharide nanocomposites reinforced with graphene oxide and keratin-grafted graphene oxide. *Industrial and Engineering Chemistry Research*, **51**, 3619–3629 (2012).
<https://doi.org/10.1021/ie200742x>
- [43] Dhayal V., Hashmi S. Z., Kumar U., Choudhary B. L., Kuznetsov A. E., Dalela S., Kumar S., Kaya S., Dolia S. N., Alvi P. A.: Spectroscopic studies, molecular structure optimization and investigation of structural and electrical properties of novel and biodegradable chitosan-GO polymer nanocomposites. *Journal of Materials Science*, **55**, 14829–14847 (2020).
<https://doi.org/10.1007/s10853-020-05093-5>
- [44] Wang Y., Shi Z., Yin J.: Facile synthesis of soluble graphene *via* a green reduction of graphene oxide in tea solution and its biocomposites. *ACS Applied Materials and Interfaces*, **3**, 1127–1133 (2011).
<https://doi.org/10.1021/am1012613>
- [45] Wang X., Bai H., Yao Z., Liu A., Shi G.: Electrically conductive and mechanically strong biomimetic chitosan/reduced graphene oxide composite films. *Journal of Materials Chemistry*, **20**, 9032–9036 (2010).
<https://doi.org/10.1039/C0JM01852J>
- [46] Lu Y., Fan L., Yang L-Y., Huang F., Ouyang X-K.: PEI-modified core-shell/bead-like amino silica enhanced poly(vinyl alcohol)/chitosan for diclofenac sodium efficient adsorption. *Carbohydrate Polymers*, **229**, 115459 (2020).
<https://doi.org/10.1016/j.carbpol.2019.115459>
- [47] Cheng Q., Jiang L., Tang Z.: Bioinspired layered materials with superior mechanical performance. *Accounts of Chemical Research*, **47**, 1256–1266 (2014).
<https://doi.org/10.1021/ar400279t>

Research article

Lignin-liquid crystalline elastomeric composites for shape memory applications and their thermomechanical properties

Peerawat Prathumrat¹, Mostafa Nikzad^{1*}, Elnaz Hajizadeh², Manunya Okhawilai³,
Igor Sbarski¹

¹Department of Mechanical and Product Design Engineering, School of Engineering, Swinburne University of Technology, 3122 Hawthorn, VIC, Australia

²Department of Mechanical Engineering, Faculty of Engineering and Information Technology, University of Melbourne, 3010 Parkville, VIC, Australia

³Metallurgy and Materials Science Research Institute, Chulalongkorn University, Pathumwan, 10330 Bangkok, Thailand

Received 4 June 2022; accepted in revised form 27 August 2022

Abstract. Liquid crystalline elastomers (LCEs) are stimuli-responsive materials with potential use in shape memory applications. Though particularly suited for shape memory, the LCEs however have some drawbacks such as low shape fixity (R_f) and slow recovery time. To overcome these limitations, new lignin-filled elastomeric liquid crystalline (ELC) composite materials were fabricated. The lignin used is a by-product of Kraft pulping process, which was obtained from renewable resources abundant in nature. Here, we show that the aromatic structure of lignin increases the netpoints density at the microscopic level in the ELC composite systems. Shape memory effects are enhanced by incorporating up to only 7 wt% of lignin, resulting in an R_f of 97% for the composites. Concurrently, these composites were able to maintain their shape recovery (R_r) of nearly 100%. The recovery time of the composites reduces with increasing lignin content due to the higher elastic energy released from the netpoints based on the lignin structure. The ELC composites with 7 wt% lignin could fully recover within 70 s, while the neat LCE counterpart took 100 s. Morphological features of dispersed lignin shows that even without surface modification and only a moderate quality of dispersion in LCE matrix, both shape memory and dynamic mechanical properties of the resultant composites can be significantly improved.

Keywords: smart materials, shape memory elastomers (SMEs), liquid crystalline elastomers (LCEs), lignin, composites

1. Introduction

Shape memory elastomers (SMEs) are a class of intelligent materials that have been utilized over the past decades in a wide range of applications, such as soft robotics, aerospace engineering, smart actuators and sensors, and biomedical devices [1–4]. These materials have the ability to deform and memorize their temporary shape and eventually recover to their original shape under applied stress and an external stimulus. Several external stimuli are currently used to activate the shape memory effects of polymeric

systems, such as heat, UV, electric and magnetic fields, water, and pH [5]. Among them, heat is commonly used for activation [6, 7]. The molecular architecture of the elastomer also plays a critical role in allowing the material to exhibit shape memory effects [8, 9]. The SMEs typically consist of two prerequisite constituents, including netpoints and switch units. The netpoints (hard segments) are responsible for determining the original shape of the SMEs due to their ability to store the elastic energy during the shape memory process [10]. This segment can also

*Corresponding author, e-mail: mnikzad@swin.edu.au

© BME-PT

help SMEs to maintain their temporary shape due to their chemical or physical crosslinks or interpenetrated networks (IPNs). The switch units (soft segments) are responsible for maintaining the temporary shape and recovering the original shape through transition temperatures [11]. A well-balanced proportion of these constituents can lead to an excellent shape memory performance via thermomechanical shape memory processes.

Liquid crystalline elastomers (LCEs) are stimuli-responsive materials that have gained increasing attention for their potential shape memory effects [12, 13]. The molecular structure of LCEs consists of mesogens (hard segment) and flexible tails (soft segment), allowing them to possess the typical underlying molecular mechanism of SMEs [8]. These materials can also respond to many external stimuli via the shape deformation process [12, 14–16]. The LCEs typically exhibit two transition temperatures: glass transition temperature (T_g) and nematic-isotropic transition temperature (T_{NI}). These transition temperatures allow the LCE structure to rearrange from solid-crystal to liquid-crystal and isotropic states. In the shape memory mechanism of LCEs, T_{NI} is utilized as a switching point because it is higher than room temperature, resulting in no interruptions from ambient conditions.

Reactive mesogens (RM)-based LCE have become a crucial nematic-LCE for SMEs [17, 18]. This class of LCEs can be thermally stimulated to mobilize its networks via a nematic-isotropic transition temperature (T_{NI}) [19]. Traugutt *et al.* [20] have studied the effect of solvent used in the synthesis process on shape memory properties of RM257-based LCE. The results showed that the shape fixity (R_f) and the shape recovery (R_r) of the case with solvent was approximately 62.8 and 99.5%, respectively. These properties were higher than the case without the solvent. Guin *et al.* [21] have reported that combining two reactive (diacrylate) mesogens, RM82 and RM257, in the LCE system results in an excellent thermal actuation up to 11 cycles, provided that the LCE structure remains stable and can maintain an actuation behavior through thermal deformation processes.

Other LCE systems have also been developed to study the shape memory effects. Wen *et al.* [22] synthesized a multiple-shape memory LCE from a novel polyurethane with exchangeable carbamate functional groups. This LCE system indicated two liquid crystal phases, including smectic-A and nematic,

showing two transition temperatures: smectic-nematic transition temperature (T_{SmN}) and nematic-isotropic transition temperature (T_{NI}). As a result, these materials showed the R_f of 84.5 and 88.6% for the first and second temporary shapes and an outstanding R_r of 99% for both shapes. Rousseau and Mather [23] studied the shape memory properties of main-chain smectic-C LCE synthesized by benzoate mesogenic groups. This LCE revealed an R_f of 83.6% and an excellent R_r of 99.1% via a thermal-induced process.

These reported works on neat LCEs show their excellent potential as candidates for shape memory materials and possessing a significant R_r characteristic. However, there seems to be a shortcoming in achieving full R_r using these LCEs systems, and importantly that all the critical compounds used in their preparation produced from non-renewable sources and hence limiting their applications for large and high-volume applications. It is also noteworthy to mention that currently available systems are synthesized from expensive compounds, making their wider uptake cost-prohibitive. Another key performance attribute that requires further improvement is the longer recovery time of shape memory applications developed from the existing homogenous LCE systems [24]. These shortcomings are some key barriers to the further adoption of these promising class of smart materials for the development of exotic industrial and space applications.

To address the aforementioned shortcomings and further improve the shape memory characteristics of LCEs, creating composites of LCE and naturally derived compounds such as lignin is one promising option. Thanks to the high concentration of aromatic compounds and the complex interconnect molecular structures of monolignols, often providing large surface areas, they can be incorporated as rigid fillers into the LCE matrix to provide synergistic effects not available in the existing homogenous systems, otherwise. These composite LCEs can therefore provide mitigation strategies for improved R_r and being abundant as well as renewably obtained, increase sustainability in terms of cost and scalability. An example of such lignin sources is obtained from Kraft pulping process as a by-product, which contributes to 85% of the total lignin manufacturing globally [25]. This biomaterial is a three-dimensional macromolecular polymer constructed from three different phenylpropane monomer units; p-coumaryl alcohol, coniferyl alcohol, and syringyl alcohol [26]. It has gained increasing

attention in many research areas due to its remarkable properties, including low cost, renewability, biodegradability, high thermal stability, anti-oxidation, and high UV absorption properties [27–29]. These properties also promote lignin as a significant natural resource fulfilling the global demand for other environmentally benign polymeric materials.

In shape memory applications, incorporating lignin into the shape memory polymeric systems increases the density of netpoints (hard segment) in the composites due to its networked phenolic structures and intermolecular hydrogen bonding [30]. These characteristics can enhance the R_f of the polymeric composites to approximately 100% [31]. This biomaterial can also improve the tensile modulus and strength of the composites, resulting in broadening areas of engineering applications [32, 33]. Moreover, the copolymeric structures of lignin-co-poly(ester-amine-amide) exhibited a triple-shape memory effect via a thermomechanical process [34]. Therefore, given an appropriate molecular structure of lignin, this material offers potential as a good filler in preparing LCE-based shape memory elastomeric composites with improved intrinsic properties, including dynamic mechanical and shape memory properties.

To achieve the desired characteristics in the shape memory applications, we considered the liquid crystalline elastomeric composites in which Kraft lignin-based bio-filler is added to diacrylate mesogens-based nematic LCE. This work focuses on the synthesis and characterization of new elastomeric liquid crystalline (ELC) composites with the goal of understanding how lignin improves shape memory properties and other underlying characteristics of composite materials. The nematic-type LCE was synthesized from diacrylate mesogens named RM257 and pentaerythritol tetra (3-mercaptopropionate) (PETMP) via a base-catalyzed thiol-Michael addition reaction. The lignin with different weight ratios was physically mixed to generate the ELC composites. The shape memory characteristics were measured, including R_f , R_r , and recovery time. The effect of lignin filler is also studied on the thermal, dynamic mechanical, and morphological properties of the composites.

2. Experiments

2.1. Materials

The chemicals used in this study include diacrylate mesogen named 1,4-bis(4-(3-acryloyloxypropyl)oxy)benzoyl-oxy]-2-methylbenzene (RM257), which

was purchased from Daken Chemical (China). Kraft lignin (alkali lignin), pentaerythritol tetra (3-mercaptopropionate) (PETMP)-based crosslinking agent, and dipropyl amine (DPA)-based catalyst were purchased from Sigma-Aldrich, Inc. (Australia). Toluene was purchased from Thermo Fisher Scientific Australia PTY LTD (Australia). All these materials were used as received without further purification.

2.2. Sample preparation

The LCE samples were prepared following the same procedure reported in our previous work [17]. Briefly, RM257 monomers were dissolved by adding 40 wt% of toluene and heated at 80 °C in an oven until a homogenous solution was achieved. The solution was then left to cool down to room temperature. To develop composites, Kraft lignin was added at different mass ratios of 3, 5, and 7 wt% into the solution and was stirred until a well-dispersed mixture was achieved. In the next step, 36 wt% of PETMP was added to the system and stirred for several minutes. Dipropyl amine (DPA) was separately diluted in toluene at a mass ratio of 1:50, and subsequently, 14 wt% of the diluted DPA was added into the monomer mixture. All the constituents were instantaneously stirred and subsequently placed in a vacuum oven for 1 min to remove the bubble that occurred during mixing. The mixture was immediately transferred into the mold and left to cure at room temperature for 24 h. After the polymerization was completed, the LCE samples became glossy white and transparent elastomeric materials. Finally, the samples were heated to remove the solvent at 80 °C for 12 h before characterization. Figure 1 shows the molecular structure and the samples of all the monomers, LCE, and ELC composite after completing the synthesis process.

3. Characterization of LCE and composites

3.1. Fourier transform infrared spectroscopy (FTIR)

FTIR analysis was conducted on structural characterization of LC monomer (RM257), Kraft lignin, LCE, and ELC composite samples. The FTIR Nicolet iS5 (Thermo Scientific) was utilized to characterize the chemical compositions of the samples. The spectra were scanned in a transmittance mode with a scan range of 4000 to 400 cm^{-1} , and the scan times were 64 scans per sample.

3.2. Thermal properties

A differential scanning calorimeter (DSC) 2960 (TA Instruments, USA) was employed to characterize the thermal properties of LCE and composite samples. The sample mass of 5 to 10 mg was used and sealed in an aluminum pan. The heating rate of $5\text{ }^{\circ}\text{C}\cdot\text{min}^{-1}$ and cooling rate of $3\text{ }^{\circ}\text{C}\cdot\text{min}^{-1}$ were set for running the sample in the temperature range of $-40\text{ }^{\circ}\text{C}$ to $150\text{ }^{\circ}\text{C}$. The samples were run under an N_2 atmosphere with a dispersed rate of $110\text{ ml}\cdot\text{min}^{-1}$. The phase transitions of LC monomer, LCE, and ELC composites were characterized.

A thermogravimetric analyzer (TGA) Q50 (TA Instruments, USA) was used to measure the thermal stability of the samples. The sample mass used was in the range of 10 to 20 mg. The testing temperature was ramped from 25 to $800\text{ }^{\circ}\text{C}$ in the air with a heating rate of $10\text{ }^{\circ}\text{C}\cdot\text{min}^{-1}$. Thermal degradation temperatures and derivative thermogravimetric (DTG) curves of LCE and ELC composites were determined.

3.3. Dynamic mechanical properties

A discovery hybrid rheometer (DHR) HR-1 (TA Instruments, USA) was used for dynamic mechanical analysis (DMA) in a tensile mode. The dynamic mechanical properties of the LCE and ELC composites were measured in an oscillation procedure. The sample dimensions were $30\times 6\times 1.2\text{ mm}^3$ for $L\times W\times T$. The temperature was ramped from -10 to $120\text{ }^{\circ}\text{C}$ with a heating rate of $3\text{ }^{\circ}\text{C}\cdot\text{min}^{-1}$. The axial displacement and frequency were set at $25\text{ }\mu\text{m}$ and 1 Hz , respectively. The storage modulus of LCE and ELC composites at nematic and isotropic states was measured using storage modulus curves at 25 and $110\text{ }^{\circ}\text{C}$, respectively. The nematic-isotropic temperatures (T_{NI}) of all samples were determined from the second peak of the $\tan\delta$. This temperature was then used as a switching point in a shape memory process.

3.4. Shape memory properties

A DHR with a tensile mode was also used to evaluate the shape memory properties, including R_f and R_r of LCE and ELC composites. Shape memory testing was conducted via a four-step thermomechanical process under a stress-controlled condition. The sample was pre-heated at $105\text{ }^{\circ}\text{C}$, above its T_{NI} , and stretched with a $5\%\cdot\text{min}^{-1}$ strain rate for 10 min. The sample was cooled down to $25\text{ }^{\circ}\text{C}$ with a cooling rate of $5\text{ }^{\circ}\text{C}\cdot\text{min}^{-1}$. The force was unloaded, and the sample

was kept at $25\text{ }^{\circ}\text{C}$ for 10 min. The sample was reheated at $105\text{ }^{\circ}\text{C}$ to recover with a heating rate of $5\text{ }^{\circ}\text{C}\cdot\text{min}^{-1}$ and kept at this temperature for 20 min. The R_f and R_r were calculated in the unloading and reheating steps by Equations (1) and (2):

$$R_f = \frac{\epsilon_i}{\epsilon_m} \cdot 100\% \quad (1)$$

$$R_r = \frac{\epsilon_m - \epsilon_p(n)}{\epsilon_m - \epsilon_p(n-1)} \cdot 100\% \quad (2)$$

where ϵ_i is the residual strain in the unloading step after deformation, ϵ_m is a maximum strain applied to the samples, ϵ_p is the strain after recovery of the samples, and n is the number of cycles.

The recovery angle of LCE and ELC composites was measured as a function of time to study the effect of Kraft lignin on the recovery time of the specimens. The rectangular-shaped samples were preheated in an oven at $105\text{ }^{\circ}\text{C}$ for 20 min. Then, they were deformed to a U-shape and cooled down to room temperature. The U-shaped samples were then put into an oven at $105\text{ }^{\circ}\text{C}$, where a degree protractor was set inside. A video camera was used to record the shape recovery behavior of these samples until they were completely reversed to a rectangular shape. This method was reported by Likitaporn *et al.* [35].

3.5. Scanning electron microscopy (SEM)

The surface morphology of the ELC composites fraction was studied using a scanning electron microscope (Zeiss Supra 40VP, Germany) at an accelerating voltage of 15 kV. The micrographs were taken at magnifications of $100\times$ to $200\times$. The exposed surface was coated with Au for 1 min before analyzed.

4. Results and discussion

The molecular structures of the respective liquid crystalline monomer, namely, RM257 and the cross-linking agent named PETMP used to polymerize liquid crystalline elastomer, are shown in Figure 1a. These two compositions were reacted using a DPA-based catalyst via a thiol-Michael addition reaction. This catalyst was responsible for accelerating the reaction between the electron-deficient vinyl groups of RM257 structures and the thiol groups of PETMP [36]. This reaction was completed after curing at room temperature for 24 h. For the ELC composites, Kraft lignin was physically mixed into the LCE system at 3, 5, and 7 wt%. Figure 1b displays the

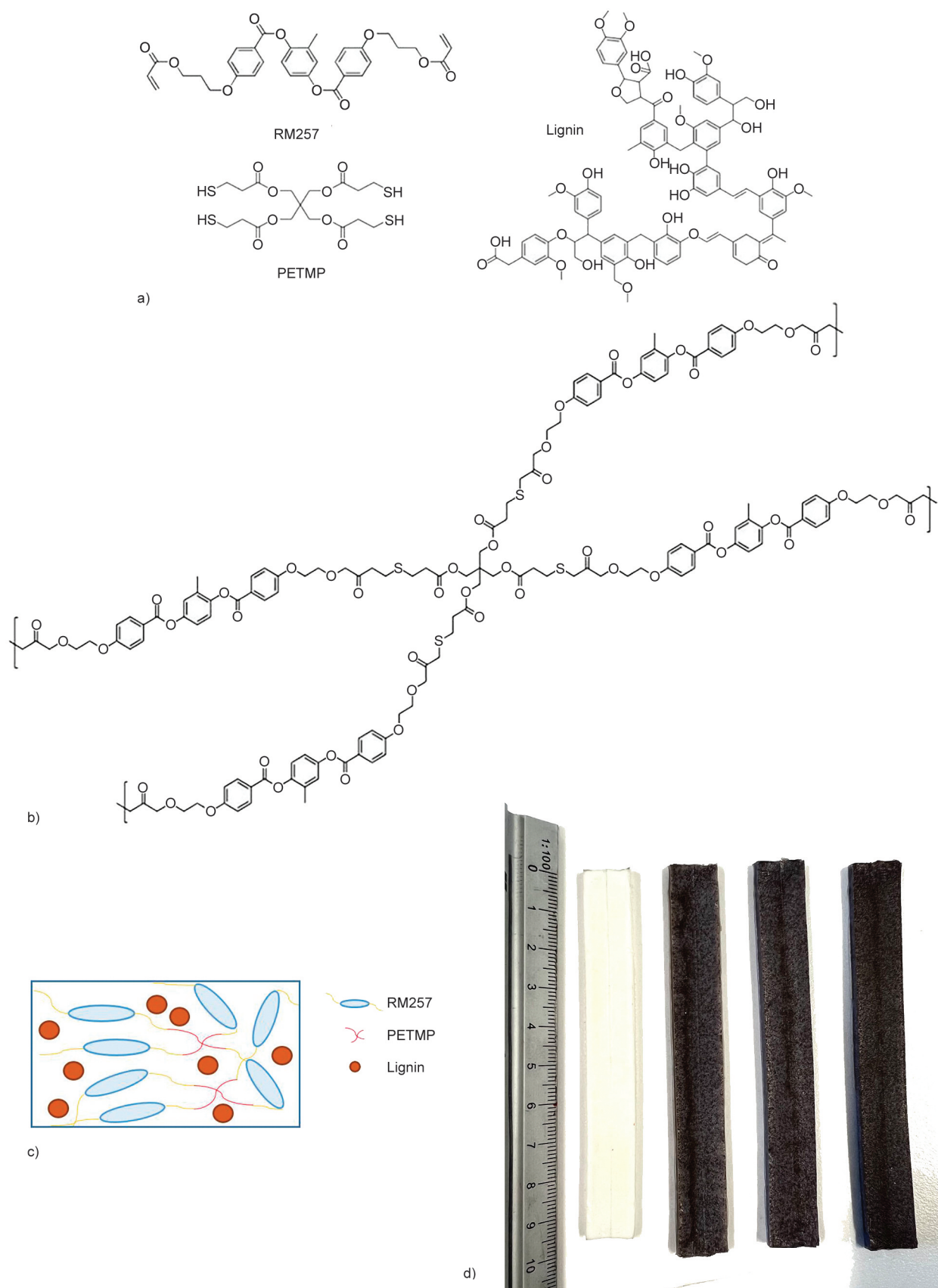


Figure 1. Molecular structures of RM257 monomers and a four-armed PETMP crosslinking agent (a); molecular structure of the crosslinked LCE (b); schematic of the ELC composites with lignin filler (c); an image of the LCE and ELC composite samples with Kraft lignin (d), from left to right; neat LCE, ELC composites with 3, 5, and 7 wt% lignin, respectively.

molecular structure of lignin utilized in this work, which is from a pulping process. The schematic of lignin-filled in ELC composites is shown in Figure 1c. In addition, the neat LCE and ELC composite samples with different weight ratios of Kraft lignin after completing the synthesis process are shown in Figure 1d.

4.1. FTIR analysis

The FTIR spectra of Kraft lignin, LC monomers (RM257), neat LCE, and ELC composites were collected to study their chemical compositions. The FTIR spectrum of Kraft lignin was observed in Figure 2a. The broad peak at 3215 cm^{-1} corresponds to the O–H stretching of hydrogen-bonded aromatic and aliphatic groups. The peaks observed at 2934 and 1424 cm^{-1} correspond to the C–H stretching in methyl and methylene groups. The peaks at 1592 and 1511 cm^{-1} correspond to aromatic ring vibration. The O–H vibration of phenolic groups is observed at 1369 cm^{-1} . The peaks at 1215 and 1029 cm^{-1} are attributed to vibration in the syringyl and guaiacyl structures [37]. The O–H stretching of secondary and primary alcohols is observed at 1123 and 1079 cm^{-1} . The peak at 853 cm^{-1} corresponds to the out-of-plane vibration of the C–H bond of aromatic deformation. These FTIR peaks of Kraft lignin are similar to those reported by Kong *et al.* [38] and Brazil *et al.* [39].

The FTIR spectra of LC monomers (RM257), LCE, and ELC composites with different Kraft lignin contents are divided into region 1 (3800 to 2200 cm^{-1}) and region 2 (1800 to 400 cm^{-1}), as illustrated in Figures 2b, 2c, and 2d. In region 1 (Figure 2b), the FTIR peaks of RM257 monomers and the LCE sample present a slight shift in the range of 2992 to 2842 cm^{-1} . This is possibly due to the formation of inter- and intramolecular bonding of C–H stretching groups [37]. Figure 2c focuses in the range of 3800 to 3000 cm^{-1} of the FTIR curve, where it can be observed that the FTIR peaks slightly intensifies in the region corresponding to stretching of the O–H groups, indicating contributions of hydrogen bonding due to further increase of the lignin in the composite. In region 2 (Figure 2d), the FTIR spectrum of LC monomers (RM257) exhibits a significant peak at 808 cm^{-1} , corresponding to the out-of-plane vibration of the C–H bond of the acrylate group. While a 1715 cm^{-1} peak relates to the C=O stretching of the mesogenic acrylate ester group. These peaks were similarly reported by Kamal and Park [13]. For the LCE sample, the peaks at 1636 and 810 cm^{-1} disappear due to the interaction of acrylate groups of RM257 and thiol groups of PETMP. This interaction also reduces the height of a 1411 cm^{-1} peak of the acrylate groups of the RM257 monomers. For the ELC composites, the FTIR spectrum

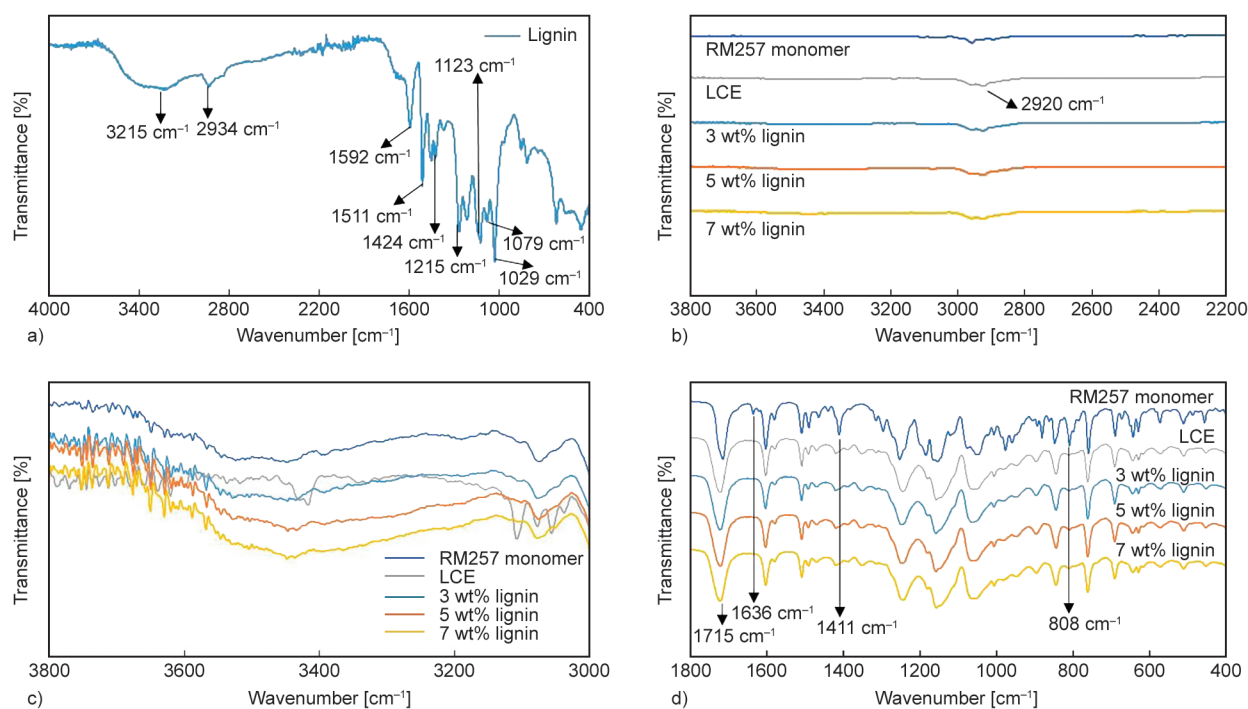


Figure 2. The FTIR spectra of Kraft lignin (a), and region 1 and region 2 of RM257 monomer, LCE and ELC composites from 3800 to 2200 cm^{-1} (b), 3800 to 3000 cm^{-1} (c), and 1800 to 400 cm^{-1} (d).

of these samples with different lignin contents has no noticeable change compared to the neat LCE sample spectrum due to a small amount of lignin content filled in the LCE system.

4.2. Thermal properties

DSC was utilized to study the thermal properties of the LC monomer, LCE, and ELC composites. Figure 3 shows the phase transitions of RM257 monomers with well-defined temperature changes. The monomers were heated first at a rate of $5\text{ }^{\circ}\text{C}\cdot\text{min}^{-1}$ and then cooled at $3\text{ }^{\circ}\text{C}\cdot\text{min}^{-1}$. In the heating step, the heat flow of these monomers shows a minor endothermic peak at $41\text{ }^{\circ}\text{C}$ and two significant peaks at 76 and $128\text{ }^{\circ}\text{C}$. The minor peak at $41\text{ }^{\circ}\text{C}$ is attributed to a crystal-crystal phase transition of the monomers [40]. Meanwhile, the two significant peaks correspond to solid crystalline-nematic (T_{CrN}) and nematic-isotropic (T_{NI}) transition temperatures. These phase transition behaviors were previously reported by Kim *et al.* [40]. In addition, the exothermic peaks that occur in the cooling step at 127 and $31\text{ }^{\circ}\text{C}$ correspond to T_{NI} and re-crystallization temperature, respectively. This figure depicts that the monomers can reorient their molecular structure from isotropic state to nematic-liquid crystal and solid crystalline states upon the change in the temperature.

Figure 4 depicts the DSC thermograms of LCE and ELC composites at various Kraft lignin contents

from 3 to 7 wt%. A neat LCE curve demonstrates a glass transition temperature (T_g) at $-4\text{ }^{\circ}\text{C}$ and T_{NI} at $96\text{ }^{\circ}\text{C}$. Meanwhile, T_g of the ELC composites increases with increasing Kraft lignin content. The observed enhancement in the T_g of the composites is because Kraft lignin has condensed rigid phenolic moieties that suppress the thermal mobility of the composite structures compared to neat LCE samples [41, 42]. However, T_{NI} of the ELC composites could not be detected by standard DSC due to its lower resolution, and hence these were determined from Tan delta under dynamic mechanical analysis to identify all the phase transitions. The values of T_g of neat LCE and all ELC composites are included in Table 1.

The thermal stability of the LCE and ELC composite samples was studied using thermogravimetric analysis (TGA). This property is defined as the ability of the polymers to resist heat and thermal decomposition upon an increase in temperature [43]. Figure 5 depicts the TGA and derivative thermogravimetric (DTG) thermograms of the neat LCE, Kraft lignin, and the ELC composites with 3, 5, and 7 wt% lignin contents. From the thermograms, the TGA curve of the Kraft lignin exhibits a slight decrease at approximately $100\text{ }^{\circ}\text{C}$ due to the water evaporation. The significant degradation of this biomaterial occurs in the temperature range of 100 and $550\text{ }^{\circ}\text{C}$. The maximum weight loss from a DTG curve is $436\text{ }^{\circ}\text{C}$, which is suggested to be due to the fragmentation of

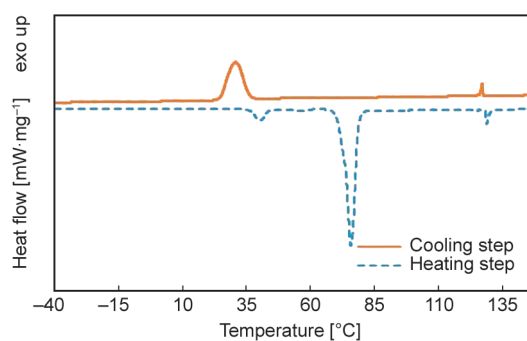


Figure 3. DSC thermogram of liquid crystalline monomer (RM257).

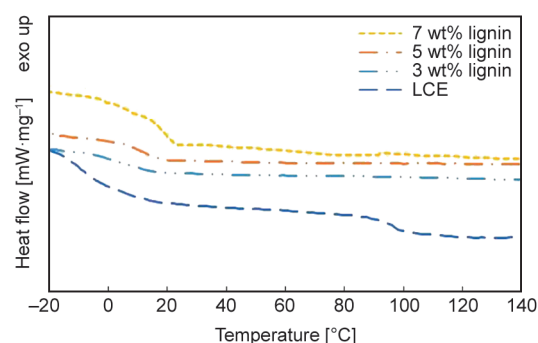


Figure 4. DSC thermograms of liquid crystalline elastomer (LCE) and ELC composites with different mass ratios of Kraft lignin.

Table 1. DSC and DMA results of LCE and ELC composites at various weight ratios of Kraft lignin.

Samples	DSC		DMA		
	T_g [°C]	T_{NI} [°C]	T_{NI} [°C]	E' at $25\text{ }^{\circ}\text{C}$ [MPa]	E' at $110\text{ }^{\circ}\text{C}$ [MPa]
Neat LCE	-4	96	97	6.5	0.3
ELC composites + 3wt% lignin	4	–	78	11.9	1.0
ELC composites + 5wt% lignin	11	–	86	14.2	1.7
ELC composites + 7wt% lignin	16	–	76	60.3	4.8

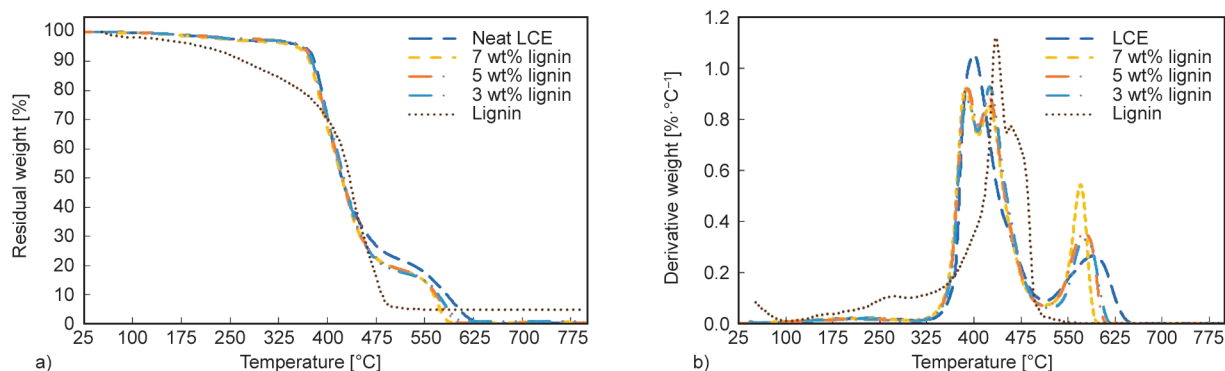


Figure 5. TGA (a) and DTG (b) thermograms of the LCEs, Kraft lignin, and ELC composites with different lignin content, tested in air.

carbohydrates, aromatic rings, and inter-linkages releasing phenols into a vapor phase [39, 44]. Meanwhile, the residual weight of lignin at 700°C is approximately 4.8%.

The neat LCE sample indicates two maximum peaks at 403 and 591 °C, relating to a two-step degradation. The first peak corresponds to the fragmentation of aliphatic chains in the LCE structure. However, the second peak relates to the degradation of aromatic rings in a mesogens segment. For ELC composites with 3 to 7 wt% Kraft lignin content, three distinct steps of degradation are observed in the DTG curve. The peaks at 392 and 580 °C are the degradation of aliphatic chains and mesogens of LCE, respectively. Meanwhile, the DTG peak at 431 °C is the fragmentation of Kraft lignin in the composite samples. From these thermograms, incorporating Kraft lignin into the LCE matrix barely affects an improvement in the thermal stability of the composites. The ELC composites exhibit their thermal properties similar to the neat LCE samples.

4.3. Dynamic mechanical properties

Storage modulus (E') and $\tan\delta$ of LCE and ELC composites were investigated using a DHR in the tensile mode. Figure 6 shows the storage modulus (E') of the LCE and ELC composites as a function of temperature. The results show that the LCE has two thermal relaxations identified as glass transition temperature (T_g) and nematic-isotropic temperature (T_{NI}). These transition temperatures manifest the changes in the chain mobility and orientational order of the LCE and ELC composite structures. In the nematic state, the E' at above T_g dramatically drops to a lower modulus value due to the internal nematic director (\bar{n}) relaxation modes of the orientational order of the LCE structures [45]. Above this point, the E' shows

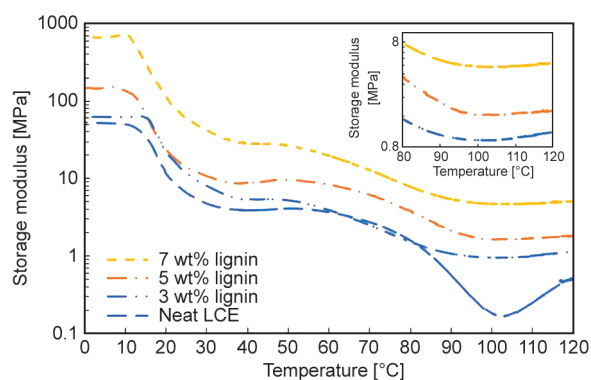


Figure 6. Storage modulus (E') of LCE and ELC composites with various lignin contents.

a minimum corresponding to T_{NI} . In the isotropic phase, the E' shows an upturn due to the entropic rubber elasticity of the LCE [45].

For the composite samples, the E' curves show similar trends in thermal relaxations to that of the neat LCE. It, therefore, seems that the amount of Kraft lignin has no dramatic effects on the orientational and positional orders of the LCE structures at elevated temperatures. However, in absolute terms, Kraft lignin content significantly increases the storage modulus (E' values) of the ELC composites in both nematic and isotropic states at 25 and 110 °C. The results show that the E' of the neat LCE at these states are 6.5 and 0.3 MPa, respectively. The E' of the composites increases upon the addition of Kraft lignin by approximately an order of magnitude at nematic state and well above that at isotropic states summarized in Table 1. This enhancement in the storage modulus in the composites compared to neat LCE was expected as the rigid aromatic structures of lignin increase the stiffness of the composite structures [33, 46].

$\tan\delta$ of LCE and ELC composite samples are shown in Figure 7. $\tan\delta$ is the ratio of energy dissipated

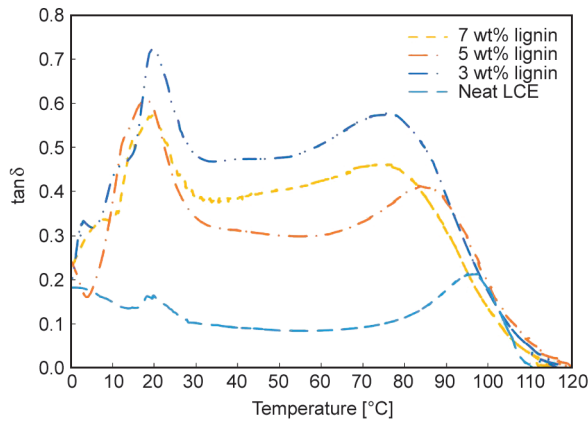


Figure 7. Tan δ of neat LCE and ELC composites at various lignin contents.

per cycle of sinusoidal deformation (loss modulus, E'') over the storage modulus, E'/E' . From the diagram, the overall trend in tan delta curves of all composite samples is similar to the neat LCE. They exhibit two distinct peaks at different temperature regions. The first peak corresponds to T_g , and the second peak is defined as T_{NI} . For shape memory applications, T_{NI} is typically used as the switching temperature between the original and temporary shapes because this temperature is commonly higher than the room temperature and hence less sensitive to changes in the ambient conditions. Table 1 also summarizes the T_{NI} of all samples, and it can be observed that incorporating lignin into the LCE reduces this temperature. As the temperature increases, the kinetic energy of the structural unit in both lignin and LCE rises, which results in both increased overall free volume and enhanced mobility of the molecules in LCE matrix and the lignin filler. This is the possible driving factor for the further interaction between the functional groups of the two polymers. With the increased interaction, and perhaps through diffusion-based mechanism, the rigid lignin structure

seems to disrupt the orientational order of the LCE structure and hence the earlier observed onset of nematic to isotropic transition in the LCE composites.

4.4. Shape memory properties

Shape memory properties of the LCE and ELC composites, including R_f and R_r , were characterized by a DHR in tensile mode. The samples were deformed and recovered via a thermal-induced process using T_{NI} as a switching temperature. The R_f is the ability to maintain a temporary shape of the samples after unloading at a low temperature. The R_r relates to the recoverability of the samples to their original shape upon being reheated to an elevated temperature. The values of these two key shape memory properties were calculated by Equations (1) and (2). Figure 8 illustrates changes in the strain of the neat LCE and 3 wt% Kraft lignin ELC composites in various steps of the shape memory process. The results show that the R_f of the neat LCE sample is 91.2%. Meanwhile, the LCE exhibits an excellent R_r , approximately 99.7%. For the ELC composites, the R_f significantly improved with increasing Kraft lignin content, as indicated in Table 2, where composites show an R_f of nearly 100%. It is suggested that the aromatic structures of lignin with strong intermolecular hydrogen bonding can enhance the netpoints density in the composite system, leading to an improved R_f of the composite samples [30, 47].

Table 2. Shape memory properties of the neat LCE and ELC composites.

	Samples			
	Neat LCE	ELC composites + 3 wt% lignin	ELC composites + 5 wt% lignin	ELC composites + 7 wt% lignin
R_f [%]	91.2	95.6	94.7	97.0
R_r [%]	99.7	99.5	99.8	99.6

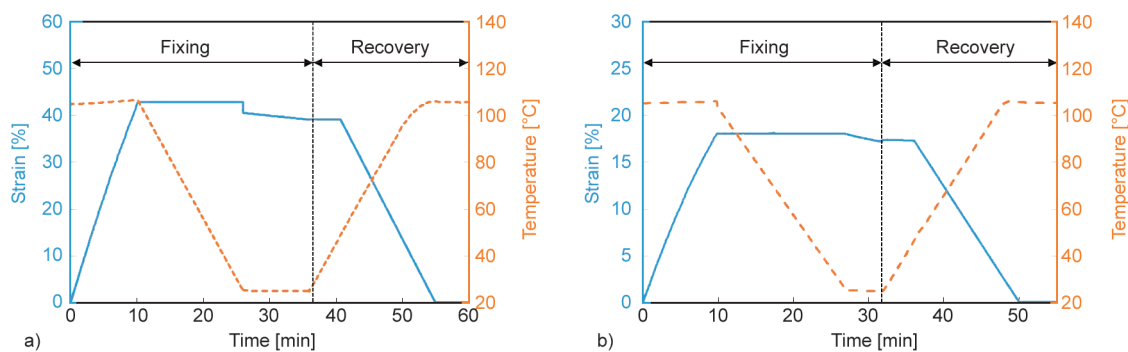


Figure 8. Changes in the strain as a function of the temperature of neat LCE sample (a) and ELC composite with 3 wt% lignin (b) via the thermomechanical shape memory process.

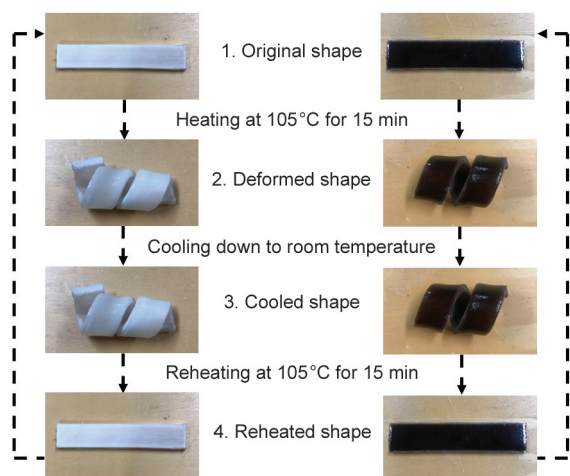


Figure 9. Steps of the thermomechanical shape memory process of LCE and 7 wt% lignin-ELC composites.

Figure 9 illustrates the steps taken during the thermomechanical shape memory process for the cases of neat LCE and ELC composites with 7 wt% lignin. A rectangular shape of various samples was first heated at 105 °C for 15 min by a heat gun. Then, the sample was manually deformed to a curled shape at this temperature. It is then cooled down to room temperature to maintain the temporary shape in this step. In the recovery step, the curl-shaped sample was reheated at 105 °C, resulting in a gradual recovery of the sample to its original rectangular shape. As a comparison, the shape memory behavior of the composite samples was also studied through a similar thermal-induced process, which turned out to be similar to the neat LCEs; however, the recovery time is faster than the neat LCE sample.

To evaluate the recovery time of LCE and ELC composite samples at a well-defined temperature, we measured their recovery angle over time through the following protocol. The rectangular-shaped samples with 3 mm thickness were deformed to a U-shape at 105 °C (above their T_{NI}). The samples were then cooled down to room temperature to fix this shape. The samples were placed in an oven, and their shape recovery behavior over time was quantified through readings of a degree protractor set inside the oven (see Figure 11). The initial U-shape of the samples was set as 0° on the protector. A video camera recorded the recovery angle of the samples as a function of time at 105 °C until the samples recovered to a rectangular shape (180°).

Figure 10 shows the recovery angles of all the samples as a function of time. It further shows that the angle of the neat LCE sample initiates its recovery

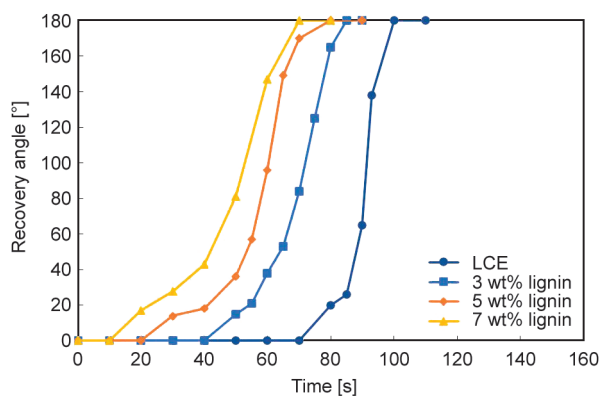


Figure 10. Recovery angle of the neat LCE and ELC composites with various lignin contents as a function of time.

at 70 s and fully recovers at 100 s. In addition, the presence of Kraft lignin content reduces the recovery time of the composite samples. The ELC composites with 3, 5, and 7 wt% Kraft lignin start to recover at 40, 20, and 10 s, respectively. Eventually, all-composite samples recover to a rectangular shape within 85, 75, and 70 s, respectively. These results further suggest that lignin operates as extra netpoints or hard segments in the shape memory mechanism, leading to an enhanced ability to store a higher degree of elastic energy during the deformation process [48]. The release of this energy during the recovery process associated with the mobility of the flexible tails of the LCE structure enables the ELC composites to recover faster than the neat LCE.

Figure 11 illustrates a series of screenshots of the recovery behavior of all LCE and ELC composites at various times through their recovery process at 105 °C. It is observed that lignin improves the recoverability of the ELC composite samples compared to the neat LCE.

4.5. Scanning electron microscopy (SEM)

The surface morphology of the 7 wt% lignin ELC composites fracture was studied using SEM analysis with magnifications of 100× to 200×. This analysis allows the investigation of the dispersion of Kraft lignin particles in the LCE matrix. Figure 12 illustrates that the Kraft lignin particles are spherical and embedded within the matrix. In this case, the spherical shape of Kraft lignin is necessary for its isotropic reinforcement [49]. The Kraft lignin is liable to agglomerate in the LCE matrix due to the stronger cohesion and weaker adhesion forces to the phenolic structures between the lignin particles [50]. The particles further exhibit a large scatter in the particle

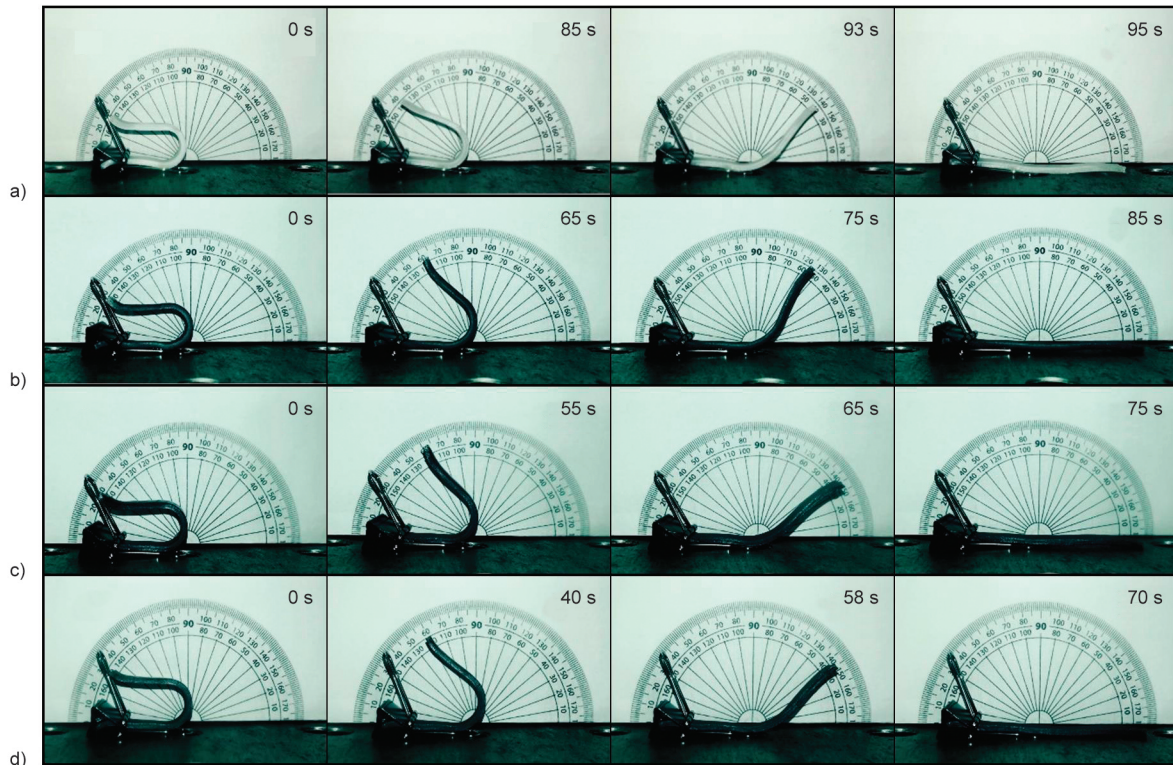


Figure 11. Screenshots of recovery angle at various times during the recovery process of LCE and ELC composites at 105 °C, recorded by a video camera; a) neat LCE, b) ELC composite with 3 wt% lignin, c) ELC composite with 5 wt% lignin, and d) ELC composite with 7 wt% lignin.

size range, which is mainly 20 to 100 μm . From this figure, even though the lignin particles exhibit poor dispersion and no surface modification, this filler can improve the properties of the composite samples. It can be confirmed by the DMA results that an addition of Kraft lignin content improves the storage modulus of the ELC composites compared with the neat LCE counterpart. In this case, the lignin particles are responsible for the rigid reinforcing phase due to their high stiffness.

For shape memory applications, Kraft lignin distributes throughout the LCE matrix, allowing an increase in the netpoints density in the composite structures. Furthermore, the ability to hydrogen bonding of this filler with other molecular structures contributes to the netpoints density of the composites [47]. Thus, the addition and distribution of this biomaterial in the LCE samples can improve the shape memory characteristics, including R_f as well as recovery time of the ELC composites based on RM257.

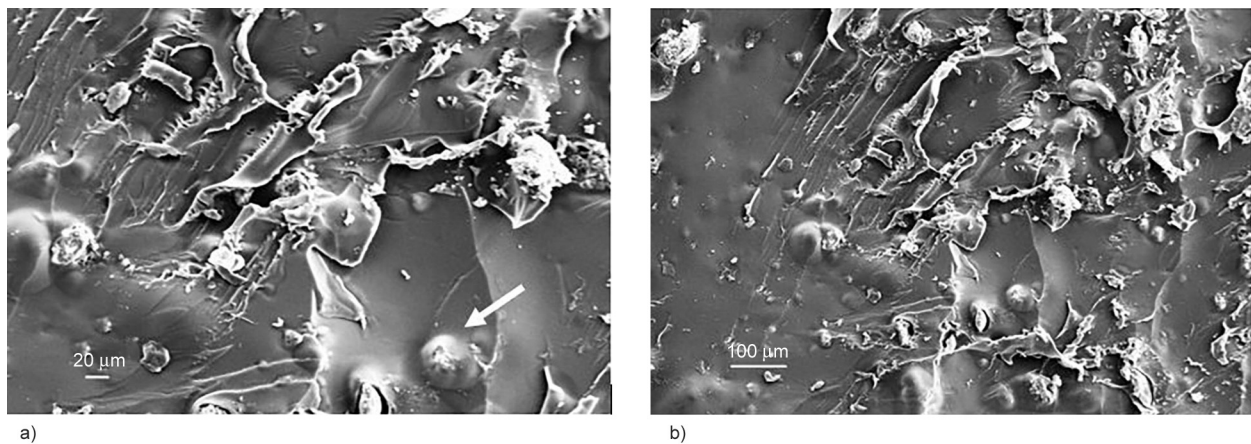


Figure 12. SEM fractured surface of ELC composites with 7 wt% lignin at 20 μm (a) and 100 μm (b). Arrows point out lignin particles.

5. Conclusions

In this work, we successfully fabricated new diacrylate mesogen-based ELC composites with Kraft lignin as the biobased filler for shape memory applications. The results of the lignin-ELC composites indicate excellent R_f via a thermomechanical shape memory process of nearly 100%. Specifically, the addition of lignin improves the R_f of the ELC composites in the range of 94.% to 97.0% upon its addition in the range 3 to 7 wt%, respectively. This bio-material can also reduce the recovery time of the composites when heated at a high temperature. The 7 wt% lignin composites could fully recover within 70 s, while the neat LCE sample showed a full recovery in 100 s.

Lignin-ELC composites as a novel combination, provide an excellent opportunity to develop more sustainable shape memory composite materials, given that they can be obtained from renewable resources and are abundant in nature. Lignin offers versatile chemistry due to its intrinsic structural aromatic compounds available through functional groups, viz. p-coumaryl, coniferyl, and syringyl alcohol.

Furthermore, the presence of Kraft lignin imparts improved dynamic mechanical properties in the composites by especially promoting the storage modulus as a key indicator of structures' true stiffness. The tendency of lignin particles to form spherical agglomerates at a macroscopic scale provides for an isotropic reinforcing effect in the ELC composites while enhancing the shape memory characteristics of the resultant composites.

The overall improved thermal and mechanical stabilities of the ELC composite improve the robustness of the applications where these are employed and hence enhance their long-term durability against environments exerting high thermal and mechanical stresses. Based on these results, the lignin-ELC composites have the potential to enable more sustainable applications of shape memory elastomeric composites in a variety of industrial environments for smart sensing and actuations such as soft robotics, smart actuators and sensors, and high-end space engineering.

Acknowledgements

P. Prathumrat would like to acknowledge Premika Govindaraj of Swinburne University of Technology for her initial assistance on the HR-1 DHR training.

References

- [1] Gong X., Tan K., Deng Q., Shen S.: Athermal shape memory effect in magnetoactive elastomers. *ACS Applied Materials and Interfaces*, **12**, 16930–16936 (2020). <https://doi.org/10.1021/acsami.0c01453>
- [2] Lai S.-M., Wang X.-F.: Shape memory properties of olefin block copolymer (OBC)/poly(ϵ -caprolactone) (PCL) blends. *Journal of Applied Polymer Science*, **134**, 45475 (2017). <https://doi.org/10.1002/app.45475>
- [3] Ramaraju H., Ul-Haque A., Verga A. S., Bocks M. L., Hollister S. J.: Modulating nonlinear elastic behavior of biodegradable shape memory elastomer and small intestinal submucosa(SIS) composites for soft tissue repair. *Journal of the Mechanical Behavior of Biomedical Materials*, **110**, 103965 (2020). <https://doi.org/10.1016/j.jmbbm.2020.103965>
- [4] Chen Z., Li Y., Yao C.: Biomass shape memory elastomers with rapid self-healing properties and high recyclability. *Biomacromolecules*, **22**, 2768–2776 (2021). <https://doi.org/10.1021/acs.biomac.1c00465>
- [5] Zhang Y., Hu Q., Yang S., Wang T., Sun W., Tong Z.: Unique self-reinforcing and rapid self-healing polyampholyte hydrogels with a pH-induced shape memory effect. *Macromolecules*, **54**, 5218–5228 (2021). <https://doi.org/10.1021/acs.macromol.0c02657>
- [6] Prathumrat P., Tiptipakorn S., Rimdusit S.: Multiple-shape memory polymers from benzoxazine–urethane copolymers. *Smart Materials and Structures*, **26**, 065025 (2017). <https://doi.org/10.1088/1361-665X/aa6d47>
- [7] Salaeh S., Das A., Wießner S.: Design and fabrication of thermoplastic elastomer with ionic network: A strategy for good performance and shape memory capability. *Polymer*, **223**, 123699 (2021). <https://doi.org/10.1016/j.polymer.2021.123699>
- [8] Prathumrat P., Nikzad M., Hajizadeh E., Arablouei R., Sbarski I.: Shape memory elastomers: A review of synthesis, design, advanced manufacturing, and emerging applications. *Polymers for Advanced Technologies*, **33**, 1782–1808 (2022). <https://doi.org/10.1002/pat.5652>
- [9] Xiao X., Hu J., Gui X., Qian K.: Shape memory investigation of α -keratin fibers as multi-coupled stimuli of responsive smart materials. *Polymers*, **9**, 87 (2017). <https://doi.org/10.3390/polym9030087>
- [10] Behl M., Lendlein A.: Shape-memory polymers. *Materials Today*, **10**, 20–28 (2007). [https://doi.org/10.1016/S1369-7021\(07\)70047-0](https://doi.org/10.1016/S1369-7021(07)70047-0)
- [11] Lendlein A., Behl M., Hiebl B., Wischke C.: Shape-memory polymers as a technology platform for biomedical applications. *Expert Review of Medical Devices*, **7**, 357–379 (2010). <https://doi.org/10.1586/erd.10.8>

- [12] Michal B. T., McKenzie B. M., Felder S. E., Rowan S. J.: Metallo-, thermo-, and photoresponsive shape memory and actuating liquid crystalline elastomers. *Macromolecules*, **48**, 3239–3246 (2015).
<https://doi.org/10.1021/acs.macromol.5b00646>
- [13] Kamal T., Park S.-Y.: Shape-responsive actuator from a single layer of a liquid-crystal polymer. *ACS Applied Materials and Interfaces*, **6**, 18048–18054 (2014).
<https://doi.org/10.1021/am504910h>
- [14] Lee K. M., Koerner H., Vaia R. A., Bunning T. J., White T. J.: Light-activated shape memory of glassy, azobenzene liquid crystalline polymer networks. *Soft Matter*, **7**, 4318–4324 (2011).
<https://doi.org/10.1039/C1SM00004G>
- [15] Beyer P., Zentel R.: Photoswitchable smectic liquid-crystalline elastomers. *Macromolecular Rapid Communications*, **26**, 874–879 (2005).
<https://doi.org/10.1002/marc.200500093>
- [16] Yu Y., Nakano M., Ikeda T.: Directed bending of a polymer film by light. *Nature*, **425**, 145 (2003).
<https://doi.org/10.1038/425145a>
- [17] Prathumrat P., Sbarski I., Hajizadeh E., Nikzad M.: A comparative study of force fields for predicting shape memory properties of liquid crystalline elastomers using molecular dynamic simulations. *Journal of Applied Physics*, **129**, 155101 (2021).
<https://doi.org/10.1063/5.0044197>
- [18] Lee K. M., Bunning T. J., White T. J.: Autonomous, hands-free shape memory in glassy, liquid crystalline polymer networks. *Advanced Materials*, **24**, 2839–2843 (2012).
<https://doi.org/10.1002/adma.201200374>
- [19] Burke K. A., Mather P. T.: Soft shape memory in main-chain liquid crystalline elastomers. *Journal of Materials Chemistry*, **20**, 3449–3457 (2010).
<https://doi.org/10.1039/B924050K>
- [20] Traugott N. A., Volpe R. H., Bollinger M. S., Saed M. O., Torbati A. H., Yu K., Dadivanyan N., Yakacki C. M.: Liquid-crystal order during synthesis affects main-chain liquid-crystal elastomer behavior. *Soft Matter*, **13**, 7013–7025 (2017).
<https://doi.org/10.1039/C7SM01405H>
- [21] Guin T., Settle M. J., Kowalski B. A., Auguste A. D., Beblo R. V., Reich G. W., White T. J.: Layered liquid crystal elastomer actuators. *Nature Communications*, **9**, 2531 (2018).
<https://doi.org/10.1038/s41467-018-04911-4>
- [22] Wen Z., McBride M. K., Zhang X., Han X., Martinez A. M., Shao R., Zhu C., Visvanathan R., Clark N. A., Wang Y., Yang K., Bowman C. N.: Reconfigurable LC elastomers: Using a thermally programmable monodomain to access two-way free-standing multiple shape memory polymers. *Macromolecules*, **51**, 5812–5819 (2018).
<https://doi.org/10.1021/acs.macromol.8b01315>
- [23] Rousseau I. A., Mather P. T.: Shape memory effect exhibited by smectic-C liquid crystalline elastomers. *Journal of the American Chemical Society*, **125**, 15300–15301 (2003).
<https://doi.org/10.1021/ja039001s>
- [24] Tokumoto H., Zhou H., Takebe A., Kamitani K., Kojio K., Takahara A., Bhattacharya K., Urayama K.: Probing the in-plane liquid-like behavior of liquid crystal elastomers. *Science Advances*, **7**, eabe9495 (2021).
<https://doi.org/10.1126/sciadv.abe9495>
- [25] Yu O., Kim K. H.: Lignin to materials: A focused review on recent novel lignin applications. *Applied Sciences*, **10**, 4626 (2020).
<https://doi.org/10.3390/app10134626>
- [26] Norberg I., Nordström Y., Drouge R., Gellerstedt G., Sjöholm E.: A new method for stabilizing softwood kraft lignin fibers for carbon fiber production. *Journal of Applied Polymer Science*, **128**, 3824–3830 (2013).
<https://doi.org/10.1002/app.38588>
- [27] Zong E., Liu X., Liu L., Wang J., Song P., Ma Z., Ding J., Fu S.: Graft polymerization of acrylic monomers onto lignin with $\text{CaCl}_2\text{-H}_2\text{O}_2$ as initiator: Preparation, mechanism, characterization, and application in poly(lactic acid). *ACS Sustainable Chemistry and Engineering*, **6**, 337–348 (2018).
<https://doi.org/10.1021/acssuschemeng.7b02599>
- [28] Nisha S. S., Nikzad M., Al Kobaisi M., Truong V. K., Sbarski I.: The role of ionic-liquid extracted lignin micro/nanoparticles for functionalisation of an epoxy-based composite matrix. *Composites Science and Technology*, **174**, 11–19 (2019).
<https://doi.org/10.1016/j.compscitech.2019.02.009>
- [29] Sternberg J., Pilla S.: Materials for the biorefinery: High bio-content, shape memory kraft lignin-derived non-isocyanate polyurethane foams using a non-toxic protocol. *Green Chemistry*, **22**, 6922–6935 (2020).
<https://doi.org/10.1039/D0GC01659D>
- [30] Chen S., Liu J.: Liquid metal enabled unconventional heat and flow transfer. *ES Energy and Environment*, **5**, 8–21 (2019).
<https://doi.org/10.30919/eseec8c318>
- [31] Liu L.-Y., Karaaslan M. A., Hua Q., Cho M., Chen S., Rennecker S.: Thermo-responsive shape-memory polyurethane foams from renewable lignin resources with tunable structures—properties and enhanced temperature resistance. *Industrial and Engineering Chemistry Research*, **60**, 11882–11892 (2021).
<https://doi.org/10.1021/acs.iecr.1c01717>
- [32] Xu Y., Odelius K., Hakkarainen M.: One-pot synthesis of lignin thermosets exhibiting widely tunable mechanical properties and shape memory behavior. *ACS Sustainable Chemistry and Engineering*, **7**, 13456–13463 (2019).
<https://doi.org/10.1021/acssuschemeng.9b02921>
- [33] Nguyen N. A., Meek K. M., Bowland C. C., Naskar A. K.: Responsive lignin for shape memory applications. *Polymer*, **160**, 210–222 (2019).
<https://doi.org/10.1016/j.polymer.2018.11.055>

- [34] Sivasankarapillai G., Li H., McDonald A. G.: Lignin-based triple shape memory polymers. *Biomacromolecules*, **16**, 2735–2742 (2015).
<https://doi.org/10.1021/acs.biomac.5b00655>
- [35] Likitaporn C., Mora P., Tiptipakorn S., Rimdusit S.: Recovery stress enhancement in shape memory composites from silicon carbide whisker-filled benzoxazine-epoxy polymer alloy. *Journal of Intelligent Material Systems and Structures*, **29**, 388–396 (2018).
<https://doi.org/10.1177/1045389x17708041>
- [36] Nair D. P., Podgórski M., Chatani S., Gong T., Xi W., Fenoli C. R., Bowman C. N.: The thiol-michael addition click reaction: A powerful and widely used tool in materials chemistry. *Chemistry of Materials*, **26**, 724–744 (2014).
<https://doi.org/10.1021/cm402180t>
- [37] de Freitas A. d. S., Rodrigues J. S., Maciel C. C., Pires A. A., Lemes A. P., Ferreira M., Botaro V. R.: Improvements in thermal and mechanical properties of composites based on thermoplastic starch and kraft lignin. *International Journal of Biological Macromolecules*, **184**, 863–873 (2021).
<https://doi.org/10.1016/j.ijbiomac.2021.06.153>
- [38] Kong F., Wang S., Gao W., Fatehi P.: Novel pathway to produce high molecular weight kraft lignin–acrylic acid polymers in acidic suspension systems. *RSC Advances*, **8**, 12322–12336 (2018).
<https://doi.org/10.1039/C7RA12971H>
- [39] Brazil T. R., Costa R. N., Massi M., Rezende M. C.: Structural, morphological, and thermal characterization of kraft lignin and its charcoals obtained at different heating rates. *Materials Research Express*, **5**, 045502 (2018).
<https://doi.org/10.1088/2053-1591/aab7c2>
- [40] Kim N., Li Q., Kyu T.: Effect of trans-cis photoisomerization on phase equilibria and phase transition of liquid-crystalline azobenzene chromophore and its blends with reactive mesogenic diacrylate. *Physical Review E*, **83**, 031702 (2011).
<https://doi.org/10.1103/PhysRevE.83.031702>
- [41] Gordobil O., Delucis R., Egüés I., Labidi J.: Kraft lignin as filler in PLA to improve ductility and thermal properties. *Industrial Crops and Products*, **72**, 46–53 (2015).
<https://doi.org/10.1016/j.indcrop.2015.01.055>
- [42] Chung Y-L., Olsson J. V., Li R. J., Frank C. W., Waymouth R. M., Billington S. L., Sattely E. S.: A renewable lignin–lactide copolymer and application in bio-based composites. *ACS Sustainable Chemistry and Engineering*, **1**, 1231–1238 (2013).
<https://doi.org/10.1021/sc4000835>
- [43] Charles J., Ramkumaar G. R., Azhagiri S., Gunasekaran S.: FTIR and thermal studies on nylon-66 and 30% glass fibre reinforced nylon-66. *E-Journal of Chemistry*, **6**, 909017 (2009).
<https://doi.org/10.1155/2009/909017>
- [44] Tejado A., Peña C., Labidi J., Echeverria J. M., Mondragon I.: Physico-chemical characterization of lignins from different sources for use in phenol–formaldehyde resin synthesis. *Bioresource Technology*, **98**, 1655–1663 (2007).
<https://doi.org/10.1016/j.biortech.2006.05.042>
- [45] Saed M. O., Elmadih W., Terentjev A., Chronopoulos D., Williamson D., Terentjev E. M.: Impact damping and vibration attenuation in nematic liquid crystal elastomers. *Nature communications*, **12**, 6676 (2021).
<https://doi.org/10.1038/s41467-021-27012-1>
- [46] Kargarzadeh H., Galeski A., Pawlak A.: PBAT green composites: Effects of kraft lignin particles on the morphological, thermal, crystalline, macro and micromechanical properties. *Polymer*, **203**, 122748 (2020).
<https://doi.org/10.1016/j.polymer.2020.122748>
- [47] Amini M., Hasheminejad K., Montazeri A.: Engineering the shape memory parameters of graphene/polymer nanocomposites through atomistic simulations: On the effect of nanofiller surface treatment. *Smart Materials and Structures*, **31**, 025010 (2021).
<https://doi.org/10.1088/1361-665x/ac4194>
- [48] Liu Y., Zhang W., Zhang F., Leng J., Pei S., Wang L., Jia X., Cotton C., Sun B., Chou T-W.: Microstructural design for enhanced shape memory behavior of 4D printed composites based on carbon nanotube/poly(lactic acid) filament. *Composites Science and Technology*, **181**, 107692 (2019).
<https://doi.org/10.1016/j.compscitech.2019.107692>
- [49] Hu L., Stevanovic T., Rodrigue D.: Compatibilization of kraft lignin-polyethylene composites using unreactive compatibilizers. *Journal of Applied Polymer Science*, **131**, 41040 (2014).
<https://doi.org/10.1002/app.41040>
- [50] Klapiszewski L., Jamrozik A., Strzemiescka B., Matykiewicz D., Voelkel A., Jesionowski T.: Activation of magnesium lignosulfonate and kraft lignin: Influence on the properties of phenolic resin-based composites for potential applications in abrasive materials. *International Journal of Molecular Sciences*, **18**, 1224 (2017).
<https://doi.org/10.3390/ijms18061224>